

2006-2010

**China National Report on Meteorology  
and Atmospheric Sciences**

*For*

The 25thd General Assembly of IUGG  
Melbourne, Australia, 28 June -7 July, 2011

By Chinese National Committee for  
The International Union of Geodesy and Geophysics  
Beijing, China

June, 2011

## PREFACE

As a rule, the International Association of Meteorology and Atmospheric Sciences (IAMAS) requests each of her member countries to submit, every four years, a progress report on the relevant operational and research fields, and exchange the report with other members during the International Union of Geodesy and Geophysics (IUGG) Assembly that is held every four years as well. During the last thirty years, the China National Committee for IAMAS has regularly composed its report. This National Report of the China National Committee for IAMAS is prepared for the XXV General Assembly of IUGG, Melbourne, Australia, 28 June -7 July, 2011 and introduces some advances and achievements in meteorology and atmospheric sciences in China mainly during 2006-2010.

The National Report consists of 14 papers that cover the following fields: middle atmosphere, weather and climate effects of the Tibetan Plateau, meteorological satellite and satellite meteorology, East Asian monsoon system, Atmospheric electricity, climate change, meso-scale atmosphere, data assimilation, nonlinear atmospheric dynamics and predictability for weather and climate, climate and weather predictions, carbon and nitrogen cycles, and etc. Those papers were also sent out for peer-review. If they are accepted, they will be published in a Special Issue of "Advances in Atmospheric Sciences" which is the journal of the China National Committee for IAMAS. Through this report you could briefly understand what Chinese Scientists have done and what they are going to do in China. We hope that this report will strengthen domestic exchanges and enhance international cooperation so that meteorology and atmospheric sciences in China will develop further, and we will be able to contribute more to the outside world.

Chinese National Committee for IAMAS

Lu Daren, Chairman

Yu Rucong, Vice-Chairman

Bian Jianchun, Secretary-General

June, 2011

# Characteristics, Processes and Causes of the Spatio-Temporal Variabilities of the East Asian Monsoon System

HUANG Ronghui (黄荣辉), CHEN Jilong (陈际龙), WANG Lin (王林) and Lin Zhongda (林中达)

Center for Monsoon System Research, Institute of Atmospheric Physics, Chinese Academy of Sciences, Beijing 100080

## ABSTRACT

Recent advances in the studies on the characteristics, processes and causes of the spatio-temporal variabilities of the East Asian monsoon (EAM) system are reviewed in this paper. Many studies have improved our understanding of the basic characteristics of horizontal and vertical structures, the annual cycle between the East Asian summer monsoon (EASM) system and the East Asian winter monsoon (EAWM) system, the characteristics of the spatio-temporal variabilities of the EASM system and the EAWM system, especially the characteristics of multi modes of their spatio-temporal variabilities. Moreover, some new results have been achieved in investigations on the air-sea interaction and air-land interaction processes affecting these variabilities of EAM system, and from these studies, the EAM system can be viewed as an atmosphere-ocean-land coupled system, i.e., the EAM climate system. Besides, further progresses have been made in the studies on the internal physical mechanism of the EAM climate system variability, especially on the characteristics and property of the EAP pattern teleconnection over East Asia and the North Pacific and the "Silk Road pattern" teleconnection along the westerly jet stream in the upper troposphere over the Asian continent, in addition to in the studies on the dynamical effect of quasi-stationary planetary wave activity on the EAM system variability. Finally, some scientific problems on the EAM system variabilities, which needs to studies further, are also put forward in this paper.

**Key words:** East Asian monsoon system, spatio-temporal variations, climate system, the EAP pattern teleconnection

## 1. Introduction

The East Asian monsoon (EAM) system features strong southerly wind in summer, i.e., the East Asian summer monsoon (EASM), and strong northerly wind in winter, i.e., the East Asian winter monsoon (EAWM). Generally, the southerly wind with wet air prevails over eastern China, Korea and Japan in summer, but the northwesterly wind with dry air prevails over North China, Central China, and Northeast China, Korea and Japan, and northeasterly wind over East China, South China and the Indo-China Peninsula in winter. The strong summer monsoon flow can bring a large amount of water vapor into East Asia and can cause severe climate disasters such as droughts and floods and hot summers etc in eastern China, Korea and Japan (e.g., Huang et al., 1998; Huang and Zhou, 2002; Huang et al., 2008). While the strong winter monsoon flow can bring a large amount of cold and dry air into East Asia and can cause climate disasters such as low-temperature and severe snow storms in

Northwest China, Northeast China, North China, Korea and Japan in winter and severe dust-storms in Northwest China and North China in spring etc(e.g., Chen et al. 2000; Huang et al. 2007; Gu et al., 2008). Besides, the strong EAWM can triggers strong convective activities over the maritime continent of Borneo and Indonesia (e.g., Chang et al., 1979; Lau and Chang, 1987). Moreover, many studies (e.g., Tao and Chen, 1987; Chen et al., 1991; Ding, 1994; Chang et al., 2000; Huang et al., 2003; Huang et al., 2004; Huang et al., 2007) have shown that the EAM system play an important role in the global climate variability, especially in the climate variability over East Asia.

The climate variability in China is mainly influenced by the EAM system (e.g., Zhu, 1934; Tu and Huang, 1944; Tao and Chen, 1987). Since the interannual and interdecadal variabilities of EAM system are significant, climatic disasters such as droughts and floods in summer and severe cold surges, freezing rain and low temperature in winter frequently occur in China (e.g., Huang and Zhou, 2002; Huang, 2006; Gu et al., 2008; Huang et al., 2010). Especially, since the 1980s, severe climatic disasters over large areas have caused huge damage to agricultural and industrial productions in China. Each year, the economic losses due to droughts and floods can reach over 200 billion yuan (i.e., about US\$30 billion), (e.g., Huang et al., 1999; Huang and Zhou, 2002). For example, the particularly severe floods occurred in the Yangtze River basin and the Songhua and Nen River valleys in the summer of 1998 caused the losses as high as 260 billion yuan (i.e., about US\$ 38 billion)(e.g., Huang et al, 1998). In addition, from the winter of 2009 to the summer of 2010, many severe climatic disasters occurred in China, such as particularly severe low-temperature and snowstorms in Northeast China, Northwest China and North China from November 2009 to January 2010, the particularly severe drought in Southwest China from the autumn of 2009 to the spring of 2010, severe floods in South China and the Yangtze River basin during the period of May-July and particularly severe floods in the middle and eastern Northeast China from late July to early August and in late August, and severe hot summer in Northwest China, South China, the Yangtze River basin and North China. These severe climatic disasters have caused huge losses over those in the summer of 1998. Moreover, the persistent droughts in North China and southern Northeast China since the late 1990s to now not only brought huge losses to agriculture and industry, but also seriously affected the water resources and ecological environment in these regions.

The occurrences of the above-mentioned climatic disasters are closely associated with the spatio-temporal variabilities of the EAM system. (e.g., Huang, 2006; Huang, 2010). While the EAM system variabilities are influenced not only by the internal dynamical and thermodynamical processes in the atmosphere, but also by the interactions among various spheres of the air-sea-land coupled system. As shown by Webster et al. (1998), the monsoon can be seen as an atmosphere-ocean-land coupled system. Similarly, the EAM system can be also seen as a coupled system including atmosphere, ocean and land surface, which is called as the EAM climate system to distinguish it from a general circulation system proposed by Tao and Chen (1987)(e.g., Huang et al., 2004; Huang et al., 2007). The EAM climate system

include the EAM circulation, the western Pacific subtropical high and the mid-and high latitude disturbances in the atmosphere, the thermal states of the western Pacific warm pool and convective activity around the Philippines, the thermal state of the tropical Indian Ocean and ENSO cycle in the tropical Pacific in the Ocean, the dynamical and thermal effects over the Tibetan Plateau, and the land surface process in the arid and semi-arid areas of Northwest China, and the snow cover over the Eurasian continent and the Tibetan Plateau in the land surface processes etc. The characteristics of the spatio-temporal variabilities of this system and their impacts on the climatic disasters in China have been analyzed further for recent years, and the internal and external physical processes that influence these variabilities have been also discussed in more detail recently.

This paper attempts to summarize the advances in the studies on the characteristics, causes and processes of the spatio-temporal variabilities of the EAM system, especially on the spatio-temporal variations of the EASM and EAWM systems, the impacts and processes of the air-sea-land coupling system on the EAM system variability and the internal dynamical and thermodynamical in the EAM system variability. The review mainly focuses on the research progresses in China during the recent five years.

## **2. Climatological characteristics of the EASM system**

Since there are close associations among the South Asian monsoon (SAM), the East Asian monsoon (EAM) and the North Australian monsoon (NAM), some scholars considered them as three subsystems of the Asian-Australian monsoon system (e.g., Webster et al., 1998). However, it should be seen that the characteristics of EAM system are different from those of SAM and NAM systems. According to the study by Tao and Chen (1987), the EASM system is not only a part of tropical monsoon, but also is of a property of subtropical monsoon because it is influenced by the western Pacific subtropical high and the disturbances over middle latitudes. But the South Asian summer monsoon (SASM) is only tropical monsoon. Therefore, the characteristics of the spatio-temporal variations of the EASM system may be different from those of the South Asian summer monsoon (SASM) system.

### ***2.1 Characteristics of circulation structure in the EASM system***

The investigation by Tao and Chen (1985) showed the main components of the EASM system include: the Indian SW monsoon flow, the Australian cold anticyclone, the cross-equatorial flow along the east to 100° E, the monsoon trough (or ITCZ) over the South China Sea (SCS) and the tropical western Pacific, the western Pacific subtropical high and the tropical easterly flow, the Meiyu (or Baiu in Japan, or Changma in Korea) frontal zones, and the disturbances over mid-latitudes. Therefore, the EASM system is a relatively independent monsoon circulation system although it links to the SASM.

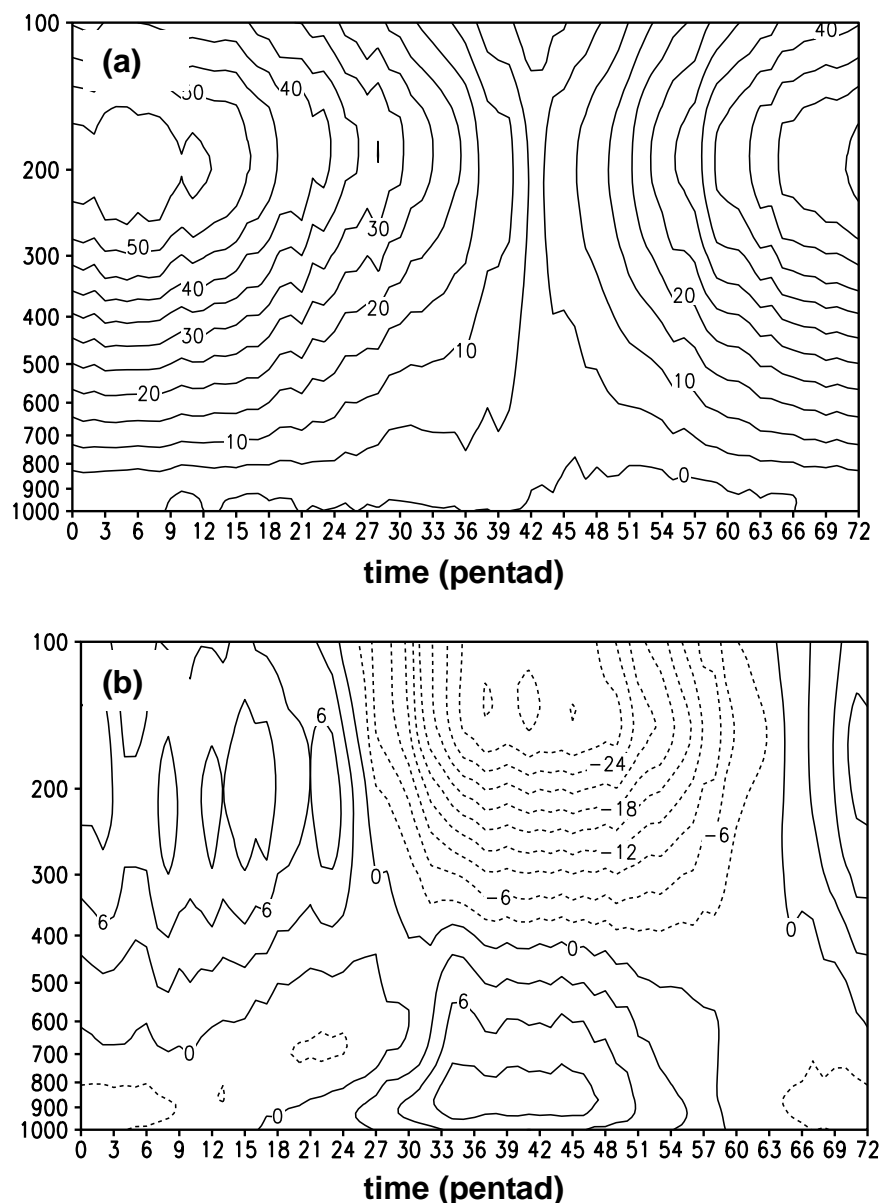


Fig. 1. Altitude-time cross section of zonal wind averaged for 1979~2003 over (a) East Asia ( $20^{\circ}\sim 45^{\circ}\text{N}$ ,  $100^{\circ}\sim 140^{\circ}\text{E}$ ) and (b) South Asia ( $0^{\circ}\sim 25^{\circ}\text{N}$ ,  $60^{\circ}\sim 100^{\circ}\text{E}$ ). Unit: m/s. The solid and dashed lines in Figs.1a and 1b indicate the westerly and easterly winds, respectively. The data is from NCEP/NCAR reanalysis data (e.g., Kalnay et al. 1996).

Recently, Chen and Huang (2006) analyzed the climatological characteristics of wind structure of the EASM system over the area ( $0^{\circ}\sim 45^{\circ}\text{N}$ ,  $100^{\circ}\text{E}\sim 140^{\circ}\text{E}$ ) and the SASM system over the area ( $0^{\circ}\sim 25^{\circ}\text{N}$ ,  $60^{\circ}\text{E}\sim 100^{\circ}\text{E}$ ) in boreal summer, respectively. The result shows that the vertical structure of zonal flow in the EASM region includes the vertical easterly shear in the region to the south of  $25^{\circ}\text{N}$ , such as the SCS and the tropical western Pacific, and the vertical westerly shear in the subtropical region to the north of  $25^{\circ}\text{N}$ , such as the mainland of China, Korea and Japan, as shown in Fig.1a. However, as shown in Fig.1b, the SASM system purely belongs to the tropical monsoon with strong zonal flow and vertical easterly shear, i.e., low-level westerly wind and high-level easterly wind.

Moreover, as shown in Fig.2a, the EASM system is composed of the tropical and

subtropical summer monsoons with significant meridional flow and vertical northerly shear, i.e., low-level southerly wind and high-level northerly wind. And compared to the meridional component of wind field in the SASM system shown in Fig.2b, the low-level southerly wind in the EASM region are stronger than those in the SASM system.

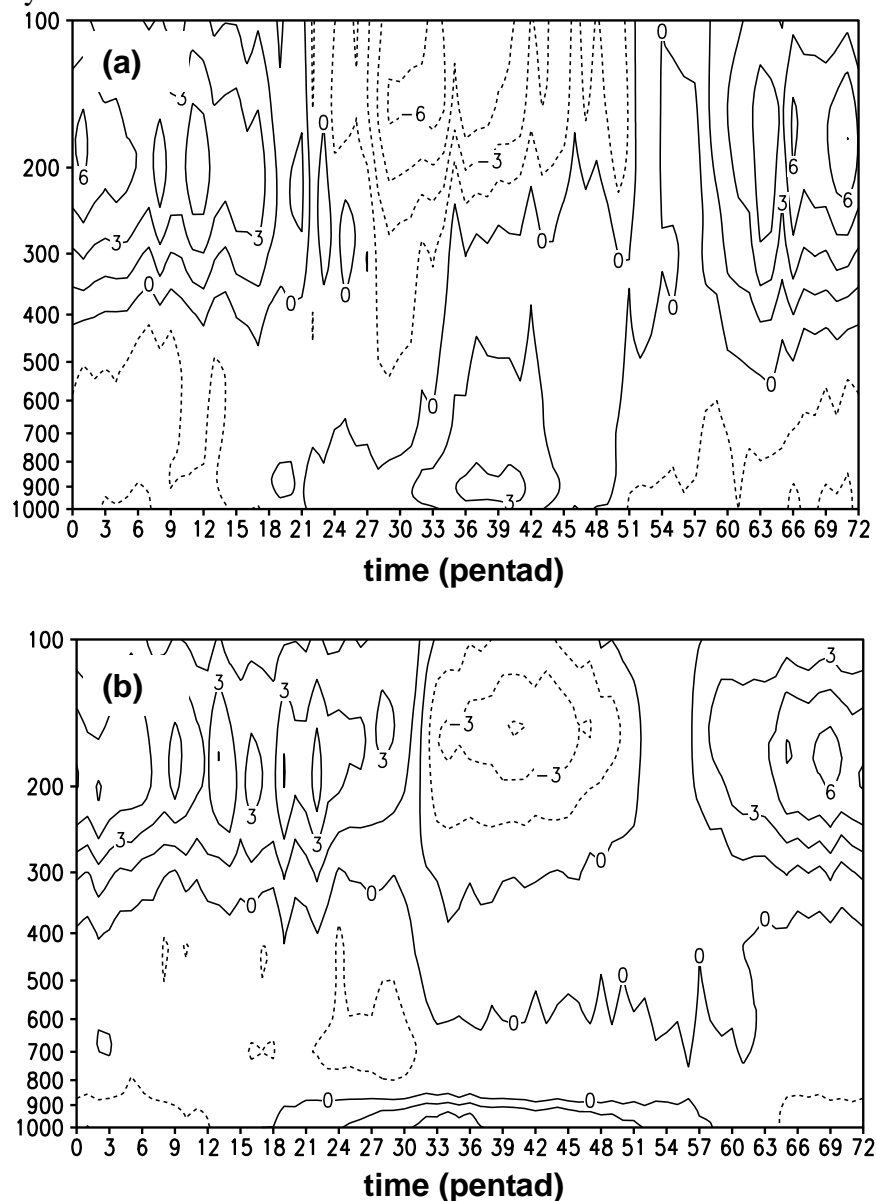


Fig. 2. As in Fig.1 except for the meridional wind

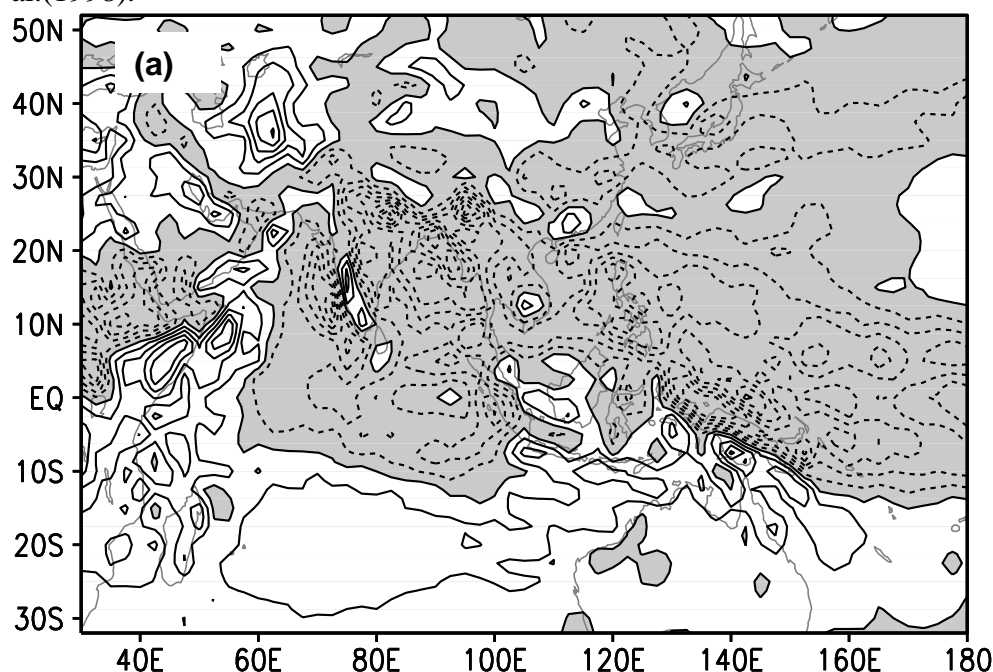
The differences between the annual cycle of wind field in the EAM system and that in the SAM system can be also seen from the altitude-time cross sections of zonal and meridional winds over East Asia and South Asia, as shown in Fig. 1 and Fig.2. From Fig.1a, it may be seen that the strong westerly wind prevails in the lower troposphere below 500hPa and the strong easterly wind is found in the upper troposphere above 500hPa from early June over South Asia. However, from early October, the westerly wind becomes into the easterly wind in the lower troposphere below 700hPa, while the easterly wind becomes into the westerly wind in the upper

troposphere above 500hPa over this region. Therefore, in the SAM region, the annual cycle between summer and winter monsoons is obvious in zonal wind field. However, compared Fig.1a with Fig. 1b, the seasonal reverse of zonal wind in the troposphere over East Asia is not significant than that in the SAM region. As shown in Fig. 2a, the seasonal reverse of meridional wind obviously occurs in both the lower troposphere and the upper troposphere over East Asia in early June and mid-September, respectively.

From the above-mentioned analyses, it may be seen that the annual cycle between summer and winter monsoons mainly appears in the meridional component of wind field in the EASM region, which is different from that in the SAM system.

## 2.2 Characteristics of water vapour transports in the EASM region

Recently, Chen and Huang (2007) again analyzed the characteristic of water vapour transports over the EASM and the SASM regions using the ERA-40 reanalysis data for 1979~2002. Their result showed that the characteristic of water vapour transports in the EASM region are greatly different from that in the SASM system. They pointed out that the anomalous summer monsoon rainfall in East Asia is mainly influenced by the three branches of water vapor transports coming from the Bay of Bengal, the South China Sea and the tropical western Pacific, respectively. And their study showed that in the SASM region, the zonal transport of water vapour is dominant and the meridional transport is relatively smaller, but the meridional transport of water vapour is dominant in the EASM region. And as shown in Fig.3a and Fig.3b, the convergences of water vapour transports, which are closely associated with monsoon rainfall, are due to the moisture advection and convergences of wind field in the EASM region, but those are mainly due to the convergences of wind field in the SASM region. The result is in good agreement with those analyzed by Huang et al.(1998).



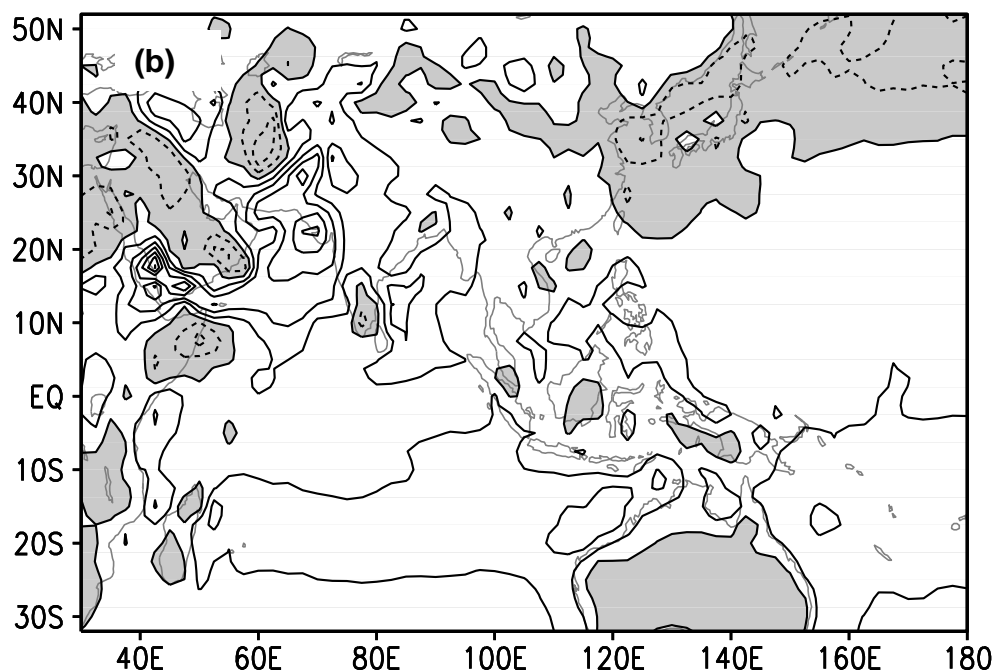


Fig. 3 Distributions of the divergence of water vapor transport due to (a) the divergence of wind field and (b) the moisture advection in the Asian monsoon region during boreal summer. Units: mm/d. The solid and dashed lines in Figs.3a and 3b indicate divergence and convergence, respectively, and areas of convergence are shaded. The data is from the ERA-40 reanalysis data (e.g. Uppala et al., 2005)

Huang and Chen (2010) analyzed the differences between the summertime water vapor transports in the EASM region and those in the arid and semi-arid region of Northwest China using the daily data of the ERA-40 reanalysis. The results showed that there are some obvious differences between the summertime water vapor transport in the EASM region and that in arid and semi-arid region. Since a large amount of water vapor are transported by the Asian summer monsoon flow from the Bay of Bengal, the South China Sea and the tropical western Pacific into the EASM region, the meridional water vapor transport fluxes are larger than the zonal water vapor transport fluxes in South China and the Yangtze River valley. But influenced by the westerly zone over mid-latitudes, the summertime zonal water vapor transport fluxes are larger than the meridional water vapor transport fluxes, and their divergence mainly depends on the moisture advection in the arid and semi-arid region of Northwest China. Moreover, either zonal or meridional water vapor transport fluxes in the arid and semi-arid region are smaller about one order than those in the EASM region, which causes summertime rainfall is very small in Northwest China.

### **2.3 Characteristics of rainfall cloud system in the EASM system**

Recently, Du and Huang(2010) pointed out that just due to the differences of the circulation structure and water vapor transport between the EASM region and the SASM region, the rainfall cloud system in the EASM region is different from that in the SASM region. They analyzed the characteristics of spatio-temporal distributions of convective rainfall and stratiform rainfall from TRMM(Tropical Rainfall Measuring Mission) precipitation data for 12 years. And their results showed that the

spatial distributions of convective rainfall and stratiform rainfall mainly exhibit a variation with latitude in the EASM region. In the subtropical monsoon region to the north of 25°N, the ratio between stratiform rainfall and total rainfall is about 60% in summer and it becomes high in proportion to latitude in the north of 25°N, and this ratio is variable with reason. But in the low-latitudes to the south of 25°N, the summertime rainfall is mainly due to the convective cloud system, whose ratio to total rain is about 50%, and this ratio always is same in this region. Thus, the summertime rainfall cloud-system in the EASM system is mainly due to stratiform cloud system in the north of 25°N and due to convective cloud system in the south of 25°N. However, the summertime rainfall cloud-system in the SASM system is mainly due to convective cloud system. Fu et al. (2008), and Liu and Fu (2010) analyzed the seasonal characteristics of convective rainfall and stratiform rainfall in Asian monsoon region and climatological characteristics of convective rainfall and stratiform rainfall in summer over South China using the TRMM data for 10 years. Their result also showed the ratio between stratiform rainfall and total rainfall is similar to that between convective rainfall and total rain in South China. These studies can explain that the summertime rainfall cloud-system in the EASM system is a mixing of stratiform cloud-system and convective cloud-system. This may lead to the difficulty of cumulus parameterization in numerical modeling of the EASM system (e.g., Cheng et al., 1998)

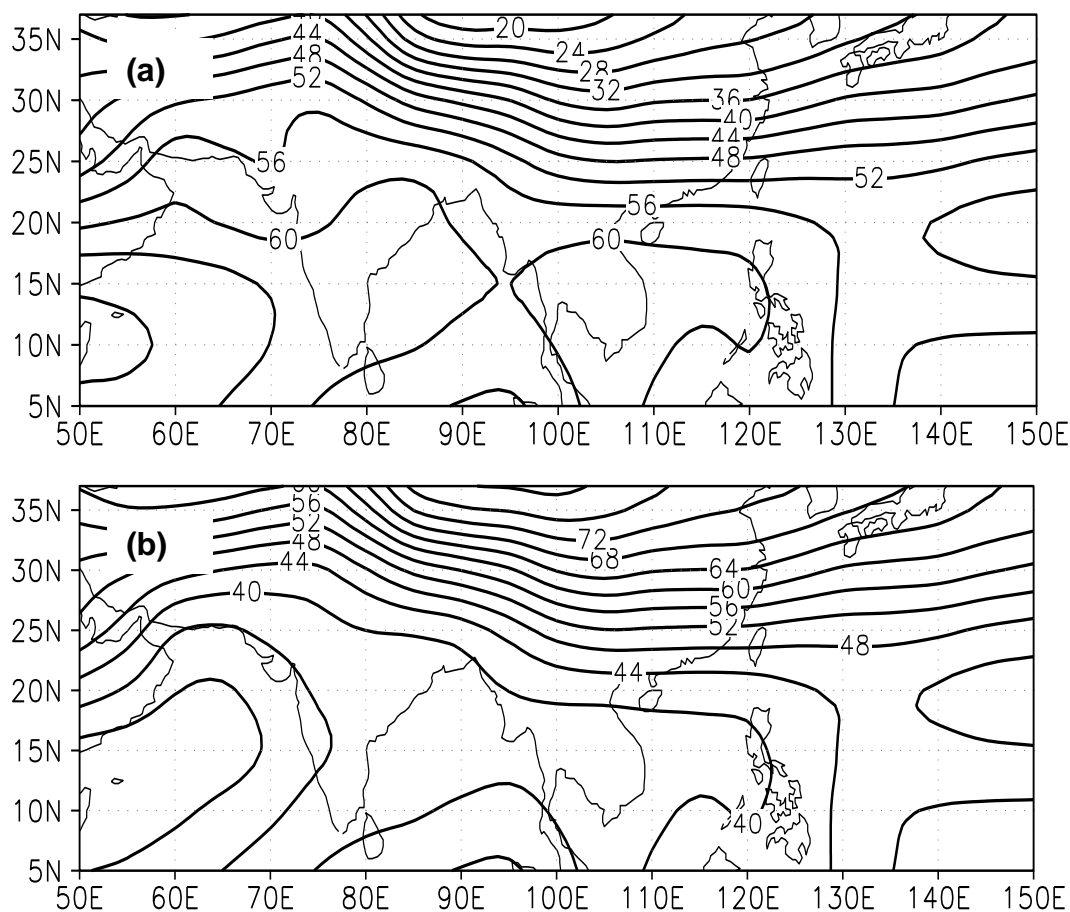


Fig. 4 Distributions of the average summertime rainfall (percentage) for 1988~2009

due to (a) convective rainfall and (b) stratiform rainfall, analyzed from TRMM data (e.g., Iguch et al., 2000)

From the above-mentioned results, it may be well explained that the EASM system is different from the SASM system and is a relatively independent monsoon system although it is also influenced by the SASM system.

### **3. Characteristics of the spatial-temporal variabilities of the EASM system**

Since the EASM system variability is influenced by not only the SASM and the western Pacific subtropical high (e.g., Tao and Chen, 1987; Huang and Sun, 1992), but also the mid-and high latitude disturbances (e.g., Tao and Chen, 1987), the spatio-temporal variations of the EASM system are significant but very complex. And these variations have an important impact on the spatio-temporal variations of climate disasters in China (e.g., Huang et al., 2007; Huang et al., 2008; Huang et al., 2010), thus, the spatio-temporal variabilities of EASM system, especially summer monsoon rainfall in East Asia, are emphasized in this Section.

#### **3.1 Interannual variations of onset and northward advances of the EASM system**

According to the studies by Tao and Chen (1987), the earliest onset of Asian summer monsoon (ASM) is over the SCS and the Indo-China Peninsula, and it is generally called as the South China Sea monsoon (SCSM) in China. But Ding and He (2006) recently proposed that the earliest onset of the ASM is over the tropical eastern Indian Ocean. The early or late onset of the ASM has an important impact on the interannual variability of summer monsoon rainfall in East Asia (e.g., Huang et al., 2005, 2006c)

In order to investigate the interannual variability of onset date and process of the SCSM, it is necessary to define an index for measuring the SCSM onset. Generally, the appearance of strong convective activity and the southwesterly flow over the SCS signals the onset of the SCSM. However, there are many definitions of the SCSM onset (e.g., Wang et al., 2004). Compared with other definitions of the SCSM onset, the definition proposed by Liang and Wu (2002) appears to be more reasonable and was used in our studies (e.g., Huang et al., 2005; Huang et al., 2006c). Huang et al. (2005, 2006c) pointed out that the SCSM onset is closely associated with the thermal state of the tropical western Pacific and the convective activity around the Philippines. In order to explain the impact of convective activity over the tropical western Pacific on the SCSM onset, the relationship between the SCSM onset date and convective activity around the Philippines (i.e.,  $10^{\circ}\sim 20^{\circ}\text{N}$ ,  $110^{\circ}\sim 140^{\circ}\text{E}$ ) in spring is analyzed by Huang et al. (2006c) using the observed date of high cloud amount (HCA) obtained by GMS satellite. As shown in Fig.5, there is an out-phase relationship between the SCSM onset date and the HCA around the Philippines in spring. The correlation coefficient between them reaches to  $-0.76$ , which exceeds the 99% confidence level. This can explain well that the convective activity around the Philippines has a great influence on the SCSM onset. In a spring with strong convective activity around the Philippines, which is generally found in a warming period of the tropical western Pacific, the SCSM onset is early. On the other hand, the SCSM onset is late in a spring with weak convective activity around the Philippines, which is generally found in a cooling period of the tropical western Pacific. The result

shows that the interannual variability of SCSM onset date is very large and is closely associated with the thermal states of the tropical western Pacific, especially the convective activity around the Philippines in spring.

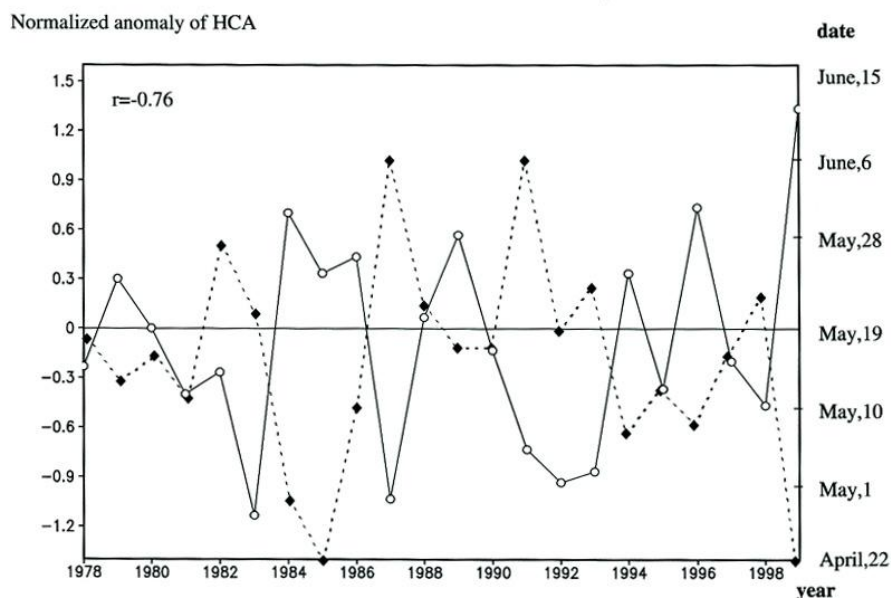


Fig. 5 Interannual variations of normalized high cloud amount (HCA) averaged for the area around the Philippines (i.e.,  $10^{\circ}\sim 20^{\circ}\text{N}$ ,  $110^{\circ}\sim 140^{\circ}\text{E}$ ) in spring (solid line) and the SCSM onset date (dashed line) (from Liang and Wu, 2002). The observed data of HCA is obtained from Monthly Report on Climate System JMA

Huang et al. (2006c) also analyzed the influence of the thermal state of the tropical western Pacific on the SCSM onset process. Their results show as follows: When the tropical western Pacific is in a warming state in spring, since the western Pacific subtropical high shifts eastward, the twin anomalous cyclones can early appear over the Bay of Bengal and Sumatra before the SCSM onset. Thus, the south westerly flow and strong convective activities can be intensified over Sumatra, the Indo-China Peninsula and the SCS in mid-May. This leads to early onset of the SCSM, as shown in Fig. 6a. On the other hand, when the tropical western Pacific is in a cooling state in spring, since the western Pacific subtropical high anomalously shifts westward, the twin anomalous anticyclones are located over the equatorial eastern Indian Ocean and Sumatra from late April to mid-May. Thus, the southwesterly flow and convective activities cannot be early intensified over the Indo-China Peninsula and the SCS, only when the western Pacific subtropical high moves eastward, then the weak trough located over the Bay of Bengal can be intensified and becomes into a strong trough. As a result, the strong southwesterly wind and convective activities can be generally intensified over the Indo-China Peninsula and the SCS in late May. This leads to late onset of the SCSM, as shown in Fig. 6b.

Following the SCSM onset, the monsoon will move northward over East Asia. Huang and Sun (1992) discussed well the dependence of the northward advance of the EASM system on the thermal state of the tropical western Pacific. And Huang et al.

(2005) investigated further the interannual variations of the intraseasonal variability of EASM system characterized as the northward advances and southward retreat of the EASM system. Their results showed the northward advances of the EASM system after the onset over the SCS are also influenced by the thermal state of the tropical western Pacific in summer, and there are close relationships among the thermal states of the tropical western Pacific, the convective activity around the Philippines, the western Pacific subtropical high, and the summer monsoon rainfall in East Asia. As shown in Fig. 6a, when the thermal state in the tropical western Pacific is in a warming state, i.e., the warm sea water is accumulated in the West Pacific warm pool in summer, the convective activity is intensified from the Indo-China Peninsula to the east of the Philippines. In this case, the western Pacific subtropical high shifts unusually northward, and the summer monsoon rainfall may be below normal in the Yangtze and Huaihe River basins of China, South Korea, and Japan, and drought may occur in these regions. On the other hand, as shown in Fig.6b, when the thermal state in the tropical western Pacific is in a cooling state, the convective activity is weak around the Philippines in summer, in this case, the western Pacific subtropical high may shift southward. And the summer monsoon rainfall may be above normal in the Yangtze and the Huaihe River valleys of China, South Korea, and Southwest Japan. Therefore, following a spring with late onset of the SCSM, severe floods may occur in the Yangtze River and Huaihe River valley, but droughts will be caused in North China in summer, such as in the summers of 1998 and 2010

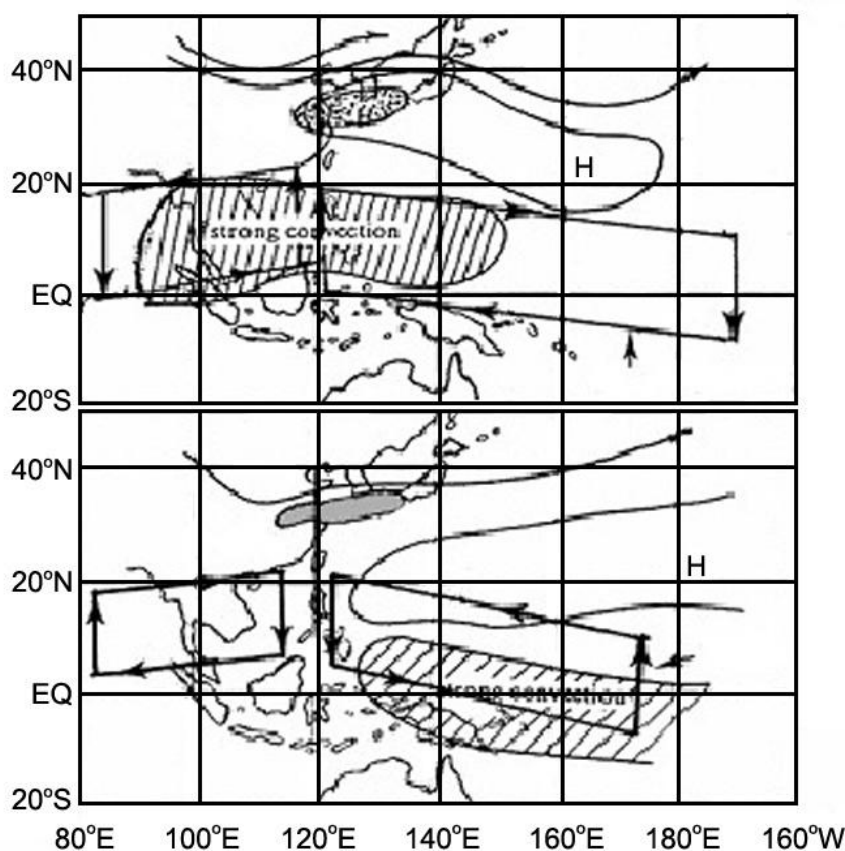


Figure 6. Schematic map of the relationships among the thermal states of the tropical

western Pacific (TWP)(i.e., Eq.~14° N, 130°~150° E) in spring, the convective activity around the Philippines, the western Pacific subtropical high, the onset of SCSM and the summer monsoon rainfall in East Asia. (a) in the warming state of the TWP; (b) in the cooling state of the TWP.

Therefore, the thermal state of the tropical western Pacific, especially the oceanic heating content (OHC) anomaly in the area of NINO. west (i.e., Eq.~14° N, 130°~150° E) in spring (March-May) and summer can be considered as a physical factor affecting the SCSM onset and summertime droughts and floods in the Yangtze River and the Huaihe River valleys, South Korea and Japan, especially, Fig.6 may be considered as a conceptive map of seasonal prediction for summertime droughts and floods in eastern China.

### ***3.2 Characteristics of multi-modes in the spatio-temporal variabilities of the EASM system***

The characteristics of multi-modes of the spatio-temporal variabilities of the EASM system is shown not only in monsoon rainfall, but also in water vapor transport in this system.

Huang et al. (2006b, 2007) analyzed the spatio-temporal variabilities of the summertime (June-August) precipitation in eastern China using the observed precipitation data at 160 stations in China. From the analyzed results, they proposed that there are characteristics of multi-modes i.e., meridional tripole pattern and meridional dipole pattern, in spatial distributions of the EASM system variability. Thus, the characteristics of multi-modes of the spatio-temporal variabilities of the EASM system are discussed further in the following.

Recently, Huang et al. (2010) analyzed further the leading modes of summertime precipitation anomalies in eastern China using more detail precipitation, i.e., precipitation data at 516 observational stations of China, and the EOF analysis method. The result also showed that there are two leading modes in the spatio-temporal variations of the summertime precipitation anomalies in eastern China. The first mode exhibits an characteristic of quasi-biennial oscillation with a meridional tripole pattern in spatial distribution shown in Figs. 7a and 7b, and this mode is also of interdecadal variability in addition to the interannual variability. Moreover, as shown in Fig.8b, the second mode exhibits an characteristic of obvious interdecadal variability, and it is of a characteristic of meridional dipole pattern in spatial distribution shown in Fig.8a. Therefore, the spatio-temporal variabilities of EASM system are characterized by multi-modes.

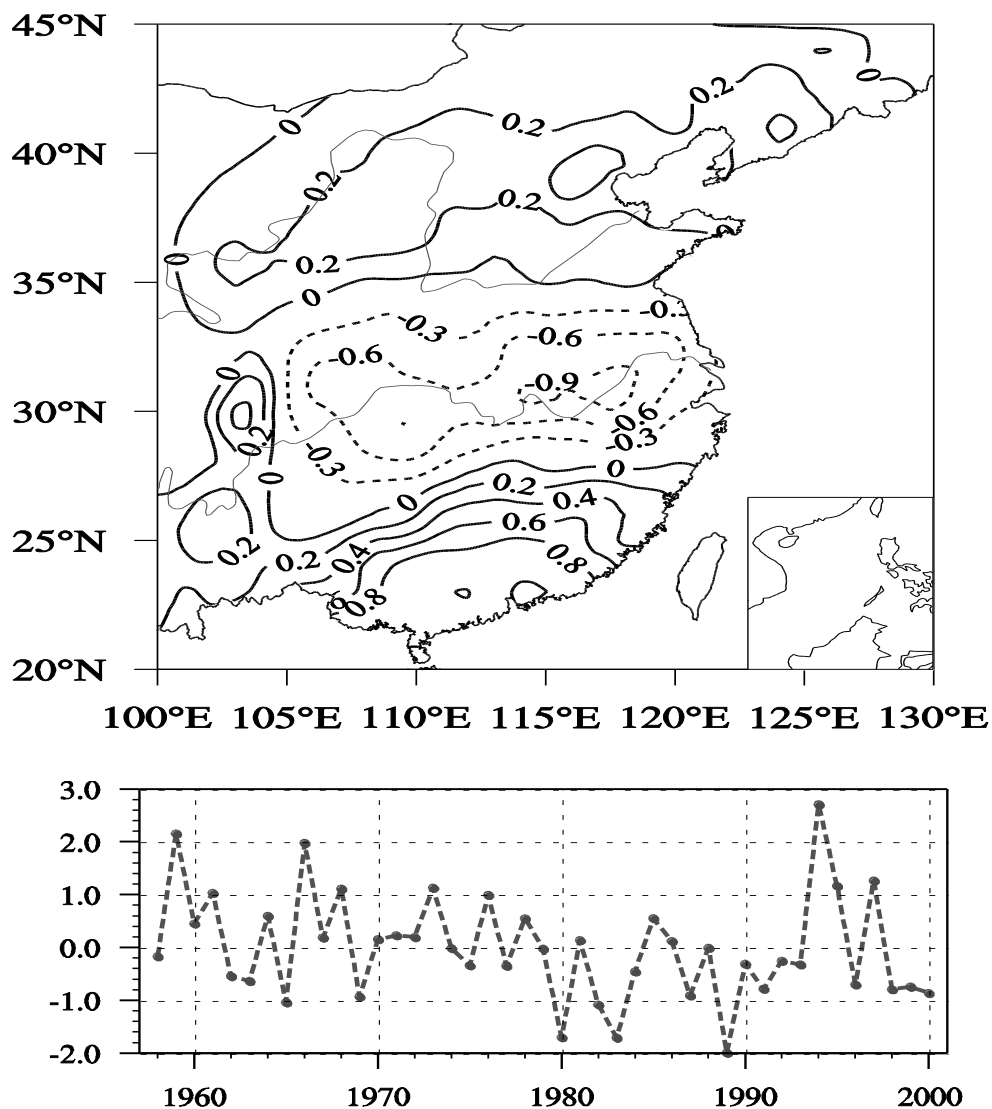


Figure 7 (a). Spatial distribution and corresponding time coefficient series of the first component of EOF analysis (i.e., EOF1) of summertime (JJA) rainfall in eastern China for 1958~2000. The solid and dashed lines in Fig.7a indicate positive and negative signals, respectively, and the EOF1 explains 15.3% of the variance. The precipitation data is from the precipitation dataset at 756 stations of China by China Meteorological Administration (CMA)

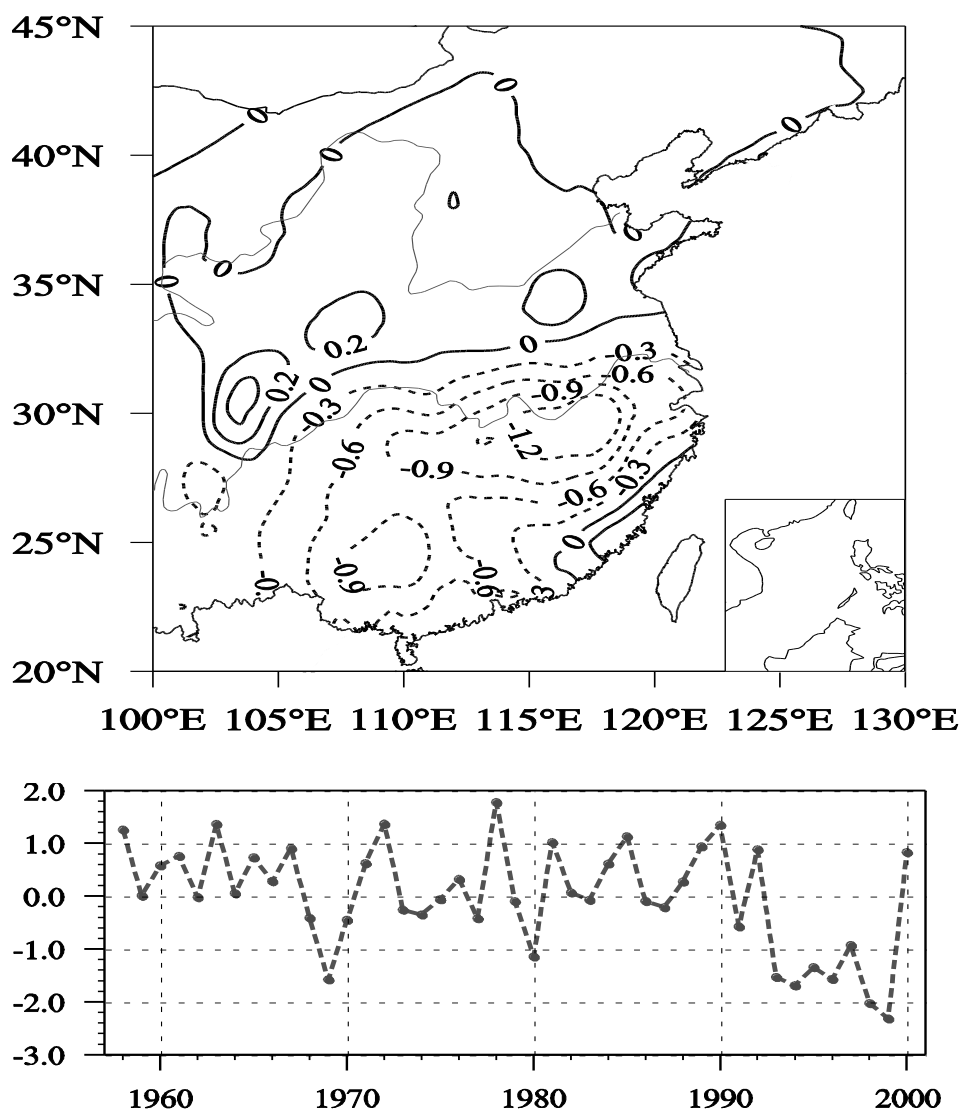


Figure 8. As in Fig.7 except for the EOF2, the EOF2 explains 13.2% of the variance.

The interannual variability with the meridional tripole pattern in spatial distribution of EASM system variability can be also seen from the distributions of summertime droughts and floods in eastern China. As shown in Figs.9a~d, the summertime monsoon rainfall in the summers of 1980, 1983, 1987 and 1998 was above normal in the Yangtze River and the Huaihe River valleys and below normal in South China and North China, respectively. These caused severe floods in the Yangtze River and the Huaihe River valleys and droughts in South China and North China in these summers, respectively. Oppositely, the summertime monsoon rainfall in the summers of 1976 and 1994 was below normal in the Yangtze River and the Huaihe River valleys and above normal in South China and North China, as shown in Fig.9e and Fig.9f, respectively. Thus, severe droughts were caused in the Yangtze River and the Haihe River valleys and floods in South China in these two summer, respectively.

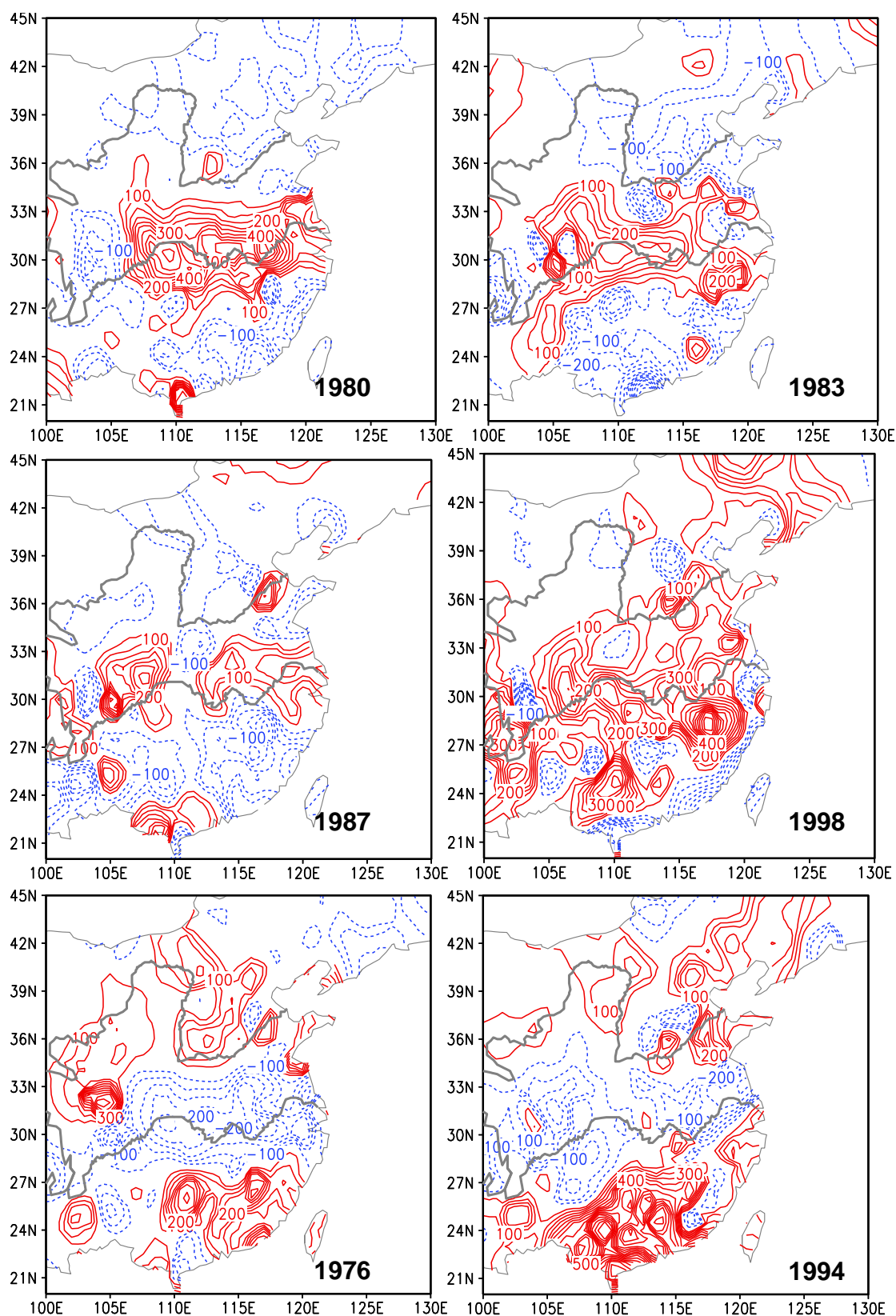


Fig.9. Distributions of monsoon rainfall anomalies (percentage) in the summers with the typical flood (a)1980, (b)1983, (c)1987and (d)1998 and in the summers with the typical drought (e) 1976 and (f)1994 in the Yangtze River and the Huaihe River valleys. The solid and dashed countous indicate positive and negative anomalies, respectively.

The above-mentioned studies show that the characteristic of quasi-biennial oscillation appears not only in the interannual variability of SASM system(e.g., Yasunari and Suppiah, 1984), but also in the interannual variability of EASM system. As pointed out by Ding (2007), thus, the quasi-biennial oscillation may be a leading mode of the Asian summer monsoon including the EASM and the SASM systems.

The characteristics of multi-modes in the spatio-temporal variabilities of EASM system are shown not only in the spatio-temporal variabilities of monsoon rainfall, but also in water vapor transports in the EASM system. Recently, Huang et al.,(2010) analyzed further the spatio-temporal variabilities of water vapor transport fluxes in the EASM system using the daily four times of moisture and wind fields of ERA-40 reanalysis (Figures are omitted). From their analyzed results, it can be also seen that there are also two leading modes i.e., meridional tripole pattern and meridional dipole pattern, in spatial distributions of the EOF1 and EOF2 of zonal water vapor transport fluxes in the EASM region. There are also obvious interannual variability with a quasi-biennial oscillation and interdecadal variability in the corresponding time series of the EOF1 of zonal water vapor transports in the EASM region, respectively. And from the corresponding time series of the EOF1 of meridional water vapor transport in the EASM region, it can be clearly seen that there is an obvious interdecadal variability. From the late 1950s to the early 1970s, the norward water vapor transport was strong, but it became weaker from the early 1970s to the early 1990s, and it again became strong from the early 1990s to the late 1990s. However, from the result analyzed by Zhou et al., (2010) using NCEP/NCAR reanalysis data, it can be seen that the corresponding time coefficients of EOF1 of summertime water vapor transport field exhibits a decreasing trend from 1951 to 2005.

The study by Huang et al. (2010) also showed that the multi-modes of the spatio-temporal variabilities of monsoon rainfall in eastern China are closely associated with those of water vapor transports over East Asia.

### ***3.3 Interdecadal variability of the EASM system***

The EASM system has not only obvious interannual variability, but also significant interdecadal variability, especially in monsoon rainfall over East Asia.

Early in the 1990s, Huang et al. (1999), analyzed the interdecadal variations of summer monsoon rainfall and pointed out that the summer monsoon rainfall in North China obviously decreased from the late 1970s to the early 1990s, thus, the prolonged severe droughts occurred in this region. And they also pointed out that an opposite phenomenon appeared in the Yangtze River and the Huaihe River valleys and Northwest China. In these regions, summer rainfall obviously increased from the late 1970s. Chen et al. (2004) systematically discussed the characteristics of the climate change in China during the last 80 years, and their results also showed that the interdecadal fluctuations of summer (June-August) monsoon rainfall are more obvious than surface air-temperature in East Asia.

Recently, many studies showed that the EASM rainfall occurred significant interdecadal variations not only in the late 1970s, but also in the early 1990s (e.g., Kwon et al., 2007; Ding et al., 2008; Deng et al., 2009; Huang et al., 2010). This

interdecadal oscillation may be also presented in the corresponding time-coefficient series of the EOF1 and EOF2 of summer rainfall in eastern China shown in Fig.7b and Fig.8b, and the oscillation exhibits a meridional tripole pattern or a meridional dipole pattern in the spatial distribution shown in Fig.7a and Fig.8a (e.g., Huang et al., 2010). As pointed out by Huang et al. (2010), these two leading modes of monsoon rainfall variability in the EASM region have a significant interdecadal variability. As shown in Fig.10, during 1958~1977 period, the anomaly distributions of summertime monsoon rainfall in eastern China exhibited a “+,-,+” meridional tripole pattern distributions from the south to the north. And during 1978~1992 period, opposite anomaly distributions to those during 1958~1977 period appeared in this region. But during 1993~1998 period, since the role of the second leading mode of the summertime monsoon rainfall variability over eastern China was intensified, as shown in Fig.10, the anomaly distributions of summertime rainfall appeared a combination of “+,-,+” meridional tripole pattern and “+,-” meridional dipole pattern from the south to the north, which caused the obvious increase of summer monsoon rainfall in South China.

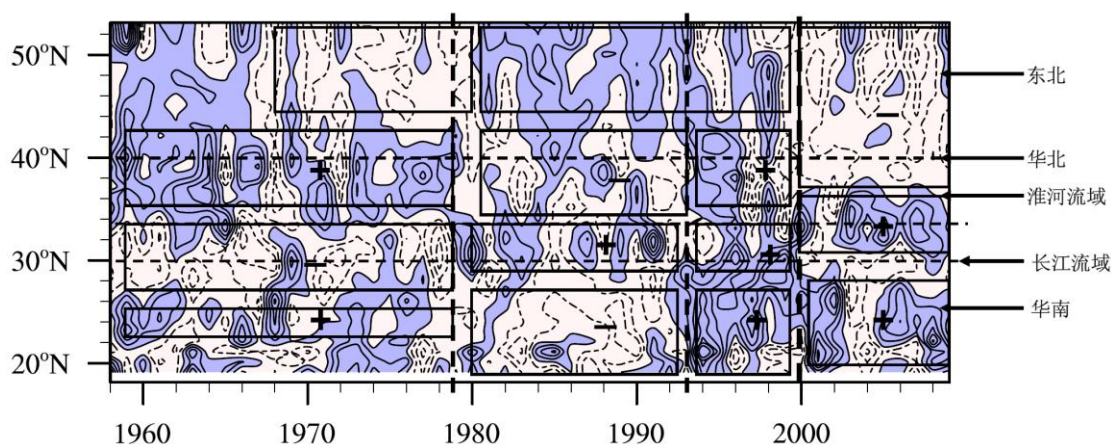


Fig.10 Latitude-time cross section of summertime (June~August) rainfall anomalies (percentage) along 115°E (average for 110°~120°E) in eastern China. The solid and dashed lines indicate positive and negative anomalies, respectively, and the positive anomalies are shaded. The precipitation data is from the dataset of precipitation at 756 stations of China by CMA.

The results analyzed by Huang et al. (2010) also showed that the interdecadal variability of leading modes of summertime monsoon rainfall variability in eastern China is closely associated with the interdecadal variability of water vapor transport fluxes by summer monsoon flow over East Asia. Furthermore, their result also showed that the interdecadal variability of water vapor transport fluxes over East Asia is associated with not only the interdecadal variation of the East Asia/Pacific pattern teleconnection of summer circulation anomalies over East Asia (e.g., Nitta, 1987; Huang and Li, 1987, 1988), but also the interdecadal variation of the EU pattern teleconnection of summer circulation anomalies over mid-and high latitudes (e.g.,

Wallace and Gutzler, 1981).

However, according to the analysis (e.g., Huang et al., 2010), a interdecadal variation of summer water vapor transport over East Asia, which is closely associated with the summer monsoon circulation, occurred in the late 1980s. This is in agreement with the results obtained from monsoon circulation by Wu et al., (2008) and Zhang et al. (2008). Thus, it may be seen that there is small difference between the interdecadal variability of summer monsoon rainfall in eastern China (e.g. Kwon et al. 2007; Ding et al., 2008; Deng et al., 2009; Huang et al., 2010) and the interdecadal variability of summer monsoon circulation over East Asia (e.g., Wu et al., 2008; Zhang et al., 2008). This may be due to that the summer rainfall variability depends not only on the moisture advection by the monsoon flow, but also on the convergence of the monsoon circulation.

The above-mentioned studies mainly focused on the interdecadal variability of summer climate over East Asia occurred in about 1978 and 1992, respectively(e.g., Huang et al., 1999; Huang et al., 2004; Huang et al., 2006; Zhang et al., 2007; Kwon et al., 2007; Ding et al., 2008; Deng et al., 2009; Huang et al., 2010). Recently, Huang et al. (2010) pointed out that the summer monsoon rainfall variability in China, especially in North China, Northeast China and Northwest China, occurred again a climate jump in the late 1990s. As shown in Fig.10, the climate jump occurred in the late 1990s in China characterized as the decrease of summer rainfall in North China, the southern part of Northeast China and the eastern part of Northwest China and the increase in the Huaihe River valley. Thus, the rainfall anomaly distributions caused by this climate jump appeared a dipole pattern with droughts in the northern part but floods in the southern part of China. Huang et al. (2010) studied the interdecadal variability of July~September (JJAS) mean rainfall in northern China using the daily observational rainfall data for 1961~2008 in China. Their study also showed that the summer monsoon rainfall obviously became weak in northern China including the southern part of Northwest China, North China and the eastern part of Northeast China. This result can demonstrate further the occurrence of the climate jump in the late 1990s suggested by Huang et al. (2010).

The result analyzed by Huang et al. (2010) from the upper-level circumglobal teleconnection in boreal summer also revealed the cause of the interdecadal variation of the JJAS mean rainfall in northern China occurred in the late 1990s. In order to study the relationship between them, they defined further two indices following Ding and Wang (2005), i.e., CGTI-1 and CGTI-2. These two indices are defined as the normalized geopotential height anomaly at 200hPa averaged for the area ( $35^{\circ}\sim 40^{\circ}\text{N}$ ,  $60^{\circ}\sim 70^{\circ}\text{E}$ ) during the period of June~September and as the difference of the normalized geopotential height at 200hPa between the area ( $40^{\circ}\sim 50^{\circ}\text{N}$ ,  $20^{\circ}\sim 10^{\circ}\text{W}$ ) and the area ( $60^{\circ}\sim 65^{\circ}\text{N}$ ,  $15^{\circ}\sim 25^{\circ}\text{E}$ ) during the period of June~September, respectively. As shown in Fig. 11a, the correlation coefficient between the CGTI1 index and the normalized JJAS mean rainfall anomaly averaged for North China is 0.50, which exceed 99% confidence level. And as shown in Fig.11b, the correlation coefficient between the CGTI-2 index and the JJAS mean rainfall averaged for Northwest China reaches to 0.53, which also exceed 99% confidence level. From Fig.11a and Fig.11b,

it can be seen that both the CGTI-1 index and the CGTI-2 index are negative, and JJAS mean rainfall in both North China and Northwest China are below normal after 1999, which are very different from those before 1999. Therefore, from the interdecadal variation of the upper-level circumglobal teleconnection, it can be also seen that a interdecadal variation of the EASM system may occur in the late 1990s.

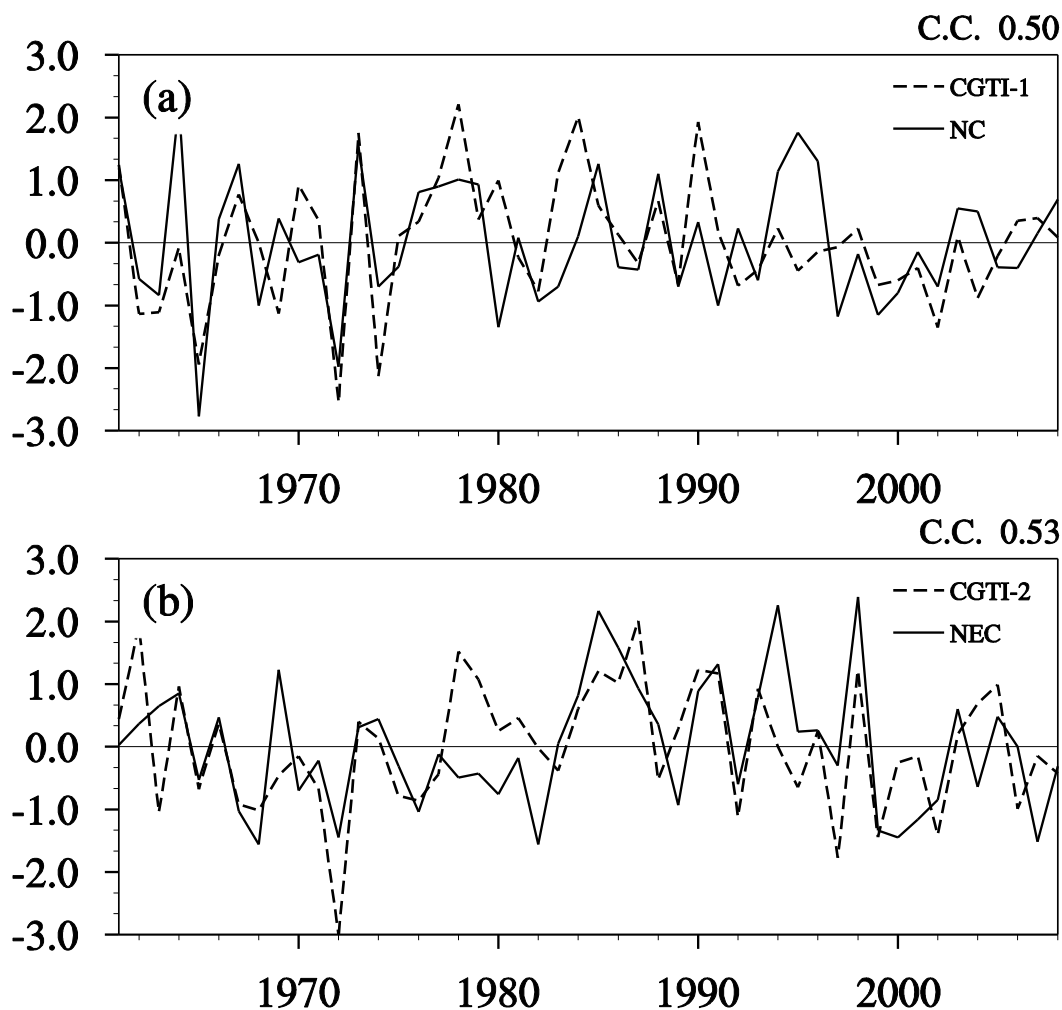


Fig.11 The time series of (a) the CGTI-1 index and (b) CGTI-2 index and the normalized JJAS mean rainfall anomalies averaged for (a) North China and (b) Northwest China. The definitions of the CGTI-1 index and the CGTI-2 index are following Ding and Wang (2005)

#### 4. Characteristics of the spatio-temporal variabilities of the EAWM system

East Asia is also a region of strong winter monsoon. The EAWM system includes: strong northwesterly wind over North China, Northeast China, Korea and Japan and strong northeasterly wind along the coast of Southeast China, South China and the Indo-China Peninsula (e.g., Chen et al., 1991; Ding, 1994), the East Asian trough at 500hPa over Northeast China, and the East Asian jet with its maximum in the upper

troposphere over Southeast Japan, which is associated with intense baroclinicity, large vertical wind shear and strong cold advection (e.g., Ding, 1994; Chen et al. 2003; Wang et al., 2010). As the EASM system variability, there are also complex spatio-temporal variabilities in the EAWM system.

#### ***4.1 Interannual variability of the EAWM system***

The strength of the EAWM system is a major concern in most previous studies on the interannual variability of the EAWM system, and many indices are defined to describe the EAWM strength (e.g., Chen and Graf 1998; Wu and Wang, 2002; Jhun and Lee, 2004; Li and Yang, 2010; Wang and Chen, 2010a). For example, Chen and Graf (1998) and Chen et al. (2000) defined the EAWM index as the normalized meridional wind anomalies at 10 m averaged for the East China Sea ( $25^{\circ}$  ~ $40^{\circ}$  E,  $120^{\circ}$  ~ $140^{\circ}$  E) and the South China Sea ( $10^{\circ}$  ~ $25^{\circ}$  N,  $110^{\circ}$  ~ $130^{\circ}$  E) from November to March of the next year. And Wu and Wang (2002) defined it as the sum of zonal sea surface pressure differences ( $110^{\circ}$  E minus  $160^{\circ}$  E) over  $20^{\circ}$ ~ $70^{\circ}$  N with a  $2.5^{\circ}$   $\times$   $2.5^{\circ}$  interval in latitude and longitude. Their results showed that there is a significant interannual variations in the EAWM strength.

Recently, Huang et al. (2007) investigated the characteristic of the intrannual variability of the EAWM strength using the index defined by Wu and Wang (2002) and pointed out that the EAWM strength has a significant interannual variability with an oscillation of quasi-four years, as shown in Fig.12a and Fig.12b. Their result also showed that there is an obvious difference between the EAWM intensity in the winter of 2005 (Dec., 2005~Feb., 2006) and that in the winter of 2006 (Dec.,2006~Feb.,2007), which caused the different winter climate anomalies in the Northern Hemisphere, especially in East Asia. The similar phenomena also occurred in January, 2008 and the winter of 2009. A prolonged cooling and severe snowstorms attacked most of China in January 2008, which caused that one hundred and twenty-nine people died and the economic losses reached up to 150 billion Chinese Yuan (e.g., Gu et al., 2008; Wang et al., 2009b). And in the winter of 2009, frequent severe cold weather attacked many areas of mid-latitude Northern Hemisphere including northern China with record-breaking blizzards, snowstorms, and low temperatures, which caused extensive damage to the traffic, agriculture and fishery (e.g., Wang and Chen, 2010b).

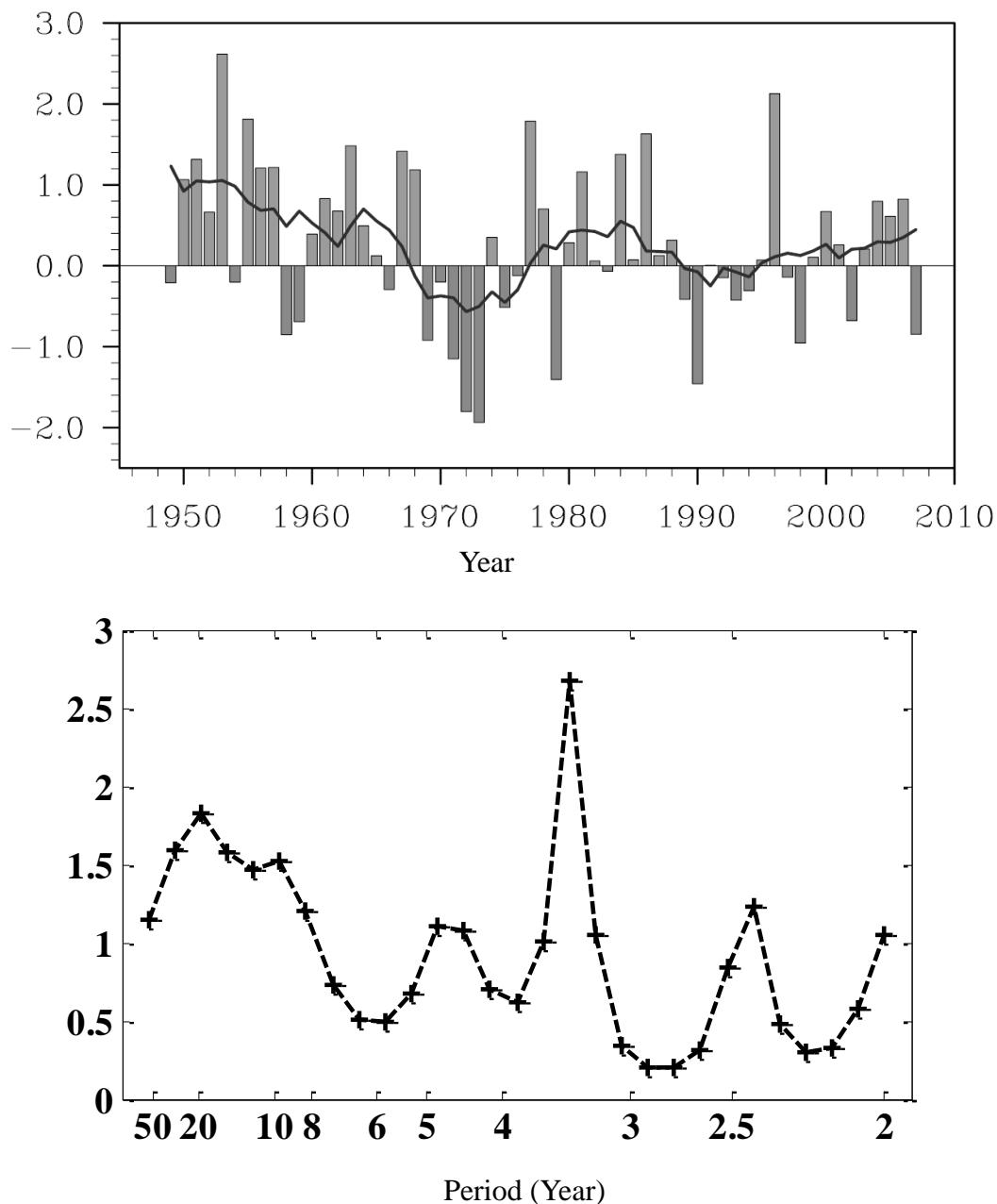


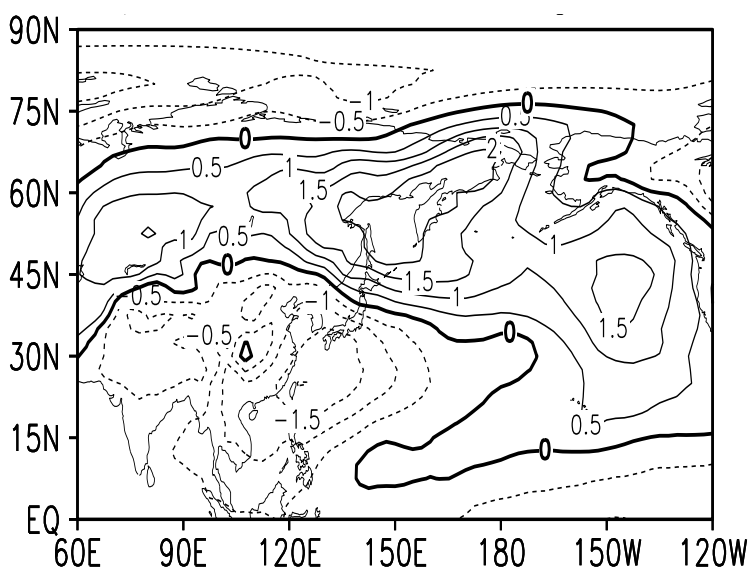
Fig.12 (a) Interannual variations of the EAWM index and (b) the dominant period analyzed by using the analyzing method of entropy spectrum. The definition of the EAWM index is from Wu and Wang (2002), and data is from the NCEP/NCAR reanalysis (e.g., Kalnay et al., 1996)

#### **4.2 Characteristic of multi-modes in the spatio-temporal variabilities of the EAWM system**

In recent years, it is realized that the variability of EAWM system is complex and has multi-modes characteristics (e.g., Kang et al., 2006; Kang et al., 2009; Wang et al., 2010a; Wang and Chen, 2010a). Based on the observations from 160 stations in China, Kang et al. (2006, 2009) first identified two leading modes of wintertime surface air temperature in China on both interdecadal and interannual time scales. The first

leading mode reflects a variability of surface air temperature in total China, which is related to the strength of the EAWM system. And the second leading mode describes a surface air-temperature oscillation between northern and southern parts of China. Moreover, Wu et al. (2006) also suggested that there are also two distinct modes in the spatio-temporal variations of the EAWM system, and these two leading distinct modes mainly reflect the variability of meridional and zonal winds in winter, respectively. Besides, from the EOF analysis of the wintertime surface air temperature in East Asia, Wang et al. (2010a) also obtained a northern mode and a southern mode for the wintertime surface air temperature variability in East Asia.

As the above-mentioned second leading modes of the spatio-temporal variations of the EAWM system, the pathway of the EAWM exhibits significant interannual variation, which is associated with the tilt of East Asian trough (EAT) axis in winter (e.g., Wang et al., 2009a). When the tilt of EAT axis is small, as shown in Fig.13. the southern pathway is strong. In this case, the major cold air flows along the coast of China and penetrates into the Southern Hemisphere, which leads to the occurrence of significant cooling phenomena in the SCS and Southeast Asia and warming phenomena in the northern part of East Asia. Thus, the tropical rain belt in Southeast Asia can be pushed southward by stronger northerly wind, and more precipitation can be observed in the East Asian continent. In contrast, when the tilt of EAT axis is large, as shown in Fig.13b, the eastern pathway is strong. In this case, more cold air flows into the North Pacific with a weakened southern branch of airflow, and the climate anomalies are generally reversed. Therefore, the variability of EAWM pathway has a modulation effect on the regional climate in East Asia and Southeast Asia.



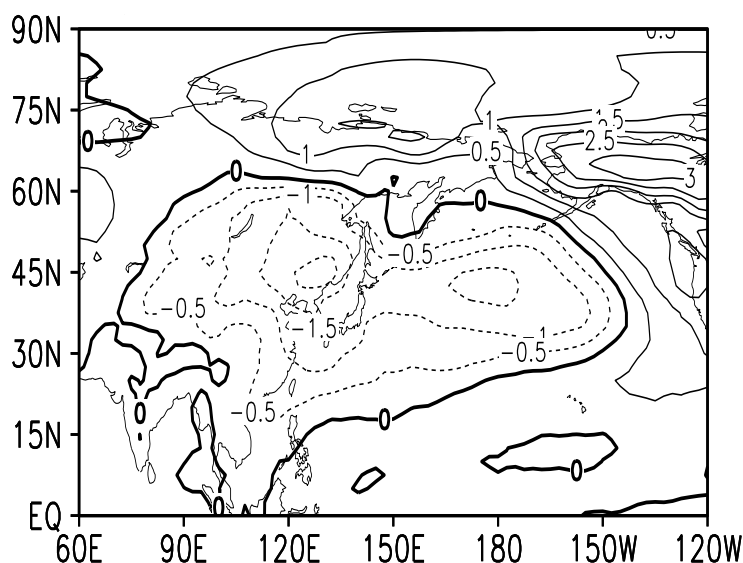


Fig.13 Distributions of the 850hPa air temperature anomalies for 5 strong winters with (a) strong southern EAWM pathway and (b) strong eastern EAWM pathway. The solid and dashed countours indicate positive and negative anomaly, respectively, and countour intervals are  $0.5^{\circ}\text{C}$ . Data is from the ERA-40 reanalysis (e.g., Uppala et al., 2005). The figure is from Wang et al. (2009a).

Besides, further analysis implies that the North Pacific SST can influence the interannual variability of the EAWM pathway through the air-sea interaction. When warm (cold) SST anomalies are observed over the North Pacific from the preceding summer to autumn, the EAWM tends to take the southern (eastern) pathway in the following winter (e.g., Wang et al., 2009a).

#### 4.3 Interdecadal variability of the EAWM system

The EAWM system is characterized by obvious interdecadal variability in addition to interannual variability (e.g., Jhun and Lee, 2004; Huang and Wang, 2006; Wang et al., 2009b; Wang and Chen, 2010a). The observational studies revealed that the strength of the EAWM system was significantly weakened after 1987 (e.g., Huang and Wang, 2006; Kang et al., 2006; Wang et al., 2009b; Wang and Chen, 2010a). Compared with the period of 1976-1987, both the Siberian High/Aleutian Low (e.g., Wang et al., 2009a) and the sea surface wind stress along the coasts of East Asia (e.g., Cai et al., 2006) are weakened for the period of 1988-2001, which is accompanied with less cold-waves (e.g., Wang et al., 2009b) and frequent warm-winters (e.g., Wang and Ding, 2006; Kang et al., 2008b) in China. Wang et al. (2009b) analyzed the numbers of cold waves in China for the winters during 1957-2001 according to the record in the NCC-CMA cold wave almanac and revealed that there are 15.4 general cold waves on average for each winter. The corresponding numbers are 16 for the strong EAWM period (1976-87), but drop to 13.2 for the weak EAWM period (1988-2001), as shown in Fig.14.

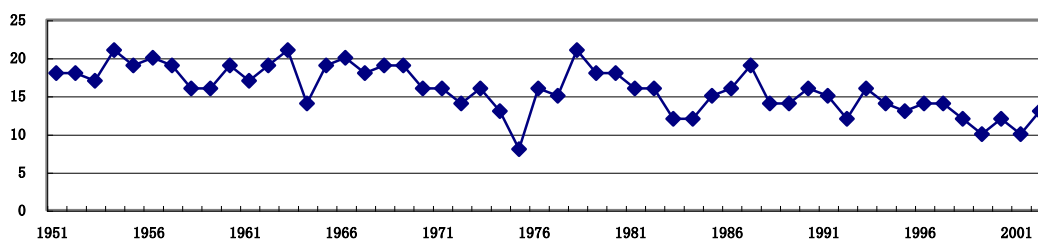


Fig.14 Interannual variation of occurring times of general cold surges in China

As mentioned above, although there is clear decreasing trend for the number of cold waves over China for 1988~2001 (e.g., Wang and Ding, 2006; Wang et al. 2010), but the frequency of severe cold winters tends to increase from the early 21th century (e.g., Ding and Ma, 2007; Huang et al., 2008; Ma et al., 2008; Hong and Li, 2009; Lu and Chang, 2009; Wen et al., 2009; Wang and Chen, 2010b). This shows that the continuous warm-winters after 1987 in China have ended before 2008 (e.g., Ma et al., 2008; Wang et al., 2009b). Thus, it is possible that the EAWM system may undergo another interdecadal variation from recent years (e.g., Wei et al., 2011).

#### ***4.4 Impact of the EAWM system variability on wintertime rainfall in China and the marine environment over the offshore area of China***

The above-mentioned studies show that the EAWM system variability has an important impact on surface air temperature over China. The EAWM system variability also has a significant impact on rainfall in autumn, winter and next spring over China. Zhou (2010) investigated the impact of the EAWM system variability on winter (i.e., January, February, and March, JFM in short) rainfall over southeastern China including South China and Central China and East China by using station observational data for 1951~2003. His study showed that there is a significant correlation between the EAWM variability and JFM rainfall over southeastern China. In a winter (JFM) with the weak EAWM, then the southwesterly wind anomalies at 700hPa dominate over the SCS, which can transport more water vapor from the Bay of Bengal and the SCS into southeastern China. In this case, the westerly jet is weakened over East Asia and displaces southward, contributing to the intensification of ascending motion over southeastern China. These can cause the increase of wintertime (JFM) rainfall in southeastern China. Moreover, Gu et al. (2008) investigated the impact of the EAWM variability on wintertime snow storms in China, especially on severe blizzard freezing rain and low temperature in January, 2008. Their result showed that the East Asian trough stayed in a stable state for long time in January, 2008, which led to the continuous southward-instruction of cold air along the Mongolian Plateau to Central China, Southwest China and South China. Meanwhile, the western Pacific subtropical high shifted anomalously northward and westward, which led to the northward transport of a large amount of wet air along the west edge of the subtropical high from the Bay of Bengal and the SCS, and the southwest flow with wet air converged with cold air from the Mongolian Plateau in the Yangtze River valley. Thus, the prolonged heavy snowfall and low temperature occurred in

Central China, South China, the eastern part of Southwest China and the Yangtze River valley in January, 2008.

The EAWM system variability has a significant impact not only on severe cold waves and heavy snowfall in China, but also on the marine environment in the offshore area of China including the Baohai Sea, the Yellow Sea, the East China Sea and the SCS and its adjacent ocean. According to the result analyzed by Cai et al. (2006), since the EASM and the EAWM systems became weak over the offshore area of China and its adjacent ocean, the sea surface wind stresses, especially the meridional sea surface wind stresses, have been weakened over the offshore area of China from the 1980s, which has caused obvious warming in this ocean area. This can provide a favorable marine environment for the frequent occurrence of red tides in the offshore area of China.

### **5. Influence of air-sea –land interactions on the EAM system variability**

As shown by Webster et al. (1998), the monsoon is not only an atmospheric circulation system, but also an atmosphere-ocean-land coupled system. The interannual and interdecadal variabilities of EAM system are influenced not only by many circulation system such as the SASM system, the western Pacific subtropical high, the disturbances in mid-and high latitudes(e.g., Tao and Chen, 1967), but also by other factors such as thermal states of the West Pacific warm pool and convective activity around the Philippines, ENSO cycles in the tropical Pacific, the thermal state of the tropical Indian Ocean, the dynamical and thermal effects over the Tibetan Plateau, and the land surface process in the arid and semi-arid area of Northwest China and the snow cover on the Tibetan Plateau and the Eurasian continent and so on. As shown in Fig. 15, these factors affecting the EAM system variability are various components of an atmosphere-ocean-land coupled system, and these components are interactions. Therefore, this coupled system may be called as the EAM climate system (e.g., Huang et al., 2004a; Huang et al., 2006a; Huang et al., 2007; Huang, 2009).

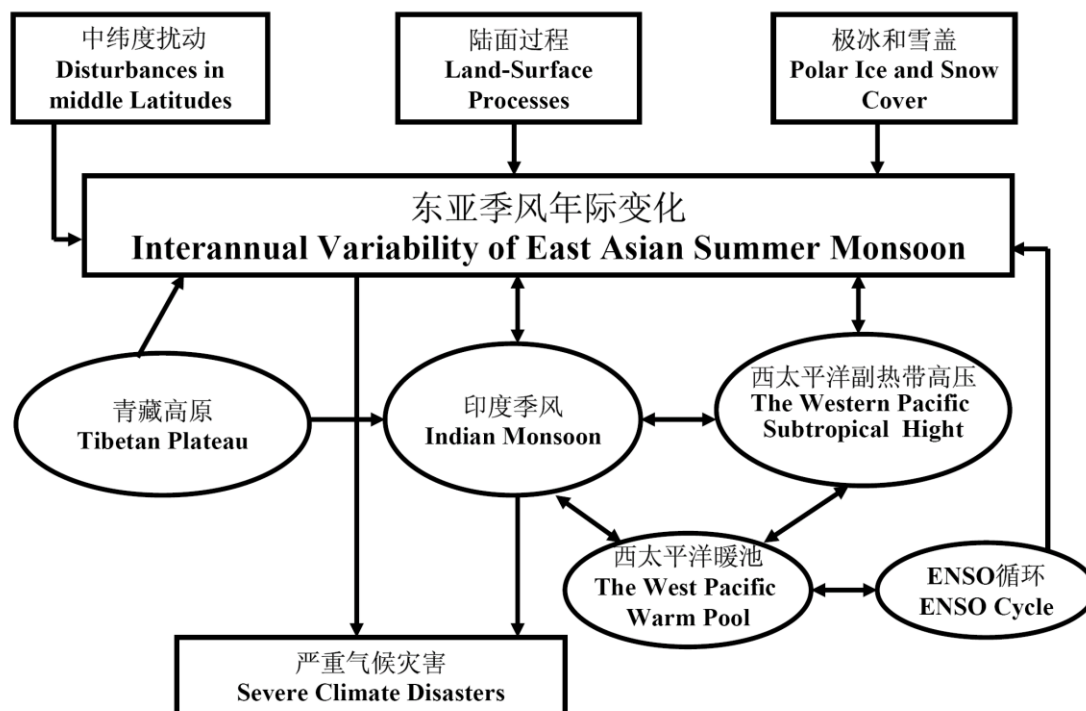


Figure 15 Schematic map of various components of the EAM climate system

In order to understand the causes of the EAM climate system variability, it is necessary to analyze the interactive processes between the atmosphere and oceans and between the atmosphere and land surface in the EAM climate system. However, because there are complex interactions among these components of the EAM climate system, only the impacts of atmosphere-ocean and atmosphere-land coupling components of this climate system on the EAM system variability are simply discussed in the following.

### 5.1 Thermal effect of the tropical western Pacific on the EAM system variability

The tropical western Pacific is a region of the highest SST in the global sea surface. Due to the warm state of this region, the air-sea interaction is very strong and the ascending branch of the Walker circulation is over the region. This leads to strong convergence of the air and moisture and strong convective activity and heavy rainfall there (e.g., Connejo-Garrido and stone, 1977; Hartmann et al., 1981). Thus, the tropical western Pacific has an important thermal effect on the EAM system variability.

The studies by many scholars (e.g., Nitta, 1987; Huang and Li 1987, 1988; Kurihara, 1989; Huang and Sun, 1992) showed that the thermal states of tropical western Pacific and convective activity around the Philippines play important roles in the interannual variability of EASM system. Moreover, Huang et al. (2005) further investigated the relationship between the intraseasonal variations of the western Pacific subtropical high and the thermal state of the tropical western Pacific in summer. It is further identified that there is a close relationship between the anomalous northward shift of the western Pacific subtropical high and the intensified convective activities around the Philippines. When the tropical western Pacific is in a

warming state in summer, the convective activities are strong around the Philippines, then there are abrupt northward shifts of the western Pacific subtropical high from South China to the Yangtze River and the Huaihe River valley in early or mid-June and from the Yangtze River and the Huaihe River valley to North China and Northeast China in late June or early July. Thus, the summer monsoon rainfall may be weak in the Yangtze River and the Huaihe River valley. Oppositely, when the tropical western Pacific is in a cooling state in summer, the convective activities are weak around the Philippines, then there are not abrupt northward shifts of the western Pacific subtropical high from South China to the Yangtze River and the Huaihe River valley in early or mid-June and from the Yangtze River and the Huaihe River valley to North China and Northeast China in late June or early July. Thus, the Mei-yu front is maintained for long time and the summer monsoon rainfall may be strong in the Yangtze River and the Huaihe River valley, as shown in Fig.6a and Fig.6b.

Huang et al. (2004), and Huang et al. (2006b) investigated the interannual variability of thermal state of the tropical western Pacific and its impact on interannual variability with the quasi-biennial oscillation of the EASM system. It has been pointed out that there is a dominant quasi-biennial oscillation in the interannual variations of thermal state of the tropical western Pacific. As studied by Huang et al. (2006b), the oscillation has a great impact on the interannual variability with the quasi-biennial oscillation of the EASM system. As shown in Fig.16, when the tropical western Pacific is in a warming state in a winter and coming spring, convective activity generally is stronger around the Philippines in coming spring and summer. This can cause the northward shift of the western Pacific subtropical high due to the EAP pattern teleconnection (e.g., Nitta, 1987; Huang and Li, 1987, 1988), which leads to weak monsoon rainfall in the Yangtze River valley of China, Japan and South Korea. At the same time, the convergence due to the strong convective activity around the Philippines can cause strong upwelling in the tropical western Pacific, which will bring a cooling state into the tropical western Pacific in the next winter. Since a cooling state will appear in the tropical western Pacific in the next winter, weak convective activity will be caused around the Philippines in the spring and summer of the third year. This will cause the southward shift of the western Pacific subtropical high due to the EAP pattern teleconnection, which will lead to strong monsoon rainfall in the Yangtze River valley of China in the summer of the third year. At the same time, the divergence due to the weak convective activity around the Philippines will cause weak upwelling in the tropical western Pacific in the spring and summer of the third year, which will bring again a warming state into the tropical western Pacific. The period of the process is about two~three years.

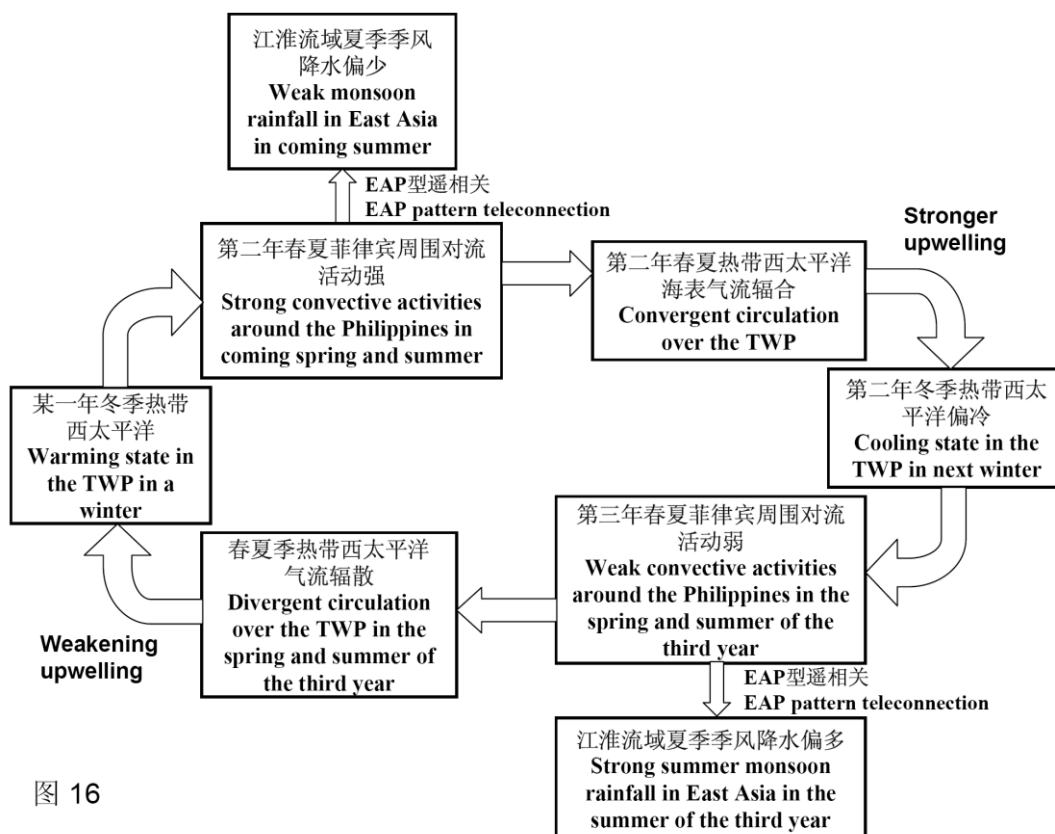


图 16

Figure 16 Conceptive diagram of the quasi-biennial oscillation of the EASM system related to the air-sea coupling system over the tropical western Pacific

The thermal state of the tropical western Pacific has a significant effect not only on the interannual variability of the EASM system, but also on the intraseasonal variability of this system, as described in Section 3 (e. g., Huang et al. 2005, 2006b).

### 5.2 Impact of ENSO cycles in the tropical Pacific on the EAM system variability

It is well known that ENSO cycles are one of the most striking phenomena of air-sea interaction in the tropical Pacific and has a great influence on the EAM system variability.

Huang and Wu's study (1989) first showed that summer monsoon rainfall anomalies over East Asia depend on the stages of ENSO cycle in the tropical Pacific. From the composite analyses of summer monsoon rainfall anomalies for different stages of ENSO cycles during the period of 1951~2000, Huang and Zhou (2002) pointed out that droughts in North China tend to occur in the developing stage of El Niño events, but floods tend to occur in the Yangtze River valley of China during the decaying stage of El Niño events, as shown in Figs.17a and 17b, respectively. For example, severe floods occurred in the Yangtze River valley in the summers of 1998 and 2010, These summers just were the decaying state of El Niño events events occurred in 1997 and 2009.

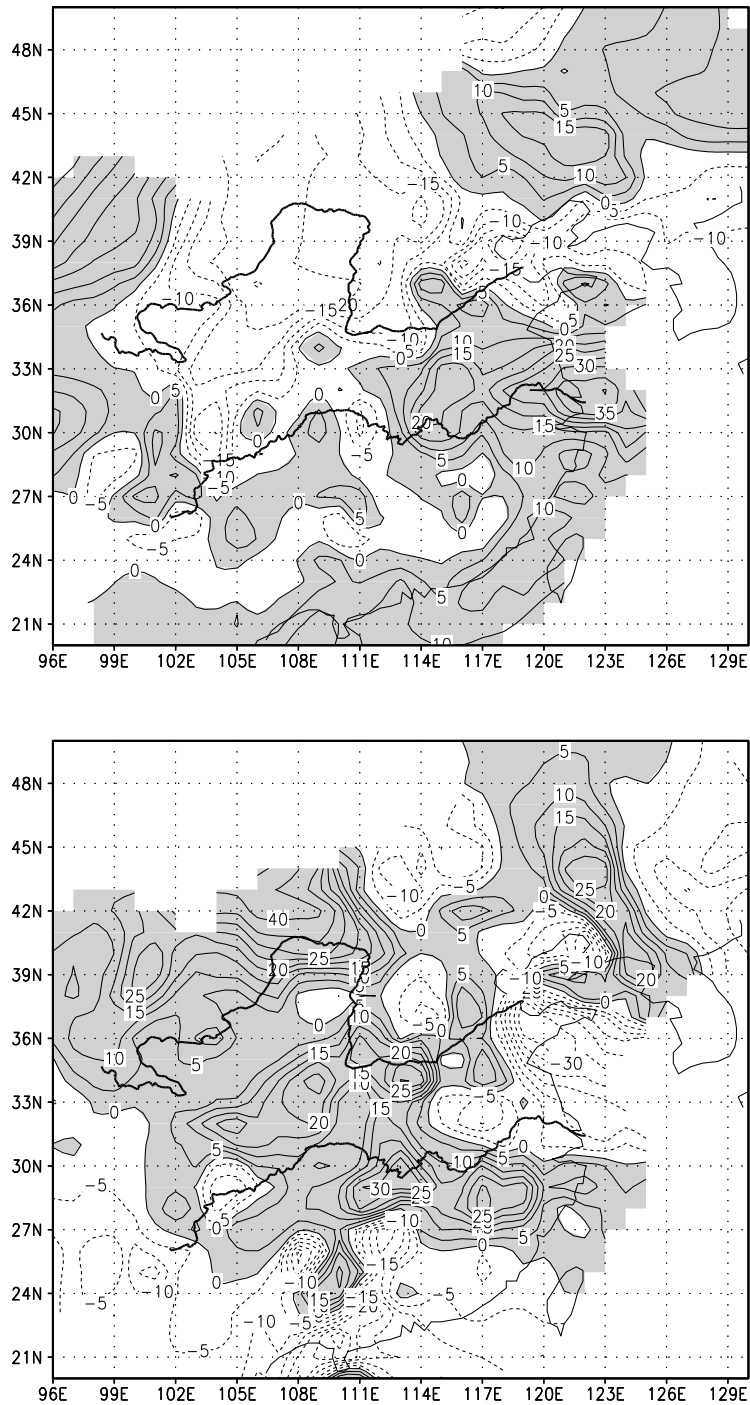


Fig. 17 Composite distributions of summer (June-August) rainfall anomalies (in percentage) over China (a) for the summers in the developing stage and (b) for the summers in the decaying stage of El Niño events occurred during the period from 1951 to 2000. The solid and dashed contours indicate positive and negative anomalies, respectively, and positive rainfall anomalies are shaded.

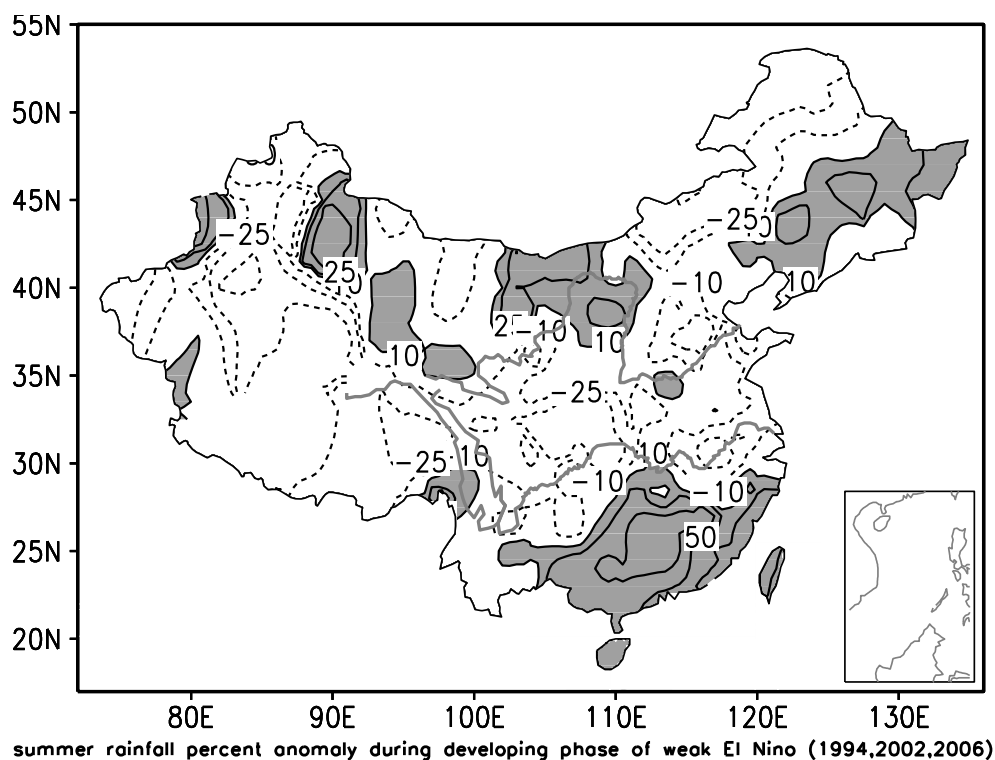
As mentioned above, Huang and Wu (1989) first pointed out that an important impact of El Niño events on the EASM system variability is in their decaying phase, which is generally called as the delayed impact of El Niño events. Later, Zhang et al.

(1996), Zhang and Huang (1998) investigated the process and mechanism of the delayed impact of El Niño events on the EASM system variability and pointed out that this delayed effect may be due to the appearance of an anomalous anticyclonic circulation in the lower troposphere over the tropical western Pacific after the mature phase of El Niño events. And the southwesterly anomalies in the western side of the anticyclonic anomaly circulation will intensify the southwesterly flow, which can cause the strengthening of the southwest monsoon over Southeast China. Wang et al. (2003) studied further the formation mechanism of the anomalous anticyclonic circulation over the tropical western Pacific. Their study showed that in a winter with the mature stage of El Niño event, the weakening convective activities over the tropical western Pacific caused by the weakening Walker circulation and negative anomalies of sea water temperature in the tropical western Pacific can trigger an cooling Rossby in the tropical western Pacific and can form an anomalous anticyclonic circulation in the lower troposphere over the tropical western Pacific, and then, this anomaly circulation can be maintained to following spring.

ENSO cycles also have a significant influence on the annual cycle between the EAWM and EASM in the EAM systems. Chen (2002), and Huang et al. (2004b) proposed that the EAWM system variability is also associated with ENSO cycles. Chen(2002) analyzed the composite distributions of meridional wind anomalies at 850hPa and rainfall anomalies for various stages of ENSO cycles. These composite distributions show that in the winter before the developing stage of an El Niño event, there are anomalous northerly winds along the coastal areas of China, i.e., the EAWM is strong, and an anomalous cyclonic circulation over the tropical western Pacific, which is helpful to the developing of El Niño event. Later, the western Pacific subtropical high will be weak during the following summer, and the northeasterly anomalies will be caused over the Yangtze River and the Huaihe River valleys and the southeastern coast of China. Thus, a weak EASM will appear in the summer when an El Niño event is in its developing stage. Following the developing stage, the El Niño event can generally reach its mature phase, then an anticyclonic anomaly circulation will begin to appear over the tropical western Pacific (e.g., Zhang et al., 1996; Zhang and Huang, 1998; Wang et al., 2003) and anomalous southwesterly winds will prevail in the southeastern coast of China and the SCS. This shows that a weak EAWM may appear in the winter when an El Niño event is in its mature phase. Following the winter, the El Niño event may be in its decaying stage, the anomalous anticyclonic circulation will be intensified over the tropical western Pacific, which represents the strengthening of the western Pacific subtropical high. In this case, anomalous southwesterly winds distribute over the region from South China to the Yangtze River valley, which shows that a strong EASM may appear over the Yangtze River and the Huaihe River valleys in the summer when an El Niño event is in its decaying phase.

Recently, there are several studies on the leading modes of the tropical Pacific SST variability (e.g., Achok et al., 2007; Weng et al., 2007; Zhang and Huang, 2008; Huang and Huang, 2009). Their studies showed there are two leading modes in the tropical Pacific SST anomalies. These two leading modes are characterized by positive SST anomalies in the tropical eastern Pacific and the tropical central Pacific,

i.e., the eastern Pacific warming pattern and the central Pacific warming pattern (i.e., El Niño motoki), respectively. Huang and Huang (2009) analyzed the impact of El Niño motoki on the EAM system variability, especially on summertime rainfall over eastern China. The analyzed results showed that summertime rainfall anomaly distributions during the developing and decaying stages of an El Niño motoki are very different from those shown in Fig.17a and Fig.17b. As shown in Fig.18a, in the summer with the developing stage of El Niño motoki, summer monsoon rainfall may be below normal in the Huaihe River valley and above normal in South China. But in the summer with the decaying stage of El Niño motoki, summer rainfall may be above normal in the Huaihe River valley and below normal in North China and the region to the South of the Yangtze River, as shown in Fig.18b.



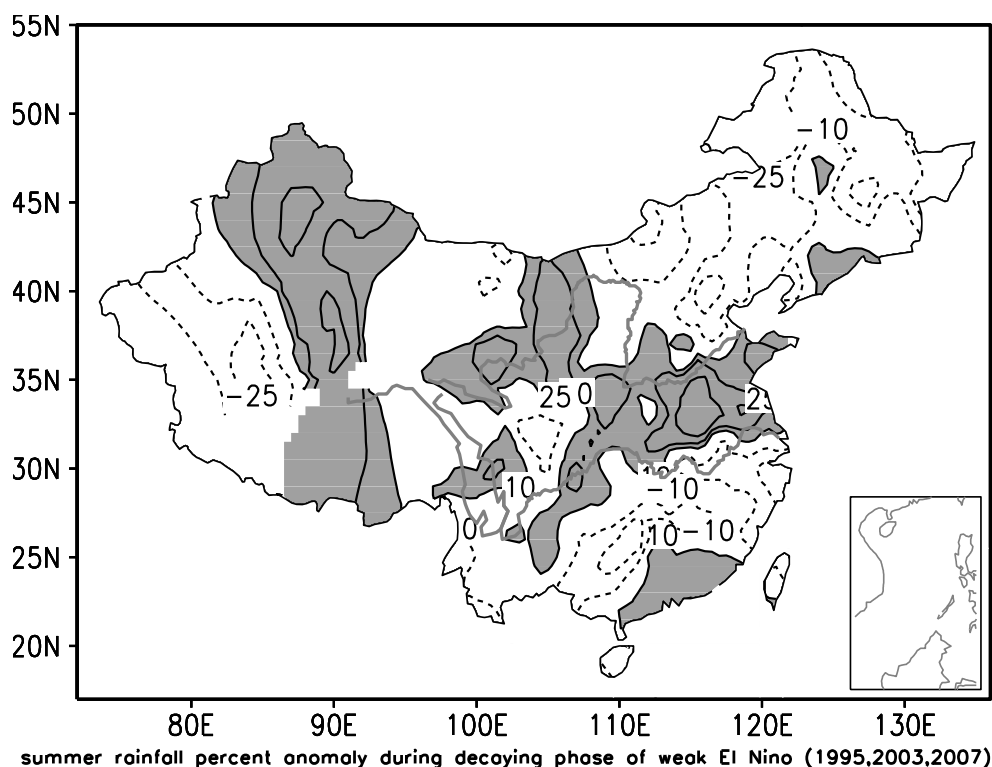


Figure 18 Composite distributions of summer rainfall anomalies (percentage) in China (a) for the summers of 1994, 2002 and 2006 (i.e., the developing stage of El Niño motoki) and (b) for the summer of 1995, 2003 and 2007 (i.e. the decaying stage of El Niño motoki). The solid and dashed contours indicate positive and negative anomalies, respectively, and areas of positive anomalies are shaded.

### 5.3 Impact of PDO on the EAM system variability

The studies have shown that there are significant decadal oscillations in the North Pacific SST, i.e., PDO, and this oscillation has an important impact on the atmospheric circulation over the North Pacific (e.g., Trenberth and Hurrell, 1994; Bond and Harrison, 2002). The PDO has a significant impact on the EAM system variability on interdecadal time scale. As mentioned above, the mature phase of El Niño (La Niña) events is usually accompanied by a weaker (stronger) EAWM system. However, according to the study by Wang et al. (2008), the impact of ENSO cycle on the EAWM system variability may be modulated by the Pacific Decadal Oscillation (PDO). When the PDO is in its high phase, there is no significant relationship between ENSO and EAWM system on the interannual timescale because the ENSO-EAWM teleconnection is no significant. Oppositely, when the PDO is in its low phase, ENSO cycle has strong impact on the EAWM system, occurring significant low-level temperature over East Asia. Because the PDO is in its high phase after the mid-1970s, the impact of ENSO cycles on the EAWM system became weak during the period. However, in the winters before the mid-1970s, the ENSO cycle has a significant influence on the North Pacific Oscillation (NPO) and the EAWM system variability.

The PDO also has an important influence on the EASM system variability.

Recently, Zhang et al. (2007) analyzed the interdecadal variations of summertime rainfall in eastern China and their association with the temporal evolution of the PDO. Their results showed that the interdecadal variations of summertime rainfall pattern in eastern China and the EASM circulation are well related to the PDO in the North Pacific. Moreover, Deng et al. (2009) pointed out that the first interdecadal variation of summertime rainfall pattern over eastern China occurred in the mid-and late 1970s may be influenced by the transition of the PDO from negative phase to positive phase, and the second interdecadal variation of the rainfall pattern occurred in the late 1980s and the early 1990s may be association with the warming of the western North Pacific to the south of Japan, especially the warming around the Philippines.

#### ***5.4 Impact of the North Indian Ocean on the EASM system variability***

The tropical Indian Ocean also has an important thermal effect on the EASM system variability. The studies by Annamalai et al. (2005), and Yang et al. (2007) have explained that the SST anomalies in the Indian Ocean have an important effect on the EASM system variability and climate anomalies over East Asia. Xie et al. (2009) proposed that the Indian Ocean has a capacitor-like effect on the climate variability over the Indo-Western Pacific during the summer following El Niño.

Recently, many studies focus the thermal role of the tropical northern Indian Ocean in the delayed impact of El Niño events on the EASM system. For example, Li et al. (2008), Huang and Hu (2008), and Huang and Hu et al. (2010) studied systematically the thermal effect of the tropical northern Indian Ocean on the anomalous anticyclonic circulation in the low troposphere over the western North Pacific in summer, which can cause the delayed impact of El Niño on the EASM system. Huang and Hu (2008) pointed out further that the interannual variation of the western North Pacific anomalous anticyclone is closely associated with the SST anomalies in the tropical northern Indian Ocean in summer, but it has not an obvious correlation with the SST anomalies in the western South Indian Ocean. And the low-level anomalous anticyclonic circulation over the Northwest Pacific caused by the summertime warming SST in the tropical northern Indian Ocean has been well simulated by Huang and Hu (2008) using the ECHAM 5.0 climate model. It has been demonstrated consistently by Li et al. (2008) using five AGCMs that the Indian Ocean warming can trigger an anticyclonic anomaly circulation in the lower troposphere over the subtropical western Pacific, intensifying the southwesterly flow to East China and a Gill-type response with the intensified South Asian high in the upper troposphere. The two circulation systems are favorable to the enhancement of the EASM system.

Moreover, Huang and Hu et al. (2010) also investigated the interdecadal variation of the relationship between the SST in the tropical northern Indian Ocean and the Northwest Pacific low-level anticyclonic anomaly circulation in boreal summer using both observations and AGCM simulations. Their results showed the low-level anticyclonic anomaly circulation over the Northwest Pacific is positively correlated with the summertime SST in the tropical northern Indian Ocean after the mid-1970s, but the correlation between them was weak for the period of 1958~1976. And their

numerical simulations with a 21-member ensemble AGCM (ECHAM5.0) also showed that there is an interdecadal variation in the relationship between the low-level anticyclonic anomaly circulation over the Northwest Pacific and the summertime SST in the tropical Indian Ocean after the mid-1970s.

The above-mentioned studies showed that a basin-scale warming trend occurred in the tropical Indian Ocean from the mid-1970's, and this should cause the intensification of the low-level anticyclonic anomaly circulation and the strong southwesterly flow over East Asia from the mid-1970s. However, according to the results studied by Huang et al. (2004a, 2006, 2010), the EASM system has substantially become weak from the mid-1970s, especially from the late 1990s, although it was stronger during the period of 1993~1998. Thus, these results cannot supply that there is a causal relationship between the tropical Indian Ocean warming and the interdecadal weakening of the EASM system from the mid-1970s (e.g., Li et al., 2008; Huang and Hu et al., 2010).

The tropical Indian Ocean has not only a significant impact on the low-level anomaly circulation over the Northwest Pacific, but also an important thermal effect on the South Asian high. The variations of the South Asian high (SAH) are closely associated with precipitation and circulation over Asia (e.g., Tao and Zhu, 1964). According to the result investigated by Zhang et al. (2002), in the summer when the SAH shifts eastward, the summer monsoon rainfall may be above normal in Southern Japan, the Korea Peninsula and the Yangtze River valley of China. On the other hand, in the summer when the SAH shifts westward, the summer monsoon rainfall may be below normal in these regions. And Zhang et al. (2005) pointed out that the SAH is also linked to global circulation and precipitation in summer. A strengthened SAH is generally accompanied by a strengthened and westward western Pacific subtropical high, and weakened mid-Pacific trough, and intensified Mexican high. Moreover, increasing precipitation may appear in South Asia, Central America, Australia and Central Africa, and decreasing precipitation may be caused over the Pacific and the Mediterranean Sea. Besides, a strengthened SAH can lead to the intensification of the subtropical high over the extratropical North Pacific (Zhao et al., 2009). Therefore, the SAH variability is also a factor affecting the EASM system.

From the numerical simulations with five AGCMs, Li et al. (2008) pointed out the tropical Indian Ocean warming can trigger the intensification of the SAH in the upper troposphere over South Asia. Recently, the result simulated by Huang et al (2010) using ECHAM 5.0 AGCM also showed that when the tropical Indian Ocean is in a warming state, the SAH will be strengthened and its center will shift southward over South Asia. Moreover, they proposed a possible mechanism of the connection between the thermal state of the tropical Indian Ocean and the SAH variability, i.e., the warming SST in the tropical Indian Ocean can cause the increase of the equivalent potential temperature in the atmospheric boundary layer and can alter the temperature profile of the moist atmosphere over the tropical Indian Ocean. This will induce significant positive geopotential height anomalies over South Asia, and the SAH is thus intensified.

### ***5.5 The Impact of land surface processes on the EASM system variability***

Because monsoon circulations result fundamentally from the land-sea thermal contrast, the EAM system variability is influenced not only by the thermal state of the tropical Pacific and tropical Indian Ocean, but also by the thermal state of the Eurasian continent.

The spring Eurasian snow cover greatly influences the thermal state of the Eurasian continent, thus, it has an important impact on the following summer climate over East Asia. Recently, Wu et al. (2008), and Zhang et al. (2008) analyzed the cause of the significant decadal shift of the summer climate over eastern China occurred in the late 1980s, which was proposed from the interdecadal variability of the summer monsoon index defined by Wang et al. (2001). This decadal shift of the summer climate over eastern China in the late 1980s proposed by Wu et al. (2008) and Zhang et al. (2008) may be similar to the decadal shift of the summer rainfall to South China in the early 1990s proposed by Ding et al. (2008), Deng et al. (2009), and Huang et al. (2010). As shown in Subsection 3.3. Wu et al. (2008) and Zhang et al. (2008) revealed that the decadal climate shift of the summer monsoon rainfall belt to South China is closely associated with the decadal variability of the spring snow cover over the Eurasian continent. And their studies showed that there is a good negative correlation between them. They also investigated the physical processes of this correlation and pointed out that the snow cover variability in spring Eurasian continent can excite a Rossby wave-train over high latitudes from spring to summer, which can lead to an anomalous high over North China and a weak low over South China. Thus, more monsoon rainfall can be caused in South China.

The snow cover over the Tibetan Plateau is a part of the snow cover over the Eurasian continent. Ye and Gao (1979) first pointed out that the Tibetan Plateau has important thermal and dynamic effects on the interannual variability of the EASM system. Later, many investigators also emphasized the thermal effect of the Tibetan Plateau on the EASM system variability (e.g., Huang, 1984, 1985; Wu and Zhang, 1997).

Recently, some studies focus the thermal effect of snow cover over the Tibetan Plateau on the EASM system variability. Wei et al. (2002,2003) analyzed the interannual and interdecadal variations of the days and depth of snow cover over the Tibetan Plateau using the observed data of daily snow cover at 72 observational stations located in the Tibetan Plateau for 1960~1999. They discovered that there are obvious interannual and interdecadal variations of the days and depth of snow cover on the Tibetan Plateau. Moreover, these variations of snow cover over the Tibetan Plateau also have an important impact on the summer monsoon rainfall in the middle and upper reaches of the Yangtze River valley(e.g., Wei et al. 2002, 2003; Huang et al., 2004a).

### ***5.6 Thermal effect of the sensible heating in the arid and semi-arid region of Northwest China on the EASM system variability***

The EAM system variability is greatly influenced by the thermal states of the Eurasian continent, especially the thermal states in the arid and semi-arid of Northeast China and Central Asia, because the sensible heating in these regions is larger than that in the EASM region in spring and summer, as shown in Fig.19. Zhou and Huang

(2006), Zhou (2010), and Zhou and Huang (2010) analyzed the interannual and interdecadal variations of the difference between the surface temperature and the surface air temperature, i.e.,  $T_s - T_a$ , and sensible heating in spring in the arid and semi-arid region of Northwest China and Central Asia and their impact on summer monsoon rainfall in China. Their results showed that the strongest sensible heating over the Eurasian continent is located at Northwest China and Central Asia in spring, thus, this region may be seen as a “warm lying surface” in the Eurasian continent. They also pointed out that the  $T_s - T_a$  and sensible heating over this region have an obvious interdecadal variability. Before the late 1970s, the sensible heating anomalies in spring were negative, but the sensible heating anomalies became largely positive from the late 1970s. And Zhou and Huang (2008, 2010) discussed a possible physical process of the thermal effect of the sensible heating anomalies in the arid and semi-arid region of Northwest China on the EASM system variability. Their analyses showed that since the sensible heating became strong during the period of 1978~2000, the cyclonic circulation anomaly was intensified over Northwest China. This was closely associated with the anomalous ascending motion over Northwest China, which could contribute to anomalous descending motion over North China. Moreover, their results also showed that during the period of 1978~2000, the air temperature at 300hPa appeared an obvious decrease, but increase near the surface over the Northwest China in summer over Northwest China. This caused the enhancement of vertical convective-instability, which contributed to the strengthening of ascending motion and the increase of rainfall in Northwest China after 1978. Moreover, influenced by the anomalous ascending motion over Northwest China, an opposite phenomenon occurred over North China, i.e., anomalous descending motion was caused over North China and the vertical convective- instability became weak over North China. This could contribute to the decrease of summer rainfall in North China after the late 1970s. Therefore, the intensification of spring sensible heating over Northwest China and Central Asia may be one of the causes of the interdecadal variability of the EASM system occurred in the late 1970s.

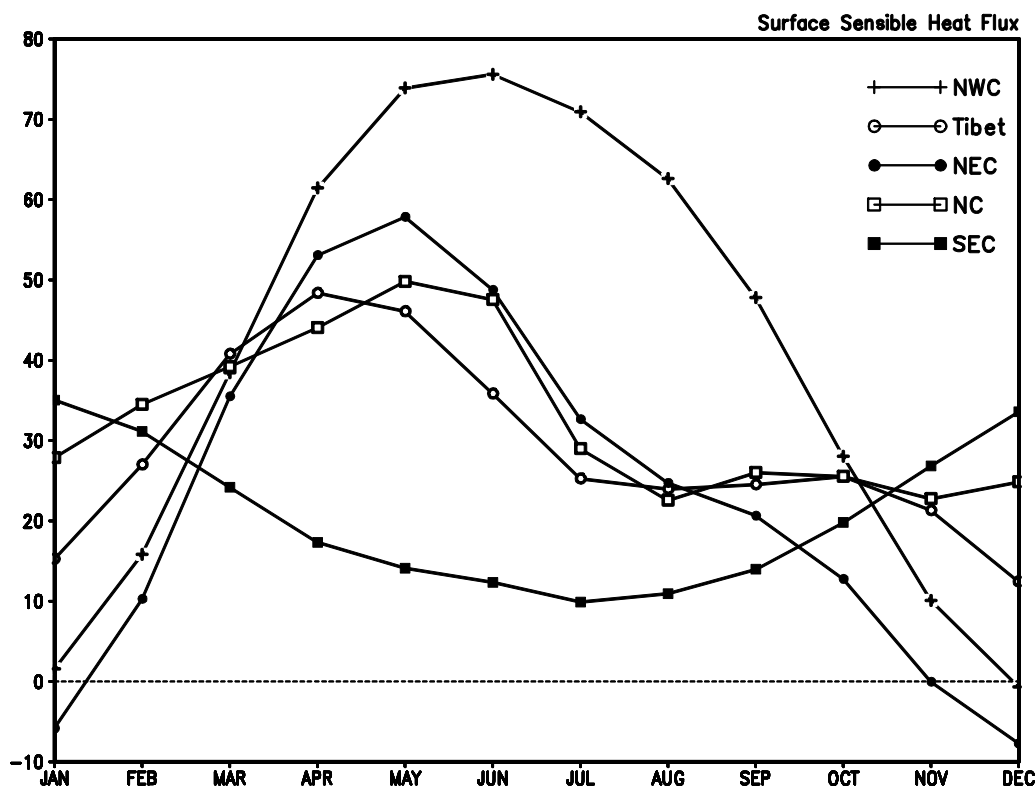


Figure 19 Climatological mean monthly sensible heating flux in various regions of China Units:  $W/m^2$ . Data is from the ERA-40 reanalysis (e.g. Uppala et al., 2005)

## 6. The internal dynamic processes in the EAM climate system

As shown in Section 5, the EAM system variability is closely associated not only with the variabilities of various component of the EAM climate system including sea-land-air interactions, but also with the internal dynamical and thermodynamical processes in the EAM climate system. Just because of the dynamical and thermodynamical processes in this system, there are close relationships among the variabilities of various components of this system. Therefore, it is necessary to discuss the internal dynamical and thermodynamical processes in the EAM climate system.

### 6.1 The property of the East Asia/Pacific (EAP) pattern teleconnection and its role in the EASM system variability

As well known, the interannual and interdecadal variabilities of the EASM system are dominated by the meridional teleconnection. The meridional teleconnection is generally referred to as the P-J pattern (e.g., Nitta, 1987) or the EAP pattern (e.g., Huang and Li, 1987, 1988). Studies on the role of the EAP pattern teleconnection in the processes of the EASM system variability, its characteristics and property have been proceeded further in the recent years.

During recent years, many studies on the role of the EAP pattern teleconnection in the meridional tripole pattern distribution of the EASM system variability have been made by using the reanalysis data and observational data (e.g., Huang et al. 2006b, 2007b, 2010). As described in Sections 3, there is an obvious meridional tripole

pattern either in the anomaly distributions of summer monsoon rainfall in eastern China or in the anomaly distributions of the summertime water vapour transport fluxes over East Asia on interannual and interdecadal time scales (e.g., Huang et al. 2006b, 2010). As a result, the distributions of droughts and floods in eastern China also exhibit a characteristic of the meridional tripole pattern. Huang et al. (2006b, 2007b) used the EAP pattern teleconnection proposed by Nitta (1987), and Huang and Li (1987, 1988) to interpret the physical mechanism of the above-mentioned meridional tripole pattern of the spatio-temporal variabilities of the EASM system. And Huang et al (2006b, 2007b, 2010) pointed out that the distributions of summertime atmospheric circulation anomalies with the meridional tripole pattern over East Asia and the western North Pacific can be caused by the heating anomaly due to thermal anomaly of the tropical western Pacific or convective activity anomaly around the Philippines through the EAP pattern teleconnection. Of course, this meridional tripole pattern of circulation anomalies over East Asia is also associated with thermal anomaly over the North Atlantic through the EU pattern teleconnection over mid-and high latitudes proposed by Wallace and Gutzler (1981).

An important progress in the recent research on the internal dynamical processes is the further understanding of the property of EAP pattern teleconnection. Early in the 1980s, the EAP pattern teleconnection has been considered as a northward propagating Rossby wave-train excited by the anomalous heating due to convective activity around the Philippines (e. g., Nitta 1987; Huang and Li, 1987, 1988). This shows that the EAP pattern teleconnection can be seen as a thermal mode of summertime circulation variability over East Asia and the Northwest Pacific. However, Kosaka and Nakamura (2006) proposed that this meridional teleconnection can efficiently gain kinetic energy and available potential energy from the basic flow over East Asia and the western North Pacific, thus, the meridional teleconnection can be also considered as a dynamical mode of summertime circulation variability over these regions. As pointed out by Lu et al. (2006), there are two leading modes in the atmospheric circulation anomalies over East Asia and the western North Pacific. The first mode is associated with the circulation variation over the tropical region, which is mainly attributed by the external SST forcing. The second mode is a meridional teleconnection mode, which is mainly resulted from internal atmospheric variability. Therefore, the EAP pattern teleconnection may be considered as a combination of the thermal mode and the dynamical mode of summertime circulation variability over East Asia and the western North Pacific.

Moreover, Kosaka and Nakamura (2006) also presented the three-dimensional structure of the EAP pattern teleconnection and revealed its meridional and vertical coupled characteristics. Lu and Lin et al. (2009) proposed that this vertical and meridional coupled teleconnection can be depicted by zonal shift of the western Pacific subtropical high in the subtropical lower troposphere and the meridional displacement of the East Asian jet stream (EAJS) in the upper troposphere over Asia. Actually, the meridional displacement of the EAJS is the leading mode of interannual variation of upper-tropospheric zonal wind anomalies over East Asia and the western North Pacific.

On the other hand, Lu and Lin (2009) suggested that the precipitation anomaly in the EASM system plays a crucial role in maintaining this meridional teleconnection. The climatological mean and interannual standard deviation of the subtropical precipitation over East Asia is about 7.0mm/ and 1.0mm/, which is comparable to the counterparts over the tropical western Pacific. Thus, as a strong heating sources, the strong precipitation in the EASM system can significantly feedback to the meridional teleconnection. This explains further that the meridional teleconnection is more proper to be viewed as a thermal-dynamical mode.

### ***6.2 The “Silk Road pattern” teleconnection along the Asian jet in the upper troposphere and its role in the EASM system variability***

Yang et al. (2002) analyzed the association of Asian-Pacific-American winter climate with the East Asian jet stream (EAJS) on interannual times scale. They proposed that the EAJS is coupled to a teleconnection pattern extending from the Asian continent to North America with the strongest signals over East Asia and the West Pacific in boreal winter. Moreover, Lu et al. (2002), Lu and Kim(2004), and Lin and Lu (2005) analyzed the variability of meridional circulation anomalies in the upper troposphere over the Northern Hemisphere for the boreal summers of 1986~2000 using the HadAM3 data. Their results showed that there is an obvious teleconnection pattern in the meridional circulation anomalies along the Asian jet in the upper troposphere over the region from West Asia to East Asia. Later, Enomoto et al. (2003) analyzed further the formation for the high ridge near Japan (i.e., the Bonin high) and pointed out that the high ridge is formed as a result of the propagation of stationary Rossby-waves along the Asian jet in the upper troposphere, and the teleconnection is called as “the Silk Road pattern” in their study. Lu and Kim (2004) also pointed out that this teleconnection may be due to the eastward propagation of the Rossby wave-train along the westerly jet stream at 200hPa.

Recently, from the analysis of isentropic potential vorticity, Tao and Wei (2006) demonstrated further that the northward advance or southward retreat of the western Pacific subtropical high may be associated with the propagation of the Rossby wave-train along the Asian jet in the upper troposphere because it may form a high ridge or a low trough along the eastern coast of China. From the analysis of the relationship between the summer monsoon rainfall anomalies in East Asia and the circulation anomalies in the upper troposphere over the Eurasian continent, Hsu and Lin (2006) also pointed out that the meridional triple structure of summertime monsoon rainfall anomalies over East Asia is related to the propagation of the Rossby wave-train along the Asian jet at the upper troposphere in addition to the EAP pattern teleconnection over East Asia and the western North Pacific.

According to the study by Lu (2004), the EAP pattern teleconnection exhibits a intraseasonal difference between early summer and late summer in addition to its interannual variability, generally, it is weak in June, but strong in July and August. And Lu(2004) also pointed out that this intraseasonal difference attributes to two main reasons. First, June is a transition month from spring with a strong vertical westerly shear over the western North Pacific to late summer (July and August) with a strong vertical easterly shear, thus, the vertical shear over the western North Pacific is near

zero in June. The near-zero vertical shear is unfavorable for the coupling of external mode and internal mode excited by the precipitation anomaly in the western North Pacific, thus, it weakens the meridional teleconnection (e.g., Lu 2004; Lin and Lu 2008). The second, in late July, the EAJIS abruptly jumps northward from  $40^{\circ}$  N in mid-July to  $45^{\circ}$  N in late July (e.g., Lin and Lu 2008), and when the jet axis is located more northward, the vertical shear is favorable for the coupling of external mode and internal mode, both the lower-and upper-level responses are significantly stronger, then, the meridional teleconnection can become stronger (e.g., Kosaka and Nakamura 2010; Ye and Lu, 2010). This can explain that the EAP pattern teleconnection is modulated by the “Silk Road pattern” teleconnection.

From the above-mentioned studies, it may be seen that the meridional tripole structure of summertime circulation anomalies over East Asia may be also associated not only with the EAP pattern teleconnection, but also with the “Silk Road pattern” teleconnection along the Asian jet in the upper troposphere. This also show that the “Silk Road pattern” teleconnection can modulate the EAP pattern teleconnection

### ***6.3 Impact of quasi-stationary planetary wave activity on the EAWM system variability***

As discussed in Subsections 6.1 and 6.2, both the EAP pattern teleconnection and the “Silk Road pattern” teleconnection are closely association with the propagations of quasi-stationary planetary waves over the Northern Hemisphere in summer. Thus, quasi-stationary planetary wave activity has a significant impact on the EASM system variability. Similarly, quasi-stationary planetary wave activity also has an important effect on the EAWM system variability.

Early in the 1980s, Huang and Gambo (1982) investigated the three-dimensional propagations of quasi-stationary planetary waves responding to forcing by topography and stationary heat sources in the troposphere in boreal winter with a 34-level model in addition E-P flux of waves. They pointed out that there are two wave guides in the three-dimensional propagations of quasi-stationary planetary waves in the Northern Hemisphere winter, except for the polar wave guide by which the quasi-stationary planetary waves can propagate from the troposphere to the stratosphere over high latitudes (e.g., Dickinson, 1968), there is an other waveguide, i.e., the so-called low-latitude wave guide, by which the waves can propagate from the lower troposphere over mid-and high latitudes to the upper troposphere over low latitudes. Based on the above-mentioned studies, Chen et al. (2002, 2003, 2005), and Chen and Huang (2005) studied systematically the interannual variations of propagating wave guides for quasi-stationary waves with the wave E-P fluxes using the NCEP/NCAR and ERA-40 reanalysis data and AGCM simulation data, respectively. Their results presented that there is an evident out-phase oscillation between these two wave guides for quasi-stationary planetary waves. When the polar wave guide is strong (weak) in a winter, Oppositely the low latitude wave guide may be weak (strong), Moreover, the anomalous propagation of quasi-stationary planetary waves characterized as the convergence/divergence of the wave E-P fluxes can induce a dipole mode in the anomaly distribution of zonal mean zonal wind. This shows that due to the wave-flow interaction, the interannual oscillation of these two wave guides for quasi-stationary

planetary waves has a significant influence on the Arctic Oscillation (AO), which is closely related to the EAWM system variability (e.g., Gong et al., 2001; Gong and Ho, 2003) through the Northern Annular Mode (NAM) proposed by Thompson and Wallace (1998, 2000).

Recently, some studies showed that the stratospheric circulation anomalies can influence the EAWM system variability. Accompanied with the anomalous cold event occurred over South China in January 2008, a downward propagation of stratospheric zonal wind anomalies was observed in the polar region of the Northern Hemisphere (e.g., Gu et al., 2008; Yi et al., 2009). And in December 2009, the anomalous cold events over East Asia were also accompanied with significant downward propagations of stratospheric signals (e.g., Wang and Chen, 2010b). Therefore, the preceding upward propagation of anomalous planetary waves from the troposphere into the stratosphere and the succeeding downward propagation of anomalous zonal flow and low temperature in the stratosphere and its impact on the troposphere may play some key roles in the processes of these cold events.

The activity of planetary waves also experiences obvious interdecadal variation, which is well related to the EAWM system variability (e.g., Huang and Wang, 2006; Wang et al., 2009b). Compared to the period of 1976-87, the southward propagation of quasi-stationary planetary waves after 1988 was enhanced along the low-latitude wave guide in the troposphere, and the upward propagation of waves into the stratosphere was reduced along the polar wave guide, as shown in Fig.20a and Fig.20b. This can cause a weakened subtropical jet around  $35^{\circ}$  N due to the convergence of the wave E-P fluxes. The East Asian jet stream was then weakened, which led to the weakening of the EAWM system from 1988. In addition, the amplitude of quasi-stationary planetary waves was significantly decreased around  $45^{\circ}$  N, which was related to the reduced upward propagation of waves from the lower troposphere after 1988. The decreased amplitude of planetary waves can weaken both the Siberian high and the Aleutian low and led to the decrease of the pressure gradient between them, and then, the EAWM system was weakened. Further analyses indicate that the planetary wave zonal wavenumber 2 played the dominant role in this process of the interdecadal variability (e.g., Wang et al., 2009b).

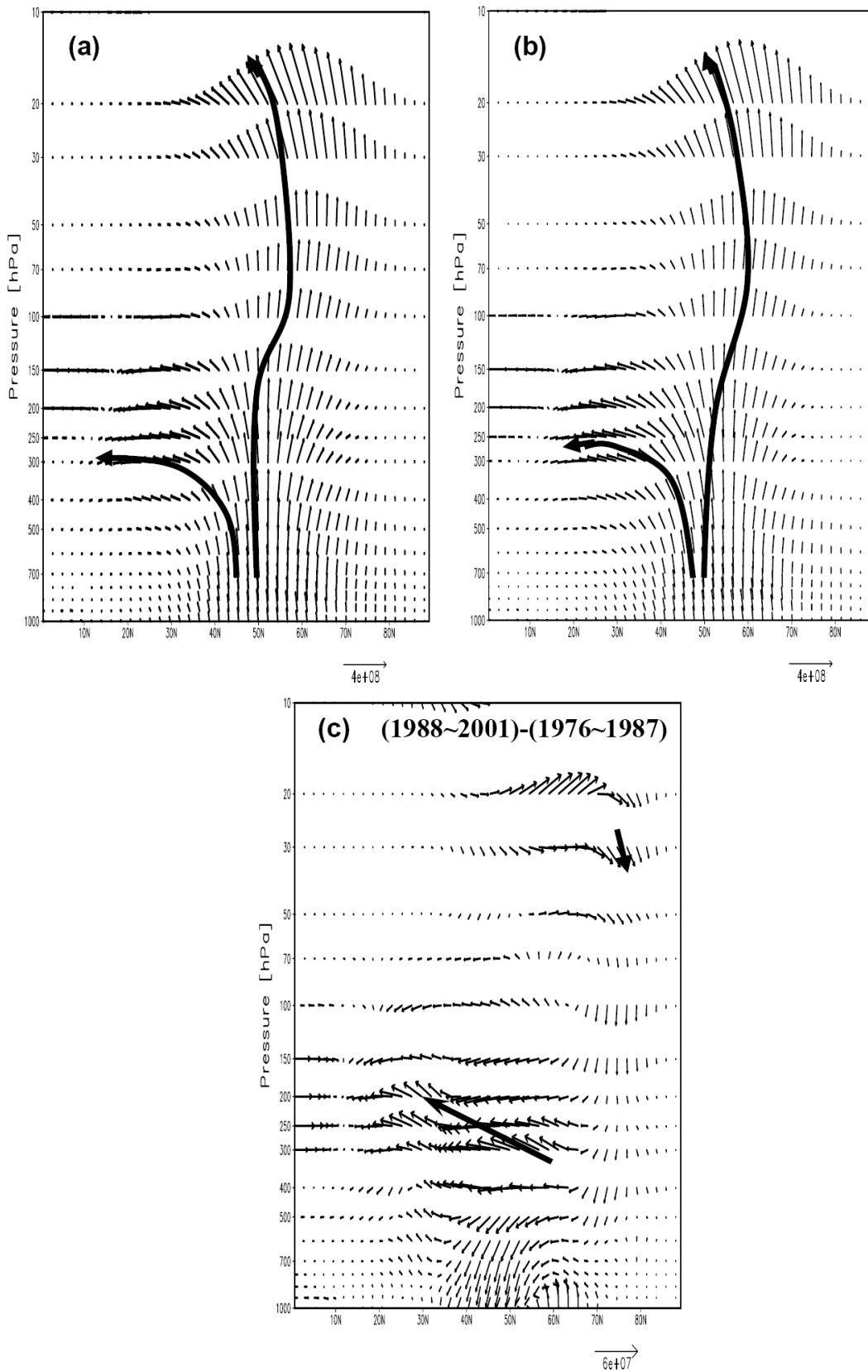


Fig. 20 Composite distribution of the E-P fluxes ( $\times \rho^{-1}$ ) for the quasi-stationary planetary waves 1~3 averaged for the boreal winters of (a) 1976~1987, and (b)

1988~2001, and (c) difference between them. Data is from the ERA-40 reanalysis data (e.g., Uppala et al., 2005)

## 7. Conclusions and remarks for future studies

From the above review, it can be seen that, recently, there are many significant advancements in understanding the characteristics and causes of the spatio-temporal variabilities of the EAM system that are closely associated with the occurrence of climate disasters in China. And the basic physical processes of the variabilities, both internal and external, that influence these variabilities have been also studied further.

However, It should be pointed out that many problems on the basic physical processes of the EAM climate system variability and their impacts on climate disasters in China still remain unclear. For example, the association among the onset, active and break of the EASM and the EAWM over East Asia and annual cycle processes between them, the association of the EAM system with the SAM and the NAM systems, the interactions and their physical processes among different time-scale variabilities of various components of the EAM system, the effect of extratropical process on the EAM variabilities, the physical mechanism of the second leading mode, i.e., the meridional dipole pattern distribution, of the EASM system variability, and the evolution trend of the EAM system under the background of the global warming and so on are not clearly understood. These problems still are important issues for future studies and should be investigated further. Especially, the EAM climate system variabilities on interannual and interdecadal time scales and their physical mechanism should be emphasized in future studies. If the physical processes of these variabilities cannot be revealed further, the improvement of seasonal and annual predication of climate disasters such as droughts, floods, cold winter and hot summer etc. in China may be difficult. Therefore, understanding of the dynamical and thermodynamical processes affecting the spatio-temporal variabilities of the EAM climate system still is a main objective of future studies. We may believe that through the implementation of some National Research Programs, it is possible to further understand the physical mechanism of the spatio-temporal variabilities of the EAM system.

**Acknowledgments.** This paper was supported by the National Basic Research Program (973 Projects) under Grant No. 2010CB950403, 2009CB421405, and National Special Scientific Research Project for Public Interest (Meteorology) under Grant No. GYHY201006021, and the National Natural Science Foundation of China under Grant No. 40730952, respectively.

## REFERENCES

- Annamalai, H., P. Liu, and S. P. Xie, 2005: Southwest Indian Ocean SST variability: Its local effect and remote influence on Asian monsoon. *J. Climate*, **18**, 4150~4167.
- Ashok, K., S. Behera, and A. S. Rao, et al., 2007: El Niño motoki and its teleconnection. *J. Geophys. Res.*, **112**, C11007, doi:10.1029/2006JC003798.
- Bao, M., and R. H. Huang, 2006: Characteristics of the interdecadal variations of heavy rain over China in the last 40 years. *Chinese J. Atmos. Sci.*, **30**, 1057~1067.

(in Chinese)

- Bond, N. A., and D. E. Harrison, 2000: The Pacific decadal oscillation, air-sea interaction and central North Pacific winter atmospheric regions. *Geophys. Res. Lett.*, **27**, 731~734.
- Cai, R. S., J. L. Chen, and R. H. Huang, 2006: The response of marine environment in the offshore area of China and its adjacent ocean to recent global climate change. *Chinese J. Atmos. Sci.*, **30**, 1019~1033. (in Chinese)
- Cennejo-Garrido, A. G., and P. H. Stone, 1977: On the heat source of the Walker circulation. *J. Atmos. Sci.*, **34**, 1155~1162.
- Chang, C. P., J. Erickson, and L.M. Lau, 1979: Northeasterly cold surges and near-equatorial disturbances over the winter- MONEX area during 1974. Part I: Synoptic aspects. *Mon. wea. Rev.*, **107**, 812~829.
- Chang, C. P., Y. S. Zhang, and T. Li, 2000: Interannual and interdecadal variations of the East Asian summer monsoon and tropical Pacific SSTs. I.II. *J. Climate*, **13**, 4310~4340.
- Chen, J. L., and R. H. Huang, 2006: The comparison of climatological characteristics among Asian and Australian monsoon subsystem, Part I, The wind structure of summer monsoon. *Chinese J. Atmos. Sci.*, **30**, 1091~1102. (in Chinese)
- Chen, J. L., and R. H. Huang, 2007: The comparison of climatological characteristics among Asian and Australian monsoon subsystems. Part II. Water vapor transport by summer monsoon. *Chinese J. Atmos. Sci.*, **31**, 766~778. (in Chinese)
- Chen, L. X., Q. G. Zhu, and H. B. Luo, 1991: *East Asian Monsoon*, China Meteorological Press, Beijing, 362pp. (in Chinese)
- Chen, L. X., X. J. Zhou, and W. L. Li, et al., 2004: Characteristics of the climate change and its formation mechanism in China during the last 80 years. *Acta Meteorologica Sinica*, **62**, 634~646.(in Chinese)
- Chen, W., 2002: The impact of El Niño and La Niña events on the East Asian winter and summer monsoon cycle. *Chinese. J. Atmos. Sci.*, **26**, 595~610. (in Chinese)
- Chen, W., and Hans-F. Graf, 1998: The interannual variability of East Asian winter monsoon and its relationship to global circulation. *Max-Planck-Institute für Meteorologie, Report No. 250*.
- Chen, W., Hans-F. Graf, and R. H. Huang, 2000: Interannual variability of East Asian winter monsoon and its relation to the summer monsoon. *Adv. Atmos. Sci.*, **17**, 48-60.
- Chen, W., Hans-F. Graf, and M. Takahashi, 2002: Observed interannual oscillation of planetary wave forcing in the Northern Hemisphere winter. *Geophys. Res. Letter*. **29**(22), 2073, doi:1029/2002 GL016062.
- Chen, W., M. Takahashi, and Hans-F. Graf, 2003: Interannual variations of stationary planetary wave activity in the Northern winter troposphere and stratosphere and their relations to NAM and SST. *J. Geophys. Res.*, **108** (D24), 4797, doi:10.1029/2003 HD003834.
- Chen, W., S. Yang, and R. H. Huang, 2005: Relationship between stationary planetary wave activity and the East Asian winter monsoon. *J. Geophys. Res.*, **110**, D 14110, doi:10. 1029/2004JD 5669.
- Cheng, A. N., W. Chen and R. H. Huang, 1998: The sensitivity of numerical simulation of the East Asian monsoon to different cumulus parameterization schemes. *Adv. Atmos. Sci.*, **15**, 204~220.
- Deng, W. T., Z. B. Sun, G. Zeng, and D. H. Ni, 2009: Interdecadal variation of summer precipitation pattern over eastern China and its relationship with the North Pacific SST. *Chinese J. Atmos. Sci.*, **33**, 835~846. (in Chinese)

- Dickinson, R. E., 1968: Planetary Rossby waves propagating vertically through weak westerly wind wave guides. *J. Atmos. Sci.*, **25**, 984~1002.
- Ding, Q., and B. Wang, 2005: Circumglobal teleconnection in the Northern Hemisphere summer. *J. Climate*, **18**, 3483~3505.
- Ding, Y. H., 1994: *Monsoon over China*. Kluwer Academic Publishers, 420 pp.
- Ding, Y. H., 2007: The variability of the Asian summer monsoon. *J. Meteor. Soc. Japan*. **85**(B), 21~54.
- Ding, Y. H., and X. Ma, 2007: Analysis of isentropic potential vorticity for a strong cold wave in 2004/2005 winter. *Acta Meteorologica Sinica*, **65**, 695~707. (in Chinese)
- Ding, Y. H., Z. Y. Wang, and Y. Sun, 2008: Interdecadal variation of the summer precipitation in East China and its association with decreasing Asian summer monsoon. Part I: Observed evidences. *Int. J. Climatol.* **28**, 1139~1145.
- Du, Z. C., R. H. Huang, G. Huang and J. L. Chen, 2010: Differences between the rainfall cloud system in East Asia and that in South Asia and its possible cause. *Chinese J. Atmos. Sci.*, (submitted) (in Chinese)
- Enomoto, T., B. J. Hoskins, and Y. Matsuda, 2003: The formation mechanism of the Bonin high in August. *Quart. J. Roy. Meteor. Soc.*, **129**, 157~178.
- Fu, Y. F., Y. H. Lin and G. S. Liu, et al., 2003: Seasonal characteristics of precipitation in 1998 over East Asia as derived from TRMM PR. *Adv. Atmos. Sci.*, **20**, 511~529.
- Gong, D. Y., S. W. Wang, and J. H. Zhu, 2001: East Asian winter monsoon and Arctic Oscillation. *Geophys. Res. Letters*, **28**, 2073~2076.
- Gong, D. Y., and C. Ho, 2003: Arctic Oscillation signals in the East Asian summer monsoon. *J. Geophys. Res.*, **108**, 4066, doi:10.1029/2003JD002193.
- Gu, L., K. Wei, and R. H. Huang, 2008: Severe disaster of blizzard, freezing rain and low temperature in January 2008 in China and its association with the anomalies of East Asian monsoon system. *Clim. & Envir. Res.* **13**, 405~418.(in Chinese)
- Hartmann, D. H., H. Hendon, and R. A. Houze, 1984: Some implications of the meso-scale circulations in tropical cloud clusters for large-scale dynamics and climate. *J. Atmos. Sci.*, **41**, 113~121.
- Hong, C. C., and T. Li, 2009: The extreme cold anomaly over Southeast Asia in February 2008: Roles of ISO and ENSO. *J. Climate*, **22**, 3786~3801. doi:10.1175/2009JCLI2864.1.
- Hsu, H. H., and S. M. Lin, 2006: The tripole pattern of East Asian summer rainfall. *Proceedings of the Symposium on Asian monsoon*, Kuala Lumpur, Malaysia, 4~7, April, 2006. 28~29.
- Huang, G., and K. M. Hu, 2008: Impact of North Indian Ocean SSTA on Northwest Pacific lower larger anomalous anticyclone in summer. *J. of Nanjing Institute of Meteorology*, **31**, 750~757. (in Chinese)
- Huang, G., K. M. Hu, and S. P. Xie, 2010: Strengthening of tropical Indian Ocean teleconnection to the Northwest Pacific since the mid-1970s: An atmospheric GCM study. *J. Climate*, **23**, doi:10.1175.2010JCL13577.1
- Huang, G., X. Qu, and K. M. Hu, 2010: The impact of the tropical Indian Ocean on South Asian high in boreal summer. *Adv. Atmos. Sci.*, **27**, (to be published)
- Huang, G., Y. Liu, and R. H. Huang, 2010: The interannual variability of summer rainfall in the arid and semi-arid region in northern China and its association with the Northern Hemisphere circumglobal teleconnection. *Adv. Atmos. Sci.*, (to be published)
- Huang, P., and R. H. Huang, 2009: Relationship between the modes of winter tropical

- Pacific SSTAs and the intraseasonal variations of the following summer rainfall anomalies in China. *Atmos & Ocea. Sci., Lett.*, **25**, 295~300.
- Huang, R. H., 1984: The characteristics of the forced planetary wave propagations in the summer Northern Hemisphere. *Adv. Atmos. Sci.*, **1**, 85-94.
- Huang, R. H., 1985: Numerical simulation of the three-dimensional teleconnections in the summer circulation over the Northern Hemisphere. *Adv. Atmos. Sci.*, **2**, 81-92.
- Huang, R. H., 2006: Progresses in research on the formation mechanism and prediction theory of severe climatic disasters in China. *Adv. Earch. Sci.*, **21**, 564~575.
- Huang, R. H., 2009: Recent progresses in studies of variations and anomalies of East Asian monsoon (EAM) climate system and formation mechanism of severe climate disasters in China. *Bulletin of the Chinese Academy of Sciences*, **23**, 222~225.
- Huang, R. H., and K. Gambo, 1982: The response of a hemispheric multi-level model atmosphere to forcing by topography and stationary heat sources. Parts I, II. *J. Meteor. Soc. Japan*, **60**, 78~108.
- Huang, R. H., and W. J. Li, 1987: Influence of the heat source anomaly over the tropical western Pacific on the subtropical high over East Asia. *Proceedings of the International Conference on the General Circulation of East Asia*, Chengdu, April 10-15, 1987, 40-51.
- Huang, R. H., and W. J. Li, 1988: Influence of the heat source anomaly over the tropical western Pacific on the subtropical high over East Asia and its physical mechanism. *Chinese J. Atmos. Sci.*, **14**, Special Issue, 95~107. (in Chinese)
- Huang, R. H., and Y. F. Wu, 1989: The influence of ENSO on the summer climate change in China and its mechanisms. *Adv. Atmos. Sci.*, **6**, 21-32.
- Huang, R. H., and F. Y. Sun, 1992: Impact of the tropical western Pacific on the East Asian summer monsoon. *J. Meteor. Soc. Japan*, **70**, (1B), 243-256.
- Huang, R. H., and L. T. Zhou, 2002: Research on the characteristics, formation mechanism and prediction of severe climate disasters in China. *J. Nature Disasters*, **11**, 1-9. (in Chinese).
- Huang, R. H., and L. Wang, 2006: Interdecadal variation of Asian winter monsoon and its association with the planetary wave activity. *Proceedings of the Symposium on Asian Monsoon*, Kuala Lumpur, Malaysia, 4~7 April, 2006, 126.
- Huang, R. H., and J. L. Chen, 2010: Characteristics of the summertime water vapor transports over the eastern part of China and those over the western part of China and their difference. *Chinese J. Atmos. Sci.*, **34**, 1035~1047. (in Chinese)
- Huang, R. H., Y. H. Xu, and P. H. Wang, 1998a: The features of the particularly severe flood over the Changjiang (Yangtze River) basin during the summer of 1998 and exploration of its cause. *Clim. & Envir. Res.*, **3**, 300~313. (in Chinese)
- Huang, R. H., Z. Z. Zhang, G. Huang and B. H. Ren, 1998: Characteristics of the water vapor transport in East Asian monsoon region and its difference from that in South Asian monsoon region in summer. *Chinese J. Atmos. Sci.*, **22**, 460~469. (in Chinese)
- Huang, R. H., Y. H. Xu, and L. T. Zhou, 1999: The interdecadal variation of summer precipitations in China and the drought trend in North China. *Plateau Meteor.*, **18**, 465~476. (in Chinese).
- Huang, R. H., L. T. Zhou, and W. Chen, 2003: The progress of recent studies on the variabilities of the East Asian monsoon and their causes. *Adv. Atmos. Sci.*, **20**, 55~69.
- Huang, R. H., G. Huang, and Z. G. Wei, 2004a: Climate variations of the summer

- monsoon over China. *East Asian Monsoon*, Chang, C. P. Ed., World Scientific Publishing Co. Pte. Ltd., 213~270.
- Huang, R. H., W. Chen, B. L., Yan and R. H. Zhang, 2004b: Recent Advances in studies of the interaction between the East Asian winter and summer monsoon and ENSO cycle. *Adv. Atmos. Sci.*, **21**, 407~424.
- Huang, R. H., L. Gu, and Y. H. Xu, 2005: Characteristics of the interannual variations of onset and northward advance of the East Asian summer monsoon and their associations with thermal states of the tropical western Pacific. *Chinese J. Atmos. Sci.*, **29**, 20~36. (in Chinese)
- Huang, R. H., R. S. Cai, H. L. Chen, and L. T. Zhou, 2006a: Interdecadal variations of droughts and floodings in China and their association with the East Asian climate system. *Chinese J. Atmos. Sci.*, **30**, 730~743. (in Chinese)
- Huang, R. H., J. L. Chen, G. Huang, and Q. L. Zhang, 2006b: The quasi-biennial oscillation of summer monsoon rainfall in China and its cause. *Chinese J. Atmos. Sci.*, **30**, 545~560. (in Chinese)
- Huang, R. H., L. Gu, L. T. Zhou, and S. S. Wu, 2006c: Impact of the thermal state of the tropical western Pacific on onset date and process of the South China Sea summer monsoon. *Adv Atmos. Sci.*, **23**, 909~924.
- Huang, R. H., K. Wei, J. L. Chen, and W. Chen, 2007a: Research on the East Asian winter monsoon anomalies in the winters of 2005 and 2006 and their relation to the quasi-stationary planetary wave activities over the Northern Hemisphere. *Chinese J. Atmos. Sci.*, **31**, 1033~1048. (in Chinese)
- Huang, R. H., J. L. Chen, and G. Huang, 2007b: Characteristics and variations of the East Asian monsoon system and its impacts on climate disasters in China. *Adv. Atmos. Sci.*, **24**, 993~1023.
- Huang, R. H., L. Gu, J. L. Chen, and G. Huang, 2008: Recent progresses in studies of the temporal-spatial variations of the East Asian monsoon system and their impacts on climate anomalies in China. *Chinese J. Atmos. Sci.*, **32**, 691~719. (in Chinese)
- Huang, R. H., J. L. Chen, and Y. Liu, 2010: Interdecadal variation of the leading modes of summertime precipitation anomalies in eastern China and its association with water vapor transport over East Asia. *Chinese J. Atmos. Sci.*, **34**, (to be published). (in Chinese)
- Iguchi, T., T. Kozu, and R. Meneghini, et al., 2000: Rain profiling algorithm for the TRMM precipitation radar. *J. App. Meteor.*, **39**, 2038~2052.
- Jhun, J. G., and E. J. Lee, 2004: A new East Asian winter monsoon index and associated characteristics of the winter monsoon. *J. Climate*. **17**, 711~726.
- Kalnay, E. M., and Coauthors, 1996: The NCEP/NCAR 40-year reanalysis project.. *Bull Amer. Meteor. Soc.*, **77**, 437~471.
- Kang, L. H., W. Chen, and K. Wei, 2006: The interdecadal variation of winter temperature in China and its relation to anomalies in atmospheric general circulation. *Clim. & Environ. Res.*, **11**, 330~339. (in Chinese)
- Kang, L. H., W. Chen, L. Wang, and L. Chen, 2009: The interdecadal variation of winter temperature in China and their relation with the atmospheric circulation and sea surface temperature. *Clim. & Environ. Res.*, **14**, 45~53. (in Chinese)
- Kosaka, Y., and H. Nakamura, 2006: Structure and dynamics of the summertime Pacific-Japan (PJ) teleconnection pattern. *Quart. J. Roy. Meteor. Soc.*, **132**, 2009~2030.
- Kosaka, Y., and H. Nakamura, 2010: Mechanisms of meridional teleconnection observed between a summer monsoon system and a subtropical anticyclone. Part I:

- the Pacific-Japan pattern. *J. Climate*, (to be accepted).
- Kurihara, K., 1989: A climatological study on the relationship between the Japanese summer weather and the subtropical high in the western northern Pacific. *Geophys. Mag.*, **43**, 45-104.
- Kwon, M. H., G. J. Jhun, and K. J. Ha, 2007: Decadal change in east Asian summer monsoon circulation in the mid-1990s. *J. Geophys. Res. Lett.*, **34**, L21706, doi:10.29/2007GL031977.
- Lau, K. M. and C.P. Chang, 1987: Planetary scale aspects of the winter monsoon and atmospheric teleconnections. *Monsoon Meteorology*, Chang, C. P. and T. W. Krishnamurti, Eds. Oxford Uni. Press, 161-201.
- Li, S. L., J. Lu, G. Huang, and K. M. Hu, 2008: Tropical Indian Ocean basin warming and East Asian summer monsoon. A multiple AGCM study. *J. Climate*, **21**, 6080~6088.
- Li, Y., and S. Yang, 2010: A dynamical index for the East Asian winter monsoon. *J. Climate*, **23**, doi: 10.1175/2010JCLI3375.1.
- Liang, J. Y, and S. S. Wu, 2002: A study of southwest monsoon onset date over the South China Sea and its impact factors. *Chinese J. Atmos. Sci.*, **26**, 844~855. (in Chinese)
- Lin, Z. D., and R. Y. Lu, 2005: Interannual meridional displacement of the East Asian upper-tropospheric jet stream in summer. *Adv. Atmos. Sci.*, **22**, 199~211.
- Lin, Z. D., and R. Y. Lu, 2008: Abrupt northward jump of the East Asian upper-tropospheric jet stream in mid-summer. *J. Meteor. Soc. Japan*, **84**, 857~856.
- Lin, Z. D., R. Y. Lu, and W. Zhou, 2009: Change in early-summer meridional teleconnection over the western North Pacific and East Asia around the late 1970s, *Int. J. Climatol.*, **29**, doi: 10.1002/joc.2038.
- Liu, P., Y. F., Fu, 2010: Climatic characteristics of summer convective and stratiform precipitation in southern China based on measurements by TRMM precipitation radar. *Chinese J. Atmos. Sci.*, **34**, 802~814. (in Chinese)
- Lu, M. M., and C. P. Chang, 2009: Unusual late-season cold surges during the 2005 Asian winter monsoon: Roles of Atlantic blocking and the central Asian anticyclone. *J. Climate*, **22**, 5205~5217. doi:10.1175/2009JCLI2935.1.
- Lu, R. Y., 2004: Associations among the components of the East Asian summer monsoon system in the meridional direction. *J. Meteor. Soc., Japan*, **82**, 155~165.
- Lu, R. Y., and B. J. Kim, 2004: The climatological Rossby wave source over the STCZs in the summer Northern Hemisphere. *J. Meteor. Soc. Japan*, **82**, 657~669.
- Lu, R. Y., and Z. D. Lin, 2009: Role of subtropical precipitation anomalies in maintaining the summertime meridional teleconnection over the western North Pacific and East Asia. *J. Climate*, **22**, 2058~2072.
- Lu, R. Y., J. H. Oh, and B. J. Kim, 2002: A teleconnection pattern in upper-level meridional wind over the North African and Eurasian continent in summer. *Tellus*, **54A**, 44~55.
- Lu, R. Y., Y. Li, and B. Dong, 2006: External and internal summer atmospheric variability in the western North Pacific and East Asia. *J. Meteor. Soc. Japan*, **84**, 447~462.
- Ma, X., H. Y. Ding, H. Xu, and J. H. He, 2008: The relation between strong cold waves and low-frequency waves during the winter of 2004/2005. *Chinese J. Atmos. Sci.* **32**: 380~394. (in Chinese)
- Nitta, Ts., 1987: Convective activities in the tropical western Pacific and their impact on the Northern Hemisphere summer circulation. *J. Meteor. Soc. Japan*, **64**, 373-390.

- Tao, S. Y., and F. K. Zhu, 1964: The variation of 100hPa circulation over South Asia in summer and its march and withdraw of the western Pacific subtropical high. *Acta Meteorologica Sinica*, **34**, 385~395. (in Chinese)
- Tao, S. Y., and L. X. Chen, 1985: The East Asian summer monsoon. *Proceedings of International Conference on Monsoon in the Far East*. Tokyo, Nov 5~8. 1985, 1~11.
- Tao, S. Y., and L. X. Chen, 1987: A review of recent research on the East Asian summer monsoon in China. *Monsoon Meteorology*, Chang, C. P. and T. N. Krishnamurti, Eds., Oxford University Press, 60-92.
- Tao, S. Y., and J. Wei, 2006: The westward, northward advance of the subtropical high over the West Pacific in summer. *J. of Applied Meteor. Sci.*, **17**, 513~524. (in Chinese)
- Trenberth, K. E, and J. W. Hurrell, 1994: Decadal atmosphere-ocean variations in the Pacific. *Climate Dyn.* **9**, 303~319.
- Tu, C. W., and S. S. Huang, 1944: The advance and retreat of the summer monsoon. *Meteor. Mag.*, **18**, 1-20.
- Uppala, S. M., P. W. Kallberg, and A. J. Simmons, et al., 2005: The ERA-40 reanalysis. *Quat. J. Roy. Meteor. Soc.*, **131**, 2961~3012.
- Wallace, J. M., and D. S. Gutzler, 1981: Teleconnection in the geopotential height field during the Northern Hemisphere winter. *Mon. Wea. Rev.*, **109**, 748~812.
- Wang, B., R. G. Wu, and T. Li, 2003: Atmosphere-warm ocean interaction and its impacts on Asian-Australian monsoon variation. *J. Climate*, **16**, 1195~1211.
- Wang, B., H. Lin, Y. S. Zhang, and M. M. Lu, 2004: Definition of South China Sea monsoon onset and commencement of the East Asia summer monsoon. *J. Climate*, **17**, 699~710.
- Wang, B., Z. Wu, C. P. Chang, J. Liu, J. Li, and T. Zhou, 2010: Another look at interannual-to-interdecadal variations of the East Asian winter monsoon: The northern and southern temperature modes. *J. Climate*. **23**, 1495~1512. doi:10.1175/2009JCLI3243.1.
- Wang, L., and W. Chen, 2010a: How well do existing indices measure the strength of the East Asian winter monsoon? *Adv. Atmos. Sci.*, **27**, 855~870. doi: 10.1007/s00376-009-9094-3.
- Wang L., and W. Chen, 2010b: Downward Arctic Oscillation signal associated with moderate weak stratospheric polar vortex and the cold December 2009. *Geophys. Res. Lett.*, **37**, doi:10.1029/2010GL042659.
- Wang L., W. Chen, and R. H. Huang, 2008: Interdecadal modulation of PDO on the impact of ENSO on the east Asian winter monsoon. *Geophys. Res. Lett.*, **35**, L20702, Doi:10.1029/2008GL035287.
- Wang, L., W. Chen, W. Zhou, and R. H. Huang, 2009a: Interannual variations of East Asian trough axis at 500 hPa and its association with the East Asian winter monsoon pathway. *J. Climate*. **22**, 600~614.
- Wang, L., R. H. Huang, and L. Gu, 2009b: Interdecadal variations of the East Asian winter monsoon and their associated with quasi-stationary planetary wave activity. *J. Climate*. **22**, 4860~4872.
- Wang, Z. Y., and Y. H. Ding, 2006: Climate change of the cold wave frequency of China in the last 53 years and the possible reasons. *Chinese J. Atmos. Sci.*, **30**, 1068~1076.(in Chinese)
- Webster, P. J., V. O. Magana, T. B. Palmer, J. Shukla, R. A. Tomas, M. Yanai, and T. Yasunari, 1998: Monsoons: processes, predictability, and the prospects for prediction. *J. Geophys. Res.*, **103**, 14451~14510

- Wei, K., W. Chen, and W. Zhou, 2011: The change of East Asian cold season evolution since 2000. *Adv. Atmos. Sci.*, **27**, 69~79
- Wei, Z. G., R. H. Huang, and W. Chen, et al., 2002: Spatial distributions of interdecadal variations of the snow at the Tibetan Plateau. *Chinese J. Atmos. Sci.*, **26**, 496~508.(in Chinese)
- Wei, Z. G., R. H. Huang, and W. J. Dong, 2003: Interannual and interdecadal variations of air temperature and precipitation over the Tibetan Plateau. *Chinese J. Atmos. Sci.*, **27**, 157~170. (in Chinese)
- Wen, M., S. Yang, A. Kumar, and P. Zhang, 2009: An analysis of the large-scale climate anomalies associated with the snowstorms affecting China in January 2008. *Mon. Wea. Rev.*, **137**, 1111~1131.
- Weng, H. Y., K. Ashok, and S. Behera, et al., 2007: Impacts of recent El Niño motoki on dry/wet conditions in the Pacific rim daring boreal summer. *Climate Dynamics*, **29**, 113~129.
- Wu, B. Y., and J. Wang, 2002: Winter Arctic Oscillation, Siberian high and East Asian winter monsoon. *Geophys. Res. Lett.*, **29**, 19, 1897, doi:10.1029/2002 GL015373.
- Wu, B. Y., R. H. Zhang, and R. D'Arrigo, 2006: Distinct modes of the East Asian winter monsoon. *Mon. Wea. Rev.* **134**, 2165~2179.
- Wu, B. Y., K. Yang, and R. H. Zhang, 2008: Eurasian snow cover variability and its association with summer rainfall in China. *Adv. Atmos. Sci.*, **26**, 31~44.
- Wu, G. X., and Y. S. Zhang, 1997: Tibetan Plateau forcing and the timing of the monsoon onset over South Asia and the South China Sea. *Mon. Wea. Rev.*, **126**, 917~927.
- Xie P. P., and P. A. Arkin, 1997: Analyses of global monthly precipitation using gauge observations, satellite estimates and numerical model prediction. *J. Climate.*, **9**, 804~858.
- Xie. S. P., K. M. Hu, J Hafner, H. Tokinaga, Y. Du, G. Huang and T. Sampe, 2009: Indian Ocean capacitor effect on Indo-Western Pacific climate during the summer following El Niño. *J. Climate*, **22**, 730~747.
- Yang, J. L., Q. Y. Liu, S. P. Xie, Z. Y. Liu, and L. X. Wu, 2007: Impact of the Indian ocean SST basin mode on the Asian summer monsoon. *Geophys. Res. Lett.*, **34**, L02708, doi:10.1029/2006GL028571.
- Yang, S., K. M. Lau, and K. M. Kim, 2002: Variations of the East Asian jet stream and Asian-Pacific-American climate anomalies. *J. Climate*, **15**, 306~325.
- Ye, D. Z., and Y. X. Gao, 1979: *Tibetan Plateau Meteorology*. Science Press, Beijing, 279pp. (in Chinese).
- Ye, H., and R. Y. Lu, 2010: Subseasonal variation in ENSO-related East Asian rainfall anomalies during summer and its role in weakening the relationship between the ENSO and summer rainfall in eastern China since the late 1970s. submitted to *J. Climate*.
- Yi, M., Y. Chen, R. Zhou, and S. Deng, 2009: Analysis on isentropic potential vorticity for the snow calcmity in South China and the stratospheric polar vortex in 2008. *Plateau Meteor*, **28**, 880~888. (in Chinese)
- Zhang, P., S. Yang, and V. E. Kousky, 2005: South Asian high and Asian-Pacific-American climate teleconnection. *Adv. Atmos. Sci.*, **22**, 915~923.
- Zhang, Q., G. X. Wu, and Y. F. Qian, 2002: The bimodaity of the 100hPa South Asian high and its association on the climate anomaly over Asia in summer. *J. Meteor. Soc. Japan*, **80**, 733~744.
- Zhang, Q. Y., J. M. Lu, L. M. Yang, J. Wei and J. B. Peng, 2009: The interdecadal variation of precipitation pattern over China during summer and its relationship

- with the atmospheric internal dynamic processes and extra-forcing factors. *Chinese J. Atmos. Sci.*, **31**, 1290~1300. (in Chinese)
- Zhang R. H., and R. H. Huang, 1998: Dynamical effect of zonal wind stress over the tropical Pacific during the occurring and decaying stage of El Niño events. Part I: Data diagnostic and theoretical analysis. *Chinese J. Atmos. Sci.*, **22**, 587~599. (in Chinese)
- Zhang R. H., A. Sumi, and M. Kimoto, 1996: Impact of El Niño on the East Asian monsoon: A diagnostic study of the 86/87 and 91/92 events. *J. Meteor. Soc. Japan*, **74**, 49-62.
- Zhang R.H., A. Sumi, and M. Kimoto, 1999: A diagnostic study of the impact of El Niño on precipitation in China. *Adv. Atmos. Sci.*, **16**, 229~241.
- Zhang, R. H., B. Y. Wu, P. Zhao and J. P. Han, 2008: The decadal shift of the summer climate in the late 1980s over East China. *Acta Meteorologica Sinica*, **66**, 697~706. (in Chinese )
- Zhang, Z. H., and G. Huang, 2008: Different types of El Niño events and their relationship with China summer climate anomaly. *J. of Nanjing Institute of Meteorology*, **31**, 782~789. (in Chinese)
- Zhao, P., X. Zhang, Y. Yi, and J. Chen, 2009: Remotely modulated tropical-North Pacific Ocean-atmosphere interactions by the South Asian high. *Atmos. Res.*, **94**, 45~60.
- Zhou, L. T., 2010: Impact of East Asian winter monsoon on rainfall over southeastern China and its dynamical process. *Int. J. Climatol.*, **30**, doi:10.1002/Joc.2101.
- Zhou, L. T., 2010a: Characteristics of temporal and spatial variations of sensible heat flux in the arid and semi-arid region of Eurasia. *Transactions of Atmos. Sci.*, **33**, 299~305. (in Chinese)
- Zhou, L. T., and R. H. Huang, 2008: Interdecadal variability of sensible heat in arid and semi-arid regions of Northwest China and its relation to summer precipitation in China. *Chinese J. Atmos. Sci.*, **32**, 1276~1288. (in Chinese)
- Zhou. L. T., and R. H. Huang, 2006: Characterisitcs of the interdecadal variability of difference between surface temperature and surface air temperature in spring in the arid and semi-arid region of Northwest China and its impact on summer precipitation in North China. *Clim. & Envir. Res.*, **11**, 1~13. (in Chinese)
- Zhou, L. T., and R. H. Huang, 2010: Interdecadal variability of summer rainfall in Northwest China and its possible causes. *Int. J. Climatol.*, **30**, 549~557, Doi:10.1002/joc.1923.
- Zhou, X. X., Y. H. Ding and P. X. Wang, 2010: Moisture transport in the Asian summer monsoon region and its relationship with summer precipitation in China. *Acta Meteorologica Sinica*, **24**, 31~42.
- Zhu, K. Z., 1934: Southeast monsoon and rainfall in China. *Chinese J. Geogr. Soc.*, **1**, 1-27. (in Chinese)

# **Advances in Meteorological Satellite and Satellite Meteorology in China (2006–2010)**

YANG Jun, FANG Zongyi, DONG Chaohua, and LI Jun  
National Satellite Meteorological Center, China Meteorological Administration  
Beijing 100081, P. R. China

## **1. Introduction**

Meteorological satellites are among the most important components of the Earth-Atmospheric observation system in China. The Chinese government has always been supporting this industry with great efforts, ensuring a healthy development of this industry from scratch, highlighted by the leaps from low-orbital to high-orbital system and the progress from experimental to operational meteorological satellites. The rapid development stage is between 2006 and 2010, marked by some critical events. For instance, the first and second satellites of the new-generation polar-orbiting meteorological satellite system (FY-3A/B) were sent into orbit during this stage, illustrating the new era of polar-orbiting meteorological satellite system in China. Some critical indices of FY-3A/B, such as the observation ability, data processing and operational applications, have reached to an international leading level. The double-satellite coverage by geostationary satellite system is another remarkable improvement realized in this stage, which enables to obtain an image every 15 minutes over China and its surrounding areas during the flood season. The satellite remote sensing theory and applications, as well as data processing capability, are greatly improved with the advancement of satellite observing system. Many achievements have been made during this five-year stage, including the remote sensing of atmospheric parameters, retrieving atmospheric trace gas composition and cloud/aerosol properties, as well as extracting surface physical/biological characteristics. Meanwhile, using the satellite remote sensing data, critical progresses are achieved in the field of weather analysis and forecast, especially in nowcasting and forecasting disastrous weather events, assimilating satellite data in numerical weather prediction (NWP) models, and monitoring the ocean/land surface. Now in China, meteorological satellites have played a critical role in weather forecast, climate change study, short-term climate prediction, monitoring of ecological system and natural disasters. This report mainly focuses on the major advances in Chinese meteorological satellite systems, and satellite data processing and application systems in the recent five years.

## **2. Advances in Chinese Meteorological Satellite**

### **2.1 The Chinese polar-orbited meteorological satellite**

The FengYun-3 (FY-3) satellite series is the second generation of Chinese polar-orbiting meteorological satellite system, including six planned satellites. The major goal of this series is to enable a global, all-sky, three-dimensional, quantitative, and multi-spectral remote sensing capability, to meet the development of modern meteorological service, especially the numerical weather prediction. Other goals

include: monitoring the large-scale severe weather events and associated natural disasters as well as the change of ecological system; providing geophysical datasets for global climate change study and climate analysis/prediction; and providing services for other areas such as agriculture, forestry, animal husbandry, oceanography, and hydrology.

The first two satellites, FY-3A and B, of the FY-3 series, were successfully launched from the Taiyuan Space Launch Center on 27 May 2008 and 05 November 2010, respectively. Both of them are experimental satellites, carrying exactly the same eleven instruments categorized into five groups: sounding mission, imaging mission, radiation mission, ozone mission, and space environment mission. The spectral coverage ranges from ultraviolet (UV), visible (VIS), near infrared (NIR), long-wave infrared (IR), to microwave (see Table 1). FY-3A was in operational use in early 2009 after half-year on-orbit testing. The FY3A satellite and its ground system have been working smoothly for more than two years. The FY-3A datasets are transferred to the ground receiving stations through the data link system between the satellite and the ground and finally collected in the data service center (located in the building of the National Satellite Meteorological Center). Multiple data products are generated using advanced scientific algorithms with robust support of computer network. These products are shared by users through different ways. FY-3A has played an important role in providing services for several critical events such as the Beijing Olympics in 2008, flood seasons, and ecological and natural disasters. FY-3B is currently in on-orbit testing and calibrating. FY-3A and B are AM and PM satellites, respectively. The FY-3A/B forms a double-satellite system which significantly increases the temporal resolution, i.e., covering the globe four times a day.

FY-3 series is an important component of the World Meteorological Organization (WMO) space-based global observing system, providing services for both China and other countries (Yang et al. 2009).

**Table 1. Primary parameters of the sensors onboard the FY-3A/B**

Instrument	Spectral coverage	No. Channels	Scanning width	Resolution	Bit Depth	Purposes
Visible and InfraRed Radiometer (VIRR)	0.44 ~ 12.5 $\mu\text{m}$	10	$\pm 55.4^\circ$	1.1 km	10bit	Cloud, vegetation, snow, ice, land/ocean surface temperature, hot spot.
Infrared Atmospheric Sounder (IRAS)	0.69 ~ 15.5 $\mu\text{m}$	26	$\pm 49.5^\circ$	17.0 km	13bit	Temperature and moisture profile, OLR
Microwave Atmospheric	50 ~ 57 GHz	4	$\pm 48.3^\circ$	50 km	13bit	Temperature profile, surface

Temperature Sounder (MWTS)						emissivity
Microwave Atmospheric Humidity Sounder (MWHS)	150 ~ 183 GHz	5	$\pm 53.35^\circ$	15 km	14bit	Moisture profile, rain rate
MEDium Resolution Spectral Imager (MERSI)	0.41 ~ 12.5 $\mu\text{m}$	20	$\pm 55.4^\circ$	0.25 ~ 1.1 km	12bit	True color image, cloud, vegetation, land type, ocean color,
Solar Backscatter Ultraviolet Sounder (SBUS)	252 ~ 340 nm	12		200 km	12bit	Ozone profile
Total Ozone Unit (TOU)	309 ~ 361 nm	6	$\pm 54^\circ$	50 km	12bit	Total column ozone
Microwave Radiation Imager (MWRI)	10.65 ~ 89 GHz	10	Conical scanning $45^\circ$	9 ~ 85 km	12bit	Precipitation and cloud water, TPW, soil moisture, snow cover.
Earth Radiation Measurement (ERM)	0.2 ~ 3.8 $\mu\text{m}$ 0.2 ~ 50 $\mu\text{m}$	2	$\pm 50.0^\circ$	35 km	16bit	Reflected solar flux, OLR
Solar Irradiance Monitor (SIM)	0.2 ~ 50 $\mu\text{m}$	1			16bit	Solar constant
Space Environment Monitor (SEM)	3.0 ~ 300 Mev 0.15 ~ 5.7 Mev					Solar proton, and electron, geomagnetic field, satellite surface charging, radiant dose, and single particle event

## 2.2 Chinese geostationary meteorological satellites

FY-2D and 2E were launched on 28 December 2006 and 23 December 2008, respectively, at the Xichang Space Launch Center. Three slots on the geostationary orbit are reserved for geostationary satellites: 123 °, 105 ° and 86.5 °. Since FY-2C, the on-orbit lifetime of Chinese geostationary satellites is significantly extended beyond their designed. For example, FY-2C was launched in October 2004 and retired in January 2010 (provided service for more than five years). The five-channel Visible and Infrared Spin-Scan Radiometer (VISSR) is onboard the FY-2C/2D/2E. Comparing to the imager onboard the experimental satellite, the five-channel VISSR carries one more IR split window channel and a NIR window channel, and enables the capability of detecting sea surface temperature and natural fire disaster (see Table 2). Currently 2D and 2E are in operation at 86.5 ° and 104.5 ° geostationary orbit, respectively, to continuously monitor environment and weather evolution, especially the typhoon and storms over China and other Asian areas. This double-satellite system greatly benefits the overlapped areas with more frequent observations on the disastrous weather events, and significant achievements have been made through the satellites' remarkable performance.

**Table 2. FY-2C/2D/2E Visible Infrared Spin-Scan Radiometer**

Spectrum	Wavelength (μm)	Noise level (K)	Spatial Resolution	Bit Depth (bit)	Purposes
VIS	0.55 ~ 0.90		1.25 km	6	Cloud mask, wind
IR1	10.3 ~ 11.3	0.4 ~ 0.2	5 km	10	Cloud, wind, SST
IR2	11.5 ~ 12.5	0.4 ~ 0.2	5 km	10	Cloud, wind, SST
IR3	6.3 ~ 7.6	0.6 ~ 0.5	5 km	10	Moisture image, wind
IR4	3.5 ~ 4.0	0.5 ~ 0.3	5 km	10	Cloud, hot spot, dust storm, fog

## 2.3 The ground application system of Chinese meteorological satellite

The ground application system is critical to fulfill the goal of meteorological satellite after the launch. It should always be updated along with the development of the meteorological satellite. Several HP and IBM servers are adopted in the ground system to meet the requirements of new-generation satellites FY-3A/B and FY-2D/2E, ensuring the high-speed data collection via multiple stations, the sharing of computer resources among multiple stations, and the effective and automatic coordination of services. The ground application system is a comprehensive operational meteorological satellite information system to deal with satellite real-time navigation, data accessing, remote sensing data processing, operational information management and services (Xu et al. 2006; Dong et al. 2009). A polar-orbiting satellite data ground

station was established in Kiruna, Sweden in 2008 in order to shorten the data collection time and improve the satellite data assimilation in NWP models. This station, together with other four ground stations in China, makes possible the global-coverage of data collection in timely manner. The ground system includes a major operation module and a supporting and extensive module (see Figure 1). Three levels of products are generated: Levels 1, 2 and 3 (see Tables 3 and 4). Level 1 includes the satellite measurements after radiometric calibration and geographical location. Level 2 includes the operational products retrieved with advanced scientific algorithms from the Level 1 datasets. Level 3 includes the operational climate products based on the 10-day and one-month composition from the Level 2 products. The Level 2 products of FY-2 geostationary satellites are listed in Table 5.

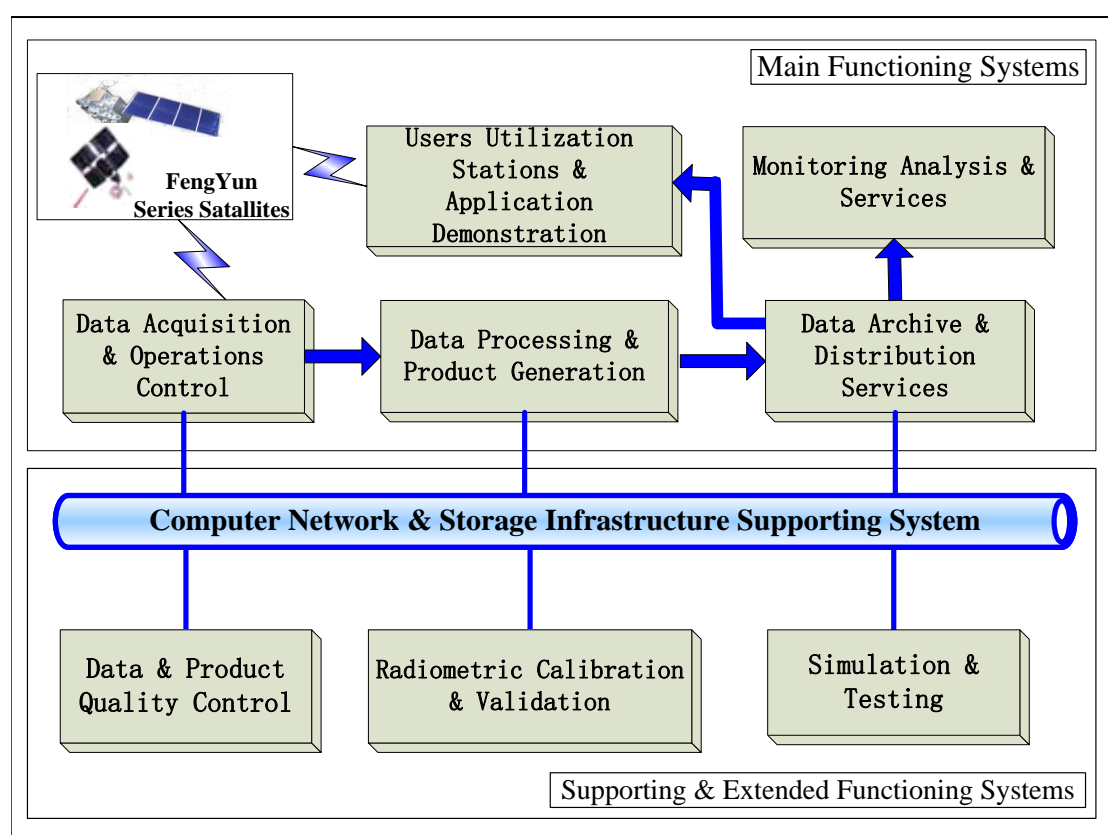


Figure 1. Fenyun satellite ground system flow chart.

**Table 3. FY-3A/B Level 1 products**

Instrument	Products	Spatial Resolution	Coverage
VIRR	Visible reflectance & IR radiances	1 km	102 min/orbit, divided into granule every 5 min (day & night)
MERSI	Visible reflectance & IR radiances	250 m-1 km	Same as VIRR (day only)
IRAS	Visible reflectance and IR radiances	17 km	China region & globe
MWRI	Microwave channel bi-Polarization brightness temperatures (10 ~ 89 GHz)	7.5 - 51 km	China region & globe
MWTS	Microwave channel brightness temperature (50 ~ 57 GHz)	50 - 75 km	China region & globe
MWHS	Microwave channel brightness temperature (150 ~ 183 GHz)	15 km	China region & globe
SBUS	Channel Reflectance (252 ~ 379 nm)	200 km	China region & globe
TOU	Reflectances (308 ~ 360nm)	50 km	China region & globe
SIM	Solar constant	N/A	One solar constant measurement per orbit
ERM	Reflected solar flux, OLR	28 km	China region & globe

**Table 4. FY-3A/B Level 2 products**

No.	Products	Resolution (km)	Coverage	Accuracy	Temporal frequency
1	Cloud mask	1 km	102 min/orbit 5 min/granule (day & night)	5% - 20%	102 min/orbit 5 min/granule (day & night)
2	Cloud top temperature	5 km	Same	0.5 - 2.0 K	Once per day/5-day/10-day/month
3	Cloud top height	5 km	Same	50 hPa	Once per day/5-day/10-day/month
4	Cloud optical thickness	5 Km	Globe	5% - 20%	Once per day
5	Cloud type	5 Km	Globe	5% - 20%	Once per day
6	Cloud coverage (total amount, high cloud amount)	5 km、10 km	Globe	5% - 20%	Once per day/5-day/10-day/month
7	Outgoing longwave radiation at TOA	5 km、50 km、17 km	Globe	3 - 8 W/m <sup>2</sup>	Twice per day/5-day/10-day/month
8	Aerosol over ocean	1 km、10 km	Ocean	15% - 30%	Once per day/5-day/10-day/month
9	Fog detection	1 km	102 min/orbit 5 min/granule (day & night)	RMS<0.25	Once per day/5-day/10-day/month
10	Total precipitable water	1 km、5 km、50 km、27X45	Land, ocean	15% - 25% 10% - 20%	Once per day/5-day/10-day/month
11	Precipitation rate at the ground	18X30 km	Globe	30%	Twice per day/5-day/10-day/month
12	Atmospheric temperature profile 1000-10hPa	50 km	Globe	1.5 - 2.5 °K	Twice per day
13	Atmospheric moisture profile 1000 -	50 km	Globe	15% - 25%	Twice per day

	300hPa				
14	Geopotential height 1000 - 10hPa	50 km	Globe	TBD	Twice per day
15	Atmospheric stability index	50 km	Globe	TBD	Twice per day
16	Total column ozone	50 km	Globe	8 - 15%	Once per day/5-day/10-day/month
17	Ozone profile	200 km	Globe	8 - 15%	Once per day/5-day/10-day/month
18	Flux at TOA from ERM scanner	35 km	Regional/globe	LW:10 Wm <sup>-2</sup> SW:30 Wm <sup>-2</sup>	Twice per day
19	Flux at TOA from ERM non scanner	120°	orbit	LW:10 Wm <sup>-2</sup> SW:30 Wm <sup>-2</sup>	Twice per day

**Table 5. FY-2C/2D/2E operational Level 2 products**

Products	Coverage	Refresh rate/day
Atmospheric motion vectors	50 N - 50 S 55 E - 155 E	4
Sea surface temperature	60 N - 60 S 45 E - 165 E	8
Upper tropospheric humidity	60 N - 60 S 45 E - 165 E	8
ISCCP dataset	60 N - 60 S 45 E - 165 E	8
Precipitation index	60 N - 60 S 45 E - 165 E	8
Quantitative precipitation estimate	60 N - 60 S 45 E - 165 E	4
Cloud type	60 N - 60 S 45 E - 165 E	8
Cloud amount	60 N - 60 S 45 E - 165 E	8
Cloud water profile	50 N - 50 S 55 E - 155 E	8
Clear sky total precipitable water	60 N - 60 S 45 E - 165 E	8
Outgoing longwave radiation	60 N - 60 S 45 E - 165 E	8
Solar radiance	60 N - 60 S 45 E - 165 E	1
Snow cover	60 N - 60 S 45 E - 165 E	1
Sea ice	60 N - 60 S 45 E - 165 E	1
Flood	China	1
Soil moisture	60 N - 60 S 45 E - 165 E	1
Fire detection	China	24
Tropical cyclone position & intensity	West Pacific Ocean & Indian Ocean	24
Dust storm	China & Mongolia	8
Fog detection	China	24
Brightness temperature	60 N - 60 S 45 E - 165 E	8

### **3. Advances in satellite meteorology studies**

#### **3.1 Satellite data processing**

##### *3.1.1 Atmospheric composition monitoring*

From 2006 to 2010, various researches in geophysical parameter retrievals have been conducted with measurements from FengYun series of satellites launched by China as well as the earth observation satellites launched by other countries. Especially, atmospheric composition monitoring is one of the most prominent areas.

Wang et al. (2010) developed an ozone retrieval algorithm using measurements from TOU onboard the FY-3 satellites. During the test run in the first year, data analysis revealed that this instrument could successfully monitor the global ozone distribution. The observations over the ozone sensitive areas, such as Antarctic and Qinghai-Tibet Plateau, the continuous monitoring of the ozone anomaly as shown in Figure 2, the comparisons of the products with other satellite observations, and in-situ measurements, as well as other available study results all confirmed that FY3A satellite could monitor the global ozone distribution with a similar precision of other international satellites.

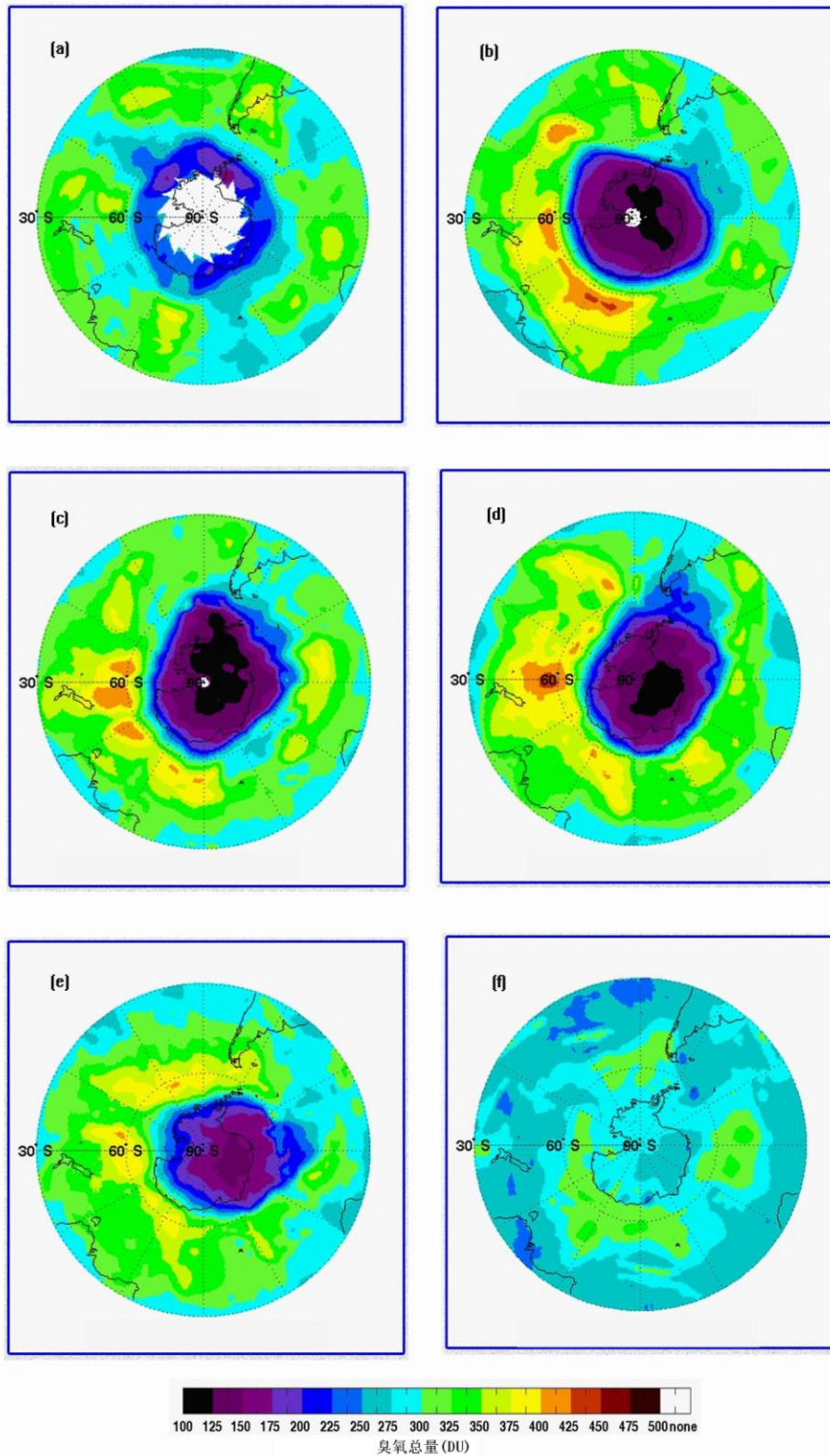


Figure 2. Evolution process of the Antarctic ozone on (a) 28 August 2008; (b) 26 September 2008; (c) 30 September 2008; (d) 08 October 2008; (e) 01 November 2008; and (f) 04 January 2009.

Jiang et al. (2006) analyzed the monthly, seasonal and annual variations of the

NO<sub>2</sub> over Beijing using the monthly averaged column density data from the Global Ozone Monitoring Experiment (GOME). It is shown that the variations agree well with the surface NO<sub>2</sub> density distribution and the correlation coefficient between them is about 0.86. Li and Zao (2008) analyzed the variation of the global column O<sub>3</sub> distribution and the tropospheric O<sub>3</sub> over China by using 20 year GOME and Measurements of Pollution in the Troposphere (MOPITT) observations. Bai et al. (2010) used SCIAMACHY and MOPITT measurements in 2000-2009 to analyze the spatial and temporal distributions of the column CO over China. It is shown that the total column volume increased in this period. The CO volume over the eastern area is larger than that over the western area. It is also shown that the CO column has a significant seasonal variation with a peak in spring.

Zhang et al. (2007) used the GOME, SCIAMACHY and Ozone Monitoring Instrument (OMI) data to obtain the tropospheric NO<sub>2</sub> variation trends over China in 1997 - 2006. It is found that the mean column density is  $9.3 \times 10^{15}$  molecule/cm<sup>2</sup> over the eastern area, which is 15 times of that over the western area. The seasonal variation characteristics are different over the eastern and western areas. The peak occurs in spring over the eastern area but in summer over the western area. The most NO<sub>2</sub> contaminated areas are mainly located in the [prosperous](#), industrial or populated areas, such as the Jing-Jin-Ji (Beijing, Tianjin, Hebei) area, Chang-Jiang Triangle Zone, Zhu-Jiang Triangle Region and Sichuan Basin.

Biyun and Chen Yuejuan (2007) used the Halogen Occultation Experiment (HALOE) data in 1991-2004 to analyze the vertical distribution characteristics of the trace water vapor and CH<sub>4</sub> in the middle atmosphere. It is found that the water vapor mixing ratio has an increasing trend and the CH<sub>4</sub> mixing ratio has decreased gradually.

### 3.1.2 Cloud property retrieval and analysis

Deriving the cloud microphysical parameters from satellite based instruments is a frontier problem in recent years in the field of remote sensing, in which China has also gained great achievements. Zhou et al. (2010) and Ye et al. (2009) used the visible and infrared data to retrieve cloud optical depth and effective radius. The former one focused on simultaneously retrieving optical depth, cloud particle effective radius and cloud top temperature by using visible, mid-infrared and thermal infrared data. The latter one used Moderate Resolution Imaging Spectroradiometer (MODIS) data for deriving cloud optical depth and particle effective radius in the presence of overlapping clouds. Guan et al. (2007) used a minimum local emissivity variance (MLEV) algorithm to simultaneously retrieve single layer cloud top height and effective emissivity spectrum with the Atmospheric InfraRed Sounder (AIRS) data. Li et al. (2009) used the LIDAR data from the Cloud-Aerosol Lidar with Orthogonal Polarisation (CALIOP) satellite to analyze multi-layer cloud distributions in China. It is shown that the overlapping cloud occurrences are 43.6%、29.6%、21.1% and 33.3% in spring, summer, autumn and winter, respectively. The double layer clouds happen most frequently and have a mean thickness of 0.9 - 20 km.

Fu et al. (2007) combined the radar and microwave imager data from the Tropical Rainfall Measuring Mission (TRMM) to differentiate the precipitating clouds from

non-precipitating clouds in Typhoon Ranaim, and derived the cloud fractions as well as particle radius, cloud water and latent heat profiles. Wang et al. (2010) analyzed and compared the cloud amounts over China and its neighborhood from CloudSat and International Satellite Cloud Climatology Project (ISCCP) data. It is found that the cloud distribution patterns are very similar, whereas the ISCCP cloud amount is relatively low.

### **3.2 Meteorological satellite data applications**

#### *3.2.1 Applications in Numerical Weather Prediction*

In the first decade of the 21st century, researchers in the numerical weather predictions and meteorological satellite data applications have devoted great efforts on the satellite data assimilation and the development of the numerical weather prediction system, as well as the corresponding radiative transfer model development and satellite data quality control. Under the joint efforts from both communities, a significant improvement has been made in weather forecasts with the satellite observations operationally assimilated into the NWP models.

In 2003, the new generation of the Chinese NWP system (GRAPES) realized the direct three-dimensional assimilation (3DVAR) of the ATOVS data from the NOAA series satellites (Ehu et al., 2008). Valuable achievements have been made in the bias correction for satellite data utilization, handling of land surface emissivity and dealing with other problems associated with the satellite sounding data assimilation (Liu et al. 2007; Gu et al. 2006). The assimilation of the atmospheric motion vector (AMV) product derived from the geostationary satellites is one of the most urgent problems needed to be addressed in the NWP assimilation system. In recent years, new improvements have been made in the determination of the cloud top height and applying quality control, and the assimilation of the AMV data has been further studied and its utilization rate has been improved (Han et al., 2007)

In recent years, the contributions of the meteorological satellite data to the Chinese numerical weather predictions have increased dramatically. For example, the assimilated satellite data account for 40% of the total data volume used in the GRAPES-GPS, which leads to a significant improvement in the medium-range numerical forecasts. In particular, it makes the confident forecast range go forward two days in the south hemisphere where the conventional observations are rarely available. In the north hemisphere with densely conventional observations, the medium-range forecasts have also been improved dramatically (Xue 2009).

In 2010, the RTTOV 7.0 radiative transfer model in GRAPES 3DVAR assimilation system was upgraded to RTTOV9.3. Additionally, the radiative transfer model called community radiative transfer model (CRTM) developed by the Joint Center for Satellite Data Assimilation (JCSDA) has been added as a new alternative. In the upgraded radiative transfer model, the complex surface emissivity and cloud modules has been added, which takes into account the snow, ice and desert effects for improving the radiance calculations at surface sensitive channels as well as water particle (cloud water, cloud ice, rain, snow and hail) effects for providing the basis of assimilating satellite data in the cloudy and precipitation situations. These modules could be used for retrieving atmospheric temperature and humidity profiles, cloud

water, cloud ice, rain and hail profiles as well as developing data utilization quality control in the cloudy conditions.

After the FY-3A was successfully launched in May 2008, the applications of the FY-3A data have attracted comprehensive attentions. According to the bilateral cooperative agreement between China Meteorological Administration (CMA) and the European Center for Medium range Weather Forecasting (ECMWF), a research program named “Application study of the FY-3A satellite data in ECMWF assimilation system” was performed by using the EMCWF operational platform. Currently, the data from MWTS, MWHS, IRAS and MWRI have been successfully assimilated into the ECMWF system. For example, the FY-3A vertical atmospheric sounding system (MWTS, MWHS, IRAS) cloud free data and the FY-3A MWRI data in all sky conditions have been used in the ECMWF IFS (Integrated Forecast System) assimilation and forecasting system. After the bias corrections, positive impacts have been obtained. The estimated observation errors of the four FY-3A instruments are slightly greater than those of the similar international instruments. By developing the bias correction module for the FY-3A instruments in the ECMWF IFS, which are used to correct the systematic deviations, residual errors follow the Gaussian distribution and more data are assimilated into the system, which leads to an improvement of the forecast performance.

According to the needs of the FY-3A data in Chinese GRAPES numerical forecasting system, a bias correction method independent of ECMWF IFS has also been developed by taking into account the specific characteristics of the FY-3A instruments. This is a novel method which addresses errors from instrument, calibration as well as assimilation methodology. Figure 3 shows the comparison results (the standard deviation of the first guess departures) from the four instruments after the bias correction. It can be seen that the estimated errors are slightly worse than those from their counterparts. Figure 4 shows the results of assimilating FY-3A instrument and corresponding similar instrument observations against the Baseline experiments (including conventional observations, SSMI and GPS data). From this figure, it is shown that assimilating MWTS data and AMSU-A (channels 3, 5, 7, 9) obtain better results than the Baseline experiments. In the north hemisphere, the MWTS and AMSU-A data obtain the similar results. While in the south hemisphere, the MWTS data obtain an improvement as much as 70% of that with the AMSU-A data. The IRAS data assimilation obtains a slightly less improvement than assimilating the MWTS data. Additionally, the impacts of the MWHS data on the assimilation are similar to those of the Metop Microwave Humidity Sounder (MHS) (Lu et al. 2009).

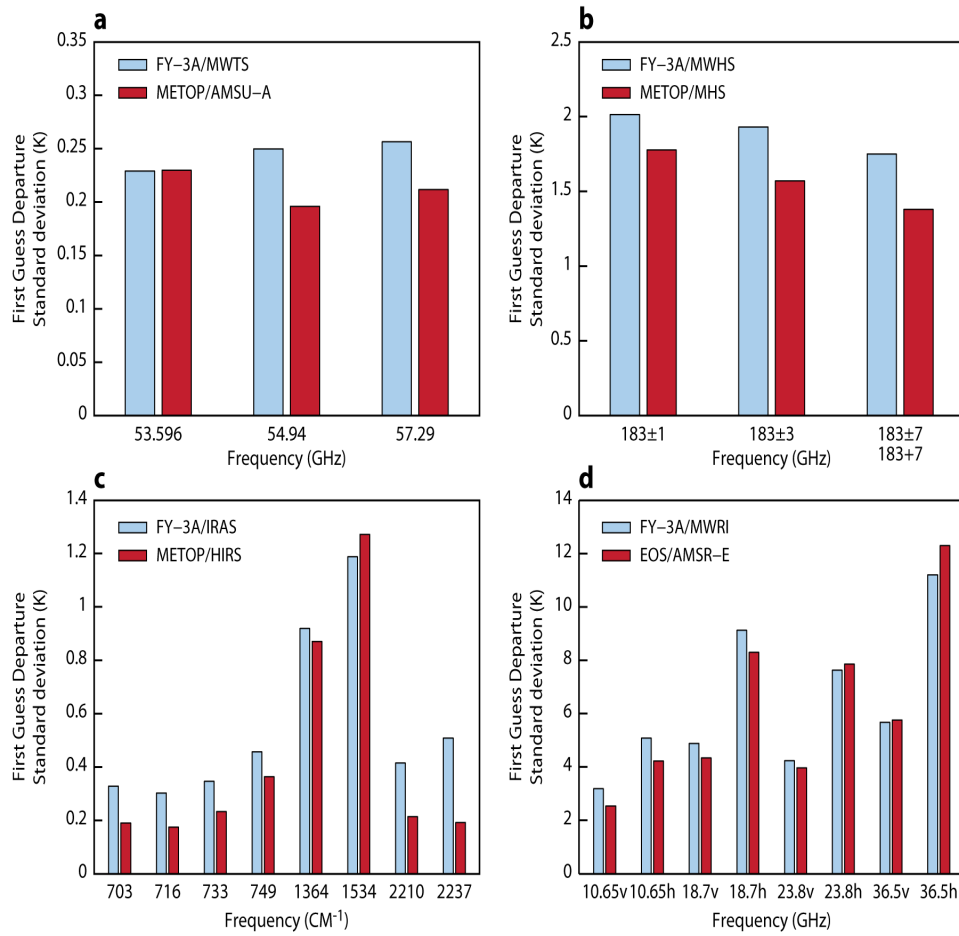


Figure 3. First guess departure standard deviations of the FY-3A data used in the assimilation system (after the bias correction).

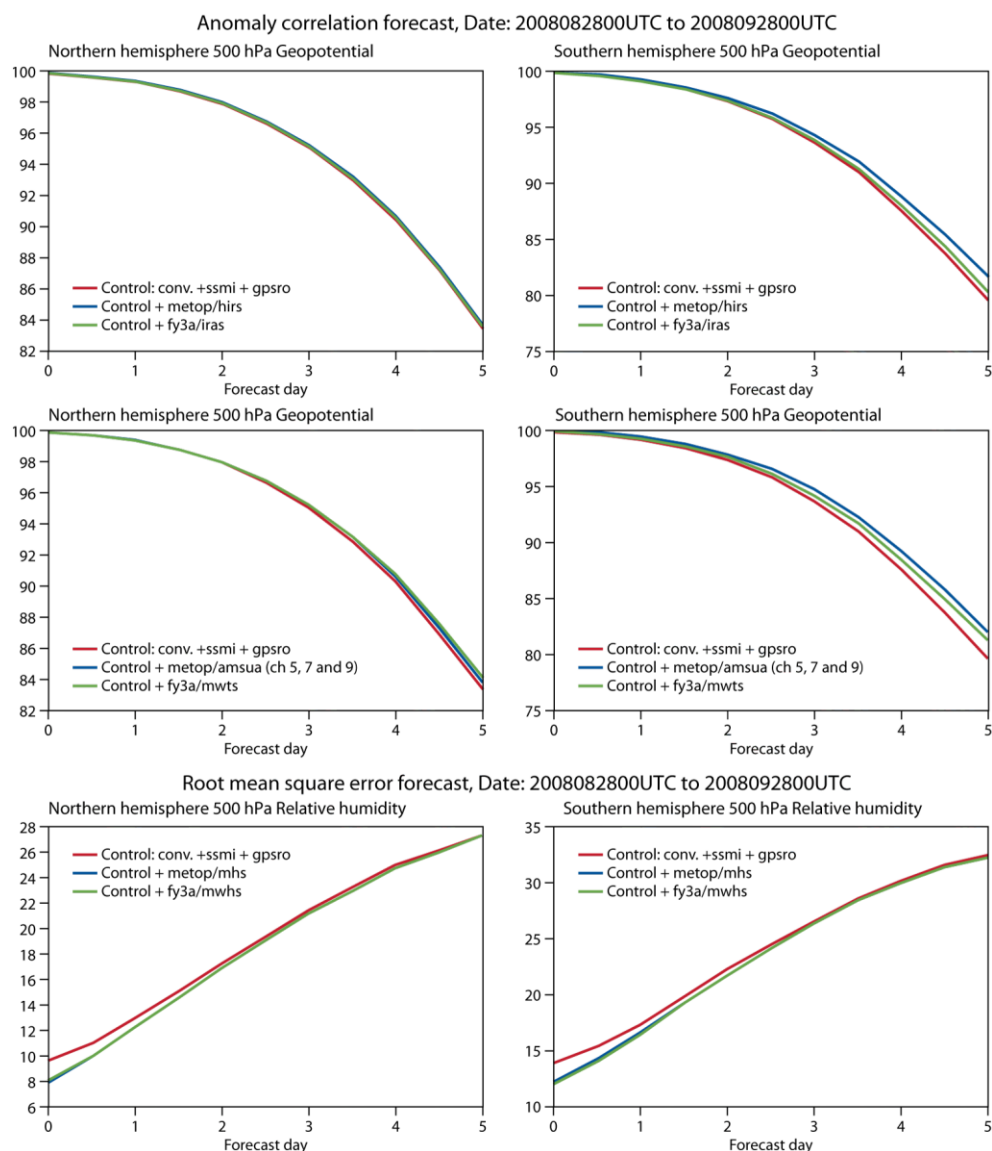


Figure 4. Baseline assimilation experiment results.

### 3.2.2 Applications in monitoring the mesoscale convective system (MCS)

Research and analysis on the satellite images show that the disasters brought by the synoptic system, such as hurricane, storm and deep convective system, are due to the MCS embedded in the synoptic system. Since the temporal resolution of geostationary satellite observations has increased to several minutes, and the instruments onboard the geostationary satellites have been improved to multispectral sensors with active and passive remote sensing methods, researchers have turned their focus from monitoring and forecasting the storm and deep convective system to the studies of MCS.

Fang and Qin (2006) reviewed the progress of satellite observed heavy rainfall cloud clusters, they commented on the recent studies on using different types of data to study the category, occurrences, and three dimensional structures of the mesoscale cloud systems, their results showed that only part of MCS in China fits the definition of MCC (Mesoscale Convective Complex). Thus it is very important to modify the

definition of MCS according to its local characteristics in China. Fei and Zheng et al., (2008) made their survey and analysis of MCS. They found that most MCS that brought heavy precipitation in China were meso- $\beta$  scale and might not have certain shape of the cloud pattern, according to Orlanski's theory of scale classification, they modified the MCS definition as the diameter of cloud cover of  $-32^{\circ}$  C is greater than 20 km and the ratio of minor axis and prolate axis is greater than 0.5. Qin (2010) analyzed the shape differences of meso- $\alpha$  scale convective system by filtering method, and found that the change of cloud shape from round to belt is mainly caused by the synoptic system changing from meso-scale cyclone to meso-scale shear line. Liu and Zhang et al. (2008) studied the microphysics of meso-scale storm clouds based on different satellite data. The properties of the convective clouds in their case studies showed thicker optical thickness, larger particle diameter, and more ice-phased particles. The optical thickness also showed positive correlation with the intensity of precipitation. Fang and Qiu (2008) calculated the radiative transfer for five channels of AMSU-B with the analysis of typical cases; they found that the brightness temperature differences (BTDs) between the AMSU-B water vapor channels were able to detect the convective clouds and the overshooting convective clouds. The convective clouds from water vapor channels with this detection technique have good relationship with heavy precipitation.

#### 4. The objective and plan for the future meteorological satellite program in China

China will consistently develop both the polar-orbiting and the geostationary meteorological satellites. Until 2015, Fengyun-3 (FY-3) series of operational polar-orbiting meteorological satellite will be launched with the duration of five years to form a network of observation by double satellites both in the morning and afternoon. There will be GPS occultation sensors and IR hyperspectral sensors that can improve the vertical sounding capability of the atmosphere. The experimental FY-3 satellite that carries with the precipitation radar will fulfill the mission of active measuring the precipitation, and the accuracy will reach the international advanced level.

In 2016 - 2020, China will establish a stable and operational FY-3 polar-orbiting meteorological satellite system with the satellite observing network comprise of morning satellite, afternoon satellite and radar satellite; improve the capabilities of hyperspectral IR sounder, hyperspectral ultraviolet spectrometer, the visible spectrophotometer, the hyperspectral near-infrared greenhouse monitor, and advance the ability of monitoring the global climate change. Detailed FY-3 series launch schedule and its payloads can be found in Table 6.

**Table 6. Detailed FY-3 series launch schedule and its payloads**

No.	Satellite	FY-3C	FY-3D	FY-3E	FY-3F
	Instrument	Morning Satellite	Afternoon Satellite	Morning Satellite	Afternoon Satellite
	Scheduled launch time	2012	2014	2016	2018
1	MEdium Resolution Spectral	√ (type I)	√ (type	√ (type	√ (type

	Imager (type I, II)		II)	II)	II)
2	Microwave Atmospheric Temperature Sounder (type II)	√	√	√	√
3	Microwave Atmospheric Humidity Sounder (type II)	√	√	√	√
4	Microwave Radiation Imager	√	√		√
5	Wind Lidar			√	
6	Infrared Hyperspectral Atmospheric Sounder		√	√	√
7	Hyperspectral Greenhouse gas Monitoring Instrument		√		√
8	Hyperspectral Ultraviolet Ozone Instrument Sounder			√	
9	Global Navigation Satellite for Radio Occultation	√	√	√	√
10	Earth Radiation Measurement (type I, II)	√ (type I)		√ (type II)	
11	Solar Irradiation Monitor	√		√	
12	Space Environment Monitoring Suite	√	√	√	√
	1)Space Environment Monitoring Unit		√	√	√
	2)Wide-angle auroral imager 3)Miniature ionosphere photometer		√	√	√
13	InfraRed Atmospheric Sounder	√			
14	Visible and InfraRed Radiometer	√			
15	Solar Backscatter Ultraviolet Sounder	√			

In 2015 time frame, China will also establish a stable and operational geostationary meteorological satellite observing system which will assure double-satellite operational system of the Fengyun-2 series, which enables the two satellite system with capability of backup each other and frequent observations over a region of 3000 km x 3000 km every five minutes. The new generation of the geostationary satellite, the FengYun 4 series (FY-4) will use the three-axis stabilization technique. During the period of 2016 - 2020, the operational FY-4 geostationary satellite will be launched. With the upgraded techniques, the new generation of geostationary weather satellite will greatly improve the observing flexibility and frequency, and fulfill the objective of vertical atmospheric sounding in the geostationary orbit with high temporal resolution, and increase the spatial

resolution of imager to several hundred meters. The experimental microwave sounding geostationary satellite will be developed and tested experimentally. The FY-4 series will also form the operational mode of double-satellite system with capability of backup each other in order to further improve the regional observing ability. The designed lifetime, launch schedule and the payloads for the continued FY-2 series and the new generation FY-4 series of geostationary satellites can be found in Table 7.

Table 7. The designed lifetime, launch schedule and the payloads on the FY-2/FY-4 geostationary meteorological satellite

Satellite name	Launch time (year)	Designed lifetime (year)	Instrument
FY-2F	2011	4	Five-channel visible and infrared spin-scan radiometer
FY-2G	2013	4	
FY-2H	2015	4	
FY-4A	2014	5	1.Multi-channel Scanning Imager
FY-4B	2017	7	2.Infrared Atmospheric Sounding Interferometer
FY-4C	2019	7	3.Lightning Imager 4.Space Environment Monitoring Instrument

China will also establish and improve the facilities of the ground segments for FY meteorological satellites, set up the operational remote sensing application systems that cover the whole nation and different provinces, cities and even counties. The satellite applications can be greatly enhanced; the satellite observing data will be more than 90% of the data assimilated in the numerical weather prediction models; and the satellite monitoring capability will be strengthened in the natural disaster, environment, agriculture, ecology, ocean etc. The meteorological satellites and their applications in China will be closer to the international advanced level.

#### References:

- Bai, Wen-guang, Peng Zhang, and Xinying Zhang et al., 2010: Temporal and Spatial Distribution Characteristics of Carbon Monoxide Column over China Based on Satellite Observations, *Journal of Applied Meteorological Science*, 21(4): 473~483 (In Chinese with English Abstract).
- Bi, Yun, Yuejuan Chen, and Li Xu et al., 2007: Analysis of H<sub>2</sub>O and CH<sub>4</sub> Distribution Characteristics in the Middle Atmosphere Using HALOE Data, *Chinese Journal of Atmospheric Sciences*, 31(3):440-448 (In Chinese with English Abstract).
- Dong, Chao-hua, Jun Yang, and Wen-jian Zhang, et al., 2009: An Overview of a

- New Chinese Weather Satellite FY-3A, *Bulletin of American Meteorological Society*, 90: 1531 – 1544.
- Fang, Zongyi, and Danyu Qin, 2006: A Review of Satellite Observed Heavy Rainfall Cloud Clusters. *Journal of Applied Meteorological Sciences*, 17(5): 583-593 (In Chinese with English Abstract).
- Fang, Xiang, Hong Qiu, and Zhigang Cao, et al., 2008: Research on Severe Convective Cloud Identification Using AMSU-B Microwave Data. *Meteorological Monthly*, 34(3):22-29 (In Chinese with English Abstract).
- Fei, Zengping, Yongguang Zheng, Yan Zhang and Hongqing Wang, 2008: MCS Census and Modification of MCS Definition Based on Geostationary Satellite Infrared Imagery. *Journal of Applied Meteorological Sciences*, 19(1): 82-90 (In Chinese with English Abstract).
- Fu, Yunfei, Dong Liu, and Yu Wang et al., 2007: Characteristics of Precipitating and Non-precipitating Clouds in Typhoon RANAN as Viewed by TRMM Combined Measurements. *Acta Meteorologica Sinica*, 65 (3): 316-3280.
- Guan, Li, Wenan Xiao and Hung-Lung Huang, 2007: Retrieval of Cloud Parameters Using Infrared Hyperspectral Observations, *Chinese Journal of Atmospheric Sciences*, 31(6):1123-1128 (In Chinese with English Abstract).
- Han Wan, Jishan Xue, 2007: Adaptive tuning of background error and satellite radiance observation error for operational variational assimilation. *Proceedings of SPIE*, 6970,44:1-9,doi:10.1117/12,774771.
- Gu, Songqiang, Zhenghui Wang, and Fuzhong Weng et al., 2006: A Study for Improving a Microwave Land Surface Emissivity Model with NOAA/AMSU Data and the GRAPES 3DVar System. *Plateau Meteorology*, 25 (6): 1101-1106 (In Chinese with English Abstract).
- Jiang, Wenhua, Jianzhong Ma, and Peng Yan et al., 2006: Characterization of NO<sub>2</sub> Pollution Changes in Beijing Using GOME Satellite Data. *Journal of Applied Meteorological Sciences*, 17(1): 67-72 (In Chinese with English Abstract).
- Li, Ying, Chunsheng Zhao, Yuanyuan Fang and Huan Yu, 2007: Analysis of Distribution and Seasonal Change of Tropospheric Ozone Residual in Recent 20 Years Using Satellite Data. *Journal of Applied Meteorological Sciences*, 18(2): 181~186 (In Chinese with English Abstract).
- Li, Jiming, Jianping Huang, and Yuhong Yi et al., 2009: Analysis of Vertical Distribution of Cloud in East Asia by Space-Based Lidar Data. *Chinese Journal of Atmospheric Sciences*, 33(4): 698 - 707 (In Chinese with English Abstract).
- Liu, Jian, Wenjian Zhang, and Yuanjing Zhu, et al., 2007: Case Study on Cloud Properties of Heavy Rainfall Based upon Satellite Data. *Journal of Applied Meteorological Sciences*, 18(2): 158-164 (In Chinese with English Abstract).
- Liu, Zhiquan, Fengying Zhang, and Xuebao Wu et al., 2007: A Regional ATOVS Radiance-bias Correction Scheme for Radiance Assimilation. *Acta Meteorologica Sinica*, 65 (1): 113-123.
- Lu, Qifeng, 2009: Bill Bell, Peter Bauer, Niels Bormann. Assessment of FY-3A satellite data. *ECMWF Newsletter*, 122: 18-20.
- Matricardi, M. and A. McNally, 2008: An assessment of the accuracy of the RTTOV

- fast radiative transfer model using IASI data. *Proceedings of ITSC-16*, Angra dos Reis, Brazil 7-13 May 2008.
- Peng, Liang and Zhanyu Yao, 2008: Satellite Microwave Retrieval Test for Non-precipitating Cloud Liquid Water in Henan Area. *Journal of Applied Meteorological Sciences*, 19(5):539~546 (In Chinese with English Abstract).
- Qin, Danyu, 2010: A Case Study of Meso- $\alpha$ -scale Convective System Shape Differences Using Filtering Analysis. *Chinese Journal of Atmospheric Sciences*, 34(1): 154-162 (In Chinese with English Abstract).
- Wang, Shuaihui, Zhigang Han, and Zhigang Yao, 2010: Comparison of Cloud Amounts from ISCCP and CloudSat over China and Its Neighborhood. *Chinese Journal of Atmospheric Sciences*, 34(4):767-779 (In Chinese with English Abstract).
- Weng, F., Y. Han and P. Van Delst et al., 2005: JCSDA Community Radiative Transfer Model (CRTM), *Proceedings of the 14th International TOVS Study Conference (ITSC-XIV)*, 25–31 May 2005, Beijing, China.
- Wang, W. H., X. Y. Zhang, and X. Q. An et al., 2010: Analysis for retrieval and validation results of FY-3 Total Ozone Unit (TOU). *Chinese Sci. Bull*, 55(17), doi: 10.1007/s11434-010-3240-2.
- Xue, Jishan, 2009: Scientific issues and perspective of assimilation of meteorological satellite data. *Acta Meteorologica Sinica*, 67 (6): 902-911
- Xu, Jianmin, Yinsheng Niu, and Chaohua Dong et al., 2006: Ground Segments for FengYun Meteorological Satellites. *Engineering Sciences*, 8(11):13-18 (In Chinese with English Abstract).
- Yang, Jun, Chaohua Dong, and Naimeng Lu et al., 2009: FY-3A - the New Generation Polar-Orbiting Meteorological Satellite of China. *Acta Meteorologica Sinica*, 67(4): 501-509 (In Chinese with English Abstract).
- Ye, Jing, Wangbiao Li, and Wei Yan, 2009: Retrieval of the optical thickness and effective radius of multilayered cloud using MODIS data. *Acta Meteorologica Sinica*, 67(4): 613-622 (In Chinese with English Abstract).
- Zhang, Xinying, Peng Zhang, and Yan Zhang et al., 2007: The trend, seasonal cycle, and sources of tropospheric NO<sub>2</sub> over China during 1997–2006 based on satellite measurement, *Science in China (Series D: Earth Sciences)*, 50(12):1877-1884, DOI: 10.1007/s11430-007-0141-6
- Zhou, Qing, Fengsheng Zhao and Wenhua Gao, 2010: Retrieval of Cloud Radiative Properties from FY-2C satellite Data. *Chinese Journal of Atmospheric Sciences*, 34(4):827-842 (In Chinese with English Abstract).
- Zhu Guofu, Xue Jishan, Zhang Hua, et al., 2008: Direct assimilation of satellite radiance data in GRAPES variational assimilation system. *Chinese Sci Bull*, 53:3465-3469.

## Progress in the study of the carbon and nitrogen cycles in China

Xu Yongfu, Huang Yao, Li Yangchun

State Key Laboratory of Atmospheric Boundary Layer Physics and Atmospheric Chemistry, Institute of Atmospheric Physics, Chinese Academy of Sciences, Beijing 100029, China

### ABSTRACT

This paper presents the recent advances in the study of the carbon-nitrogen cycling and their relationship with climate change that have been made in China over the last four years. There are many studies involved with the estimate of carbon budget in the Chinese terrestrial ecosystem. It is known from these studies that a net carbon sink 0.19-0.26 PgC/a was obtained for the Chinese terrestrial ecosystem. It has been estimated that land soil contains about 8.3 GtN. Increases in population and use of fertilizer have resulted in the accumulation of nitrogen in the land. The ocean margins have received more nitrogen due to transport from the rivers, which affects the carbon and nitrogen in the ocean margins. Meanwhile, atmospheric nitrogen deposition has been increasing, so it will probably influence the carbon and nitrogen cycling in the open ocean in the future.

The continental shelves are generally a sink for atmospheric CO<sub>2</sub> at mid-high latitudes and a source of CO<sub>2</sub> at low latitudes. Although the Changjiang River estuary sediment may absorb atmospheric CO<sub>2</sub>, its main stream generally emits CO<sub>2</sub>. The outer Changjiang Estuary served as a moderate or significant sink of atmospheric CO<sub>2</sub> in winter, spring and summer, while it turned to a net source in autumn. Phytoplankton can take up carbon at a rate of  $6.4 \times 10^8 \text{ t a}^{-1}$  with a clear seasonal variation in the China Sea (Bohai Sea, the Yellow Sea, the East China Sea, and the South China Sea). The global ocean carbon model estimated that the global ocean absorbed anthropogenic CO<sub>2</sub> at the rates of 1.64 and 1.73 Pg C a<sup>-1</sup> for the two cases in the 1990s.

Many researchers have pointed out the impacts of climate change on the carbon and nitrogen cycles. Generally, it was found that elevated atmospheric CO<sub>2</sub> and N addition can stimulate NPP. So far their combined effect on NEE in the terrestrial ecosystem needs to be further studied. It was found that soil organic carbon and total nitrogen ratio (C/N) was about 10.8 in paddy fields, higher than 9.9 in upland fields. However, the regional variation of C/N ratio is very large in upland fields.

The AVIM-GOALS model has been used to study the land carbon cycle and its relation with climate change. The model well generated the interannual variations of the spatial and temporal distributions of the surface air temperatures and precipitation. Using the AVIM2, the future of land carbon change has been investigated. It was obtained that under the forcing of future climate change, NPP for China will increase continuously to the middle periods of the 21st century, and then will decrease gradually.

**Key words:** Carbon cycle, nitrogen cycle, climate change, Chinese terrestrial ecosystem, China Sea

## 1. Introduction

Climate and life on the earth are linked through various interacting cycles and feedback mechanisms. Over the past decades, it has been recognized that global climate has been changing, particularly since the industrial revolution, which is associated with biogeochemical cycles of elements, including the carbon and nitrogen cycles.

Both carbon and nitrogen are main components of living organisms. Carbon exists in the Earth system in the many different forms such as CO<sub>2</sub>, carbonate, organic compounds, etc, which are continuously cycled. Because of the burning of fossil fuels and carbon emissions from land-use change, atmospheric CO<sub>2</sub> has increased by more than 30% above the pre-industrial level. Understanding of carbon cycle processes in the various reservoirs and their changes, recognition of the feedback mechanisms of the interactions of carbon cycle with climate change, ecosystems, and human activities, prediction of future climate change and its impacts are all hot topics of the current research fields.

Nitrogen in the atmosphere is in a form (N<sub>2</sub>) unavailable to most organisms. Microbes turn this nitrogen into nitrates and other compounds through the process of nitrogen fixation, which plants or algae assimilate into their tissues. As world population increases, a large amount of nitrogenous fertilizer produced by the industrial process has been used to make the significant increase in food production over the past decades. Both the nitrogen used in food production and the nitrogen generated during fossil-fuel combustion are emitted to the environment. The increase of these sources of anthropogenic nitrogen affects the environment. In addition, accumulation of nitrogen in the environment leads to the increased interaction of nitrogen with other biogeochemical element cycles. It is important to understand whether and how these interactions affect global climate change.

Carbon and nitrogen are naturally tightly coupled, which occurs with specific elemental stoichiometries (e.g. Redfield ratio). Human activity has perturbed the global nitrogen and carbon cycles. The increased nitrogen available to plants probably stimulates the productivity. Hence, it is important to understand the processes that control the C/N ratios of autotrophic organisms on land and in the ocean. The carbon sink in the Northern Hemisphere terrestrial biosphere is due to CO<sub>2</sub> fertilization and/or nitrogen fertilization. Like CO<sub>2</sub>, Atmospheric N<sub>2</sub>O has significantly increased. The connection between air temperature and atmospheric CO<sub>2</sub> and N<sub>2</sub>O levels further demonstrates that global carbon and nitrogen cycles are closely coupled to climate change.

Chinese scientists have been working on these research fields for a long time, and obtained a lot of achievements in some research fields. This paper tries to summarize the research work by Chinese scientists over the recent 4 years.

## 2. Terrestrial carbon and nitrogen cycles

Carbon cycle and carbon budgets in the terrestrial ecosystem play an important role in its response to global climate change. Recent researches show that over last several years, the increase in atmospheric CO<sub>2</sub> accounted for 45% of the global

emission, and the rest has been absorbed by the land (30%) and oceans (25%).

The terrestrial ecosystem is consistent of many different varieties of complicated systems. It is difficult to determine which system is storing carbon. Researches indicate that over the last 20 years, the northern mid- and higher-latitude terrestrial ecosystem is a large carbon sink. It is important to find out whether Chinese terrestrial ecosystem is carbon sink and how large the sink is. Chinese scientists have done a lot of researches, and obtained some important results.

## **2.1 Carbon budget**

### **2.1.1 Forest**

Forests covered 18.2% of China based on the 6th national forest inventory completed during 1999–2003, with an area of 174.9 Mha (State Environmental Protection Administration, 2007). Using the national forest inventory data, Fang et al. (2007) pointed out that forest biomass carbon stock increased significantly during the 1980s and 1990s, and obtained a carbon sink of  $58.4 \pm 25.8$  TgC/a and  $92.2 \pm 43.7$  TgC/a during the 1980s and 1990s, respectively.

Many researchers estimated changes in forest soil organic carbon (SOC). Based on a multiple regression equation of SOC that depends on a normalized difference vegetation index (NDVI) and climatic factors (temperature and precipitation), Piao et al. (2009) estimated an increased rate of  $4.0 \pm 4.1$  Tg C a<sup>-1</sup> between 1982 and 1999. Using a biogeochemical model (InTEC), Wang et al. (2007) estimated that forest SOC increased at a rate of 7.84 Tg C a<sup>-1</sup> during 1950–1987, but declined sharply at a rate of 61.54 Tg C a<sup>-1</sup> during 1988–2001. Chen et al. (2008) estimated that Chinese forest soils lost 6.0 Tg C a<sup>-1</sup> based on a model simulation. Using the forest area of 130 Mha (mean of 1980–2000), the SOC sequestration rate in China was estimated to be  $4.7 \pm 4.3$  Tg C a<sup>-1</sup> (Huang et al., 2010a), which is mainly attributed to reforestation and afforestation (Fang et al., 2007, State Environmental Protection Administration, 2009).

### **2.1.2 Grassland**

Natural grassland in China is approximately 400 Mha, accounting for 41.7% of the nation (State Environmental Protection Administration, 2007). Piao et al. (2009) estimated an increase of the grassland biomass stock by  $7.0 \pm 2.5$  TgC/a during the 1980s and 1990s. However, as pointed out by them, the increasing grassland biomass does not contribute to a net long-term sink because carbon incorporated into plants is harvested at least once per year and released back as CO<sub>2</sub> into the atmosphere through the food web within the year. Based on a multiple regression equation of SOC that is driven by NDVI and climatic factors, Piao et al. (2009) estimated that the rate of increase of SOC in Chinese grassland (331 Mha) was  $(6.0 \pm 1.0)$  Tg C a<sup>-1</sup> between 1982 and 1999. However, using a large number of field measurements, Yang et al. (2009, 2010) found no significant changes in SOC of northern grassland and Qinghai-Tibetan alpine grassland (total 196 Mha).

### **2.1.3 Cropland**

China is a typical agricultural country, with arable land of 130 Mha and an annual harvest area of 150 Mha. Fang et al. (2007) estimated that the cropland biomass stock was increased by 13 TgC/a during the 1980s and 1990s. Similar to the grassland

biomass, this sink does not contribute to a net long-term sink. Compared with natural ecosystems, SOC in cropland shows great sensitivity to human activities such as tillage, fertilization and irrigation. By a synthetical analysis of datasets extracted from 132 publications, Huang and Sun (2006) reported that the concentration of SOC increased in 53%–59%, decreased in 30%–31% and stabilized in 4%–6% of the national croplands. As a whole, the cultivated layer (0–20 cm) of cropland soils in China sequestered 15–20 Tg C a<sup>-1</sup> between 1980 and 2000. A further investigation showed that the average rate of SOC sequestration in the topsoil to ~30 cm depth ranged from 16.6–27.8 Tg C a<sup>-1</sup> over the same period (Sun et al., 2010). Recent estimates of SOC sequestration in Chinese cropland made by Xie et al. (2007), Lu et al. (2009), Yu et al. (2009) and Pan et al. (2010) are similar to estimates by Huang and Sun (2006) and Sun et al. (2010). By running a biogeophysical model Agro-C (Huang et al., 2009) that has been widely validated in China, Huang et al. (2008) estimated that the croplands in China that cover an area of over 98 Mha sequestered 14.5–20.3 Tg C a<sup>-1</sup> from 1980 to 2000. Combining the estimates from various studies, the average rate of SOC sequestration in Chinese cropland (130 Mha) was estimated to be 21.7±4.3 Tg C a<sup>-1</sup> during this period (Huang et al., 2010a). This is substantially attributed to the improvements in crop production (Huang et al., 2007), residue incorporation, manure amendment and extension of zero and reduced tillage practices (Huang and Sun, 2006; Lu et al., 2009).

#### **2.1.4 Shrubland**

Shrubland is a widely distributed biome type in China, covering about 200 Mha (Fang et al., 2007; Piao et al., 2009). Researches on the carbon balance of this important system are very scarce. Using in situ biomass and satellite greenness information, Piao et al. (2009) estimated that shrubland was a net sink at the rates of 21.7±10.2 Tg C a<sup>-1</sup> in biomass and 39.4±9.0 Tg C a<sup>-1</sup> in the soils during 1982–1999. The increase in SOC of shrubland was higher than that of forest, grassland and cropland. It should be pointed out that there exists large uncertainty for the SOC sink, because the regression model used for estimating SOC is only able to interpret 33% of the observed SOC variation.

#### **2.1.5 Wetland**

Wetland in China is about 65.9 Mha excluding rivers and ponds. Marshland is the largest natural wetland in China, covering an area of ~12 Mha (China Wetland Resources Development and Environmental Protection Research Group, 1998). An estimated ~3 million ha of marshland in northeast China was converted to cropland over the period 1950–2000 (Huang et al., 2010b). Using datasets from the literature and field measurements, Huang et al. (2010b) investigated loss of SOC due to marshland conversion in northeast China. They estimated that 2.91Mha of marshland were converted to cropland over the period 1950–2000. Marshland conversion resulted in SOC loss of 240 Tg in the cropland over the 50 years. The annual carbon loss was estimated to be 6.2±1.8Tg a<sup>-1</sup> during 1980–2000 (Huang et al., 2010b).

### **2.2 Impacts on carbon balance**

According to the inventory-satellite method, Piao et al. (2009) gave the carbon sink of 177±73.4 TgC/a for the period of 1980–1999 in the Chinese terrestrial

ecosystems including forest, shrubland, grassland and cropland. In order to take the other ecosystems into account, Piao et al. (2009) used the results of an ensemble of atmospheric inversions and the results of five process-based global ecosystem model to estimate the carbon balance and to quantify the effect of CO<sub>2</sub> and climate change on the carbon balance of China. Results from the process-based models and atmospheric inversion gave the carbon sink of 173±39 TgC/a for the period of 1980-2002 and 350±330 TgC/a for the period of 1996-2005, respectively. After considering the “lateral fluxes” including the emissions of non-CO<sub>2</sub> compounds, wood products, food products, etc., the sink from the inversion was reduced to 261 TgC/a. Thus, Piao et al. (2009) concluded a net carbon sink in the range of 0.19-0.26 PgC/a. It is obvious that there is still large uncertainty for the estimation of carbon sink in the Chinese ecosystems. There are many factors and causes influencing the carbon cycle and carbon balance.

### 2.2.1 Datasets and Methods

All estimates of carbon sinks in the terrestrial ecosystems rely on the observed data sets and involved methods. The uncertainty for forest is mainly from forest inventory data and the involved method. As used in Fang et al. (2007) and Piao et al. (2009), an approach called biomass expansion factor (BEF) was used to estimate the forest biomass carbon storage. Several parameters were involved with their BEF approach. Although each set of parameter values was based on the field measurements for each forest type, the BEF model derived error might be high for some particular provinces (Fang et al., 2007).

For the estimate of grassland biomass used in Fang et al. (2007), besides grassland resource inventory, the uncertainty is mainly from remote sensing data and the estimation of belowground biomass. A relationship between NDVI and aboveground biomass was used to estimate the magnitude and spatiotemporal changes of grassland aboveground biomass. Belowground biomass was simply estimated based on the ratio of belowground to aboveground biomass. Certainly, there are many error sources. A large error of 36% is from remote sensing data, as pointed out by Fang et al. (2007).

Fang et al. (2007) established a relationship between vegetation productivity (NPP) and carbon sink for all vegetation types to derive the carbon sink of shrub. An additional approach called “carbon sink efficiency” (CSE) was used in their study. Both methods actually rely on the estimate of NPP for forest and grassland, which obviously induces the large uncertainty.

In general, estimates of change in SOC are usually made by using the measurements of SOC over a significant period (IPCC, 2006). Certainly, a sufficient number of measurement sites are required to reduce the uncertainty. The measured data of SOC in woodland and shrubland in the 2000s are rather deficient in China. Hence, the errors have been introduced into the measurement-based estimate. Currently, models are widely used to estimate the terrestrial carbon budget on regional and global scales, but the validity of the models, utility of model input parameters, and upscaling processes may restrict the accuracy of the estimates (Huang et al., 2008). Regression models have been developed by Piao et al. (2009) to estimate the changes in SOC. However, these models can only explain 23%–53% of the

variation in the observed values for SOC storage (Huang et al., 2010a). It is obvious that use of these models to estimate SOC at will lead to a large uncertainty. As Piao et al. (2009) pointed out, the model results from five global ecosystem models were not taken as “best estimates”, because non of the models explicitly considers changes in land use and land management. Furthermore, the models were not carefully validated in the region of China, including the simulation of climate change. Although the method of atmospheric inversions is very useful, the uncertainty is generally large because many errors are introduced into the estimate, including scarce atmospheric network stations, transport model and the assumed fossil-fuel emissions (Piao et al., 2009).

### **2.2.2 Land use change**

Land use change plays an important role in the terrestrial carbon cycling. Conversion of one land use to another probably alters carbon storage. Since the 1980s, China has actively carried out large-scale reforestation and afforestation programmes. Fang et al. (2001) pointed out that these plantations resulted in an increase of forest biomass carbon stocks. The forest (20% canopy coverage) area of 11 Mha in China was increased between the periods of 1989–1993 and 1999–2003 (Fang et al., 2007), which is different from the estimate by Liu et al. (2004) who reported that the forest and grassland areas decreased by 1.0 Mha and 3.35 Mha, respectively. A continuous increase in the forest carbon biomass is expected because of the increase of forest area and the forest regrowth in the future (Fang et al., 2007).

Many researchers have estimated that vegetation and soil C are increased when conversion of cropland to forest, afforestation and reforestation are implemented (Fang et al., 2001; Xie et al, 2008; Zhang et al., 2008; Huang et al, 2009). Carbon can be still accumulated at 610 kg C ha<sup>-1</sup> in the old growth forest (stand age greater than 400 years) soil in southern China (Zhou et al., 2006). These studies mostly focus on the change in topsoil organic C sequestration, rather than in deep soil. Field and laboratory measurements show that extraneous disturbances such as N addition can affect the mineralization of “old carbon” in deep soils under temperate old-growth forests in northeast China (Xu et al. 2009). Hence, the dynamic of carbon in deep soils and its response to extraneous disturbances should be taken into account for soil C sequestration.

The afforestation area was greatly increased in China increased in the last three decades. It was reported that the area of shelter trees increased by 53 Mha from 1978 to 2007 (National Bureau of Statistics of China, 2009). During the period of 2003–2007, the plantations of shelter trees accounted for 73% of the national afforestation (Huang et al., 2010a). It is obvious that afforestation increases the biomass stock and also affects the carbon storage in the soil.

### **2.2.3 Grassland management**

Grazing is a significant factor influencing the grassland system. Over the last three decades, overgrazing and irrational reclamation of grassland have become increasingly serious issues in China. According to the 2006 Report on the State Environment in China, 204 counties in 266 semi-pastoral and semi-agricultural regions were overgrazed (Huang et al., 2010a). It has been estimated that the

degradation rate of grassland was  $1.3 \text{ Mha a}^{-1}$  in the late 1980s and  $2.0 \text{ Mha a}^{-1}$  in the early 2000s. As a result, about 90% of the natural grassland in China has degraded to some degree (State Environmental Protection Administration, 2009). Du (2006) estimated that in the major pastoral region of north China, in the mid-1980s degraded grassland made up 39.7% of the total available grassland, but this amount increased to 50.2% in the mid-1990s.

Grassland degradation decreases SOC stocks (Zou et al., 2007). An analysis of the literature data shows the decrease in SOC stocks by 27-55% in the degraded pastures, relative to non-degraded pastures (Huang et al., 2010a). SOC stocks also decline significantly with increasing grazing intensity (Wang et al., 2007; Dong et al., 2007; Qiu et al., 2007). SOC stocks in the lightly, moderately and heavily grazed pastures were  $30 \pm 12\%$ ,  $35 \pm 14\%$  and  $50 \pm 15\%$  (Huang et al., 2010a), respectively, lower than that in non-grazing pasture. Enclosures play an important role for the degraded grasslands (Xue et al., 2008; Jia et al., 2009; Pei et al., 2008; He et al., 2008). It is found that SOC can increase by 28% after 20 years of enclosure, and by 1.6 and 4.5 times after 14–23 and 40–50 years of vegetation restoration, respectively, when compared with that in the initial 0–4 years (Huang et al., 2010a). In terms of meta-analysis, Shi et al. (2009) obtained that the losses of SOC in the grassland with various grazing intensities exceeded the SOC increase in enclosure and grazing forbidden grassland. Although it is obvious that human activities have significantly affected SOC stocks in China's grasslands over the last three decades, the quantities of human-induced SOC changes have not been determined on a national scale (Huang et al., 2010a).

#### **2.2.4 Climate change and other**

Climate change is one of the most important factors influencing the carbon balance because photosynthesis and respiration are associated with climate and soil properties. Precipitation is a particularly important driver for the growth of vegetation. The study has shown that summer precipitation in China has significantly increased, which may have benefited vegetation growth (Fang et al., 2004). Temperature and soil properties such as exchangeable metal concentration and metal-to-C ratio of soil extracts and clay affect the function of soil carbon sequestration and microbial carbon utilization (e.g. Xu et al., 2007; Xu et al., 2006). Recent studies have shown that soil microbial biomass C concentrations and metabolic quotients of the soils are useful soil parameters for studying soil C availability and soil C sequestration (Xu et al., 2007).

As the development of economy in China, development of urbanization has been enhanced. Large rural population has moved to cities. These have resulted in many alterations. Change in energy use is one of these changes. In the past 30 years, firewood, charcoal, and crop straw that had been used as major supplies in most areas have been steadily replaced by the use of fossil fuel. This transition has decreased the collection of fuel wood, and increased fossil fuel emissions, which led to the recovery of shrublands (Piao et al., 2009).

Because crop production significantly increased between 1950 and 1999 (Huang et al., 2007), the amount of residue and root input to the soil was also

increased. Recent agriculture practice showed a decreasing removal of crop residues and an expansion of reduced and zero tillage, which are likely to increase the carbon sink in the cropland (Piao et al., 2009). Meanwhile, this type of agriculture practice eventually increases SOC. Generally, the estimates of SOC change are made on basis of surface soil layers. However, some studies (Gu et al., 2004; Wang et al., 2007; Pan et al., 2008) suggest the SOC accumulation in deep soil layers. Thus, the SOC accumulation in China has been probably underestimated.

### 2.3 Nitrogen cycle

Natural nitrogen is continuously cycled through many different processes of lightening, biological nitrogen fixation, nitrification, denitrification, etc. Therefore, biological fixation, atmospheric emission and deposition could maintain the nitrogen balance. Two anthropogenic activities have considerably increased reactive nitrogen. This is due to the development of intensive agriculture and a rapid growth in energy consumption. In order to meet food production and other industrial activities, anthropogenic nitrogenous fertilizer (ammonia) was created, whereas the increase in energy production by burning of fossil fuels mainly generated nitrogen oxides that are converted to different nitrogen forms through different chemical processes in the atmosphere. Therefore, more and more reactive N in both reduced and oxidized forms is being emitted into the atmosphere and re-deposited onto the surfaces of terrestrial and marine ecosystem. For these processes, a particularly important gas of N<sub>2</sub>O is produced, and its concentration in the atmosphere has been increased.

With the increase of population and alternation of food structure, agriculture practices in some East Asian countries have been changed. High input systems with greater use of fertilizer nitrogen and greater numbers of animals have been employed, which leads to the impacts on the environment. The changing pattern of lifestyle and farming substantially impacts the balance of material cycles including carbon and nitrogen.

#### 2.3.1 Nitrogen budget

A number of studies have focused on the different aspects of N budget in China. Using China's county level agricultural database of 1980 and 1990, Bao et al. (2006) studied the fate of the large amounts of nitrogen (N) brought into the agricultural environment by human activities in the Changjiang River basin. Results showed that anthropogenic reactive N exceeded the terrestrial bio-fixed N, and human activities had significantly altered the N cycle in this region. The total inputs of N in 1980 and 1990 were 8.0 and 12.9 Tg N, respectively, whereas the total N outputs were 4.41 Tg N in 1980 and 6.85 Tg N in 1990. Thus, the excess N that was stored in farmland was 1.51 Tg N at 1980 and 2.67 Tg N at 1990, respectively, and losses through transport to water bodies in 1980 was 2.08 and 3.38 Tg N in 1990, respectively.

Deng et al. (2007) also studied the nitrogen budget of the Changjiang River delta region and evaluated the effect of the human-altered nitrogen cycle on the environment. They obtained that the total nitrogen input to the region was 2.94 Tg in 2002, and the average nitrogen input per unit area was 291 kg hm<sup>-2</sup> a<sup>-1</sup>, which is 4.5 times the average level at national scale. The nitrogen flux on land reached 224 kg hm<sup>-2</sup> a<sup>-1</sup>, which was defined as nitrogen use in fertilizer plus livestock and human waste per area. Most of the nitrogen input was associated with agriculture. Total

nitrogen output from the region was  $1.66 \sim 1.95 \text{ Tg a}^{-1}$ , resulting in a nitrogen surplus of  $0.99 \sim 1.28 \text{ Tg a}^{-1}$ . It is obvious that their nitrogen surplus is much smaller than the estimate by Bao et al. (2006).

Using a compartment model, Sun et al. (2007) studied the nitrogen distribution and cycling of atmosphere-plant-soil system in the typical meadow *Calamagrostis angustifolia* wetland (TMCW) and marsh meadow *Calamagrostis angustifolia* wetland (MMCW) in the Sanjiang plain. They obtained that the N wet deposition was  $0.757 \text{ gN/(m}^2 \text{ a)}$ , and total inorganic N was the main body ( $0.640 \text{ gN/(m}^2 \text{ a)}$ ). The ammonia volatilization amounts of TMCW and MMCW soils in growing season were  $0.635$  and  $0.687 \text{ gN/m}^2$ , and the denitrification gaseous lost amounts were  $0.617$  and  $0.405 \text{ gN/m}^2$ , respectively. Soil organic N was 93.98% and 92.16% of total nitrogen in these two plant-soil systems, respectively.

Based on a data set of 2480 soil profiles and a map of Chinese soil types, Tian et al. (2006) investigated the storage and spatial distribution of soil nitrogen (N) in China. Results showed that the total N storage in China was  $8.29 \text{ Pg}$  in the 1990s, representing 5.9–8.7% of the total global N storage. N density varied substantially with soil types and regions. Peat soils in the southeast of Tibet, southwest China, showed the highest mean N density with a value of  $7314.9 \text{ g/m}^3$  among all soil types. This was more than 30 times of the lowest N density of brown desert soils in the western desert and arid region. N density also varied with land cover types in China. Wetlands in southwest China exhibited the highest N density at  $6775.9 \text{ g/m}^3$  and deserts in northwest China had the least at  $447.5 \text{ g/m}^3$ .

Using the mass balance approach, Gu (2009) studied the N cycling in an urban–rural complex system called the Greater Hangzhou Area (GHA). Results showed that total N input into the GHA was at  $274.66 \text{ Gg/yr}$  in 2004, and total output was at  $227.33 \text{ Gg/yr}$ , indicating that N was accumulated at  $47.33 \text{ Gg/yr}$ , which indicates that N input and output to and from the GHA were increased by 130% and 131%, respectively, compared with the amounts in 1980. Human activities resulted in 73% of N input by means of synthetic fertilizers, human food, animal feed, imported N containing chemicals, fossil fuel combustion, and other items. More than 69.3% of N was released into the atmosphere, and riverine N export accounted for 22.2% of total N output.

Ju et al. (2006) studied the annual N budget and groundwater nitrate-N concentrations in the field in three major intensive cropping systems of wheat-Maize rotations, greenhouse vegetable and apple orchards in Shandong province, north China. Nitrate leaching was evident in all three cropping systems and the groundwater in shallow wells (<15 m depth) was heavily contaminated in the greenhouse vegetable production area, where total N inputs were much higher than crop requirements and the excessive fertilizer N inputs were only about 40% of total N inputs.

### 2.3.2 Atmospheric deposition

Atmospheric nitrogen deposition refers to the process whereby airborne nitrogenous compounds, including inorganic N, organic N and particulate N, are deposited on the Earth's surface by wet deposition and/or dry deposition, which is one of the N cycling processes. However, long-term inputs of inorganic nitrogen from

atmospheric deposition can affect the N balance, which probably results in some negative effects on terrestrial ecosystems such as soil acidification, nutrient imbalance, losses of plant community diversity, increased susceptibility to environmental stresses, etc. The deposited N actually comes from the atmospheric N emission, including the emission from the terrestrial ecosystems and the ocean.

Zhang et al. (2006) established a monitoring network of nine sites to study the spatial and temporal variation of atmospheric nitrogen (N) deposition in the North China Plain (NCP) over a two-year period. It was obtained that the annual bulk deposition of inorganic N in the North China Plain ranged from 18.4 to 38.5 kg/hm<sup>2</sup>, with an average of 28.0 kg/hm<sup>2</sup>. Annual bulk deposition of inorganic N in the Beijing area (32.5 kg/hm<sup>2</sup>) was higher than that in Shandong and Hebei provinces (21.2 kg/hm<sup>2</sup>). It was observed that there was a significant spatial variation of bulk deposition in the Beijing area, and that 60% of bulk deposition occurred from June to September. Their results suggested that reduced N in precipitation was dominant in rural regions, whereas oxidized N was the major form in urban regions. Wet N deposition made up 73% of the bulk deposition, implying that dry N deposition was important in the North China Plain.

Zhang et al. (2008) have reviewed the effects of N deposition on the fluxes of greenhouse gases from forest soils. The effects of N deposition on greenhouse gas fluxes from forest soils were positive or negative, depending on forest type, N-status of the soil, and the rate of N deposition. In forest ecosystems where biological processes were generally limited by N supply, N additions either stimulated soil respiration or had no significant effect, whereas in "N saturated" forest ecosystems, N additions decreased CO<sub>2</sub> emission, reduced CH<sub>4</sub> oxidation, and increased N<sub>2</sub>O flux from the soil. The change in greenhouse gas fluxes from the soil was also related to the status of soil available carbon and its interaction with N turnover in soil. By comparing three temperate forests dominated with *Pinus sylvestris* L., *Cryptomeria japonica* and *Quercus serrata*, respectively, it was shown that there was a smallest effective concentration of the added nitrate that could inhibit CH<sub>4</sub> consumption in the *Pinus* forest soil, which indicated that CH<sub>4</sub> consumption of the soil was more sensitive to NO<sub>3</sub><sup>-</sup>-N addition (Xu and Inubushi 2007). Concentrations of soil available carbon and glucose addition remarkably affect the uptake of atmospheric CH<sub>4</sub> by soil (Xu and Inubushi, 2007; Xu et al., 2008).

Fan et al. (2009) carried out a 2-year monitoring study to estimate nitrogen deposition to a typical red soil forestland in southeastern China. They obtained that the total inorganic nitrogen deposition was 83.7 kg ha<sup>-1</sup> a<sup>-1</sup> in 2004 and 81.3 kg ha<sup>-1</sup> a<sup>-1</sup> in 2005, respectively. The dry deposition accounted for 78.6% of total nitrogen deposition, in which ammonia contributed 86.1%. Their results showed that intensive agricultural practices such as excessive nitrogen fertilization and livestock production were responsible to atmospheric inorganic nitrogen. He et al. (2010) also studied atmospheric N deposition onto agricultural ecosystems, especially on the North China Plain because of extremely intensive agricultural systems and rapid urbanization in this region. They monitored total N deposition at two locations, Dongbeiwang near Beijing and Quzhou in Hebei province, over a two-year period from 2005 to 2007

using an  $^{15}\text{N}$  tracer method and the integrated total N input (ITNI) system. Their results showed that total airborne N inputs to a maize–wheat rotation system at both locations were from 99 to 117 kg N ha $^{-1}$  a $^{-1}$ , with higher N deposition during the maize season (57–66 kg N/ha) than the wheat season (42–51 kg N/ha).

### 2.3.3 Atmospheric emissions

The nitrogen emitted to the atmosphere is mainly  $\text{N}_2\text{O}$ ,  $\text{NH}_3$  and  $\text{NO}_x$ . Xiong et al. (2008) analyzed the impacts of population growth, food preferences and agriculture practices on the nitrogen cycling in East Asia. They pointed out that in China, fertilizer nitrogen input had increased from 0.54 Tg in 1961 to 28 Tg in 2005, and the animal population increased dramatically, from 27 to 1,013 million. As a result 13 Tg N was lost to the environment in 2005 as nitrous oxide, ammonia or nitrate. They estimated that China emitted 1.05 TgN of  $\text{N}_2\text{O}$  and 9.42 TgN of  $\text{NH}_3$  to the atmosphere in 2004. He et al. (2010) estimated that in China,  $\text{NH}_3$  and  $\text{NO}_x$  emissions were estimated to be up to 10.4 Tg  $\text{NH}_3\text{-N}$  and 3.4 Tg  $\text{NO}_2\text{-N}$  in 2000, derived mainly from agricultural activities and industrial emissions (including transportation and power plants), respectively.

Zou et al. (2009) investigated nitrogen fertilizer-induced direct nitrous oxide ( $\text{N}_2\text{O}$ ) emissions during the rice-growing season in Mainland of China between the 1950s and the 1990s. Results showed that total nitrogen input during the rice-growing season increased from 87.5 kgN ha $^{-1}$  in the 1950s to 224.6 kgN ha $^{-1}$  in the 1990s, and that seasonal  $\text{N}_2\text{O}$  emissions increased from 9.6Gg  $\text{N}_2\text{O-N}$  each year in the 1950s to 32.3Gg  $\text{N}_2\text{O-N}$  in the 1990s. In the 1990s,  $\text{N}_2\text{O}$  emissions during the rice growing season made up 8–11% of the reported annual total of  $\text{N}_2\text{O}$  emissions from croplands in China, implying that paddy rice development could have contributed to mitigating agricultural  $\text{N}_2\text{O}$  emissions in the past decades. Zou et al. (2010) further estimated annual synthetic fertilizer N-induced direct  $\text{N}_2\text{O}$  emissions (FIE- $\text{N}_2\text{O}$ ) from Chinese croplands during 1980–2000. Annual FIE- $\text{N}_2\text{O}$  was estimated to be 115.7 Gg  $\text{N}_2\text{O-N}$  yr $^{-1}$  in the 1980s and 210.5 Gg  $\text{N}_2\text{O-N}$  yr $^{-1}$  in the 1990s. Upland croplands contributed most to the national total of FIE- $\text{N}_2\text{O}$ , accounting for 79% in 1980 and 92% in 2000.

Wolf et al. (2009) reported year-round  $\text{N}_2\text{O}$  flux measurements with high and low temporal resolution at ten steppe grassland sites in Inner Mongolia, China. Results showed that short-lived pulses of  $\text{N}_2\text{O}$  emission during spring thaw dominated the annual  $\text{N}_2\text{O}$  budget. The  $\text{N}_2\text{O}$  emission pulses were highest in ungrazed steppe and decreased with increasing stocking rate, suggesting that grazing decreased rather than increased  $\text{N}_2\text{O}$  emissions. They also pointed out that by neglecting these freeze–thaw interactions, existing approaches may have systematically overestimated  $\text{N}_2\text{O}$  emissions over the last century for semi-arid, cool temperate grasslands by up to 72 percent.

Huang and Tang (2010) studied the relation between improving nitrogen use efficiency (NUE) and reduction of nitrous oxide ( $\text{N}_2\text{O}$ ) emission in cropland. The results showed that improving NUE to 40% could cut 4.4 million tons of synthetic N use per year. As a result of this reduction, the direct  $\text{N}_2\text{O}$  emission from croplands together with  $\text{CO}_2$  emission from the industrial production and transport of synthetic N could be reduced by 27%, equivalent to 40 Tg  $\text{CO}_2\text{-eq. a}^{-1}$ . They concluded that

improving N management could greatly reduce GHG (N<sub>2</sub>O and CO<sub>2</sub>) emissions in Chinese croplands. Using datasets from the literature and field measurements, Huang and Tang (2010) estimated that marshland conversion to cropland in northeast China over the period 1950–2000 reduced CH<sub>4</sub> emissions from the former marshland by a cumulative amount of ~28 Tg relative to 1950. Taking the loss of SOC and emissions of CH<sub>4</sub> and N<sub>2</sub>O into account, the integrated global warming potential in the 1990s, compared with the 1950s, was reduced by 21%–33% due to marshland conversion in northeast China (Huang et al., 2010b).

Zhou et al. (2010) developed a process-based site model to simulate daily N<sub>2</sub>O emission from a rice-winter wheat rotation cropping system. The three-year observations conducted in East China were used to examine the model. The simulated results showed that the model well reproduced the observed daily solar radiation, soil temperature and moisture, and also captured the dynamics and magnitude of accumulated rice aboveground biomass and mineral nitrogen in the soil. The simulated results also reflected the inter-annual variation of N<sub>2</sub>O emission, implying that the model has the capability to capture the general characteristics of N<sub>2</sub>O emission from a typical rice-wheat rotation agro-ecosystem. The results from the sensitivity analyses indicated that the simulated N<sub>2</sub>O emission was most sensitive to the fertilizer application rate and the soil organic matter content, but it was much less sensitive to variations in soil pH and texture, temperature, precipitation and crop residue incorporation rate under local conditions.

### **3. Marine carbon and nitrogen cycles**

The oceans contain the largest carbon and reactive nitrogen among three reservoirs, and have the capacity for absorbing and retaining CO<sub>2</sub>. Hence, the oceans play a very important role in the global carbon and nitrogen cycles. The research on the sink and source of both carbon and nitrogen as well as their biogeochemical processes in the ocean can help use to understand the global budget and transport of both carbon and nitrogen in the future, and to project the change of atmospheric CO<sub>2</sub>.

#### **3.1 Carbon cycle in the ocean margins**

Rivers play an important role in the transport and transformation of carbon from the land to the ocean. It has been estimated that about  $1 \times 10^{15}$  g of carbon is discharged annually from the land to the ocean through rivers and estuaries (Guo et al., 2008). Besides estuaries and marshes, coastal waters, despite comprising only a small portion of the world's ocean surface area, play a critically important role in the global oceanic carbon cycle and have recently received increasing attention (Cai et al., 2006; Zhai and Dai, 2009). Some researchers have estimated that continental shelves may absorb atmospheric CO<sub>2</sub> by up to 1Pg C a<sup>-1</sup> or 50% of known open ocean uptake (Cai et al., 2006). Cai et al. (2006) argued that that estimate of carbon uptake rate in the ocean margins was based on data from a single type of shelf located in the northern temperate zone near populated areas. Therefore, there exists a large uncertainty for the estimate of carbon cycle in the ocean margins, resulting in a difficulty of balancing the global CO<sub>2</sub> budget. In the last four years, many researches about the carbon cycle in the ocean margins, especially the estuaries and shelf of China have been made by Chinese scientists.

### 3.1.1 Carbon fluxes to the ocean from rivers

Shelves are an important area for the connection of rivers and oceans. Recently, based on the circulation and latitude, Cai et al. (2006) divided the highly heterogeneous shelves into seven provinces in terms of distinct physical and biological characteristics to estimate shelf sea-to-air CO<sub>2</sub> flux. They suggest that the continental shelves are a sink for atmospheric CO<sub>2</sub> at mid-high latitudes ( $-0.33 \text{ PgC a}^{-1}$ ) and a source of CO<sub>2</sub> at low latitudes ( $0.11 \text{ PgC a}^{-1}$ ). They have pointed out that warm temperature and high terrestrial organic carbon input are most likely responsible for the CO<sub>2</sub> release in low latitude shelves. Cai et al. (2008) made a comparative overview of the weathering intensity and HCO<sub>3</sub><sup>-</sup> flux in the world's major rivers. It was found that there was a strong correlation between specific HCO<sub>3</sub><sup>-</sup> fluxes and discharge in all four rivers (Changjiang, Huanghe, Pearl, and Mississippi rivers) with different discharge seasonality, implying that higher precipitation in drainage basins can promote higher weathering rates. They obtained that among the 25 large rivers in the world, the rivers in low, mid and high latitudes accounted for 42.6%, 47.3% and 10.1% of the total global dissolved inorganic carbon flux to the ocean, respectively, and that the rivers in the mid-latitude carried a disproportionately high dissolved inorganic carbon flux to the ocean with a relatively small (26%) amount of freshwater discharge. Their study also indicated that the HCO<sub>3</sub><sup>-</sup> flux was strongly correlated with the carbonate mineral content of river basins, while the river HCO<sub>3</sub><sup>-</sup> concentration was related to the balance of precipitation and evaporation.

Among these rivers at mid-high latitudes there are the largest Asian river (Changjiang River) and other important rivers (e.g. Huanghe, Zhujiang Rivers, etc.) in China. Li et al. (2006) studied the inorganic carbon (IC) in the Changjiang River Estuary and Jiaozhou Bay as examples of offshore sediments. Sequential extraction was used to divide inorganic carbon in the sediments into five forms. It was found that HCl form may be one of end-result of atmospheric CO<sub>2</sub>. They suggest that Changjiang River estuary sediment may absorb at least about 4.1 Tg of atmospheric CO<sub>2</sub> every year, indicating that offshore sediments play an important role in absorbing atmospheric CO<sub>2</sub>. Based on the data from a cruise in the Pearl River estuary in April 2007 along a salinity gradient, He et al. (2010) investigated the distribution, degradation and dynamics of organic carbon and its major compound classes, carbohydrates and amino acids. Their study indicated that anthropogenic sewage input appeared to be an important source of the DOC pool in the upper estuary, and  $5.3 \times 10^8 \text{ g C d}^{-1}$  of DOC could be exported out from the Lingdingyang Bay (a major subestuary of the Pearl River estuary) to the continental shelf of the South China Sea during the low flow season.

### 3.1.2 Seasonal variations of the carbon cycle

Zhai et al. (2007) examined the carbonate system with the data from four field surveys. Together with previously reported data, their study provided a full seasonal coverage with regards to CO<sub>2</sub> outgassing fluxes in the Changjiang River Estuary system for the first time. The results showed that surface pCO<sub>2</sub> ranged 650–1440  $\mu\text{atm}$  in the upper reach of the Changjiang River Estuary, 1000–4600  $\mu\text{atm}$  in the Huangpujiang River, and 200–1000  $\mu\text{atm}$  in the estuarine mixing zone, and that CO<sub>2</sub>

emission flux from the main stream of the Changjiang Estuary was at a low level of  $15.5\text{--}34.2 \text{ mol m}^{-2} \text{ yr}^{-1}$ . They estimated that including the Huangpujiang River and the adjacent Shanghai inland waters,  $\text{CO}_2$  degassing flux from the Changjiang Estuary may have represented only 2.0%–4.6% of the DIC exported from the Changjiang River into the East China Sea. Based upon more data of seven field surveys conducted during April 2005 – April 2008, Zhai and Dai (2009) studied the seasonal variation of air-sea  $\text{CO}_2$  fluxes in the outer Changjiang (Yangtze River) Estuary, on the inner shelf of the East China Sea (ECS). An obvious seasonal variation of surface  $\text{pCO}_2$  was observed in this most dynamic zone of the ECS, including  $320\text{--}380 \mu\text{atm}$  (average  $\sim 345 \mu\text{atm}$ ) in winter,  $180\text{--}450 \mu\text{atm}$  (average  $\sim 330 \mu\text{atm}$ ) in spring,  $150\text{--}620 \mu\text{atm}$  (average  $\sim 310 \mu\text{atm}$ ) in summer and  $120\text{--}540 \mu\text{atm}$  (average  $\sim 375 \mu\text{atm}$ ) in autumn. They obtained that the outer Changjiang Estuary served as a moderate or significant sink of atmospheric  $\text{CO}_2$  in winter, spring and summer, while it turned to a net source in autumn. They considered that the seasonal variation appeared to be controlled by primary productivity and air-sea exchange in the warm seasons and by mixing in the cold seasons.

Based on data from five surveys, Guo et al. (2008) examined the seasonal variations of the inorganic carbon system in the Pearl River estuary. They obtained that both DIC and total alkalinity (TALK) values in the freshwater end-members were high in the dry season ( $>2700 \mu\text{mol kg}^{-1}$  for DIC and  $>2400 \mu\text{mol kg}^{-1}$  for TALK) and substantially lower in the wet season ( $\sim 1000$  and  $700 \mu\text{mol kg}^{-1}$  for DIC and TALK), and that riverine DIC flux and drainage basin weathering rates, however, were significantly higher in the wet season ( $611 \times 10^9 \text{ mol yr}^{-1}$  and  $13.6 \times 10^5 \text{ mol km}^{-2} \text{ yr}^{-1}$ ) than in the dry season ( $237 \times 10^9 \text{ mol yr}^{-1}$  and  $5.3 \times 10^5 \text{ mol km}^{-2} \text{ yr}^{-1}$ ). They pointed out that the complex behavior of DIC and TALK in the estuarine mixing zone was mainly a result of mixing between tributaries with distinct and seasonally variable DIC and TALK values. Liu et al. (2010) evaluated the seasonal cycle and effect of phosphorus in plankton ecosystem in the waters of the Pearl River Estuary. They found that the available water volume for phytoplankton photosynthesis changed seasonally, and that primary productivity varied from about  $36 \text{ kg d}^{-1}$  in dry season to  $31 \text{ kg d}^{-1}$  in wet season.

### 3.1.3 Phytoplankton structure in the ocean margins

The phytoplankton structure and nutrients in cultural areas and aquaculture areas of Daya Bay, South China Sea, were examined by Wang et al. (2006) and Wang et al. (2009), respectively. Appropriate water temperature, salinity, sufficient dissolved silicate (DSi), as well as quick recovery of nutrients, played important roles in the high abundance of phytoplankton and frequent outbreak of blooms in the cultural areas of Daya Bay (Wang et al., 2006). The survey in the aquaculture areas of Daya Bay showed that diatoms were the predominant phytoplankton group, accounting for 93.21% of the total abundance and dissolved inorganic phosphorus (DIP) was the most necessary element for phytoplankton growth, while dinoflagellate was the second most abundant group (Wang et al., 2009). Besides Daya Bay, Dai et al. (2008) observed a phytoplankton bloom downstream of a large estuarine plume in the Pearl River estuary and the northern South China Sea in May–June 2001, and found that

during the bloom event, there was a cascade of changes, including a significantly shift of the surface water phytoplankton community structure from a pico-phytoplankton dominated community to one dominated by microphytoplankton (420  $\mu\text{m}$ ), a significant drawdown of  $\text{pCO}_2$ , a biological uptake of dissolved inorganic carbon (DIC) and an associated enhancement of dissolved oxygen and pH, demonstrating enhanced photosynthesis during the bloom. Huang et al. (2010) examined the phytoplankton community at two warm eddies in the northern South China Sea in winter 2003/2004, and found that phytoplankton communities observed in these two eddies were significantly different. In one warm eddy, the phytoplankton community was dominated by prochlorophyceae within the euphotic zone, whereas in the other warm eddy, haptophyceae was dominant in the euphotic zone. They pointed out that the difference in the phytoplankton community was due to the different origins and ages of the two warm eddies. Carbon fixed by phytoplankton and cultured algae has been discussed by Song et al. (2008) based on in situ investigation and data analysis in China coastal seas. They obtained that the carbon fixed by phytoplankton was about  $2.22 \times 10^8 \text{ t a}^{-1}$  with a clear seasonal variation in the Bohai Sea, the Yellow Sea and the East China Sea, and that the carbon fixed by phytoplankton was about  $4.16 \times 10^8 \text{ t a}^{-1}$  in the South China Sea, which is twice the total carbon fixed amount in the Bohai Sea, the Yellow Sea and the East China Sea. In addition, an adjoint data assimilation method was applied in a coupled physical–biological model of the Bohai Sea and the Yellow Sea (BYS) by Zhao and Lu (2008) to estimate the ecological parameters. Their results showed that phytoplankton data were the strongest constraints during the parameter estimation process, and that the simulated horizontal distributions of surface phytoplankton were consistent with the biological roles of seasonal stratification.

### 3.2 Carbon cycle in the open ocean

As mentioned above, there is still some controversy over the exact figure of carbon uptake in the ocean and its future changes. Just for the calculation of air-sea  $\text{CO}_2$  exchange fluxes, under the same wind velocity, different formulae can lead to a difference of up to several tens of percent in the exchange coefficient, and use of different formulae of thermodynamic constants may generate a difference of up to 3 Pa in the calculated partial pressure of  $\text{CO}_2$  at surface water (Xu et al., 2004). There are many other parameters involved with the estimate of ocean carbon uptake and storage. Because of the large area of the global oceans, the processes may be different in the different regions. Even the same process, the parameters are often region-dependent, for example, the transport coefficients of carbon in the interior ocean, the sedimentation rate of organic carbon, and so on.

The study of carbon cycle in the ocean basins can be performed with the observation data and the models. In the summers of 1999 and 2003, the partial pressure of  $\text{CO}_2$  in the air and surface waters ( $\text{pCO}_2$ ) of the Bering Sea and the western Arctic Ocean were measured by the 1<sup>st</sup> and 2<sup>nd</sup> Chinese National Arctic Research Expeditions (Chen and Gao, 2007). Using these data, Chen and Gao (2007) found that the spatial distribution of the  $\text{pCO}_2$  was different in the observed region. The surface  $\text{pCO}_2$  values gradually increased from the continental shelf waters, the

Bering Sea shelf slope, to the Bering Abyssal Plain (BAP) and the Canadian Basin. The difference was attributed to the combination of various source waters, biological uptake, and seasonal warming. As a result, it was found that Chukchi Sea was a carbon sink. They also found that SST and primary production affected the seasonal variation of surface pCO<sub>2</sub>.

Over the last four years, there have been some modeling studies about the ocean carbon cycle and some related work from Chinese scientists, including the model assessment with passive tracers such as CFCs, <sup>3</sup>H, and <sup>14</sup>C (Xu et al., 2006; Li et al., 2006; Chu et al., 2008; Ba and Xu, 2010; etc.) and the examination of transport coefficients (Xu et al., 2006; Li et al., 2007; etc.). These studies suggest that the performance with isopycnal parameterization of transport of tracers has been generally improved in the ocean general circulation models of MOM and L30T63 developed by the LASG/Institute of Atmospheric Physics, relative to the traditional horizontal diffusion mixing scheme of tracers. A gradient of tracer inventories from the west to east in the middle latitude of the North Pacific has been well simulated under the condition of relatively large isopycnal diffusivity. Based on these works, the carbon cycle in the both basin and global oceans, especially the Pacific Ocean, has been simulated.

Xu et al. (2007) used a basin-wide ocean general circulation model with the open southern boundary condition to study the uptake and distribution of anthropogenic CO<sub>2</sub> in the North Pacific. The results showed that larger isopycnal diffusivity produced larger exchange fluxes of anthropogenic CO<sub>2</sub> in the western North Pacific but smaller fluxes in the equatorial, and that during the period 1800-1997, the North Pacific took up 23.75 GtC of anthropogenic CO<sub>2</sub>. The same model with the close southern boundary condition was used to identify which location was more efficient for ocean CO<sub>2</sub> disposal in the North Pacific (Xu et al., 2009). Four injection depths at each one of fifteen locations were chosen, and the simulated results showed that the sequestration was more efficient for the injection in the east than in the west (Xu et al., 2009). Xu and Li (2009) used a global ocean general circulation model called L30T63 to study the uptake and distribution of anthropogenic CO<sub>2</sub> in the ocean. Two runs with different isopycnal diffusivities estimated that the global oceanic anthropogenic CO<sub>2</sub> uptake rate was 1.64 and 1.73 Pg C yr<sup>-1</sup> for the 1990s. They pointed out that use of large isopycnal diffusivity could generally improve the simulated results, including the exchange flux, the vertical distribution patterns, inventory, storage, etc.

### **3.3 Nitrogen cycle in ocean margins**

Nitrogen as an important nutrient plays an essential role in the life activity in the ocean. Phytoplankton takes up carbon dioxide and nutrients in the presence of light through the photosynthesis. Most common nitrogen compounds are nitrate and ammonium. These inorganic nitrogen compounds are transformed into organic nitrogen through different chemical and biological processes in the ocean. Certainly, organic nitrogen can also be transformed into inorganic nitrogen. In addition, organic nitrogen can be probably used by some species directly. Both riverine N input and atmospheric nitrogen deposition probably alters the nitrogen and carbon cycles in the ocean, which may affect primary productivity and even change ecosystem composition or function. Therefore, studies of both atmospheric inorganic and organic deposition are important for understanding of the carbon and nitrogen cycles as well

as future climate change.

Shi et al. (2006) reviewed recent studies of atmospheric organic nitrogen deposition. It was found that organic nitrogen accounted for  $39.6\% \pm 14.7\%$  of total aerosol nitrogen, and that in rainwater from continental locations,  $30.2\% \pm 15.0\%$  of dissolved nitrogen was present in organic forms, whereas in remote marine rains organic nitrogen was  $62.8\% \pm 3.3\%$  of the total nitrogen. Shi et al. (2006) pointed out that atmospheric nitrogen deposition to the world's ocean may be important, if organic nitrogen is taken into account.

Although atmospheric  $N_2O$  concentration is 3 orders of magnitude lower than that of  $CO_2$ , its greenhouse effect cannot be ignored because  $N_2O$  has a per molecule radiative forcing strength 200-300 times greater than carbon dioxide. A review of the study on the biogeochemical cycle of nitrous oxide in the oceans for the past decades has been made by Zhan and Chen (2006), in which the vertical distribution of  $N_2O$  in the oceans, its impact factors as well as formation and removal mechanisms were discussed in more detail. Using the measured data of  $N_2O$  concentrations, which was collected along cruise tracks between  $30^{\circ}S-67^{\circ}S$  and in Prydz Bay, Antarctica in the 22<sup>nd</sup> Chinese National Antarctic Research Expedition from November 2005 to March 2006, Zhan and Chen (2009) showed that the concentration of  $N_2O$  in surface seawater increased from  $8.9 \pm 0.2$  nM to  $17.9 \pm 0.3$  nM along the cruise tracks southward from  $30^{\circ}S-67^{\circ}S$  latitude and was well correlated with SST. They pointed out that distributions of SST induced the negative saturation anomaly south of the Subantarctic Front and positive saturation anomaly north of the Subantarctic Front, as a result of the positive air-sea fluxes and almost zero, respectively.

Ammonia-oxidizing archaea (AOA) have recently been found to be potentially important in nitrogen cycling in a variety of environments, especially in estuaries (Dang et al., 2008). Dang et al. (2008) studied the sedimentary AOA diversity, community structure and spatial distribution in the Changjiang Estuary and the adjacent East China Sea. It was known from the spatial distribution of putative soil-related AOA in certain sampling stations that the Changjiang freshwater discharge strongly affected the marine benthic microbial ecosystem. The transport of terrestrial archaea into the seawater and sediments might be attributed to nutrients, organic matter, suspended particles and the Changjiang diluted water, besides freshwater (Dang et al., 2008).

#### **4. Carbon-nitrogen cycle and climate change**

Climate change in the future will greatly depend on the anthropogenic emissions of greenhouse gases, particularly  $CO_2$ . The positive feedbacks between climate change and the carbon cycle have been noted, which indicates that climate warming causes the reduction of carbon uptake in the terrestrial ecosystem and oceans. Carbon uptake in the both land ecosystems and oceans is generally limited by the availability of nutrients. Nitrogen in the land ecosystems is quite sensitive to human activities, including fertilization, land-use changes, and climate change. As mentioned above, atmospheric N deposition has been increasing because of accelerating industrialization and use of N fertilizer, which will probably affect regional and global C budgets, and regulate the response and feedback of the biosphere to climate change. For projection of climate-carbon feedbacks, one of the largest uncertainties is from the estimate of the C sequestration potential in terrestrial ecosystems. However, in the early studies, N limitation to terrestrial C sequestration is generally not included in the model. Therefore, understanding of the interaction between N and C cycling is very

important.

#### 4.1 Nitrogen impacts

It is generally considered that the increase in atmospheric CO<sub>2</sub> can stimulate terrestrial C sequestration which is related to the N availability. To understand the responses of terrestrial plant species under global N enrichment, Xia and Wan (2008) conducted a meta-analysis of data from 304 studies to reveal the general response patterns of terrestrial plant species to the addition of N. It was found that across 456 terrestrial plant species included in the analysis, biomass and N concentration were increased by 53.6 and 28.5%, respectively, under N enrichment. However, the N responses were dependent upon plant functional types, with significantly greater biomass increases in herbaceous than in woody species. Stimulation of plant biomass by the addition of N was enhanced when other resources were improved. In addition, the N responses of terrestrial plants decreased with increasing latitude and increased with increasing annual precipitation.

Xia et al. (2009) conducted a field manipulative experiment of warming and N addition in a temperate steppe in the semiarid grassland of Duolun County, Inner Mongolia, China, during two contrasting hydrological growing seasons in 2006 (wet with total precipitation 11.2% above the long-term mean (348 mm)) and 2007 (dry with total precipitation 46.7% below the long-term mean). It was found that the responses of ecosystem C fluxes to warming and N addition did not change between the two growing seasons, that warming had no effect on net ecosystem C exchange (NEE) or its two components, gross ecosystem productivity (GEP) and ecosystem respiration (ER), whereas N addition stimulated GEP but did not affect ER, leading to positive responses of NEE. In the wet growing season, N addition increased forb biomass but did not affect soil moisture, leading to positive effect on NEE, whereas in the dry growing season, N addition stimulated grass biomass but reduced forb biomass, leading to the increase in NEE. At the same site, Niu et al. (2010) conducted an experimental study to examine effects of N addition on NEE in terms of nitrogen alone or combination with phosphorous (P) in both clipped and unclipped plots from 2005 to 2008. Their results showed that over the 4 years, N addition significantly stimulated growing-season NEE, on average, by 27%, and that neither the main effects of P addition or clipping nor their interactions with N addition were statistically significant on NEE in any of the 4 years. They further pointed out that the magnitude of N stimulation on NEE declined over time. Although N addition significantly increased NEE by 60% in 2005 and 21% in 2006, its effect was not significant in 2007 and 2008. They considered that N-induced shift in species composition was primarily responsible for the declined N stimulation over time.

Xu and Wan (2008) also conducted a field experiment in Duolun County between April 2005 and October 2006 to examine effects of topography, fire, N fertilization, and their potential interactions on soil respiration. The results indicated that mean soil respiration was 6.0% higher in the lower than upper slope over the 2 growing seasons, that annual burning in early spring caused constant increases in soil respiration (23.8%) over the two growing seasons. In addition, fire effects on soil respiration varied with both season and topographic position. Soil respiration in the fertilized

plots was 11.4% greater than that in the unfertilized plots. Water- and plant-mediation could be primarily responsible for the changes in soil respiration with topography and after fire, whereas the positive responses of soil respiration to N fertilization were attributable to stimulated plant growth, root activity and respiration.

In order to understand how N deposition and elevated atmospheric CO<sub>2</sub> concentration affect forest floor soil respiration in subtropical China, Deng et al. (2010) grew tree seedlings in ten large open-top chambers. Their results showed that soil respiration displayed strong seasonal patterns with higher values in the wet season (April-September) and lower values in the dry season (October-March) in all treatments. It was found that there was a significant exponential relationship between soil respiration rate and soil temperature, and a significant linear relationship between soil respiration rate and soil moisture (below 15%). Both CO<sub>2</sub> and N treatments significantly affected soil respiration, and there was a significant interaction between elevated CO<sub>2</sub> and N addition. It was observed that the stimulatory effect of individual elevated CO<sub>2</sub> (about 29% increased) was maintained throughout the experimental period. The positive effect of N addition was found only in 2006 (8.17% increased), and then was weakened over time. Their combined effect on soil respiration (about 50% increased) was greater than the impact of either one alone.

Based on the data of the second national soil survey in China, Xu et al. (2006) studied the coupling characteristics and spatial variation of soil organic carbon (SOC) and total nitrogen (TN) in the plow layers of paddy and upland fields. Results showed that SOC and TN contents were higher in paddy fields than in upland fields by 47.8% and 45.5%, respectively, but spatial variations of SOC and TN were higher in upland than in paddy fields. Soil organic carbon and total nitrogen ratio (C/N) was about 10.8 in paddy fields, higher than 9.9 in upland fields. It was found that there was a significant regional variation of C/N ratio in upland fields. SOC was positively correlated with TN, with correlation coefficients being all higher than 0.8 in paddy and upland fields except for in North China. This indicated that there existed a coupled relationship between SOC and TN.

#### **4.2 Impacts of climate change**

Using a total of 886 data sets distributed in different regions of China, which were obtained from the second National Soil Survey of China that was completed in the early 1980s, Dai and Huang (2006) investigated the relation of soil organic matter (SOM) concentration to climate and altitude. The results showed that surface SOM concentration was in general negatively correlated with annual mean temperature (T) and positively correlated with annual mean precipitation (P) and altitude (H). A further investigation suggested that multiple regression models with different combination of T, P and H could explain 41.5%–56.2% of the variability in surface SOM concentration for different geographical regions, while the driving variables are different.

Niu et al. (2008) has conducted a field experiment manipulating temperature and precipitation in a temperate steppe in northern China since 2005. The results for the first 2 yr showed that gross ecosystem productivity (GEP) was higher than ecosystem respiration, leading to net C sink (measured by NEE) over the growing season in the

study site. The interannual variation of NEE resulted from the difference in mean annual precipitation. Experimental warming reduced GEP and NEE, whereas increased precipitation stimulated ecosystem C and water fluxes in both years. Increased precipitation also alleviated the negative effect of experimental warming on NEE. They pointed out that water availability plays a dominant role in regulating ecosystem C and water fluxes and their responses to climatic change in the temperate steppe of northern China.

Based on climate change projections of 21st century under A2A, B2A and A1B offered by IPCC, Guo et al. (2010) studied the responses of yields and water use efficiencies of wheat and maize to climate change scenarios over the North China Plain. The projected climate results were used to drive CERES-Wheat and Maize models. Their simulated results show that the impacts of increased temperature and CO<sub>2</sub> on wheat and maize yields are inconsistent. Under the same scenario, the wheat yield increases due to climatic warming, whereas the maize yield decreases. The simulated results further indicate that under B2A in the 2090s, average wheat yield and maize yield will respectively increase 9.8% and 3.2% without CO<sub>2</sub> fertilization in this region, that there is a positive effect of CO<sub>2</sub> enrichment on yield and water use efficiency, and that if atmospheric CO<sub>2</sub> concentration reaches nearly 600 ppm, wheat and maize yields will increase 38% and 12% and water use efficiencies will improve 40% and 25%, respectively, in comparison to those without CO<sub>2</sub> fertilization. In that study, the N effect is not included.

Using the process-based forest growth and carbon and nitrogen model of TRIPLEX, Peng et al. (2009) investigated the potential impacts of climate change and increasing atmospheric CO<sub>2</sub> on forest net primary productivity (NPP) and carbon budgets in northeast of China. Climate change would increase forest NPP and biomass carbon but decrease overall soil carbon under all three climate change scenarios. The combined effects of climate change and CO<sub>2</sub> fertilization on the increase of NPP were estimated to be 10 - 12% for the 2030s and 28 - 37% for the 2090s. The simulated effects of CO<sub>2</sub> fertilization significantly offset the soil carbon loss due to climate change alone. There are large uncertainties in the estimate of climate change impacts, which are from many physical, biological, and social-economic processes. Tao et al. (2009b) developed a new super-ensemble based probabilistic projection approach to account for the uncertainties from CO<sub>2</sub> emission scenarios, climate change scenarios, and biophysical processes in the impact assessment model, which was used for maize production in the North China Plain in the future. The new process-based general crop model called MCWLA (Tao et al., 2009a) was used in their work. They obtained that the expected yield changes were -9.7, -15.7, -24.7% across the maize cultivation grids in Henan province during the 2020s, 2050s, and 2080s, with 95% probability intervals of (-29.4, +15.8), (-45.7, +24.0), (-92.8, +20.3) in percent of 1961–1990 yields, respectively. The corresponding value in Shandong province was also given. The temporal and spatial pattern of changes and variability in maize yield across the region were discussed in their study.

Using the regional terrestrial NPP from different observations and models over China, Mao et al. (2010) explored the relationship between NPP and climate variation at interannual and decadal scales in the Modified Sheffield Dynamic Global Vegetation Model (M-SDGVM) during 1981–2000. The results from M-SDGVM were in agreement with the NPP data from 743 sites. Compared to the 1980s, NPP in

the 1990s increased in most of China with a high degree of spatial heterogeneity. The interannual variation of the total NPP showed a more significant correlation with temperature (relativity and probability are  $R= 0.61$ ,  $P = 0.00403$ ) than with precipitation ( $R = 0.40$ ,  $P = 0.08352$ ). They also pointed out that  $\text{CO}_2$  fertilization may play a key role in the increase of terrestrial ecosystem NPP over continental China, and  $\text{CO}_2$  stimulation increases with  $\text{CO}_2$  concentrations, and also with the climate variability of the 1980s and 1990s.

### 4.3 Atmosphere-land-ocean coupled model

In the earth system, the atmosphere, land and ocean are coupled through the exchanges of momentum, energy and mass at their interfaces. For the carbon and nitrogen cycles, and their interactions with climate change, the study in the coupled system is very important. Over last several years, different coupled systems have been established.

Dan and Ji (2007) employed a two-way coupled model, Atmosphere-Vegetation Interaction Model-Global Ocean-Atmosphere-Land System Model (AVIM-GOALS), to simulate the surface physical fluxes and net primary production (NPP). Their results showed that the simulated terrestrial surface physical fluxes were generally consistent with the ERA40 in the global distribution, but the magnitudes were generally 20–40  $\text{W/m}^2$  underestimated, that the annual NPP agreed well with the IGBP NPP data except for the lower value in northern high latitudes. The results of surface physical fluxes, leaf area index (LAI) and NPP in the global mid-latitudes, especially between  $30^\circ\text{N}$ – $50^\circ\text{N}$ , exhibited a great variation of annual oscillation amplitudes. All physical and biological fields in northern mid-latitudes had the largest seasonality, and the seasonality of these fields was highly correlated with each other. Using the data and the above AVIM-GOALS model, Dan et al. (2007) analyzed the relationship between NPP and climate change. The globally averaged NPP of  $447.47 \text{ g C m}^{-2} \text{ yr}^{-1}$  was close to the IGBP data of  $450.42 \text{ g C m}^{-2} \text{ yr}^{-1}$ . The globally relative error of simulated NPP against IGBP data was about 20% and was also comparable to other global biogeochemical models. Meridional variations of globally zonal mean NPP corresponded more to the meridional change of precipitation than to that of temperature. The global NPP for all vegetation types was highly correlated with precipitation.

Different from the work by Dan et al. (2007), Zhi et al. (2009a) employed the ocean general circulation model in the coupled GOALS-AVIM to study the main characteristics of interannual variations and the correlation between the atmospheric circulation and terrestrial ecosystem. It was found that the simulated results of the interannual variations of the spatial and temporal distributions of the surface air temperatures and precipitation were generally improved by using AVIM in GOALS-AVIM. The interannual variation revealed some distinct characteristics of the geographical distribution. Both NPP and LAI had quasi 1-2-year cycles, whereas precipitation and the surface temperatures had 2–4-year cycles. Using Singular Value Decomposition (SVD) analysis, they obtained that the strengthening and weakening of the East Asian monsoon, characterized by the geopotential heights at 500 hPa and the wind fields at 850 hPa, corresponded to the spatiotemporal NPP pattern, and that

the correlations between NPP and the air temperature, precipitation and solar radiation were different in interannual variability because of the variation in vegetation types. Using the results from the same GOALS-AVIM, Zhi et al. (2009b) analyzed the Indian Ocean SST abnormality and its relations with NPP at the land surface in South Asia. Results showed that there were four dominant steady patterns of annual mean Indian Ocean SST anomaly (SSTA) in the Empirical Orthogonal Function (EOF). The first eigenvector exhibited a trend of simultaneous changes in the whole area, indicating that the Indian Ocean SST in the four seasons possesses a consistent increase or decrease. Their correlation analysis showed that the consistent warming or cooling in the equatorial Indian Ocean had a positive lag correlation with the Niño3 index of the equatorial Pacific Ocean. They pointed out that the increase or decrease of summer monsoon in the Indian Ocean and South Asia caused the precipitation abnormality in South Asia, leading to the increase or decrease of NPP abnormality in this region.

Using the modified AVIM (AVIM2), in which a soil carbon module was included, Ji et al. (2008) investigated the change in carbon exchange between Chinese terrestrial ecosystem and the atmosphere, and the carbon storage in vegetation and soil during the 21st century. Future climate data were obtained from the regional climate model of the Hadley Centre under Special Report on Emissions Scenarios (SRES) B2 scenario. The simulated results showed that in the coming 100 a, for SRES B2 scenario and constant atmospheric CO<sub>2</sub> concentration, NPP of terrestrial ecosystem in China would decrease slowly, and vegetation and soil carbon storage as well as NEP would decrease. For B2 scenario and changing atmospheric CO<sub>2</sub> concentration, NPP for China will increase continuously from 2.94 GtC a<sup>-1</sup> at the end of the 20th century to 3.99 GtC a<sup>-1</sup> by the end of the 21st century, and vegetation and soil carbon storage will increase to 110.3 GtC. Meanwhile, NEP in China will keep rising during the first and middle periods of the 21st century, and reach the peak around 2050s, then will decrease gradually and approach to zero by the end of the 21st century. Using the same AVIM2, Wu et al. (2010) further studied the impact of future climate change on terrestrial ecosystem over China at four warmer levels of 1, 2, 3 and 4 °C. Their results showed that as projected temperature increases, average NPP likely decreases in China as a whole. The Tibetan Plateau is the only ecoregion with increasing NPP as the climate becomes warmer. They pointed out that in general, the influence of climate change on the terrestrial ecosystem NPP in China would increase with the increase in temperature, and that the northwest arid region would be expected to be the most vulnerable ecoregion. However, the interaction between NPP and climate change is not considered in their studies because AVIM2 is not coupled directly to the atmospheric general circulation model. Hence, further investigation is required.

## 5. Concluding remarks

The progresses in the study of the carbon and nitrogen cycles in China has been reviewed in this paper, mainly including the carbon and nitrogen cycles in the terrestrial ecosystem and in the ocean, and their couple and climate change. Many studies have shown that the Chinese terrestrial ecosystem was a net carbon sink for the 1980s-1990s, with an estimate of 0.19-0.26 GtC/a. It can be expected that there

will be a continuous increase in the forest carbon biomass because of the increase of forest area and the forest regrowth in the future. Large uncertainty is mainly from the datasets and methods, land use change, grassland management, climate change, etc.

It has been estimated that land soil contains about 8.3 GtN. Both fertilizer nitrogen input and animal population have greatly increased from 1961 to present. Lifestyle and agriculture practices have also changed. These substantially impact the balance of material cycles including carbon and nitrogen. Generally the excess N was partly maintained in farmland, and partly transported to water bodies. Meanwhile, the increase in use of fertilizer and N emissions results in the annual bulk deposition of inorganic N. Atmospheric N deposition ranged from 18.4 to 38.5 kg/hm<sup>2</sup> in the North China Plain. The effects of N deposition on greenhouse gas fluxes depends on ecosystem types, the status of soil available carbon, the rate of N deposition, and its interaction with N turnover in soil. It was estimated that China emitted about 1. TgN of N<sub>2</sub>O, 9.4-10.4 TgN of NH<sub>3</sub>, and 3.4 Tg NO<sub>2</sub>-N to the atmosphere in 2000-2004.

It has been obtained that the continental shelves are a sink for atmospheric CO<sub>2</sub> at mid-high latitudes (-0.33 PgC a<sup>-1</sup>) and a source of CO<sub>2</sub> at low latitudes (0.11 Pg C a<sup>-1</sup>). The Changjiang River estuary sediment may absorb at least about 4.1 Tg of atmospheric CO<sub>2</sub> every year. However, the main stream of the Changjiang Estuary generally emits CO<sub>2</sub>. The outer Changjiang Estuary served as a moderate or significant sink of atmospheric CO<sub>2</sub> in winter, spring and summer, while it turned to a net source in autumn. It was obtained that the carbon fixed by phytoplankton was about 2.22 × 10<sup>8</sup> t a<sup>-1</sup> with a clear seasonal variation in the Bohai Sea, the Yellow Sea and the East China Sea, and that the carbon fixed by phytoplankton was about 4.16 × 10<sup>8</sup> t a<sup>-1</sup> in the South China Sea.

It was obtained that the surface pCO<sub>2</sub> values gradually increased from the continental shelf waters, the Bering Sea shelf slope, to the Bering Abyssal Plain (BAP) and the Canadian Basin. The difference was attributed to the combination of various source waters, biological uptake, and seasonal warming.

Over the last four years, there have been some modeling studies about the ocean carbon cycle and some related work from Chinese scientists. An ocean general circulation model is generally employed to investigate the ocean carbon cycle. Using both North Pacific and global ocean models that have been validated by several different passive tracers, the oceanic uptake of anthropogenic CO<sub>2</sub> was estimated. It was obtained that the global oceanic anthropogenic CO<sub>2</sub> uptake rate was 1.64 and 1.73 Pg C a<sup>-1</sup> for the two cases in the 1990s.

Riverine N input and atmospheric nitrogen deposition probably affect the nitrogen and carbon cycles in the ocean. Besides atmospheric inorganic N deposition, it was found that atmospheric nitrogen deposition to the world's ocean may be important because in remote marine rains organic nitrogen was 62.8% ± 3.3% of the total nitrogen. The distribution of N<sub>2</sub>O in surface seawater has also been discussed along the cruise tracks southward from 30°S–67°S latitude in the Indian Ocean section.

Under elevated atmospheric CO<sub>2</sub> and N addition, primary productivity is generally enhanced. The stimulatory effect of individual elevated CO<sub>2</sub> (about 29% increased) was observed during the experimental period. The positive effect of N addition was found. However, their combined effect on soil respiration (about 50% increased) was also observed. So far their combined effect on NEE in the terrestrial ecosystem needs to be further studied. It was found that soil organic carbon and total nitrogen ratio (C/N) was about 10.8 in paddy fields, higher than 9.9 in upland fields. However, the regional variation of C/N ratio is very large in upland fields.

A two-way coupled model, Atmosphere-Vegetation Interaction Model-Global Ocean-Atmosphere-Land System Model (AVIM-GOALS) has been used to simulate the surface physical fluxes and NPP in the terrestrial ecosystem in both inclusion and exclusion of OGCM. Using the same model with OGCM instead of SST forcing, the simulated results of the interannual variations of the spatial and temporal distributions of the surface air temperatures and precipitation were generally improved. Using the modified AVIM (AVIM2) with a soil carbon module, under the forcing of future climate change, NPP for China will increase continuously to the middle periods of the 21st century, and then will decrease gradually.

#### References:

- Ba, Q. and Xu, Y.F. (2010), Input function and simulated distributions of tritium in the North Pacific, *Sci. China Earth Sci.* 53(3):441-453, doi:10.1007/s11430-010-0004-4
- Bao, X., Watanabe, M., Wang, Q. X., Hayashi, S., and Liu, J. Y. (2006), Nitrogen budgets of agricultural fields of the Changjiang River basin from 1980 to 1990, *Science of the Total Environment*. 363 :136– 148
- Cai, W.J., Dai, M.H., and Wang, Y.C. (2006), Air-sea exchange of carbon dioxide in ocean margins: A province-based synthesis, *Geophys. Res. L.* 33, L12603, doi:10.1029/2006GL026219
- Cai, W.J., Guo, X.H., Chen, C.T.A., Dai, M.H., et al. (2008), A comparative overview of weathering intensity and HCO<sub>3</sub><sup>-</sup> flux in the world's major rivers with emphasis on the Changjiang, Huanghe, Zhujiang(Pearl) and Mississippi Rivers, *Continental Shelf Research*. 28:1528-1549
- Chen, L.Q. and Gao, Z. Y. (2007), Spatial variability in the partial pressures of CO<sub>2</sub> in the northern Bering and Chukchi seas, *Deep-Sea Res. II*. 54:2619-2629
- Chen, P. Q., Wang, X. K., Wang, L. M., et al. (2008), Carbon Budgets of Terrestrial Ecosystems and Countermeasures to Achieve Carbon Sink in China, Science Press. Beijing. 116–117(in Chinese)
- China Wetland Resources Development and Environmental Protection Research Group (1998), Reviewing the history of developing land resources in Sanjiang plain, *Territory Nat. Res. Stud.* 1: 15–19 (in Chinese)
- Chu, M. Xu, Y.F., and Li, Y.C. (2008), Influences of boundary conditions on natural radiocarbon 14C distributions in North Pacific Ocean, *J. Tropical Oceanog.* 27(6):19-27 (In Chinese)
- Dai, M.H., Zhai, W. D., Cai, W.J et al. (2008), Effects of an estuarine plume-associated bloom on the carbonate system in the lower reaches of the Pearl River estuary and the coastal zone of the northern South China Sea, *Continental Shelf Res.* 28:1416-1423
- Dai, W. H. and Huang, Y. (2006), Relation of soil organic matter concentration to climate and altitude in zonal soils of China, *Catena*. 65 : 87 – 94
- Dan, L. and Ji, J. J. (2007), The surface energy, water, carbon flux and their intercorrelated seasonality in a global climate-vegetation coupled model, *Tellus*. 59B: 425–438
- Dan, L., Ji, J. J., and He, Y. (2007), Use of ISLSCP II data to intercompare and

- validate the terrestrial net primary production in a land surface model coupled to a general circulation model, *J. Geophys. Res.* 112, D02S90, doi:10.1029/2006JD007721
- Dang, H.Y., Zhang, X.X., Sun, J., et al. (2008), Diversity and spatial distribution of sediment ammonia-oxidizing crenarchaeota in response to estuarine and environmental gradients in the Changjiang Estuary and East China Sea, *Microbiology*. 154:2084-2095
- Deng, M. H., Xie, Y. X., Xiong, Z. Q., et al. (2007), Nitrogen budgets of the Yangtse delta region and their effect on the environment, *Acta Scientiae Circumstantiae*. 27 (10): 1709 – 1716
- Deng, Q. , Zhou, G., Liu, J., Liu, S., Duan, H., and Zhang, D. (2010), Responses of soil respiration to elevated carbon dioxide and nitrogen addition in young subtropical forest ecosystems in China, *Biogeosciences*. 7 : 315-328
- Dong, Q. M., Zhao, X. Q., Ma, Y. S., et al. (2007), Effect of grazing intensity on soil organic matter and organic carbon in alpine-cold artificial grassland, *Chin Qinghai J. Anim. Vet. Sci.* 37: 6–8 (in Chinese)
- Du, Q. L. (2006), Strategy for Sustainable Development of Grassland Production in China. China Agriculture Press. Beijing. (in Chinese)
- Fan, J. L., Hu, Z.Y., Wang, T. J., Zhou, J., Wu, C. Y. H., and Xia, X. (2009), Atmospheric inorganic nitrogen deposition to a typical red soil forestland in southeastern China, *Environ Monit Assess*. 159:241–253
- Fang, J. Y., Chen, A. P., Peng, C. H., et al. (2001), Changes in forest biomass carbon storage in China between 1949 and 1998, *Science*.292:2320–2322
- Fang, J. Y., Guo, Z. D., Piao, S. L.& Chen, A. P. (2007), Terrestrial vegetation carbon sinks in China, 1981–2000, *Sci. China Ser. D* 50, 1341–1350.
- Gu, B. J., Chang, J., Ge, Y., Ge, H. L., Yuan, C., Peng, C. H., and Jiang, H. (2009), Anthropogenic modification of the nitrogen cycling within the Greater Hangzhou Area system, China
- Gu, Q. Z., Yang, X. Y., Sun, B. H., et al.(2004), Effects of long-term fertilization and irrigation on soil nutrient distribution in profile of Loess soil, *Chin. Agric. Sci. Bull.* 20: 139– 142(in Chinese)
- Guo R. P., Lin Z. L., Moa X. G., and Yang C. L. (2010), Responses of crop yield and water use efficiency to climate change in the North China Plain, *Agricultural Water Management*. 97:1185–1194
- Guo, X.H., Cai, W. J., Zhai, W. D., et al. (2008), Seasonal variations in the inorganic carbon system in the Pearl River (Zhujiang) estuary, *Continental Shelf Res.* 28:1424-1434
- He, B.Y., Dai, M.H., Zhai, W.D., et al. (2010). Distribution, degradation and dynamics of dissolved organic carbon and its major compound classes in the Pearl River estuary, China, *Marine Chemistry*. 119:52-64
- He, N. P., Yu, Q., Wu, L., et al.(2008), Carbon and nitrogen store and storage potential as affected by land-use in a *Leymus chinensis* grassland of northern China, *Soil Biol. Biochem.* 40: 2952–2959
- Huang, B.Q., Hu, J., Xu, H.Z., Gao, Z.R., Wang, D.X. (2010), Phytoplankton community at warm eddies in the northern South China Sea in winter 2003/2004,

Deep-Sea Res.II. ????

- Huang, C. D, Zhang, J., Yang, W. Q., et al. (2009), Soil organic carbon density in plantations of hilly region in the western Sichuan, J Zhejiang Forest Sic. Tech.. 29: 5–8 (in Chinese)
- Huang, M., Ji, J. J., Li, K. R., Liu Y. F., and Yang F. T. (2007), The ecosystem carbon accumulation after conversion of grasslands to pine plantations in subtropical red soil of South China, *Tellus*. 59B: 439–448
- Huang, Y. and Sun, W. J. (2006), Changes in topsoil organic carbon of croplands in mainland China over the last two decades, *Chin. Sci. Bull.* 51:1785–1803
- Huang, Y., Sun, W. J., Zhang, W., and Yu Y. Q., (2010a), Changes in soil organic carbon of terrestrial ecosystems in China: A mini-review, *Science China Life Sciences*. 53(7):766–775
- Huang, Y., Sun, W. J., Zhang, W., Yu, Y. Q., Su, Y. H. and Song, C. C., (2010b), Marshland conversion to cropland in northeast China from 1950 to 2000 reduced the greenhouse effect, *Global Change Biology*, 16:680–695
- Huang, Y. and Tang, Y. H. (2010), An estimate of greenhouse gas (N<sub>2</sub>O and CO<sub>2</sub>) mitigation potential under various scenarios of nitrogen use efficiency in Chinese croplands, *Global Change Biology*.. doi: 10.1111/j.1365-2486.2010.02187.x
- Huang, Y., Yu, Y. Q., Zhang, W., et al. (2009), Agro-C: A biogeophysical model for simulating the carbon budget of agroecosystems, *Agric For Meteorol.* 149: 106–129
- Huang, Y., Zhang, W., Sun, W. J., et al. (2007), Net primary production of Chinese croplands from 1950 to 1999, *Ecol .Appl.* 17: 692–701
- Huang, Y., Zhou, G. S., Wu, J. S., et al. (2008), Modelling Carbon Budgets of Terrestrial Ecosystems in China. Science Press. Beijing. PP.143–211(in Chinese)
- IPCC. (2006), 2006 IPCC Guidelines for National Greenhouse Gas Inventories. Prepared by the National Greenhouse Gas Inventories Programme. IGES, Japan
- Ji, J. J., Huang, M., Li, K. R. (2008), Prediction of carbon exchanges between China terrestrial ecosystem and atmosphere in 21st century, *Sci. China Ser D-Earth Sci.* 51: 885-898
- Jia, H. T, Jiang, P. A., Zhao, C. Y., et al. (2009) The influence of enclosing life on carbon distribution of grassland ecosystem, *Agric. Res. Arid Areas*. 27: 33–36(in Chinese).
- Ju, X.T., Kou .C.L., Zhang, F.S., and Christie, P. (2006), Nitrogen balance and groundwater nitrate contamination: Comparison among three intensive cropping systems on the North China Plain, *Environmental Pollution*. 143: 117-125
- Li, X.G., Song, J.M., and Yuan, H. M. (2006), Inorganic carbon of sediments in the Yangtze River Estuary and Jiaozhou Bay, *Biogeochemistry*. 77:11-197, doi: 10.1007/s10533-005-0543-5
- Li Y.C., Xu Y.F., Zhao L., and Wang M.X. (2006) Preliminary study of the simulated distribution of CFC-11 in the global ocean circulation model, *Chinese J. Atmos. Sci.* 30(4):671-681 (in Chinese)
- Li Y. C., Xu Y.F., Zhao L., and Wang M.X. (2007) Sensitivity of CFC-11 uptake in a global ocean model to subgrid-scale mixing parameterizations, *Acta Oceanolog.*

- Sinica. 29(3):31-38 (in Chinese)
- Liu, J. Y., Wang, S. Q., Chen, J. M., et al.(2004), Storages of soil organic carbon and nitrogen and land use changes in China: 1990~2000, *Acta Geographica. Sinica.* 59: 483–496 (in Chinese)
- Liu, S., Li T., Wang, G.F., Cao, W.X., Song, X.Y., Zhang J.L., Yin, J.Q., and Huang, L.M. (2010), Evaluation of cycle and effect of phosphorus in plankton ecosystem in the waters of the Pearl River Estuary, *J. Tropical Oceanogr.* 29(1):42-45 (in Chinese)
- Lu, F., Wang, X., Han, B., et al. (2009), Soil carbon sequestrations by nitrogen fertilizer application, straw return and no-tillage in China's cropland, *Glob. Change Biol.* 15: 281–305
- Mao, J.F., Dan, L., Wang, B., and Dai Y. J. (2010), Simulation and Evaluation of Terrestrial Ecosystem NPP with M-SDGVM over Continental China, *ADVANCES IN ATMOSPHERIC SCIENCES.* 27( 2): 427–442
- National Bureau of Statistics of China (2009), The past 60-year (1949-2009) in China. China Statistics Press. Beijing. (in Chinese)
- Niu S. L., Wu M. Y., Wu Y. H., Xia J. Y., Li L. H., and Wan S. Q. (2008), Water-mediated responses of ecosystem carbon fluxes to climatic change in a temperate steppe, *New Phytologist.* 177: 209–219
- Niu, S. L., Wu, M. Y., Han, Y., Xia, J. Y., Zhang, Z., Yang, H. J., and Wan, S.Q. (2010), Nitrogen effects on net ecosystem carbon exchange in a temperate steppe, *Global Change Biology.* 16:144–155
- Pan, G. X., Wu, L. S., Li, L. Q., et al.(2008), Organic carbon stratification and size distribution of three typical paddy soils from Taihu Lake region,China, *J. Environ. Sci.* 20: 456–463
- Pan, G. X., Xu, X. W., Smith, P., et al. (2010), An increase in topsoil SOC stock of China's croplands between 1985 and 2006 revealed by soil monitoring, *Agric. Ecosyst. Environ.* 136: 133–138
- Pei, S., Fu, H., Wan, C. (2008), Changes in soil properties and vegetation following exclosure and grazing in degraded Alxa desert steppe of Inner Mongolia, China, *Agric. Ecosyst Environ.* 124: 33–39
- Peng, C. H., Zhou X. L., Zhao S. Q., Wang X. P., Zhu B., Piao S. L., Fang J. Y. (2009), Quantifying the response of forest carbon balance to future climate change in Northeastern China: Model validation and prediction, *Global and Planetary Change.* 66 : 179–194
- Piao, S. L., Fang, J. Y., Ciais P., et al. (2009), The carbon balance of terrestrial ecosystems in China, *Nature.* 458: 1009–1013
- Qiu, Y., Gan, Y. M., Wang, Q., et al.(2007), Preliminary study on classified index system of grazing alpine meadow in northwest Sichuan, *Hubei Agric. Sci.*, 2007, 46: 723–726 (in Chinese)
- State Environmental Protection Administration (2007), 2006 Report on the State Environment in China, Beijing. 82–89 (in Chinese)
- State Environmental Protection Administration (2009), 2008 Report on the State

- Environment in China, Beijing. 54–56 (in Chinese)
- Shi, F., Li, Y. E., Gao, Q. Z., et al. (2009), Effects of managements on soil organic carbon of grassland in China, *Pratacultural Sci.* 26(3): 9–15(in Chinese)
- Shi, J.H., Gao, H.W., and Zhang, J. (2006), Atmospheric Organic Nitrogen Deposition and Significance in Marine Ecosystem, *Advances in Earth Science*. 21(7):721-729 (In Chinese)
- Song, J.M., Li, X.G., Yuan H.M., Zheng, G.X., Yang, Y.F. (2008), Carbon fixed by phytoplankton and cultured algae in China coastal seas, *Acta Ecologica Sinica*. 28(2):551-558 (in Chinese)
- Sun, W. J., Huang. Y., Zhang. W., and Yu, Y. Q. (2010), Carbon sequestration and its potential in agricultural soils of China, *Global Biogeochem. Cycles*, 24, GB3001, doi:10.1029/2009GB003484.
- Sun, Z. G., and Liu, J. S. (2007), Nitrogen cycling of atmosphere-plant-soil system in the typical *Calamagrostis angustifolia* wetland in the Sanjiang Plain, Northeast China, *J. Environmental Sciences*. 19:986–995
- Tao, F., Yokozawa, M., and Zhang, Z. (2009a), Modelling the impacts of weather and climate variability on crop productivity over a large area: a new process-based model development, optimization, and uncertainties analysis. *Agric. For. Meteorol.* 149: 831–850
- Tao, F. L., Zhang, Z., Liu, J. Y., and Yokozawa, M. (2009b), Modelling the impacts of weather and climate variability on crop productivity over a large area: A new super-ensemble-based probabilistic projection, *Global and Planetary Change*. 66 : 179–194
- Tian, H., S. Wang, J. Liu, S. Pan, H. Chen, C. Zhang, and X. Shi (2006), Patterns of soil nitrogen storage in China, *Global Biogeochem. Cycles*. 20, GB1001, doi:10.1029/2005GB002464.
- Wang, Q. L., Cao, G. M., Wang, C. T. (2007), The impact of grazing on the activities of soil enzymes and soil environmental factors in alpine *Kobresia pygmaea* meadow, *Plant Nutr. Fert. Sci.* 13:856–864(in Chinese)
- Wang, S., Chen, J. M., Ju, W. M., et al. (2007), Carbon sinks and sources in China's forests during 1901- 2001, *J Environ Manage*. 85: 524–537
- Wang, Z.H., Qi, Y.Z., Chen, J. F., Xu, N., Yang, Y.F. (2006), Phytoplankton abundance, community structure and nutrients in cultural areas of Daya Bay, South China Sea, *J. Marine Sys.* 62:85-94
- Wang, Z.H., Zhao, J.G., Zhang, Y. J., Gao, Y. (2009), Phytoplankton community structure and environmental parameters in aquaculture areas of Daya Bay, South China Sea, *J. Envirom. Sci.* 21:1268-1275
- Wolf, B., Zheng, X.H., Bruggemann, N., Chen, W.W., Dannenmann, M., Han, X.G., Sutton, M. A., Wu, H.H., Yao, Z.S., and Butterbach-Bahl, K. (2010), Grazing-induced reduction of natural nitrous oxide release from continental steppe, *Nature*. 464: doi:10.1038/nature08931
- Wu, S. H., Yin, Y. H., Zhao, D. S., Huang, M., Shao, X. M., and Dai, E. F. (2010), Impact of future climate change on terrestrial ecosystems in China, *Int. J. Climatol.* 30: 866–873
- Xia, J. Y., Niu, S. L., and Wan, S. Q. (2009), Response of ecosystem carbon exchange

- to warming and nitrogen addition during two hydrologically contrasting growing seasons in a temperate steppe, *Global Change Biology*. 15: 1544–1556
- Xia, J. Y. and Wan, S. Q. (2008), Global response patterns of terrestrial plant species to nitrogen addition, *New Phytologist*. **179**: 428–439
- Xie, J. S., Yang, Y. S., Chen, G. S., et al. (2008), Effect of vegetation restoration on water stability and organic carbon distribution in aggregates of degrade red soil in subtropics in China, *Acta Ecolo. Sinica*. 28: 702–709(in Chinese)
- Xie, Z. B., Zhu, J. G., Liu, G., et al. (2007), Soil organic carbon stocks in China and changes from 1980s to 2000s, *Glob. Change Biol.*. 13: 1989–2007
- Xiong, Z. Q., Freney, J. R., Mosier, A. R., Zhu, Z. L., Lee, Y., Yagi, K. (2008), Impacts of population growth, changing food preferences and agricultural practices on the nitrogen cycle in East Asia, *Nutr Cycl Agroecosyst.* 80:189–198
- Xu, Q., Rui, W. Y., Liu, J. L., Liu, Z., Yang L., Yin, Y. J., and Zhang, W. J. (2006) , Spatial Variation of Coupling Characteristics of Soil Carbon and Nitrogen in Farmland of China, *Journal of Ecology and Rural Environmen*. 22(3): 57—60 (in Chinese)
- Xu, W. H. and Wan, S. Q. (2008), Water- and plant-mediated responses of soil respiration to topography, fire, and nitrogen fertilization in a semiarid grassland in northern China, *Soil Biology & Biochemistry*. 40: 679–687
- Xu, X. K., Han, L., Wang, Y.S., and Inubushi, K. (2007), Influence of vegetation types and soil properties on microbial biomass carbon and metabolic quotients in temperate volcanic and tropical forest soils, *Soil Science and Plant Nutrition*. 53: 430-440.
- Xu, X. K., Han, L., Luo, X. B., Liu, Z. R., and Han, S. J. (2009), Effects of nitrogen addition on dissolved N<sub>2</sub>O and CO<sub>2</sub>, dissolved organic matter, and inorganic nitrogen in soil solution under a temperate old-growth forest, *Geoderma*. 151: 370-377.
- Xu, X. K., Inubushi, K., and Sakamoto, K. (2006), Effect of vegetations and temperature on microbial biomass carbon and metabolic quotients of temperate volcanic forest soils, *Geoderma*. 136: 310-319.
- Xu, X. and Inubushi, K. (2007), Effects of nitrogen sources and glucose on the consumption of ethylene and methane by temperate volcanic forest surface soils, *Chinese Science Bulletin*. 52(23): 3281-3291
- Xu, X., Yuan, B., and Wei, J. (2008), Vertical distribution and interaction of ethylene and methane in temperate volcanic forest soils, *Geoderma*. 145: 231-237
- Xu, Y.F., Aoki, S., and Harada, K. (2006), Sensitivity of the simulated distributions of water masses, CFCs, and Bomb <sup>14</sup>C to parameterizations of mesoscale tracer transports in a model of the North Pacific, *J. Phys. Oceanogr.* 36:273-285
- Xu, Y.F., Aoki, S., and Harada, K. (2009), Identification of CO<sub>2</sub> disposal locations in an ocean general circulation model of the North Pacific, *Acta Oceanolog. Sinica*. 28:15-34
- Xu, Y.F. and Li, Y.C. (2009), Estimates of anthropogenic CO<sub>2</sub> uptake in a global ocean model, *Adv. in Atmos. Sci.* 26(2):265-274
- Xu, Y.F., Zhao, L., and Li, Y.C. (2007), Numerical simulations of uptake of

- anthropogenic CO<sub>2</sub> in the North Pacific, *Chinese J. Geophys.* 50(2):404-411 (in Chinese)
- Xu, Y.F., Zhao, L., Pu, Y.F., and Li, Y.C. (2004), Uncertainties in the estimate of the air-sea exchange flux of carbon dioxide, *Earth Sci. Front.* 11(2):565-571 (in Chinese)
- Xue, B., Hu, X. L., Liu, J., et al. (2008) Influence of enclosure on soil fertility and vegetation character in the degenerative meadow. *J. Inner Mongolia Forest Sci. Tech.* 34: 18–21(in Chinese)
- Yang, Y. H., Fang, J. Y., Smith, P., et al. (2009), Changes in topsoil carbon stock in the Tibetan grasslands between the 1980s and 2004, *Glob. Change Biol.* 15: 2723–2729
- Yang, Y. H., Fang, J. Y., Ma, W. H., et al. (2010), Soil carbon stock and its changes in northern China's grasslands from 1980s to 2000s, *Glob. Change Biol.* doi: 10.1111/j.1365-2486.2009.02123.x
- Yu, Y., Guo, Z., Wu, H., et al.(2009), Spatial changes in soil organic carbon density and storage of cultivated soils in China from 1980 to 2000, *Glob. Biogeochem. Cy.* 23, GB2021, doi:10.1029/2008GB003428
- Zhai, W.D., Dai, M.H., and Guo, X.H. (2007), Carbonate system and CO<sub>2</sub> degassing fluxes in the inner estuary of Changjiang (Yangtze) River, China, *Marine Chemistry*. 107:342-356
- Zhai, W.D. and Dai, M.H. (2009), On the seasonal variation of air-sea CO<sub>2</sub> fluxes in the outer Changjiang (Yangtze River) Estuary, East China Sea, *Marine Chemistry*. 117:2-10
- Zhan, L.Y. and Chen, L.Q.(2006), A Review of the Study on NitrousOxide Cycle in the Oceans, *Advances in Earth Science*. 21(3):269-277 (In Chinese)
- Zhan, L.Y. and Chen, L.Q. (2009), Distributions of N<sub>2</sub>O and its air-sea fluxes in seawater along cruise tracks between 30 °S-67 °S and in Prydz Bay, Antarctica, *J. Geophys. Res.* 114, C03019, doi:10.1029/2007JC004406
- Zhang, G. B., Tian, D. L, Fang, X., et al.(2008), Distribution characteristics of soil organic carbon in Huitong as affected by different afforestation models for conversion of cropland to forestland, *J. Central South U Forest Tech.* 28: 8–12(in Chinese)
- Zhang, Y., Liu, X. J., Zhang, F. S., Ju, X. T., Zou G. Y., and Hu, K. L. (2006), Spatial and temporal variation of atmospheric nitrogen deposition in the North China Plain, *Acta Ecologica Sinica*. 26(6):1633–1639.
- Zhao, Q. and Lu, X.Q. (2008), Parameter estimation in a three-dimensional marine ecosystem model using the adjoint technique, *J. Marine Sys.* 74:443-452
- Zhi, H., Wang, P. X., Dan, L., Yu, Y. Q., Xu, Y. F., and Zheng W. P. (2009a), Climate-Vegetation Interannual Variability in a Coupled Atmosphere-Ocean-Land Model, *Advances in Atmospheric Sciences*. 26(3): 599–612
- Zhi, H., Wang, P. X., Yu Y. Q., Dan L., Xu Y. F., and Zheng W. P. (2009b), Simulation of Influence of Indian Ocean Sea Surface Temperature Anomaly on the Net Primary Production in South Asia, *Chinese Journal of Atmospheric*

- Sciences. 33 (5): 936–949(in Chinese).
- Zhou, G. Y., Liu, S. G., Li, Z. A., et al. (2006), Old-growth forests can accumulate carbon in soils, *Science*. 314: 1417
- Zhou, Z.X., Zheng, X.H., Xie, B.H., Han, S.H., and Liu C.Y. (2010), A Process-based Model of N<sub>2</sub>O Emission from a Rice-Winter Wheat Rotation Agro-Ecosystem: Structure, Validation and Sensitivity, *ADVANCES IN ATMOSPHERIC SCIENCES*. 27: 137–150
- Zou, C., Wang, K., Wang, T., et al. (2007), Overgrazing and soil carbon dynamics in eastern Inner Mongolia of China, *Ecol. Res.* 22: 135–142
- Zou, J.W., Huang, Y., Qin, Y.M., Liu, S.W, Shen, Q.R., Pan, G.X., Lu, Y.Y, and Liu, Q.H. (2009), Changes in fertilizer-induced direct N<sub>2</sub>O emissions from paddy fields during rice-growing season in China between 1950s and 1990s, *Global Change Biology*. 15: 229–242
- Zou J.W., Lu, Y.Y., and Huang, Y. (2010), Estimates of synthetic fertilizer N-induced direct nitrous oxide emission from Chinese croplands during 1980–2000, *Environmental Pollution*. 158: 631–635

# A Review of Atmospheric Chemistry Research in China: Photochemical Pollution, Haze, and Climate Change

MA Jianzhong<sup>1\*</sup> (马建中), XU Xiaobin<sup>1</sup> (徐晓斌), ZHAO Chunsheng<sup>2</sup> (赵春生), and  
YAN Peng<sup>1</sup> (颜鹏)

<sup>1</sup> Key Laboratory for Atmospheric Chemistry, Chinese Academy of Meteorological  
Sciences, Beijing 100081

<sup>2</sup> Department of Atmospheric Sciences, School of Physics, Peking University, Beijing  
100871

## ABSTRACT

In this paper we present a review of atmospheric chemistry research in China over the period 2006-2010 focusing on ozone chemistry, aerosol chemistry, interactions between gases and aerosols, and atmospheric chemistry and climate change. China has concurrently suffered photochemical smog, haze pollution, and climate changes over the past decade, especially in the areas of North China, the Yangtze River Delta, and the Pear River Delta. Much scientific work on atmospheric chemistry and associated research has been done to address such environmental problem. Intensive field experiments, satellite data analyses, and model simulations have shown that air pollution is changing the chemical and physical characters of the natural atmosphere over China significantly, which can exert strong anthropogenic radiative forcing and thus may have large impacts on regional and global climate.

**Key words:** ozone, aerosols, air pollution, climate change, China

## 1. Introduction

Atmospheric chemistry is a scientific discipline that studies the chemical composition and their physic-chemical processes in the natural atmosphere, the way gases, liquids, and solids in the atmosphere interact with each other and with the earth's surface and associated ecosystems, and how human activities may be changing the chemical and physical characteristics of the atmosphere (e.g., Seinfeld and Pandis, 1998; Warneck, 2000). Atmospheric chemistry is an inter-discipline which can be considered a sub-branch of either Atmospheric Sciences or Environmental Sciences. There are a number of critical environmental issues associated with a changing atmosphere, from photochemical smog, acidic deposition, toxic air pollutants, and stratospheric ozone depletion, which have been well-known by the end of last century, to haze pollution and global climate change, to which considerable scientific attention has been paid since the beginning of this century (IPCC, 2007; UNEP and C<sup>4</sup>, 2002). Much of the anthropogenic impact on the atmosphere is associated with our increasing use of fossil fuels and biomass burning as an energy source. To understand and hopefully solve these problems, a great deal of research has been/is being done around the world, and correspondingly Atmospheric Chemistry

---

\* E-mail:: mjz@cams.cma.gov.cn

has become one of the most fast-developing and active subjects of Earth Sciences over the past decades.

Being the world's largest and fastest developing country in economy, China also faces greater environmental challenges. In China, coal burning supplies about 70% of the energy consumed, and the carbonaceous aerosols and sulfur dioxide ( $\text{SO}_2$ ) from the associated exhausts constitute the primary pollutants in most areas (Yearbook, 2007). While the  $\text{SO}_2$  mixing ratio stays at high levels, the concentrations of nitrogen oxides ( $\text{NO}_x \equiv \text{NO} + \text{NO}_2$ ) have increased significantly in many areas. While air quality in cities and acid rain still remain the environmental issues (Shao et al., 2006; Tang et al., 2010), regional pollution related to photochemical smog and haze-fog has been recognized as one of the severe environmental problems in China (Zhang et al., 2008b). The most serious pollution regions are the North China (called Huabei in Chinese) region (NC) with the Beijing and Tianjin megacities included, the Yangtze River Delta region (YRD) with the Shanghai megacity included, and the Pear River Delta region (PRD) with Guangzhou and Hong Kong megacities included. Such air pollution not only has adverse effects on human health and the ecosystems, but also may have large impacts on weather and climate in urban and regional scales.

In this paper, we present a review of atmospheric chemistry research in China over the last four years, from 2006 to 2010. Our foci are photochemistry, gas-to-particle conversion, and the linkages of atmospheric chemistry to climate change. For the other studies of atmospheric chemistry in China, the reader is referred to Wang et al. (this issue) for atmospheric environment, Lü et al. (this issue) for aerosol-cloud interactions, Bian et al. (this issue) for stratospheric chemistry, and Xu et al. (this issue) for biogeochemical cycles. The contents of this paper include ozone chemistry (Section 2), aerosol chemistry (Section 3), interactions between gases and aerosols (Section 4), and atmospheric chemistry and climate change (Section 5). Conclusions and remarks are presented in Section 6.

## **2. Ozone chemistry**

### **2.1 Urban ozone pollution**

#### *2.1.1 Seasonal variation and trend analyses*

Table 1 summarizes the levels of ozone and its precursors measured in Beijing during summertime of different years. Observations at six urban sites in Beijing showed that over the 2001–2006 period average concentrations of  $\text{NO}_x$  ( $\text{NO}_x = \text{NO} + \text{NO}_2$ ) and  $\text{O}_3$  for July–September were  $49.2 \pm 5.9$  ppbv and  $26.6 \pm 2.8$  ppbv, respectively. While  $\text{NO}_x$  concentration decreased linearly at a rate of  $3.9 \pm 0.5$  ppbv/yr after 2002, ozone concentration increased at a rate of  $1.1 \pm 0.5$  ppbv/yr during 2001–2006 (Tang et al., 2009a). In contrary, analyses of satellite data from GOME (Global Ozone Monitoring Experiment) and SCIAMACHY (Scanning Imaging Absorption Spectrometer for Atmospheric Chartography) showed that tropospheric  $\text{NO}_2$  vertical column density (VCD) over all the Chinese megacities including Beijing increased significantly over this period (Zhang et al., 2007a). The seasonal variation pattern of tropospheric  $\text{NO}_2$  VCD by GOME satellite was shown to be in good agreement with that of surface  $\text{NO}_2$  concentration in Beijing (Jiang et al., 2006).

Measurements of ozone and its precursors from June 2006 to June 2007 in urban

Shanghai showed a spring maximum of ozone, winter peaks of  $\text{NO}_x$  and CO, and no apparent seasonal variation of volatile organic compounds (VOCs) (Ran et al., 2009). Ground measurements of tropospheric  $\text{NO}_2$  VCD by DOAS (different optical absorption spectrometer) in Shanghai showed that the satellite observations failed to reproduce the high  $\text{NO}_2$  amounts over the polluted experimental site (Chen et al., 2009b). It was suggested that in order to further validate the satellite measurements, extension of ground-based zenith-sky DOAS measurements is demanded to cover areas with different pollution levels within the whole satellite footprint (Chen et al., 2009b).

### 2.1.2 Chemical character and mechanism investigations

Observational analyses and model simulations revealed that the formation of ozone is limited by volatile organic compounds (VOCs) in the urban areas of Beijing, being more sensitive to  $\text{NO}_x$  levels in the suburban and more remote areas (Wang et al., 2009h; Xu et al., 2008a). Ambient concentrations of on-methane hydrocarbons (NMHCs) and oxygenated VOCs (OVOCs) and their contributions to ozone formation in Beijing were investigated by numerous studies (e.g., Liu et al., 2009d; Shao et al., 2009; Song et al., 2007; Yuan et al., 2010). It was showed that OVOCs accounted for 37%-54% of the VOC (NMHCs + OVOC) mixing ratio and the main reactive VOC compounds were aldehydes and alkenes (Shao et al., 2009). Measurements of methacrolein (MACR) and methyl vinyl ketone (MVK), the two specific products from isoprene oxidation in the atmosphere, were performed in Beijing (Pang et al., 2009; Xie et al., 2008), and the reacted isoprene was estimated to account 6–30% of the photochemically produced ozone (Pang et al., 2009). In addition to  $\text{SO}_2$ ,  $\text{NO}_x$ , and  $\text{O}_3$ , the vertical distributions of VOCs were measured in the lower boundary layer of Beijing, providing valuable data for studying the effects of meteorological and photochemical processes on urban ozone (Mao et al., 2008; Meng et al., 2008; Sun et al., 2010c).

Similarly, both model and measurement results indicated that ozone formation is clearly under VOC-sensitive regime in the city of Shanghai, and aromatics play a dominated role in the ozone production, in spite of a lower contribution to the total VOC concentrations (Geng et al., 2007; Geng et al., 2008; Ran et al., 2009). Interestingly, the ozone ‘weekend effect’ was found at the Xujiahui district of Shanghai, with ozone concentrations being higher at weekends than those on weekdays (Tang et al., 2008). Such phenomenon of ozone weekend effect was also observed at an urban site in the Jinan city of eastern China (Shan et al., 2008). Studies showed that biomass burning could have large impacts on air quality in the cities, e.g., Beijing and Guangzhou (Li et al., 2008c; Wang et al., 2007a). It was argued that the enhanced aerosol concentrations from the Southeast Asia biomass burning results in a reduction of UV intensity, and thus decreases the formation of ozone in Guangzhou (Deng et al., 2008b).

Changes in concentrations of HONO, HCHO,  $\text{O}_3$ , and  $\text{NO}_2$  were observed for an autumn period when the strong cold front was passing through Beijing (An et al., 2009). Nighttime mean HONO concentration and daily-mean HCHO and  $\text{NO}_2$  concentrations ranged 0.95-4.9 ppbv, 3.6-9.8 ppbv, and 9.5-49.3 ppbv, respectively

(An et al., 2009). The contributions from the photolysis of HONO, HCHO, and O<sub>3</sub> to the overall daily HO<sub>x</sub> production were estimated to range 56-83%, 11-36%, and 6-9%, respectively (An et al., 2009). An observational study of HNO<sub>2</sub> and NO<sub>2</sub> was also performed in Shanghai during a fall-winter period (Hao et al., 2006). Mean hourly concentrations of HNO<sub>2</sub> and NO<sub>2</sub> during this period were 1.1 ppbv and 24 ppbv, respectively (Hao et al., 2006). The temporal behavior of HONO and NO<sub>2</sub> at an urban site of Guangzhou during summertime was investigated, and high HONO mixing ratios up to 2 ppb were observed during daytime (Qin et al., 2009). A nocturnal maximum concentration of about 8.4 ppbv was detected at night, and the HONO to NO<sub>2</sub> concentration ratio ranged from 0.03 to 0.37, significantly higher than previously reported values (Qin et al., 2009). It was suggested that heterogeneous reactions of NO<sub>2</sub> on aerosol surface could be a key source of HONO and the effect of relative humidity may also play a non-negligible role (An et al., 2009; Hao et al., 2006; Qin et al., 2009).

### 2.1.3 Emission restriction effect studies

Long-range transport may have large impacts on the distribution of ozone and its precursors over urban areas (An et al., 2007; Chen et al., 2009d; Wang et al., 2009h). The ozone pollution in Beijing showed a significant spatial distribution with strong regional contribution (Wang et al., 2009h). The effects of pollutant emission restrictions implemented during the Beijing Olympic Games 2008 on air quality in Beijing and surrounding areas were investigated by numerous studies. Sharp reductions in the concentrations of ozone precursors and aerosols with comparison to no emission control periods were observed at the urban sites (Liu et al., 2009a; Wang et al., 2009e; Wang and Xie, 2009; Xin et al., 2010; Zhang et al., 2009), at the rural sites (Wang et al., 2009i; Xin et al., 2010; Zhang et al., 2009), and by satellite (Yu et al., 2010). The reduction in daily air pollutants emissions in Beijing were quantified with 47% and 57% reduction of NO<sub>x</sub> and NMVOC in August than in June 2008 (Wang et al., 2010b). Daytime ozone concentrations were observed to decrease up to ~15 ppbv in the surrounding areas including a rural site far beyond the Beijing urban area (Wang et al., 2009i; Xin et al., 2010). In the urban Beijing, the reduction of ozone was smaller (Xin et al., 2010; Zhang et al., 2009), and an increase in ozone was even reported for some control stages (Wang and Xie, 2009; Zhang et al., 2009). It should be noted that the different diurnal variation patterns of urban street ozone for summer time in Beijing were present (Chen et al., 2009c; Wang and Xie, 2009).

## 2.2 Regional ozone pollution

### 2.2.1 Seasonal variation and trend analyses

The seasonal variation of ozone in eastern China is influenced by both Asian summer monsoon and regional photochemical pollution (Lin et al., 2008; Lin et al., 2009; Meng et al., 2009; Wang et al., 2006a; Xu et al., 2008b). Table 2 summarizes the levels of ozone and other trace gases observed in non-urban areas of NC, YRD, and PRD. At Shangdianzi, a regional Global Atmosphere Watch (GAW) station in NC, both monthly mean values of ozone daily-average and that of ozone daily-peak occurred in June and September (Lin et al., 2008; Meng et al., 2009). Interestingly, while the NO<sub>x</sub> levels were still higher in spring than in summer, ozone showed the smallest diurnal variation in spring due to its largest concentrations at night (Meng et al., 2009). This indicates that the long-range transport of ozone, probably from the

stratosphere, makes a great contribution to the background ozone in NC during springtime.

The highest mixing ratios of ozone were observed in May in YRD (Wang et al., 2006a; Xu et al., 2008b). Long-term observations of surface ozone at Lin'an, a regional GAW station in YRD, during the periods between August 1991 and July 2006 showed an increasing trend of daytime values and a decreasing trend of nighttime values (Xu et al., 2008b). Such phenomena were most likely caused by the increase of  $\text{NO}_x$  concentration in YRD, which tended to enhance the ozone production during daytime and the ozone titration at night (Xu et al., 2008b). There are also distinct seasonal and diurnal cycles in ground-level ozone across the PRD region. Lower ozone concentrations were generally observed in summer, while high  $\text{O}_3$  levels were typically found in autumn (Zheng et al., 2010). Long-term measurement of surface ozone has been made at a coastal site in Hong Kong, which is strongly influenced by the outflow of Asian continental air during the winter and the inflow of maritime air from the subtropics in the summer. An increasing trend of 0.58 ppbv/yr was obtained from the data for 1994-2007 and this significant trend is most likely due to the increased emissions of ozone precursors in the upwind coastal regions of mainland China (Wang et al., 2009f). Long-term trends of yearly and seasonal averages of tropospheric ozone over the whole country and some regions of China were analyzed, based on the tropospheric ozone residue (TOR) data retrieved from satellite measurements (Xu and Lin, 2010). Significant increasing trends of TOR were found over the North China Plain for all seasons except winter, with a maximum rate of 1.10 DU per decade for summer. There were significant correlations between TOR and SOI for some Chinese regions but not for the North China Plain, suggesting that the observed increasing trend of TOR over the North China Plain may not be linked with changes in atmospheric circulations (Xu and Lin, 2010).

### 2.2.2 Pollution episode studies

Aircraft measurements in the planetary boundary layer of YRD in the fall demonstrated a large difference in the concentrations of ozone and its precursors between suburban and rural regions (Geng et al., 2009). In contrary to previous studies, the ozone chemical formation was suggested to be under a strong VOC-limited regime in the YRD region (Geng et al., 2009). Aircraft measurements showed severe ozone pollution over PRD in the fall, and in some episodes  $\text{NO}_x$  and ozone concentrations reached up to 160ppbv and 100 ppbv, respectively (Wang et al., 2008c). A high pollution level at the top of boundary layer was found under certain meteorological conditions (Wang et al., 2008c).

The sea-land circulation plays an important role on the regional ozone formation and distribution over PRD (Jiang et al., 2008; Xu et al., 2008b). During an autumn period, an intensive field measurement study was conducted simultaneously at the two non-urban sites within the inland PRD region and in Hong Kong, respectively (Guo et al., 2009). Although higher  $\text{NO}_x$  were observed at the Hong Kong site ( $45 \pm 2$  ppbv) than at the PRD site ( $31 \pm 2$  ppbv), ozone diurnal variations showed higher nighttime levels at the Hong Kong site (Guo et al., 2009), indicating the influence of long-transport on the background ozone level in Western Hong Kong. High levels of ozone and other pollutants in Hong Kong could be caused by regional transport from

the upwind PRD area, and it was estimated that the influence of regional transport could contribute 50–90% of surface ozone at nighttime and 40–70% at daytime (Wang et al., 2006b).

### 2.2.3 Chemical character investigations

A typical feature of the urban and regional photochemical pollution was observed during the Regional Integrated Experiments on Air Quality over Pearl River Delta 2004 (PRIDE-PRD2004) (Zhang et al., 2008b). The average O<sub>3</sub> concentration was ~73 ppbv in the northeast area of PRD (upwind) and increased to ~87 ppbv in the southern area of PRD (downwind). For the total oxidant O<sub>x</sub> (O<sub>3</sub>+NO<sub>2</sub>), an even more clearly increasing trend was found, from ~79 ppbv in the upwind area, to ~92 ppbv in the urban area, and further to ~116 ppbv in the downwind area (Zhang et al., 2008b; Zhang et al., 2008c). The monthly mean values of O<sub>3</sub> and O<sub>x</sub> at the two stations of NC (Shangdianzi (Lin et al., 2008) and Guocheng (Lin et al., 2009)), which are located in the northeast and southwest of Beijing, respectively, do not show such clear up-to-down wind trend feature.

Ozone production efficiency (OPE) is defined as the number of molecules of O<sub>3</sub> formed per NO<sub>x</sub> removed from atmospheric ozone-forming oxidation cycles [i.e., P(O<sub>3</sub>)/P(NO<sub>x</sub>)] (Seinfeld and Pandis, 2006). The ozone production efficiency was estimated to be generally 2–8 in PRD (Wang et al., 2010c), with higher values (10-15) during severe ozone pollution episodes (Sun et al., 2010b). Although the production of ozone in the entire PRD region is high likely to be VOC-limited (Zhang et al., 2008b), there was a study arguing that the production of ozone is possibly controlled by NO<sub>x</sub> in the northern or northeastern rural areas of PRD (Zheng et al., 2010). Based on measurements at the Shangdianzi Regional Background Station in NC during March to October 2008, OPE was calculated and its daily value varied in the range of 0.2-21.1, with an average of 4.9±3.6 (Ge et al., 2010).

There have been few measurements of VOCs reported for non-urban areas (Geng et al., 2009; Guo et al., 2009; Liu et al., 2008e; Mao et al., 2009; Tang et al., 2007). The concentrations of VOCs in YRD are relatively small at higher altitudes of PBL, with a mean value of 6 ppbv, with 52% from alkanes, 16% from alkenes, 17% from aromatics, 3% from ketones, and 5% from other VOCs, respectively (Geng et al., 2009). The aromatics were estimated to have largest contribution to the ozone chemical production in the YRD areas near Shanghai (Geng et al., 2009). It was shown that alkanes constitute the largest percentage (>40%) in mixing ratios of the quantified VOCs at six sites of PRD, and there is an exception at one major industrial site where aromatics were dominated (about 52%) (Liu et al., 2008e). While alkenes play a predominant role in the VOC reactivity for the urban area, reactive aromatics may also make a great contribution to the ozone formation in the rural area of PRD (Liu et al., 2008e). The effects of biogenic VOCs were also shown to play an important role in the PRD region (Wei et al., 2007).

## 2.3 Tropospheric chemistry and long-range transport

### 2.3.1 Model evaluations and satellite data applications

Regional chemical transport models were compared with an extensive set of observations including the TRACE-P experiment to evaluate the models' abilities in

simulating ozone and relevant species in the troposphere of East Asia (Gao et al., 2009b; Han et al., 2008a; Wang et al., 2010e; Zhang et al., 2006a; Zhang et al., 2006b). In general, the models show a good skill of simulating SO<sub>2</sub>. However, almost all models tends to under-predict NO<sub>x</sub> levels, due to larger uncertainties in either emission estimates or complex chemical mechanism represented (Han et al., 2008a). The model skills for ozone vary largely with region and season, and large differences were found among models for Southeast Asia where the observations are sparse (Han et al., 2008a).

Satellite data on have been widely used to investigate the chemical characters of air pollution in China (Li et al., 2007c; Lin et al., 2007b; Ma et al., 2006; Peng et al., 2007; Shi and Zhang, 2008; Shi et al., 2008b; Tie et al., 2006; Zhang et al., 2007a). These include aerosol optical depths from the Moderate Resolution Imaging Spectroradiometer (MODIS), tropospheric NO<sub>2</sub> vertical column densities from GOME and SCIAMACHY, tropospheric ozone residue, and tropospheric CO vertical column densities from the Measurements of Pollutants in the Troposphere (MOPITT).

The geophysical distribution, seasonal variation, and historical trend of tropospheric NO<sub>2</sub> vertical column densities over China were analyzed on the basis of measurements from the satellite instruments GOME and SCIAMACHY for the period of 1997 to 2006 (Zhang et al., 2007a). A high growth rate of tropospheric NO<sub>2</sub> over eastern China, especially above the industrial areas with a fast economical growth, such as YRD and PRD, was found (Zhang et al., 2007a). Tropospheric NO<sub>2</sub> vertical column densities over China simulated by regional models were compared with GOME and SCIAMACHY satellite data to evaluate the uncertainties in emission inventories and the accuracy of satellite data (Ma et al., 2006; Shi et al., 2008b). It was shown that the model tends to underestimate the tropospheric NO<sub>2</sub> column density in remote and rural areas of China with respect to the GOME measurements (Ma et al., 2006).

MODIS aerosol optical depths, GOME NO<sub>2</sub> column, and MOPITT CO column together with a global chemical transport model (MOZART-2) were used to characterize air pollution in the eastern China and the eastern US (Tie et al., 2006). The NO<sub>x</sub> concentrations in both regions are substantially higher than in remote regions such as over the Pacific Ocean. However, the concentrations of non-methane hydrocarbons from both anthropogenic and biogenic sources are considerably lower in the eastern China than in the eastern US, and thus the rate of photochemical ozone production and ozone concentrations during summer is significantly lower in Eastern China than in the Eastern US (Tie et al., 2006). The calculated NO<sub>2</sub> column over the eastern China by MOZART-2 is fairly consistent with the GOME measurement (Zhao et al., 2006). MOZART-2 underestimates tropospheric CO column in China with comparison to MOPITT CO due to the uncertainties of emissions (Peng et al., 2007; Zhao et al., 2006). New CO emission data were obtained by the CO budget analysis with MOZART constrained by MOPITT data (Lin et al., 2007b).

### 2.3.2 Ozone production and tracer-tagging simulations

The observations at the three mountain sites (Mount Tai, Hua and Huang) showed a striking ozone pattern of two sharp peaks in May-June and

September–October in the central east China (Li et al., 2007a). This seasonal pattern is the same as that at the ground regional stations of eastern China as observed by (Lin et al., 2008; Lin et al., 2009; Meng et al., 2009; Xu et al., 2008b). The calculated net photochemical production of ozone reaches up to 31.8, 15.1, and 11.4 ppbv day<sup>-1</sup> at Mount Tai, Hua, and Huang, respectively (Li et al., 2007a). Model simulations showed that biogenic emissions have remarkable impacts on surface ozone in eastern China, and the increase of ozone concentration reaches generally up to 10-30 ppbv in the VOC-limited areas (Wang et al., 2008a). Measurements of NMHCs were concurrently carried out at a few remote and rural sites in background atmospheres of eastern, northern, southwestern, and southern China, providing valuable information for investigating the sources of air pollution and their impacts on ozone in different regions (Tang et al., 2007; Tang et al., 2009b).

Regional emissions, photochemistry, and the monsoon activities control the regional distribution and seasonal variation of ozone and CO over China and their export to the North Pacific as simulated by the regional models (Gao et al., 2009b; Li et al., 2008a; Wang et al., 2008a) and by a nested-grid global model (GEOSChem) (Chen et al., 2009a), respectively. A CO-tagging method was implemented in GEOSChem to investigate the formation and dispersion of CO pollution over Beijing, and the results suggested that regional emissions make significant contributions to elevated CO levels over Beijing on polluted days (Chen et al., 2009a). A O<sub>3</sub>-tagging module was used in a regional model to study the source of near-ground ozone at Mt. Tai in the Central Eastern China (CEC), and the results indicated the importance of the regional-scale transport in the redistribution of ozone that are chemically produced both inside CEC and in the southern part of CEC (Li et al., 2008a). The same model with the O<sub>3</sub>-tagging module was used to study the impacts of anthropogenic emissions and stratosphere-to-troposphere exchange on surface ozone on the Tibetan Plateau, and in contrary to previous studies (e.g., Ma et al., 2002) it was concluded that the regional transport of chemically produced ozone in China is responsible for the summer maximum on the northern Tibetan Plateau (Li et al., 2009a).

### **3. Aerosol chemistry**

#### **3.1 Inorganic ions**

The hygroscopicity of aerosols is mainly determined by the composition and amount of inorganic salts they contain. Table 3 summarizes the PM<sub>2.5</sub> mass concentration and major ionic composition observed in different regions of China. The mass concentration of PM<sub>2.5</sub> is generally higher in the northern areas especially during springtime due to the dust effect. For example, in Beijing mineral dust contributes 52% in spring, 16% in summer, 17% in fall, and 22% in winter to the total mass in PM<sub>2.5</sub>, being up to 90% in dust storm (Han et al., 2007). Although Shanghai is weakly influenced by dust storm, the high mass concentration and low ionic content in spring might be caused by the dust intrusion from outside Shanghai, probably related to dust storms in northwestern China (Wang et al., 2006d). Sulfate is the major water-soluble component for all regions, and sulfate, nitrate, and ammonium are the predominated water-soluble components in the cities (Table 3). Interestingly, higher NO<sub>3</sub><sup>-</sup> than SO<sub>4</sub><sup>2-</sup> was observed in Beijing during an autumn period (Song et al., 2006),

and in Guangzhou during a winter period (Tan et al., 2009b), most probably due to strong photochemical activities and the environment conditions that favor the formation of particle nitrate occurring during the experiments. While the maximum of  $\text{SO}_4^{2-}$  content occurs in summer in Beijing, it happens in winter in Shanghai (Table 3), indicating that the formation of  $\text{SO}_4^{2-}$  is controlled by both its gas precursor ( $\text{SO}_2$ ) and photochemical oxidation capacity (OH). PM1 observed by an Aerodyne Aerosol Mass Spectrometer (AMS) during summertime in Beijing was composed of 25% sulfate, 22% nitrate, 16% ammonium, and 35% of organic aerosol (OA) species (Sun et al., 2010a).

### 3.2 Organic aerosols

#### 3.2.1 Species identification and quantification

Organic carbon aerosols (OC) contributed 30-35% to  $\text{PM}_{2.5}$ , and the secondary OC accounted for 40% of OC in Chinese urban environments (Cao et al., 2007). The ratio of OC to element carbon (EC) was on the order of 3 for the urban locations, but could reach as high as 6 at the rural sites (Zhang et al., 2008a). This indicates that more secondary organic aerosols (SOA) form in regional background than in urban atmospheres. According to a model study, SOA concentration was high in the forest areas of southern and northeastern China, with a contribution of SOA to OC of around 50%, and low in the broad areas north of the Yangtze River (Han et al., 2008b).

Over 100 individual organic compounds were identified and quantified in the  $\text{PM}_{2.5}$  samples of Beijing (Huang et al., 2006). Table 4 summarize the major compound classes, including n-alkanes, polycyclic aromatic hydrocarbons (PAHs), fatty acids, dicarboxylic acids, hopanes, and n-Alkanols, measured by several studies. Note that the measurements of these compounds in larger particles, i.e.,  $\text{PM}_{10}$  or TSP (e.g., Wang et al., 2009c; Zhao et al., 2009; Zhou et al., 2009), are not taken into account. Ambient concentrations of n-alkanes, PAHs, and hopanes in the urban air were 1–2 orders of magnitude higher than those in the mountain aerosols and 2–3 orders of magnitude higher than those in the marine samples (Wang et al., 2009a). Size distributions of these organic compounds including water-soluble OC (WSOC) were observed, providing valuable information for investigating the sources of these OC and their evolution during transport from the source to background regions (Wang et al., 2009a; Wang et al., 2009b). Significant concentrations of biogenic OC tracers were found in the forests of northeast China and south China by analyzing OC in aerosols including  $\Sigma$ isoprene oxidation products,  $\Sigma\alpha$ -pinene oxidation products, malic acids, sugar alcohols, and sugars, which were sampled at the four sites of different ecological (boreal-temperate, temperate, subtropical and tropical) regions (Wang et al., 2008d).

The fraction of WSOC generally increases from its pollution source to regional background atmospheres due to aging processes. The fraction of WSOC in total carbonaceous aerosols was found to be more than ~40% at Changdao Island, a rural site in the transport path of Asian continental outflow (Feng et al., 2007). Even so, high fraction of WSOC was observed from  $\text{PM}_{2.5}$  in Beijing in some cases (Liu et al., 2008a). Food cooking can be a significant source of OC in urban areas (Huang et al., 2006; Zhao et al., 2007). The dominant homologue from Chinese cooking styles was found to be fatty acids, which constitutes 73-85% of the quantified compounds (Zhao et al., 2007). In addition to the ion chromatography (IC) and gas chromatography (GC) mass spectrometry, new analytical technique such as the desorption electrospray ionization mass spectrometry (DESI-MS) and single particle aerosol time-of-flight mass spectrometry (ATOFMS) were applied to analyze organic acids, e.g., oxalic acid,

in atmospheric aerosols (Li et al., 2009b; Yang et al., 2009). The averaged concentrations of formic, acetic, and oxalic acids in PM<sub>2.5</sub> were reported to be 110, 78, and 353 ng m<sup>-3</sup> in Beijing, respectively (Wang et al., 2007b).

### 3.2.2 Formation mechanism studies

Analyses of oxalate-containing particles sampled in Shanghai suggested that both in-cloud processing and heterogeneous reactions occurring in hydrated/deliquesced aerosols play important roles in oxalic acid formation (Yang et al., 2009). A formation mechanism of organic salts by amines reaction with aldehydes and/or ketones in the presence of an acid was proposed to explain high molecular weight nitrogen-containing organic salts observed in urban Shanghai aerosols (Wang et al., 2010d). The results of laboratory and field experiments showed that in addition to H<sub>2</sub>O<sub>2</sub>, organic hydro-peroxides potentially play a role in the formation of WSOC via aqueous-phase reactions (Chen et al., 2008; Hua et al., 2008). It was found that the presence of (NH<sub>4</sub>)<sub>2</sub>SO<sub>4</sub>, NH<sub>4</sub>NO<sub>3</sub>, Na<sub>2</sub>SiO<sub>3</sub> and CaCl<sub>2</sub> aerosols can enhance SOA generation and increase SOA yields (Hao et al., 2007; Lu et al., 2009b).

## 4. Interactions between gases and aerosols

### 4.1 New particle formation

The new particle formation (NPF) events were observed in different regions of China, including Beijing (Shi et al., 2007; Wu et al., 2007; Wu et al., 2008; Yue et al., 2010), NC (Ma et al., 2010a; Wang et al., 2008b), YRD (Gao et al., 2009a), PRD (Gong et al., 2008; Liu et al., 2008c), and marine areas (Lin et al., 2007a). Even though NPF is typically indicated by the presence of particles with a diameter of ~2 nm, different definitions of NPF have been used based on particle number concentrations measured at larger diameters. For example, in the surface-based observational study for urban Beijing, a burst in the nucleation mode particles was considered to represent newly formed particles if the event duration exceeded 2.5 h and the number concentration of 3–10 nm particles was higher than 10<sup>4</sup> cm<sup>-3</sup>. In the aircraft observational study, the occurrence of NPF was assumed if the measured concentration of 5–10 nm particles exceeds 10<sup>4</sup> particles cm<sup>-3</sup> (Ma et al., 2010a). The NPF events were observed in urban Beijing with a frequency of 10–70% based on the long-term measurement since March 2004, with a higher NPF frequency and larger formation rates in spring, but a lower NPF frequency and higher growth rates in summer (Wu et al., 2007; Yue et al., 2010). The NPF events were thought to usually occur in conjunction with high-speed wind from the north, low relative humidity (below 45%), and intense solar radiation in urban Beijing (Wu et al., 2007; Yue et al., 2010). On the other hand, widespread NPF over the entire polluted area of North China was observed by aircraft measurements at higher altitudes (1–3 km) near clouds, where relative humidity was rather high (Ma et al., 2010a).

Atmospheric aerosol nucleation was shown to be strongly influenced by sulfuric acid (Yue et al., 2010). NPF events may involve sulfuric acid, ammonia, and oxalic acid, and organic compounds are an important contributor to the growth of the freshly nucleated particles (Yue et al., 2009; Yue et al., 2010). Low condensational sink (corresponding to low particle surface area concentration) might be one of the key factors for the NPF occurrence in Beijing (Wu et al., 2007) or NC (Wang et al., 2008b). However, no consistent connection between number concentrations of nucleation mode particles and surface concentration was found for all NPF events in PRD (Liu et al., 2008c). In spite of a vast pre-existing particle surface area, intensive NPF could occur under very high H<sub>2</sub>SO<sub>4</sub> concentrations driven by high levels of its

gaseous precursors  $\text{SO}_2$  and OH over the polluted NC region (Ma et al., 2010a). Below clouds the growth rate ( $GR$ ) of nucleation mode particles caused by the condensation of  $\text{H}_2\text{SO}_4$  vapor was estimated to be 5-21  $\text{nm h}^{-1}$  (Ma et al., 2010a), much higher than the range of 0.1-11  $\text{nm h}^{-1}$  inferred from ground-based measurements in Beijing (Wu et al., 2007; Yue et al., 2010). The latter referred to an overall nucleation rate by a range of compounds, including organics. High values of  $GR$  (2-20  $\text{nm h}^{-1}$ ) were also reported for the NPF events observed at a rural/coastal site in PRD (Liu et al., 2008c).

## 4.2 Heterogeneous reactions

### 4.2.1 Gas condensation on particles

In addition to NPF, the condensation of gases (mostly low volatile acids) on pre-existing particles is an important way of gas-to-particle conversion. The latter does not produce new particles in a sense of number, but can change the size and hygroscopicity of particles significantly (Ma et al., 2010a). Acidic gases ( $\text{HCl}$ ,  $\text{HONO}$ ,  $\text{HNO}_3$ , and  $\text{SO}_2$ ), ammonia ( $\text{NH}_3$ ), and water-soluble ions in  $\text{PM}_{2.5}$  and  $\text{PM}_{10}$  were measured during a fall period in PRD and a summer period in Beijing, respectively (Hu et al., 2008; Wu et al., 2009), and these dataset are valuable for investigating the gas-to-particle process in the atmosphere. Sulfuric acid concentrations were observed in a range of  $4.5 \times 10^6 \text{ cm}^{-3}$  to  $1.1 \times 10^7 \text{ cm}^{-3}$  in summer 2008 (Yue et al., 2010). In the cases when sulfate was the major composition of the ultrafine particles, the condensation and neutralization of sulfuric acid together with coagulation made a major contribution to the growth of these particles (Yue et al., 2010). The cases when the mass concentration of organic compounds was significantly higher than that of sulfate were observed (Yue et al., 2010). AMS measurements showed that particles smaller than 200 nm were predominately organic in general while the accumulation mode particles with diameters peaking at  $\sim 600$  nm were dominated by sulfate and nitrate in Beijing (Sun et al., 2010a). While the contribution of organic compounds to particle growth was considered as being larger than that of sulfate (Yue et al., 2010), these ultrafine particles in urban environments were suggested to be primarily associated with local combustion emissions (Sun et al., 2010a). The mixed inorganic and organic species measured in the larger accumulation mode in urban Beijing might indicate aging processes of these particulates occurring in regional scales (Sun et al., 2010a).

The condensation mode of sulfate, which is formed by the “gas-phase oxidation and condensation” process, was in the size range of 0.32–0.56  $\mu\text{m}$ , and the droplet mode of sulfate, which is formed by the “condensation and liquid-phase oxidation” process, was in the size range of 0.56–1.0 or 1.0–1.8  $\mu\text{m}$  as measured at a rural site (Xinken) of PRD during summertime (Liu et al., 2008b). Nitrate was distributed evenly over fine and coarse particles, and the coarse mode nitrate might be formed by the reaction of  $\text{HNO}_3$  with sea-salt or soil components (Liu et al., 2008b). A case study by single-particle mass spectrometry during summertime in Shanghai indicated a poor correlation between the signals of ammonium and nitrate and thus excluded the possibility of  $\text{NH}_4\text{NO}_3$  as a major form of particulate nitrate (Wang et al., 2009g). The evolution of sulfate size distributions was observed on a timescale of several hours at a rural site (Back Garden) of PRD in summer (Xiao et al., 2009). It was found that the growth of sulfate in the condensation mode was mainly due to the oxidation of  $\text{SO}_2$  ( $\sim 3\text{--}21.2$  ppbv) by OH ( $\sim 3.3 \times 10^6\text{--}1.7 \times 10^7 \text{ cm}^{-3}$ ) in the gas-phase and that oxygenated OC might also form by the gas-phase oxidation of VOC precursors (Xiao

et al., 2009).

#### 4.2.2 Surface chemical mechanism

Laboratory experimental results showed that in the presence of O<sub>3</sub>, SO<sub>2</sub> could be oxidized to sulfate on the surface of CaCO<sub>3</sub> particles, indicating that the heterogeneous reaction might be an important pathway for sulfate formation in the atmosphere (Li et al., 2006). Dust storm aerosol can interact with pollution gases and pollution aerosol during transport to Beijing, and this mechanism could be important during non-dust days (Yuan et al., 2006). Analysis of individual particles sampled during haze pollution and dust episodes in Beijing showed that a majority of collected mineral particles are covered by visible coatings of nitrates in haze samples (Li and Shao, 2009). These nitrate coatings are strongly correlated with the presence of alkaline mineral components (e.g., calcite and dolomite) which are involved in atmospheric heterogeneous reactions with two or more acidic gases (e.g., SO<sub>2</sub>, NO<sub>2</sub>, HCl, and HNO<sub>3</sub>) (Li and Shao, 2009). Also by laboratory study it was suggested that the heterogeneous reaction of NO<sub>2</sub> on CaCO<sub>3</sub> particle is unable to compete with that of HNO<sub>3</sub> in the atmosphere (Li et al., 2010a). The effect of water on the heterogeneous reactions of carbonyl sulfide (OCS) on the surface of α-Al<sub>2</sub>O<sub>3</sub> and MgO was studied by laboratory experiments, and it was found that the basic thick water layer formed on the basic component of mineral dusts may be the primary contributor to the heterogeneous hydrolysis of OCS in the troposphere (Liu et al., 2009c).

#### 4.2.3 Ozone chemistry effect

In addition to ozone and formaldehyde, nitrous acid (HONO) is considered as an important OH source in the troposphere especially in the early morning. High concentrations of HONO with a maximum of 5 ppbv were observed at both urban and rural sites of China, and even during daytime HONO still maintained at about 1 ppbv, making a dominated contribution to the overall daily HO production by photolysis (An et al., 2009; Su et al., 2008). Such strong source of HONO could not be explained by current gas-phase chemical mechanisms and were attributed to heterogeneous reactions of NO<sub>2</sub> on ground and aerosol surfaces (Su et al., 2008).

The impact of dust on tropospheric photochemistry over the Beijing megacity was evaluated with a box model (Zhu et al., 2010) and a 3-D regional chemical transport model (Xu et al., 2006). The simulation results were improved when the heterogeneous reactions were included, with the O<sub>3</sub> and HONO model results closed to the observations (Xu et al., 2006). The uncertainty in uptake coefficients of self-removal reactions results in the largest uncertainty in the impacts on trace gases, and the heterogeneous removal of NO<sub>2</sub> was found to be particularly important, because it results in significant levels of uncertainty not only for itself, but also for OH and HO<sub>2</sub> (Zhu et al., 2010). The uptake coefficients of several trace gases (e.g., NO<sub>2</sub>, SO<sub>2</sub>, acetone, carbonyl sulfide (OCS), and ethyl iodide) on mineral dust (e.g., calcite and mineral oxides) or black carbon surfaces were studied (Cui et al., 2009; Jie et al., 2008; Li et al., 2010a; Li et al., 2006; Li et al., 2007b; Liu et al., 2009c; Liu et al., 2008f; Yin et al., 2008).

## 5. Atmospheric Chemistry and climate change

### 5.1 Aerosol hygroscopicity and growth factors

The long-term trends of fog-evens and visibility in different regions of China were shown to be correlated with urbanization and industrial activities, and the impact

of aerosol pollution have been considered to play a key role especially in the general degradation of visibility in megacities (Chang et al., 2009a; Deng et al., 2008a; Niu et al., 2010; Shi et al., 2008a). Aerosol chemistry determines the hygroscopicity of aerosols, and the latter influences the size distribution and optical property of aerosols as a function of relative humidity (RH). The aerosol geometric (diameter) hygroscopic growth factor ( $GF_D$ ), defined as the ratio of the diameter of a particle at a known elevated RH below saturation to that when nominally dry (McFiggans et al., 2006), was observed below clouds by aircraft measurements during springtime over NC (Ma et al., 2010a). In this region  $GF_D$  was 1.2-1.6 at RH = 90% in the fine mode, being typical for polluted continental environments (McFiggans et al., 2006), and ~2.2 in the lower coarse mode (Ma et al., 2010a). This enhanced hygroscopicity of the coarse aerosols was probably caused by the added fraction of highly soluble inorganic acids to the mineral dust (Ma et al., 2010a). The resulting large, hygroscopic mixed dust-pollution particles are much more effective cloud condensation nuclei (CCN) than either the large insoluble desert dust or the small soluble sulfate particles (Ma et al., 2010a). The hygroscopic behavior of mineral dust was investigated by laboratory experiments (Ma et al., 2010b). It was shown that the hygroscopic behavior of  $\text{Ca}(\text{NO}_3)_2/\text{CaCO}_3$  particles is identical to that of pure  $\text{Ca}(\text{NO}_3)_2$  particles (Liu et al., 2008g).

The aerosol optical (scattering coefficient) hygroscopic growth factor  $f(\text{RH})$ , defined as the ratio of light scattering coefficient of a bulk of aerosol particles at a specific wavelength (e.g., 550nm) under a wet condition (e.g., RH = 80% or 90%) to that under a dry condition (40% RH or lower), was also investigated by ground measurements (e.g., Liu et al., 2010; Pan et al., 2009). The mean and standard deviation of  $f(\text{RH}=80\%)$  observed during summertime in Beijing was  $1.63 \pm 0.19$  (Liu et al., 2009b). The values of  $f(\text{RH}=80\%)$  measured at a rural site in the Beijing-Tianjin-Tangshan region of NC during springtime were  $1.2 \pm 0.02$  under dust episode,  $1.31 \pm 0.03$  under clean periods, and  $1.57 \pm 0.02$  during pollution periods (Pan et al., 2009). Aerosol hygroscopicity had been considered to be generally depressed with the increasing ratio of OC/ammonium sulfate in particle mass. However, a special case with high value of  $f(\text{RH})=2.21$  and high OC/ammonium sulfate ratio was observed, reflecting the special physico-chemical character of organic matter and its complex interaction with other compounds in this region (Pan et al., 2009). The mean and standard deviation of  $f(\text{RH}=80\%)$  observed during summertime in Guangzhou were  $2.04 \pm 0.28$ ,  $2.29 \pm 0.28$ , and  $2.68 \pm 0.59$  for urban aerosols, mixed aerosols, and marine aerosols, respectively. The scattering coefficient of aerosols at a rural site of PRD was estimated to increase with a factor of 1.54 and 2.31 at a RH increase from 30% to 80% and 90%, respectively (Cheng et al., 2008). While the hygroscopic properties of the observed aerosols were shown to have a negative correlation with the total carbon (TC) mass fraction (Liu et al., 2008d), the major chemical components for visibility degradation in Guangzhou were proposed to be TC and sulfate in normal days and nitrate and TC in haze days, respectively (Tan et al., 2009a). The organic coatings on individual inorganic particles may influence their surface hygroscopicity and optical properties (Li and Shao, 2010). Water dialysis of individual particles

indicated that the organic inclusions/aggregations in the K- and S-rich particles were insoluble in water but that OC from the coatings of individual particles was soluble (Li and Shao, 2010).

### **5.2 Radiative forcing and climate effects**

Over 1950-2000, the regional mean anthropogenic radiative forcing by tropospheric ozone at the tropopause (RF) was larger in eastern China ( $0.87 \text{ W m}^{-2}$ ) than the global one ( $0.51 \text{ W m}^{-2}$ ), and the negative RF by aerosols was much larger in eastern China ( $-6.08 \text{ W m}^{-2}$ ) than the global one ( $-0.57 \text{ W m}^{-2}$ ) in an absolute sense, as simulated by a unified global chemistry-aerosol-climate model (Chang et al., 2009b). With a regional climate model, the averaged indirect RF over China due to anthropogenic nitrate aerosols was estimated to be  $-1.63 \text{ W m}^{-2}$  in January and  $-2.65 \text{ W m}^{-2}$  in July, respectively (Li et al., 2009c). The increase of CO and NO<sub>x</sub> emissions in the future was simulated to have significant effects on regional chemistry and climate over eastern China (Wang et al., 2010a). The fully coupled chemistry-aerosol-climate simulation predicted a lower global burden of ozone and aerosols for year 2100 than the simulation which does not account for future changes in climate, leading to a stronger net global warming by greenhouse gases, tropospheric ozone and aerosols with a global and annual mean surface air temperature higher by 0.42 K (Liao et al., 2009). While Asian summer monsoon was shown to reduce surface layer PM<sub>2.5</sub> aerosol concentration averaged over eastern China significantly (Zhang et al., 2010), it was demonstrated that sulfate and BC aerosols in China have the effects to weaken East Asia monsoons in both summer and winter seasons (Liu et al., 2009e).

## **6. Conclusions and remarks**

In this paper we give a review of atmospheric chemistry research in China over the years 2006-2010, focusing on ozone and aerosol chemistry and the linkages of atmospheric chemistry to climate changes. China is a region that has concurrently suffered photochemical smog, haze pollution, and regional climate changes over the past decade. These environmental issues provide a great challenge, and also a chance, for the atmospheric chemistry community, especially for Chinese scientists, to promote a great advance in the science of atmospheric chemistry. North China (NC), the Yangtze River Delta (YRD), and the Pear River Delta (PRD) are the most severe polluted regions in China, and the majority of the reviewed publications have focused on atmospheric chemistry and physics that are associated with air pollution in these three regions and the Beijing, Shanghai, and Guangzhou megacities contained.

Satellite data on tropospheric vertical column densities of trace gases, e.g., NO<sub>2</sub> and CO, have been intensively used in atmospheric chemistry research in China. The analyses showed that the satellite can observe the regional distribution, seasonal variation, and historical trends of these air pollutants over China. Satellite data analyses together with model simulations can be an efficient method to investigate the chemical characters of the atmosphere in a regional scale. It should be noted that there is still a disagreement in the reported trend of NO<sub>2</sub> between satellite data and ground measurements for some region (e.g., Beijing), and more specifically-designed ground measurements, e.g., passive DOAS observation, are needed to validate the satellite

data including the ‘spatial averaging effect’.

Long-term ground observations of ozone and its precursors are still sparse in China. Analyses based on limited data showed the increasing trends of ozone at both urban (Beijing) and regional (YRD) sites with large uncertainties. While the former was associated with decreasing  $\text{NO}_x$ , the latter was attributed to increasing  $\text{NO}_x$ . It has been revealed that the formation of ozone is limited by VOCs in urban areas (e.g., Beijing, Shanghai, and Guangzhou). However, the dominating controlling factors for ozone formation in polluted rural areas (e.g., NC, YRD, and PRD) are still not very clear, although some studies declared that these regions are also VOC-limited. While the emission restrictions are very efficient in reducing ozone precursors and aerosol mass, the effect on ozone levels have shown to be quite complicated. In addition to ozone and its precursors, measurements of active intermediate products (e.g., HCHO,  $\text{H}_2\text{O}_2$ , MAR, and MVK) and hydroxyl/peroxy radicals (e.g., HO,  $\text{HO}_2$ , and  $\text{CH}_3\text{O}_2$ ) in combination with chemical model simulations are suggested to fully understand the mechanism of ozone formation in different regions.

Several studies have shown the evidences that aerosols may influence ozone chemistry by changing the photolysis rates and by providing the surface for heterogeneous reactions. High concentrations of HONO, which provides an important OH source, were observed in the urban areas even during daytime. Although the formation of so huge amount of HONO is attributed to heterogeneous reactions of  $\text{NO}_2$  on aerosol surfaces, the detail chemical mechanism has not been fully understood yet. While several laboratory studies of heterogeneous reactions have been reported, further work focusing on typical multi-component aerosols sampled in the natural atmosphere over China is recommended.

The NPF events have been observed in different regions of China. The concurrent measurements of sulfuric acid showed that atmospheric nucleation is strongly influenced by sulfuric acid. In spite of a vast pre-existing particle surface area, intensive NPF could occur under very high  $\text{H}_2\text{SO}_4$  concentrations driven by high levels of its gaseous precursors  $\text{SO}_2$  and OH over the polluted region. Field measurements and laboratory work showed that heterogeneous reaction might be an important pathway for sulfate and nitrate formation in the atmosphere. The coatings by inorganic pollution acids were shown to be very efficient in changing the hygroscopicity of natural dust aerosols. Further studies are needed to understand the role of these acids together with ammonia in the formation and growth of particles.

Large fractions of OC have been observed in different sizes of particles, including the fine and ultrafine particles. Although over 100 individual organic compounds have been identified and quantified in the particles, there is still large deficiency in the mass sum of identified OC compounds with comparison to the total OC mass. While lower carbon number compounds in the gas phase are generally investigated for ozone chemistry, many higher carbon number compounds have been identified in the particle phase. The understandings of organic chemistry in both gaseous and particulate phases are highly incomplete. Detection of organic compounds in aerosols, the conversion way of organic compounds from the gas phase to the particle phase, and the effect of organic compounds on the physical characters of aerosols, are recommended to be studied intensively.

In-situ measurements in the different regions of China have shown that photochemistry has large impacts on the formation and hygroscopicity of aerosols. The aerosol hygroscopic character influences the size distribution and optical property

of aerosols, the haze formation and visibility, and direct radiation forcing on climate as functions of relative humidity; it also affects the ability of aerosols as cloud condensation nuclei and thus indirect radiation forcing on climate. Observations on the ground and by aircraft have shown larger aerosol hygroscopic growth factor in the polluted atmosphere than in the clean atmosphere. While inorganic salts play a dominated role in the enhancement of aerosol hygroscopicity, the effect of organic compounds is quite unclear. Model studies have shown that air pollution could change the chemical and physical characters of the natural atmosphere significantly, exert strong radiative forcing, and thus result in regional climate changes in China and East Asia. It should be noted that these models generally represent an idea case with chemical and physical parameterizations derived from measurements in other regions of the world. The interactions among atmospheric chemistry, aerosols, and clouds are intricate, and model simulations constrained by comprehensive measurements are recommended to study the effect of air pollution on climate change.

### Reference:

- An, J. L., W. Zhang, and Y. Qu, 2009: Impacts of a strong cold front on concentrations of HONO, HCHO, O<sub>3</sub>, and NO<sub>2</sub> in the heavy traffic urban area of Beijing. *Atmos. Environ.*, **43**, 3454-3459, 10.1016/j.atmosenv.2009.04.052.
- An, X., T. Zhu, Z. Wang, C. Li, and Y. Wang, 2007: A modeling analysis of a heavy air pollution episode occurred in Beijing. *Atmos. Chem. Phys.*, **7**, 3103-3114.
- Cao, J. J., and coauthors, 2007: Spatial and seasonal distributions of carbonaceous aerosols over China. *J. Geophys. Res.-Atmos.*, **112**, D22S11, doi: 10.1029/2006jd008205.
- Chang, D., Y. Song, and B. Liu, 2009a: Visibility trends in six megacities in China 1973-2007. *Atmos. Res.*, **94**, 161-167, 10.1016/j.atmosres.2009.05.006.
- Chang, W. Y., H. Liao, and H. J. Wang, 2009b: Climate Responses to Direct Radiative Forcing of Anthropogenic Aerosols, Tropospheric Ozone, and Long-Lived Greenhouse Gases in Eastern China over 1951-2000. *Adv. Atmos. Sci.*, **26**, 748-762, 10.1007/s00376-009-9032-4.
- Chen, D., Y. Wang, M. B. McElroy, K. He, R. M. Yantosca, and P. Le Sager, 2009a: Regional CO pollution and export in China simulated by the high-resolution nested-grid GEOS-Chem model. *Atmos. Chem. Phys.*, **9**, 3825-3839.
- Chen, D., B. Zhou, S. Beirle, L. M. Chen, and T. Wagner, 2009b: Tropospheric NO<sub>2</sub> column densities deduced from zenith-sky DOAS measurements in Shanghai, China, and their application to satellite validation. *Atmos. Chem. Phys.*, **9**, 3641-3662.
- Chen, J. H., W. Wang, J. Y. Zhang, H. J. Liu, L. H. Ren, X. Y. Liu, W. J. Zhang, and X. Wang, 2009c: Characteristics of gaseous pollutants near a main traffic line in Beijing and its influencing factors. *Atmos. Res.*, **94**, 470-480, 10.1016/j.atmosres.2009.07.008.
- Chen, Y., C. S. Zhao, Q. Zhang, Z. Z. Deng, M. Y. Huang, and X. C. Ma, 2009d: Aircraft study of Mountain Chimney Effect of Beijing, China. *J. Geophys. Res.-Atmos.*, **114**, D08306

10.1029/2008jd010610.

Chen, Z. M., H. L. Wang, L. H. Zhu, C. X. Wang, C. Y. Jie, and W. Hua, 2008: Aqueous-phase ozonolysis of methacrolein and methyl vinyl ketone: a potentially important source of atmospheric aqueous oxidants. *Atmos. Chem. Phys.*, **8**, 2255-2265.

Cheng, Y. F., and coauthors, 2008: Relative humidity dependence of aerosol optical properties and direct radiative forcing in the surface boundary layer at Xinken in Pearl River Delta of China: An observation based numerical study. *Atmos. Environ.*, **42**, 6373-6397, 10.1016/j.atmosenv.2008.04.009.

Cui, H. X., T. T. Cheng, X. N. Yu, J. M. Chen, Y. F. Xu, and W. Fang, 2009: Laboratory simulation of SO<sub>2</sub> heterogeneous reactions on hematite surface under different SO<sub>2</sub> concentrations. *J. Environ. Sci.*, **21**, 1103-1107, 10.1016/s1001-0742(08)62388-8.

Deng, X. J., X. X. Tie, D. Wu, X. J. Zhou, X. Y. Bi, H. B. Tan, F. Li, and C. L. Hang, 2008a: Long-term trend of visibility and its characterizations in the Pearl River Delta (PRD) region, China. *Atmos. Environ.*, **42**, 1424-1435, 10.1016/j.atmosenv.2007.11.025.

Deng, X. J., and coauthors, 2008b: Effects of Southeast Asia biomass burning on aerosols and ozone concentrations over the Pearl River Delta (PRD) region. *Atmos. Environ.*, **42**, 8493-8501, 10.1016/j.atmosenv.2008.08.013.

Feng, J. L., Z. G. Guo, C. K. Chan, and M. Fang, 2007: Properties of organic matter in PM<sub>2.5</sub> at Changdao Island, China - A rural site in the transport path of the Asian continental outflow. *Atmos. Environ.*, **41**, 1924-1935, 10.1016/j.atmosenv.2006.10.064.

Fu, Q. Y., G. S. Zhuang, J. Wang, C. Xu, K. Huang, J. Li, B. Hou, T. Lu, and D. G. Streets, 2008: Mechanism of formation of the heaviest pollution episode ever recorded in the Yangtze River Delta, China. *Atmos. Environ.*, **42**, 2023-2036, 10.1016/j.atmosenv.2007.12.002.

Gao, J., T. Wang, X. H. Zhou, W. S. Wu, and W. X. Wang, 2009a: Measurement of aerosol number size distributions in the Yangtze River delta in China: Formation and growth of particles under polluted conditions. *Atmos. Environ.*, **43**, 829-836, 10.1016/j.atmosenv.2008.10.046.

Gao, L. J., M. G. Zhang, and Z. W. Han, 2009b: Model Analysis of Seasonal Variations in Tropospheric Ozone and Carbon Monoxide over East Asia. *Adv. Atmos. Sci.*, **26**, 312-318, 10.1007/s00376-009-0312-9.

Ge, B., X. Xu, W. Lin, and Y. Wang, 2010: Observational study of ozone production efficiency at the Shangdianzi regional background station. *Environ. Sci. Technol.*, **31**, 36-43.

Geng, F. H., C. S. Zhao, X. Tang, G. L. Lu, and X. X. Tie, 2007: Analysis of ozone and VOCs measured in Shanghai: A case study. *Atmos. Environ.*, **41**, 989-1001, 10.1016/j.atmosenv.2006.09.023.

Geng, F. H., X. X. Tie, J. M. Xu, G. Q. Zhou, L. Peng, W. Gao, X. Tang, and C. S. Zhao, 2008: Characterizations of ozone, NO<sub>x</sub>, and VOCs measured in Shanghai, China. *Atmos. Environ.*, **42**, 6873-6883, 10.1016/j.atmosenv.2008.05.045.

- Geng, F. H., Q. Zhang, X. X. Tie, M. Y. Huang, X. C. Ma, Z. Z. Deng, Q. Yu, J. N. Quan, and C. S. Zhao, 2009: Aircraft measurements of O<sub>3</sub>, NO<sub>x</sub>, CO, VOCs, and SO<sub>2</sub> in the Yangtze River Delta region. *Atmos. Environ.*, **43**, 584-593, 10.1016/j.atmosenv.2008.10.021.
- Gong, Y. G., H. Su, Y. F. Cheng, F. Liu, Z. J. Wu, M. Hu, L. M. Zeng, and Y. H. Zhang, 2008: Analysis on concentration and source rate of precursor vapors participating in particle formation and growth at Xinken in the Pearl River Delta of China. *Adv. Atmos. Sci.*, **25**, 427-436, 10.1007/s00376-008-0427-4.
- Guo, H., and coauthors, 2009: Concurrent observations of air pollutants at two sites in the Pearl River Delta and the implication of regional transport. *Atmos. Chem. Phys.*, **9**, 7343-7360.
- Han, L. H., G. S. Zhuang, S. Y. Cheng, and J. Li, 2007: The mineral aerosol and its impact on urban pollution aerosols over Beijing, China. *Atmos. Environ.*, **41**, 7533-7546, 10.1016/j.atmosenv.2007.05.046.
- Han, Z., and coauthors, 2008a: MICS-Asia II: Model intercomparison and evaluation of ozone and relevant species. *Atmos. Environ.*, **42**, 3491-3509, 10.1016/j.atmosenv.2007.07.031.
- Han, Z. W., R. J. Zhang, Q. G. Wang, W. Wang, J. J. Cao, and J. Xu, 2008b: Regional modeling of organic aerosols over China in summertime. *J. Geophys. Res.-Atmos.*, **113**, D11202  
10.1029/2007jd009436.
- Hao, L. Q., Z. Y. Wang, M. Q. Huang, L. Fang, and W. J. Zhang, 2007: Effects of seed aerosols on the growth of secondary organic aerosols from the photooxidation of toluene. *J. Environ. Sci.*, **19**, 704-708.
- Hao, N., B. Zhou, D. Chen, and L. M. Chen, 2006: Observations of nitrous acid and its relative humidity dependence in Shanghai. *J. Environ. Sci.*, **18**, 910-915.
- He, L. Y., M. Hu, X. F. Huang, Y. H. Zhang, and X. Y. Tang, 2006: Seasonal pollution characteristics of organic compounds in atmospheric fine particles in Beijing. *Sci. Total Environ.*, **359**, 167-176, 10.1016/j.scitotenv.2005.05.044.
- Hu, M., Z. J. Wu, J. Slanina, P. Lin, S. Liu, and L. M. Zeng, 2008: Acidic gases, ammonia and water-soluble ions in PM<sub>2.5</sub> at a coastal site in the Pearl River Delta, China. *Atmos. Environ.*, **42**, 6310-6320, 10.1016/j.atmosenv.2008.02.015.
- Hua, W., and coauthors, 2008: Atmospheric hydrogen peroxide and organic hydroperoxides during PRIDE-PRD'06, China: their concentration, formation mechanism and contribution to secondary aerosols. *Atmos. Chem. Phys.*, **8**, 6755-6773.
- Huang, J., Y. L. Feng, J. Li, B. Xiong, J. L. Feng, S. Wen, G. Y. Sheng, J. M. Fu, and M. H. Wu, 2008: Characteristics of carbonyl compounds in ambient air of Shanghai, China. *J. Atmos. Chem.*, **61**, 1-20, 10.1007/s10874-009-9121-x.
- Huang, X. F., L. Y. He, M. Hu, and Y. H. Zhang, 2006: Annual variation of particulate organic compounds in PM<sub>2.5</sub> in the urban atmosphere of Beijing. *Atmos. Environ.*, **40**, 2449-2458, 10.1016/j.atmosenv.2005.12.039.
- IPCC, 2007: *The Fourth Assessment Report of the Intergovernmental Panel on Climate Change*, Cambridge Univ. Press, Cambridge.

- Jiang, F., T. J. Wang, T. T. Wang, M. Xie, and H. Zhao, 2008: Numerical modeling of a continuous photochemical pollution episode in Hong Kong using WRF-chem. *Atmos. Environ.*, **42**, 8717-8727, 10.1016/j.atmosenv.2008.08.034.
- Jiang, W., J. Ma, P. Yan, A. Richter, J. P. Burrows, and H. Nü, 2006: Characterization of NO<sub>2</sub> pollution changes in Beijing using GOME satellite data. *J. Applied Meteor. Sci.*, **17**, 67-72.
- Jie, C. Y., Z. M. Chen, H. L. Wang, W. Hua, C. X. Wang, and S. Li, 2008: Atmospheric heterogeneous reaction of acetone: Adsorption and desorption kinetics and mechanisms on SiO<sub>2</sub> particles. *Chin. Sci. Bull.*, **53**, 1004-1010, 10.1007/s11434-007-0489-1.
- Lai, S. C., S. C. Zou, J. J. Cao, S. C. Lee, and K. F. Ho, 2007: Characterizing ionic species in PM<sub>2.5</sub> and PM<sub>10</sub> in four Pearl River Delta cities, South China. *J. Environ. Sci.*, **19**, 939-947.
- Li, H. J., T. Zhu, D. F. Zhao, Z. F. Zhang, and Z. M. Chen, 2010a: Kinetics and mechanisms of heterogeneous reaction of NO<sub>2</sub> on CaCO<sub>3</sub> surfaces under dry and wet conditions. *Atmos. Chem. Phys.*, **10**, 463-474.
- Li, J., Z. F. Wang, H. Akimoto, C. Gao, P. Pochanart, and X. Q. Wang, 2007a: Modeling study of ozone seasonal cycle in lower troposphere over east Asia. *J. Geophys. Res.-Atmos.*, **112**, D22s25  
10.1029/2006jd008209.
- Li, J., Z. Wang, H. Akimoto, K. Yamaji, M. Takigawa, P. Pochanart, Y. Liu, H. Tanimoto, and Y. Kanaya, 2008a: Near-ground ozone source attributions and outflow in central eastern China during MTX2006. *Atmos. Chem. Phys.*, **8**, 7335-7351.
- Li, J., and coauthors, 2008b: The chemistry of heavy haze over Urumqi, Central Asia. *J. Atmos. Chem.*, **61**, 57-72, 10.1007/s10874-009-9124-7.
- Li, J., Z. Wang, H. Akimoto, J. Tang, and I. Uno, 2009a: Modeling of the impacts of China's anthropogenic pollutants on the surface ozone summer maximum on the northern Tibetan Plateau. *Geophys. Res. Lett.*, **36**, 10.1029/2009gl041123.
- Li, L., Z. M. Chen, Y. H. Zhang, T. Zhu, J. L. Li, and J. Ding, 2006: Kinetics and mechanism of heterogeneous oxidation of sulfur dioxide by ozone on surface of calcium carbonate. *Atmos. Chem. Phys.*, **6**, 2453-2464.
- Li, L., Z. M. Chen, Y. H. Zhang, T. Zhu, S. Li, H. J. Li, L. H. Zhu, and B. Y. Xu, 2007b: Heterogeneous oxidation of sulfur dioxide by ozone on the surface of sodium chloride and its mixtures with other components. *J. Geophys. Res.-Atmos.*, **112**, D18301  
10.1029/2006jd008207.
- Li, L., W. Wang, J. L. Feng, D. P. Zhang, H. J. Li, Z. P. Gu, B. J. Wang, G. Y. Sheng, and J. M. Fu, 2010b: Composition, source, mass closure of PM<sub>2.5</sub> aerosols for four forests in eastern China. *J. Environ. Sci.*, **22**, 405-412, 10.1016/s1001-0742(09)60122-4.
- Li, L. J., Y. Wang, Q. Zhang, J. X. Li, X. G. Yang, and J. Jin, 2008c: Wheat straw burning and its associated impacts on Beijing air quality. *Sci. China Ser. D-Earth Sci.*, **51**, 403-414, 10.1007/s11430-008-0021-8.
- Li, M., H. Chen, X. Yang, J. M. Chen, and C. L. Li, 2009b: Direct quantification of

- organic acids in aerosols by desorption electrospray ionization mass spectrometry. *Atmos. Environ.*, **43**, 2717-2720, 10.1016/j.atmosenv.2009.02.057.
- Li, S., T. J. Wang, B. L. Zhuang, and Y. Han, 2009c: Indirect radiative forcing and climatic effect of the anthropogenic nitrate aerosol on regional climate of China. *Adv. Atmos. Sci.*, **26**, 543-552, 10.1007/s00376-009-0543-9.
- Li, W. J., and L. Y. Shao, 2009: Observation of nitrate coatings on atmospheric mineral dust particles. *Atmos. Chem. Phys.*, **9**, 1863-1871.
- Li, W. J., and L. Y. Shao, 2010: Mixing and water-soluble characteristics of particulate organic compounds in individual urban aerosol particles. *J. Geophys. Res.-Atmos.*, **115**, D02301  
10.1029/2009jd012575.
- Li, Y., C. Zhao, Y. Fang, and H. Yu, 2007c: Analysis of distribution and seasonal change of tropospheric ozone residual in recent 20 years using satellite data. *Journal of Applied Meteorological Science*, **18**, 181-186.
- Liao, H., Y. Zhang, W. T. Chen, F. Raes, and J. H. Seinfeld, 2009: Effect of chemistry-aerosol-climate coupling on predictions of future climate and future levels of tropospheric ozone and aerosols. *J. Geophys. Res.-Atmos.*, **114**, D10306  
10.1029/2008jd010984.
- Lin, P., M. Hu, Z. Wu, Y. Niu, and T. Zhu, 2007a: Marine aerosol size distributions in the springtime over China adjacent seas. *Atmos. Environ.*, **41**, 6784-6796, 10.1016/j.atmosenv.2007.04.045.
- Lin, W., X. Xu, X. Zhang, and J. Tang, 2008: Contributions of pollutants from north china plain to surface ozone at the shangdianzi GAW station. *Atmos. Chem. Phys.*, **8**, 5889-5898.
- Lin, W. L., X. B. Xu, B. Z. Ge, and X. C. Zhang, 2009: Characteristics of gaseous pollutants at Gucheng, a rural site southwest of Beijing. *J. Geophys. Res.-Atmos.*, **114**, D00g14  
10.1029/2008jd010339.
- Lin, Y. P., C. S. Zhao, L. Peng, and Y. Y. Fang, 2007b: A new method to calculate monthly CO emissions using MOPITT satellite data. *Chin. Sci. Bull.*, **52**, 2551-2558, 10.1007/s11434-007-0349-z.
- Liu, D. M., S. P. Gao, and X. H. An, 2008a: Distribution and source apportionment of polycyclic aromatic hydrocarbons from atmospheric particulate matter PM<sub>2.5</sub> in Beijing. *Adv. Atmos. Sci.*, **25**, 297-305, 10.1007/s00376-008-0297-9.
- Liu, J. F., Y. J. Mu, Y. J. Zhang, Z. M. Zhang, X. K. Wang, Y. J. Liu, and Z. Q. Sun, 2009a: Atmospheric levels of BTEX compounds during the 2008 Olympic Games in the urban area of Beijing. *Sci. Total Environ.*, **408**, 109-116, 10.1016/j.scitotenv.2009.09.026.
- Liu, S., M. Hu, S. Slanina, L. Y. He, Y. W. Niu, E. Bruegemann, T. Gnauk, and H. Herrmann, 2008b: Size distribution and source analysis of ionic compositions of aerosols in polluted periods at Xinken in Pearl River Delta (PRD) of China. *Atmos. Environ.*, **42**, 6284-6295, 10.1016/j.atmosenv.2007.12.035.
- Liu, S., M. Hu, Z. J. Wu, B. Wehner, A. Wiedensohler, and Y. F. Cheng, 2008c: Aerosol number size distribution and new particle formation at a rural/coastal site in

- Pearl River Delta (PRD) of China. *Atmos. Environ.*, **42**, 6275-6283, 10.1016/j.atmosenv.2008.01.063.
- Liu, X. G., Y. F. Cheng, Y. H. Zhang, J. S. Jung, N. Sugimoto, S. Y. Chang, Y. J. Kim, S. J. Fan, and L. M. Zeng, 2008d: Influences of relative humidity and particle chemical composition on aerosol scattering properties during the 2006 PRD campaign. *Atmos. Environ.*, **42**, 1525-1536, 10.1016/j.atmosenv.2007.10.077.
- Liu, X. G., and coauthors, 2009b: Research on the hygroscopic properties of aerosols by measurement and modeling during CAREBeijing-2006. *J. Geophys. Res.-Atmos.*, **114**, D00g16  
10.1029/2008jd010805.
- Liu, X. G., Y. H. Zhang, M. T. Wen, J. L. Wang, J. Jung, S. Y. Chang, M. Hu, L. M. Zeng, and Y. J. Kim, 2010: A closure study of aerosol hygroscopic growth factor during the 2006 Pearl River Delta Campaign. *Adv. Atmos. Sci.*, **27**, 947-956, 10.1007/s00376-009-9150-z.
- Liu, Y., M. Shao, S. H. Lu, C. C. Liao, J. L. Wang, and G. Chen, 2008e: Volatile organic compound (VOC) measurements in the pearl river delta (PRD) region, China. *Atmos. Chem. Phys.*, **8**, 1531-1545.
- Liu, Y., Q. Ma, and H. He, 2009c: Comparative study of the effect of water on the heterogeneous reactions of carbonyl sulfide on the surface of alpha-Al<sub>2</sub>O<sub>3</sub> and MgO. *Atmos. Chem. Phys.*, **9**, 6272-6286.
- Liu, Y., M. Shao, W. C. Kuster, P. D. Goldan, X. H. Li, S. H. Lu, and J. A. De Gouw, 2009d: Source Identification of Reactive Hydrocarbons and Oxygenated VOCs in the Summertime in Beijing. *Environ. Sci. Technol.*, **43**, 75-81, 10.1021/es801716n.
- Liu, Y., J. R. Sun, and B. Yang, 2009e: The effects of black carbon and sulphate aerosols in China regions on East Asia monsoons. *Tellus Ser. B-Chem. Phys. Meteorol.*, **61**, 642-656, 10.1111/j.1600-0889.2009.00427.x.
- Liu, Y. C., H. He, and Y. J. Mu, 2008f: Heterogeneous reactivity of carbonyl sulfide on alpha-Al<sub>2</sub>O<sub>3</sub> and gamma-Al<sub>2</sub>O<sub>3</sub>. *Atmos. Environ.*, **42**, 960-969, 10.1016/j.atmosenv.2007.10.007.
- Liu, Y. J., T. Zhu, D. F. Zhao, and Z. F. Zhang, 2008g: Investigation of the hygroscopic properties of Ca(NO<sub>3</sub>)<sub>2</sub> and internally mixed Ca(NO<sub>3</sub>)<sub>2</sub>/CaCO<sub>3</sub> particles by micro-Raman spectrometry. *Atmos. Chem. Phys.*, **8**, 7205-7215.
- Lu, H. X., Q. Y. Cai, S. Wen, Y. G. Chi, S. J. Guo, G. Y. Sheng, J. M. Fu, and B. Antizar-Ladislao, 2009a: Carbonyl compounds in the ambient air of hazy days and clear days in Guangzhou, China. *Atmos. Res.*, **94**, 363-372, 10.1016/j.atmosres.2009.06.014.
- Lu, Z. F., J. M. Hao, H. Takekawa, L. H. Hu, and J. H. Li, 2009b: Effect of high concentrations of inorganic seed aerosols on secondary organic aerosol formation in the m-xylene/NO<sub>x</sub> photooxidation system. *Atmos. Environ.*, **43**, 897-904, 10.1016/j.atmosenv.2008.10.047.
- Ma, J., X. Zhou, and D. Hauglustaine, 2002: Summertime tropospheric ozone over China simulated with a regional chemical transport model 2. Source contributions and budget. *J. Geophys. Res.*, **107**, 4612, 10.1029/2001jd001355.
- Ma, J., Y. Chen, W. Wang, P. Yan, H. Liu, S. Yang, Z. Hu, and J. Lelieveld, 2010a:

- Strong air pollution causes widespread haze - clouds over China. *J. Geophys. Res.*, **115**, doi:10.1029/2009JD013065.
- Ma, J. Z., A. Richter, J. P. Burrows, H. Nuss, and J. A. van Aardenne, 2006: Comparison of model-simulated tropospheric NO<sub>2</sub> over China with GOME-satellite data. *Atmos. Environ.*, **40**, 593-604, 10.1016/j.atmosenv.2005.09.029.
- Ma, Q. X., H. He, and Y. C. Liu, 2010b: In situ DRIFTS study of hygroscopic behavior of mineral aerosol. *J. Environ. Sci.*, **22**, 555-560, 10.1016/s1001-0742(09)60145-5.
- Mao, T., Y. S. Wang, J. Jiang, F. K. Wu, and M. X. Wang, 2008: The vertical distributions of VOCs in the atmosphere of Beijing in autumn. *Sci. Total Environ.*, **390**, 97-108, 10.1016/j.scitotenv.2007.08.035.
- Mao, T., Y. S. Wang, H. H. Xu, J. Jiang, F. K. Wu, and X. B. Xu, 2009: A study of the atmospheric VOCs of Mount Tai in June 2006. *Atmos. Environ.*, **43**, 2503-2508, 10.1016/j.atmosenv.2009.02.013.
- McFiggans, G., and coauthors, 2006: The effect of physical and chemical aerosol properties on warm cloud droplet activation. *Atmos. Chem. Phys.*, **6**, 2593-2649, 10.5194/acp-6-2593-2006.
- Meng, Z. Y., G. A. Ding, X. B. Xu, X. D. Xu, H. Q. Yu, and S. F. Wang, 2008: Vertical distributions of SO<sub>2</sub> and NO<sub>2</sub> in the lower atmosphere in Beijing urban areas, China. *Sci. Total Environ.*, **390**, 456-465, 10.1016/j.scitotenv.2007.10.012.
- Meng, Z. Y., X. B. Xu, P. Yan, G. A. Ding, J. Tang, W. L. Lin, X. D. Xu, and S. F. Wang, 2009: Characteristics of trace gaseous pollutants at a regional background station in Northern China. *Atmos. Chem. Phys.*, **9**, 927-936.
- Niu, S. J., C. S. Lu, H. Y. Yu, L. J. Zhao, and J. J. Lu, 2010: Fog Research in China: An Overview. *Adv. Atmos. Sci.*, **27**, 639-662, 10.1007/s00376-009-8174-8.
- Pan, X. L., P. Yan, J. Tang, J. Z. Ma, Z. F. Wang, A. Gbaguidi, and Y. L. Sun, 2009: Observational study of influence of aerosol hygroscopic growth on scattering coefficient over rural area near Beijing mega-city. *Atmos. Chem. Phys.*, **9**, 7519-7530.
- Pang, X. B., and Y. J. Mu, 2006: Seasonal and diurnal variations of carbonyl compounds in Beijing ambient air. *Atmos. Environ.*, **40**, 6313-6320, 10.1016/j.atmosenv.2006.05.044.
- Pang, X. B., Y. J. Mu, Y. J. Zhang, X. Q. Lee, and J. Yuan, 2009: Contribution of isoprene to formaldehyde and ozone formation based on its oxidation products measurement in Beijing, China. *Atmos. Environ.*, **43**, 2142-2147, 10.1016/j.atmosenv.2009.01.022.
- Pang, X. B., and X. Lee, 2010: Temporal variations of atmospheric carbonyls in urban ambient air and street canyons of a Mountainous city in Southwest China. *Atmos. Environ.*, **44**, 2098-2106, 10.1016/j.atmosenv.2010.03.006.
- Peng, L., C. S. Zhao, Y. P. Lin, X. D. Zheng, X. X. Tie, and L.-Y. Chan, 2007: Analysis of carbon monoxide budget in North China. *Chemosphere*, **66**, 1383-1389, 10.1016/j.chemosphere.2006.09.055.
- Qin, M., and coauthors, 2009: An observational study of the HONO-NO<sub>2</sub> coupling at an urban site in Guangzhou City, South China. *Atmos. Environ.*, **43**, 5731-5742, 10.1016/j.atmosenv.2009.08.017.

- Ran, L., and coauthors, 2009: Ozone photochemical production in urban Shanghai, China: Analysis based on ground level observations. *J. Geophys. Res.-Atmos.*, **114**, D15301  
10.1029/2008jd010752.
- Seinfeld, J. H., and S. N. Pandis, 1998: *Atmospheric Chemistry and Physics*, 1326 pp., John Wiley, New York.
- Shan, W. P., Y. Q. Yin, J. D. Zhang, and Y. P. Ding, 2008: Observational study of surface ozone at an urban site in East China. *Atmos. Res.*, **89**, 252-261, 10.1016/j.atmosres.2008.02.014.
- Shao, M., X. Tang, Y. Zhang, and W. Li, 2006: City clusters in China: air and surface water pollution. *Frontiers in Ecology and the Environment* **4**, 353-361.
- Shao, M., S. H. Lu, Y. Liu, X. Xie, C. C. Chang, S. Huang, and Z. M. Chen, 2009: Volatile organic compounds measured in summer in Beijing and their role in ground-level ozone formation. *J. Geophys. Res.-Atmos.*, **114**, D00g06  
10.1029/2008jd010863.
- Shen, Z. X., J. J. Cao, R. Arimoto, R. J. Zhang, D. M. Jie, S. X. Liu, and C. S. Zhu, 2007: Chemical composition and source characterization of spring aerosol over Horqin sand land in northeastern China. *J. Geophys. Res.-Atmos.*, **112**, D14315  
10.1029/2006jd007991.
- Shen, Z. X., and coauthors, 2009: Ionic composition of TSP and PM<sub>2.5</sub> during dust storms and air pollution episodes at Xi'an, China. *Atmos. Environ.*, **43**, 2911-2918, 10.1016/j.atmosenv.2009.03.005.
- Shi, C., M. Roth, H. Zhang, and Z. H. Li, 2008a: Impacts of urbanization on long-term fog variation in Anhui Province, China. *Atmos. Environ.*, **42**, 8484-8492, 10.1016/j.atmosenv.2008.08.002.
- Shi, C. E., and B. N. Zhang, 2008: Tropospheric NO<sub>2</sub> columns over Northeastern North America: Comparison of CMAQ model simulations with GOME satellite measurements. *Adv. Atmos. Sci.*, **25**, 59-71, 10.1007/s00376-008-0059-8.
- Shi, C. N., H. J. S. Fernando, Z. F. Wang, X. Q. An, and Q. Z. Wu, 2008b: Tropospheric NO<sub>2</sub> columns over East Central China: Comparisons between SCIAMACHY measurements and nested CMAQ simulations. *Atmos. Environ.*, **42**, 7165-7173, 10.1016/j.atmosenv.2008.05.046.
- Shi, Z. B., K. B. He, X. C. Yu, Z. L. Yao, F. M. Yang, Y. L. Ma, R. Ma, Y. T. Jia, and J. Zhang, 2007: Diurnal variation of number concentration and size distribution of ultrafine particles in the urban atmosphere of Beijing in winter. *J. Environ. Sci.*, **19**, 933-938.
- Song, Y., S. D. Xie, Y. H. Zhang, L. M. Zeng, L. G. Salmon, and M. Zheng, 2006: Source apportionment of PM<sub>2.5</sub> in Beijing using principal component analysis/absolute principal component scores and UNMIX. *Sci. Total Environ.*, **372**, 278-286, 10.1016/j.scitotenv.2006.08.041.
- Song, Y., M. Shao, Y. Liu, S. H. Lu, W. Kuster, P. Goldan, and S. D. Xie, 2007: Source apportionment of ambient volatile organic compounds in Beijing. *Environ. Sci. Technol.*, **41**, 4348-4353, 10.1021/es0625982.
- Su, H., Y. F. Cheng, M. Shao, D. F. Gao, Z. Y. Yu, L. M. Zeng, J. Slanina, Y. H.

- Zhang, and A. Wiedensohler, 2008: Nitrous acid (HONO) and its daytime sources at a rural site during the 2004 PRIDE-PRD experiment in China. *J. Geophys. Res.-Atmos.*, **113**, D14312  
10.1029/2007jd009060.
- Sun, J. Y., and coauthors, 2010a: Highly time- and size-resolved characterization of submicron aerosol particles in Beijing using an Aerodyne Aerosol Mass Spectrometer. *Atmos. Environ.*, **44**, 131-140, 10.1016/j.atmosenv.2009.03.020.
- Sun, Y., L. L. Wang, Y. S. Wang, D. Q. Zhang, L. Quan, and J. Y. Xin, 2010b: In situ measurements of NO, NO<sub>2</sub>, NO<sub>y</sub>, and O<sub>3</sub> in Dinghushan (112 degrees E, 23 degrees N), China during autumn 2008. *Atmos. Environ.*, **44**, 2079-2088, 10.1016/j.atmosenv.2010.03.007.
- Sun, Y., Y. S. Wang, and C. C. Zhang, 2010c: Vertical observations and analysis of PM<sub>2.5</sub>, O<sub>3</sub>, and NO<sub>x</sub> at Beijing and Tianjin from towers during summer and Autumn 2006. *Adv. Atmos. Sci.*, **27**, 123-136, 10.1007/s00376-009-8154-z.
- Sun, Y. L., G. S. Zhuang, A. H. Tang, Y. Wang, and Z. S. An, 2006: Chemical characteristics of PM<sub>2.5</sub> and PM<sub>10</sub> in haze-fog episodes in Beijing. *Environ. Sci. Technol.*, **40**, 3148-3155, 10.1021/es051533g.
- Tan, J. H., J. C. Duan, D. H. Chen, X. H. Wang, S. J. Guo, X. H. Bi, G. Y. Sheng, K. B. He, and J. M. Fu, 2009a: Chemical characteristics of haze during summer and winter in Guangzhou. *Atmos. Res.*, **94**, 238-245, 10.1016/j.atmosres.2009.05.016.
- Tan, J. H., J. C. Duan, K. B. He, Y. L. Ma, F. K. Duan, Y. Chen, and J. M. Fu, 2009b: Chemical characteristics of PM<sub>2.5</sub> during a typical haze episode in Guangzhou. *J. Environ. Sci.*, **21**, 774-781, 10.1016/s1001-0742(08)62340-2.
- Tang, G., X. Li, Y. Wang, J. Xin, and X. Ren, 2009a: Surface ozone trend details and interpretations in Beijing, 2001-2006. *Atmos. Chem. Phys.*, **9**, 8813-8823.
- Tang, J., M. Wang, H. Cheng, G. Ding, X. Yu, H. Zhou, and G. Liu, 2007: Variation characteristics of ambient NMHCs at Shangdianzi and Lin'an Regional GAW sites. *Acta Meteorologica Sinica*, **21**, 334-341.
- Tang, J., X. B. Xu, J. Ba, and S. F. Wang, 2010: Trends of the precipitation acidity over China during 1992-2006. *Chin. Sci. Bull.*, **55**, 1800-1807, 10.1007/s11434-009-3618-1.
- Tang, J. H., L. Y. Chan, C. C. Chang, S. Liu, and Y. S. Li, 2009b: Characteristics and sources of non-methane hydrocarbons in background atmospheres of eastern, southwestern, and southern China. *J. Geophys. Res.-Atmos.*, **114**, D03304  
10.1029/2008jd010333.
- Tang, W. Y., C. S. Zhao, F. H. Geng, L. Peng, G. Q. Zhou, W. Gao, J. M. Xu, and X. X. Tie, 2008: Study of ozone "weekend effect" in Shanghai. *Sci. China Ser. D-Earth Sci.*, **51**, 1354-1360, 10.1007/s11430-008-0088-2.
- Tie, X. X., and coauthors, 2006: Chemical characterization of air pollution in Eastern China and the Eastern United States. *Atmos. Environ.*, **40**, 2607-2625, 10.1016/j.atmosenv.2005.11.059.
- UNEP, and C<sup>4</sup>, 2002: *The Asia Brown Clouds: Climate and Other Environmental Impacts*, UNEP, Nairobi.
- Wang, G., K. Kawamura, M. Xie, S. Hu, S. Gao, J. Cao, Z. An, and Z. Wang, 2009a:

- Size-distributions of n-alkanes, PAHs and hopanes and their sources in the urban, mountain and marine atmospheres over East Asia. *Atmos. Chem. Phys.*, **9**, 8869-8882.
- Wang, G. H., K. Kawamura, N. Umemoto, M. J. Xie, S. Y. Hu, and Z. F. Wang, 2009b: Water-soluble organic compounds in PM<sub>2.5</sub> and size-segregated aerosols over Mount Tai in North China Plain. *J. Geophys. Res.-Atmos.*, **114**, D19208  
10.1029/2008jd011390.
- Wang, G. H., K. Kawamura, M. J. Xie, S. Y. Hu, J. J. Cao, Z. S. An, J. G. Waston, and J. C. Chow, 2009c: Organic Molecular Compositions and Size Distributions of Chinese Summer and Autumn Aerosols from Nanjing: Characteristic Haze Event Caused by Wheat Straw Burning. *Environ. Sci. Technol.*, **43**, 6493-6499, 10.1021/es803086g.
- Wang, G. L., P. C. Yang, C. X. Liu, Y. Liu, and D. R. Lu, 2010a: Impacts of future NO<sub>x</sub> and CO emissions on regional chemistry and climate over eastern China. *Adv. Atmos. Sci.*, **27**, 750-760, 10.1007/s00376-009-9101-8.
- Wang, H. L., Y. M. Zhou, Y. H. Zhuang, X. K. Wang, and Z. P. Hao, 2009d: Characterization of PM<sub>2.5</sub>/PM<sub>2.5-10</sub> and source tracking in the juncture belt between urban and rural areas of Beijing. *Chin. Sci. Bull.*, **54**, 2506-2515, 10.1007/s11434-009-0021-x.
- Wang, H. X., L. J. Zhou, and X. Y. Tang, 2006a: Ozone concentrations in rural regions of the Yangtze Delta in China. *J. Atmos. Chem.*, **54**, 255-265, 10.1007/s10874-006-9024-z.
- Wang, J. T., K. S. Lam, M. Xie, X. M. Wang, G. Carmichael, and Y. S. Li, 2006b: Integrated studies of a photochemical smog episode in Hong Kong and regional transport in the Pearl River Delta of China. *Tellus Ser. B-Chem. Phys. Meteorol.*, **58**, 31-40, 10.1111/j.1600-0889.2005.00172.x.
- Wang, M., T. Zhu, J. Zheng, R. Y. Zhang, S. Q. Zhang, X. X. Xie, Y. Q. Han, and Y. Li, 2009e: Use of a mobile laboratory to evaluate changes in on-road air pollutants during the Beijing 2008 Summer Olympics. *Atmos. Chem. Phys.*, **9**, 8247-8263.
- Wang, Q. G., Z. W. Han, T. J. Wang, and R. J. Zhang, 2008a: Impacts of biogenic emissions of VOC and NO<sub>x</sub> on tropospheric ozone during summertime in eastern China. *Sci. Total Environ.*, **395**, 41-49, 10.1016/j.scitotenv.2008.01.059.
- Wang, Q. Q., M. Shao, Y. Liu, K. William, G. Paul, X. H. Li, Y. A. Liu, and S. H. Lu, 2007a: Impact of biomass burning on urban air quality estimated by organic tracers: Guangzhou and Beijing as cases. *Atmos. Environ.*, **41**, 8380-8390, 10.1016/j.atmosenv.2007.06.048.
- Wang, S. X., M. Zhao, J. Xing, Y. Wu, Y. Zhou, Y. Lei, K. B. He, L. X. Fu, and J. M. Hao, 2010b: Quantifying the Air Pollutants Emission Reduction during the 2008 Olympic Games in Beijing. *Environ. Sci. Technol.*, **44**, 2490-2496, 10.1021/es9028167.
- Wang, T., X. L. Wei, A. J. Ding, C. N. Poon, K. S. Lam, Y. S. Li, L. Y. Chan, and M. Anson, 2009f: Increasing surface ozone concentrations in the background atmosphere of Southern China, 1994–2007. *Atmos. Chem. Phys.*, **9**, 6217-6227, 10.5194/acp-9-6217-2009.
- Wang, T., and S. D. Xie, 2009: Assessment of traffic-related air pollution in the urban

- streets before and during the 2008 Beijing Olympic Games traffic control period. *Atmos. Environ.*, **43**, 5682-5690, 10.1016/j.atmosenv.2009.07.034.
- Wang, W., J. Z. Ma, S. Hatakeyama, X. Y. Liu, Y. Chen, A. Takami, L. H. Ren, and C. M. Geng, 2008b: Aircraft measurements of vertical ultrafine particles profiles over Northern China coastal areas during dust storms in 2006. *Atmos. Environ.*, **42**, 5715-5720, 10.1016/j.atmosenv.2008.03.042.
- Wang, W., L. H. Ren, Y. H. Zhang, J. H. Chen, H. J. Liu, L. F. Bao, S. J. Fan, and D. G. Tang, 2008c: Aircraft measurements of gaseous pollutants and particulate matter over Pearl River Delta in China. *Atmos. Environ.*, **42**, 6187-6202, 10.1016/j.atmosenv.2008.06.001.
- Wang, W., and coauthors, 2008d: Polar organic tracers in PM<sub>2.5</sub> aerosols from forests in eastern China. *Atmos. Chem. Phys.*, **8**, 7507-7518.
- Wang, X., and coauthors, 2010c: Process analysis and sensitivity study of regional ozone formation over the Pearl River Delta, China, during the PRIDE-PRD2004 campaign using the Community Multiscale Air Quality modeling system. *Atmos. Chem. Phys.*, **10**, 4423-4437, 10.5194/acp-10-4423-2010.
- Wang, X. F., Y. P. Zhang, H. Chen, X. Yang, J. M. Chen, and F. H. Geng, 2009g: Particulate Nitrate Formation in a Highly Polluted Urban Area: A Case Study by Single-Particle Mass Spectrometry in Shanghai. *Environ. Sci. Technol.*, **43**, 3061-3066, 10.1021/es8020155.
- Wang, X. F., S. Gao, X. Yang, H. Chen, J. M. Chen, G. S. Zhuang, J. D. Surratt, M. N. Chan, and J. H. Seinfeld, 2010d: Evidence for High Molecular Weight Nitrogen-Containing Organic Salts in Urban Aerosols. *Environ. Sci. Technol.*, **44**, 4441-4446, 10.1021/es1001117.
- Wang, X. S., J. L. Li, Y. H. Zhang, S. D. Xie, and X. Y. Tang, 2009h: Ozone source attribution during a severe photochemical smog episode in Beijing, China. *Sci. China Ser. B-Chem.*, **52**, 1270-1280, 10.1007/s11426-009-0137-5.
- Wang, X. Y., and coauthors, 2010e: WRF-Chem simulation of East Asian air quality: Sensitivity to temporal and vertical emissions distributions. *Atmos. Environ.*, **44**, 660-669, 10.1016/j.atmosenv.2009.11.011.
- Wang, Y., G. S. Zhuang, Y. L. Sun, and Z. S. An, 2006c: The variation of characteristics and formation mechanisms of aerosols in dust, haze, and clear days in Beijing. *Atmos. Environ.*, **40**, 6579-6591, 10.1016/j.atmosenv.2006.05.066.
- Wang, Y., G. S. Zhuang, X. Y. Zhang, K. Huang, C. Xu, A. H. Tang, J. M. Chen, and Z. S. An, 2006d: The ion chemistry, seasonal cycle, and sources of PM<sub>2.5</sub> and TSP aerosol in Shanghai. *Atmos. Environ.*, **40**, 2935-2952, 10.1016/j.atmosenv.2005.12.051.
- Wang, Y., G. S. Zhuang, S. Chen, Z. S. An, and A. H. Zheng, 2007b: Characteristics and sources of formic, acetic and oxalic acids in PM<sub>2.5</sub> and PM<sub>10</sub> aerosols in Beijing, China. *Atmos. Res.*, **84**, 169-181, 10.1016/j.atmosres.2006.07.001.
- Wang, Y., J. Hao, M. B. McElroy, J. W. Munger, H. Ma, D. Chen, and C. P. Nielsen, 2009i: Ozone air quality during the 2008 Beijing Olympics: effectiveness of emission restrictions. *Atmos. Chem. Phys.*, **9**, 5237-5251.
- Warneck, P., 2000: *Chemistry of the Natural Atmosphere, 2nd Edition*,

Academic Press, San Diego.

Wei, X. L., Y. S. Li, K. S. Lam, A. Y. Wang, and T. J. Wang, 2007: Impact of biogenic VOC emissions on a tropical cyclone-related ozone episode in the Pearl River Delta region, China. *Atmos. Environ.*, **41**, 7851-7864, 10.1016/j.atmosenv.2007.06.012.

Wu, Z. J., and coauthors, 2007: New particle formation in Beijing, China: Statistical analysis of a 1-year data set. *J. Geophys. Res.-Atmos.*, **112**, D09209, doi:10.1029/2006jd007406.

Wu, Z. J., M. Hu, P. Lin, S. Liu, B. Wehner, and A. Wiedensohler, 2008: Particle number size distribution in the urban atmosphere of Beijing, China. *Atmos. Environ.*, **42**, 7967-7980, 10.1016/j.atmosenv.2008.06.022.

Wu, Z. J., M. Hu, K. S. Shao, and J. Slanina, 2009: Acidic gases, NH<sub>3</sub> and secondary inorganic ions in PM<sub>10</sub> during summertime in Beijing, China and their relation to air mass history. *Chemosphere*, **76**, 1028-1035, 10.1016/j.chemosphere.2009.04.066.

Xiao, R., and coauthors, 2009: Formation of submicron sulfate and organic aerosols in the outflow from the urban region of the Pearl River Delta in China. *Atmos. Environ.*, **43**, 3754-3763, 10.1016/j.atmosenv.2009.04.028.

Xie, X., M. Shao, Y. Liu, S. H. Lu, C. C. Chang, and Z. M. Chen, 2008: Estimate of initial isoprene contribution to ozone formation potential in Beijing, China. *Atmos. Environ.*, **42**, 6000-6010, 10.1016/j.atmosenv.2008.03.035.

Xin, J. Y., and coauthors, 2010: Variability and reduction of atmospheric pollutants in Beijing and its surrounding area during the Beijing 2008 Olympic Games. *Chin. Sci. Bull.*, **55**, 1937-1944, 10.1007/s11434-010-3216-2.

Xu, J., Y. H. Zhang, and W. Wang, 2006: Numerical study on the impacts of heterogeneous reactions on ozone formation in the Beijing urban area. *Adv. Atmos. Sci.*, **23**, 605-614, 10.1007/s00376-006-0605-1.

Xu, J., Y. H. Zhang, J. S. Fu, S. Q. Zheng, and W. Wang, 2008a: Process analysis of typical summertime ozone episodes over the Beijing area. *Sci. Total Environ.*, **399**, 147-157, 10.1016/j.scitotenv.2008.02.013.

Xu, X., W. Lin, T. Wang, P. Yan, J. Tang, Z. Meng, and Y. Wang, 2008b: Long-term trend of surface ozone at a regional background station in eastern China 1991-2006: enhanced variability. *Atmos. Chem. Phys.*, **8**, 2595-2607.

Xu, X., and W. Lin, 2010: 1979-2005 trends of tropospheric ozone over China based on the satellite data. *Advances in Climate Change Research*, **6**, 100-105.

Yan, P., J. Tang, J. Huang, J. T. Mao, X. J. Zhou, Q. Liu, Z. F. Wang, and H. G. Zhou, 2008: The measurement of aerosol optical properties at a rural site in Northern China. *Atmos. Chem. Phys.*, **8**, 2229-2242.

Yang, F., H. Chen, X. N. Wang, X. Yang, J. F. Du, and J. M. Chen, 2009: Single particle mass spectrometry of oxalic acid in ambient aerosols in Shanghai: Mixing state and formation mechanism. *Atmos. Environ.*, **43**, 3876-3882, 10.1016/j.atmosenv.2009.05.002.

Yearbook, 2007: *China Environment Yearbook 2006*, Yearbook Publisher, Beijing.

Yin, S., W. G. Wang, and M. F. Ge, 2008: The uptake of ethyl iodide on black carbon surface. *Chin. Sci. Bull.*, **53**, 733-738, 10.1007/s11434-007-0488-2.

- Yu, H., P. C. Wang, X. M. Zong, X. Li, and D. R. Lu, 2010: Change of NO<sub>2</sub> column density over Beijing from satellite measurement during the Beijing 2008 Olympic Games. *Chin. Sci. Bull.*, **55**, 308-313, 10.1007/s11434-009-0375-0.
- Yuan, B., M. Shao, S. H. Lu, and B. Wang, 2010: Source profiles of volatile organic compounds associated with solvent use in Beijing, China. *Atmos. Environ.*, **44**, 1919-1926, 10.1016/j.atmosenv.2010.02.014.
- Yuan, H., G. S. Zhuang, K. A. Rahn, X. Y. Zhang, and Y. L. Li, 2006: Composition and mixing of individual particles in dust and nondust conditions of north China, spring 2002. *J. Geophys. Res.-Atmos.*, **111**, D20208  
10.1029/2005jd006478.
- Yue, D. L., and coauthors, 2009: Characteristics of aerosol size distributions and new particle formation in the summer in Beijing. *J. Geophys. Res.-Atmos.*, **114**, D00G12, doi:10.1029/2008jd010894.
- Yue, D. L., and coauthors, 2010: The roles of sulfuric acid in new particle formation and growth in the mega-city of Beijing. *Atmos. Chem. Phys.*, **10**, 4953-4960, 10.5194/acp-10-4953-2010.
- Zhang, L., H. Liao, and J. P. Li, 2010: Impacts of Asian summer monsoon on seasonal and interannual variations of aerosols over eastern China. *J. Geophys. Res.-Atmos.*, **115**, D00k05  
10.1029/2009jd012299.
- Zhang, M. G., H. Akimoto, and I. Uno, 2006a: A three-dimensional simulation of HO<sub>x</sub> concentrations over East Asia during TRACE-P. *J. Atmos. Chem.*, **54**, 233-254, 10.1007/s10874-006-9015-0.
- Zhang, M. G., I. Uno, R. J. Zhang, Z. W. Han, Z. F. Wang, and Y. F. Pu, 2006b: Evaluation of the Models-3 Community Multi-scale Air Quality (CMAQ) modeling system with observations obtained during the TRACE-P experiment: Comparison of ozone and its related species. *Atmos. Environ.*, **40**, 4874-4882, 10.1016/j.atmosenv.2005.06.063.
- Zhang, X. Y., P. Zhang, Y. Zhang, X. J. Li, and H. Qiu, 2007a: The trend, seasonal cycle, and sources of tropospheric NO<sub>2</sub> over China during 1997-2006 based on satellite measurement. *Sci. China Ser. D-Earth Sci.*, **50**, 1877-1884, 10.1007/s11430-007-0141-6.
- Zhang, X. Y., G. S. Zhuang, J. H. Guo, K. D. Yin, and P. Zhang, 2007b: Characterization of aerosol over the Northern South China Sea during two cruises in 2003. *Atmos. Environ.*, **41**, 7821-7836, 10.1016/j.atmosenv.2007.06.031.
- Zhang, X. Y., Y. Q. Wang, X. C. Zhang, W. Guo, and S. L. Gong, 2008a: Carbonaceous aerosol composition over various regions of China during 2006. *J. Geophys. Res.-Atmos.*, **113**, D14111  
10.1029/2007jd009525.
- Zhang, X. Y., and coauthors, 2009: Changes of atmospheric composition and optical properties over Beijing —2008 Olympic Monitoring Campaign. *Bulletin of the American Meteorological Society*, **90**, 1633-1651, doi:10.1175/2009BAMS2804.1.
- Zhang, Y. H., M. Hu, L. J. Zhong, A. Wiedensohler, S. C. Liu, M. O. Andreae, W. Wang, and S. J. Fan, 2008b: Regional Integrated Experiments on Air Quality over

- Pearl River Delta 2004 (PRIDE-PRD2004): Overview. *Atmos. Environ.*, **42**, 6157-6173, 10.1016/j.atmosenv.2008.03.025.
- Zhang, Y. H., and coauthors, 2008c: Regional ozone pollution and observation-based approach for analyzing ozone-precursor relationship during the PRIDE-PRD2004 campaign. *Atmos. Environ.*, **42**, 6203-6218, 10.1016/j.atmosenv.2008.05.002.
- Zhao, C. S., X. X. Tie, G. L. Wang, Y. Qin, and P. C. Yang, 2006: Analysis of air quality in eastern China and its interaction with other regions of the world. *J. Atmos. Chem.*, **55**, 189-204, 10.1007/s10874-006-9022-1.
- Zhao, J. P., P. A. Peng, J. Z. Song, S. X. Ma, G. Y. Sheng, and J. Fu, 2009: Characterization of organic matter in total suspended particles by thermodesorption and pyrolysis-gas chromatography-mass spectrometry. *J. Environ. Sci.*, **21**, 1658-1666, 10.1016/s1001-0742(08)62470-5.
- Zhao, Y. L., M. Hu, S. Slanina, and Y. H. Zhang, 2007: Chemical compositions of fine particulate organic matter emitted from Chinese cooking. *Environ. Sci. Technol.*, **41**, 99-105, 10.1021/es0614518.
- Zheng, J. Y., L. J. Zhong, T. Wang, P. K. K. Louie, and Z. C. Li, 2010: Ground-level ozone in the Pearl River Delta region: Analysis of data from a recently established regional air quality monitoring network. *Atmos. Environ.*, **44**, 814-823, 10.1016/j.atmosenv.2009.11.032.
- Zhou, J. B., T. G. Wang, Y. P. Zhang, N. N. Zhong, P. M. Medeiros, and B. R. T. Simoneit, 2009: Composition and sources of organic matter in atmospheric PM<sub>10</sub> over a two year period in Beijing, China. *Atmos. Res.*, **93**, 849-861, 10.1016/j.atmosres.2009.04.006.
- Zhu, S., T. Butler, R. Sander, J. Ma, and M. G. Lawrence, 2010: Impact of dust on tropospheric chemistry over polluted regions: a case study of the Beijing megacity. *Atmos. Chem. Phys.*, **10**, 3855-3873.

Table 1. Summary of ozone and its precursors' concentrations (ppbv) observed in Beijing during summertime

Reference	Description	O <sub>3, max</sub>	O <sub>3</sub>	O <sub>x</sub>	CO	NO <sub>x</sub>	SO <sub>2</sub>	NMHC	HCHO	CH <sub>3</sub> CHO
(Tang et al., 2009a)	Six IAP sites, Jul-Sept, 2001	84 <sup>a</sup>	27	60		48				
(Tang et al., 2009a)	Six IAP sites, Jul-Sept, 2002	83 <sup>a</sup>	22	61		60				
(Tang et al., 2009a)	Six IAP sites, Jul-Sept, 2003	85 <sup>a</sup>	28	63		53				
(Tang et al., 2009a)	Six IAP sites, Jul-Sept, 2004	84 <sup>a</sup>	25	59		51				
(Tang et al., 2009a)	Six IAP sites, Jul-Sept, 2005	85 <sup>a</sup>	31	63		45				
(Tang et al., 2009a)	Six IAP sites, Jul-Sept, 2006	83 <sup>a</sup>	28	58		40				
(Xin et al., 2010)	Five IAP sites, Jul-Sept, 2008	62 <sup>b</sup>	37	53		18	3			
(Chen et al., 2009c)	Street site, August, 2006		39	72	3360	49	20			

---

(Chen et al., 2009c)	CRAES site, August, 2006		36	66	1410	39	13		
(Zhang et al., 2009)	CAMS site, August, 2006	154 <sup>c</sup>			1400	25	16		
(Zhang et al., 2009)	CAMS site, August, 2008	118 <sup>c</sup>			647	16	4		
(Shao et al., 2009)	PKU site, August 2004							28	
(Shao et al., 2009)	PKU site, August 2005							36	
(Shao et al., 2009)	PKU site, August 2006							31	9.2 3.9

---

a: daily maximum; b: 8-h maximum; c: hourly maximum.

Table 2. Summary of ozone and its precursors observed in non-urban areas of NC, YRD, and PRD

Sources	Description	O <sub>3</sub>	NO <sub>x</sub>	CO	SO <sub>2</sub>	NMHC	Suppl.
(Meng et al., 2009)	NC, rural, annual	31	13	742	8	-	O <sub>x</sub> : 43
(Lin et al., 2009)	NC, rural, annual	29	29	1520	17	13.7 <sup>b</sup>	O <sub>x</sub> : 47
(Geng et al., 2009)	YRD, suburban, PBL, fall, daytime	35	23	4500	18	4.6	Carbonyl: 0.83
(Geng et al., 2009)	YRD, rural, PBL, fall, daytime	55	5	3500	4	4.6	Carbonyl: 0.83
(Guo et al., 2009)	PRD, suburban, fall	32	45	570	9	26	Carbonyl: 26
(Guo et al., 2009)	PRD, suburban, fall, daytime	35	48	600	10	26	Carbonyl: 26
(Guo et al., 2009)	PRD, rural, fall	40	31	1050	32	39	Carbonyl: 43
(Guo et al., 2009)	PRD, rural, fall, daytime	59	27	1120	32	39	Carbonyl: 43
(Zhang et al., 2008b) <sup>a</sup>	PRD, rural, fall	54	10	730	5	39	
(Wang et al., 2008c)	PRD, rural, PBL, fall, daytime	53	32	-	28	-	

<sup>a</sup> Only the data for one rural site are taken into account. The data for NMHC is estimated from the work of Liu et al (2008e).

<sup>b</sup> The data for NMHC is estimated from the work of Shao et al. (2009).

Table 3a. Summary of PM<sub>2.5</sub> mass concentration and major ionic composition observed in Beijing

Sources	Description	PM <sub>2.5</sub> mass ( $\mu\text{g m}^{-3}$ )	SO <sub>4</sub> <sup>2-</sup> (%)	NO <sub>3</sub> <sup>-</sup> (%)	NH <sub>4</sub> <sup>+</sup> (%)	Ca <sup>2+</sup> (%)	Na <sup>2+</sup> (%)
(Song et al., 2006)	BJ, spring	134	18	17	9.1	-	-
(Song et al., 2006)	BJ, summer	99	29	5.6	7.5	-	-
(Song et al., 2006)	BJ, fall	106	14	17	6.8	-	-
(Song et al., 2006)	BJ, winter	61	14	8.2	5.6	-	-
(Song et al., 2006)	BJ, annual	96	19	12	7.3	-	-
(Han et al., 2007)	BJ, dust	536	1.5	0.3	0.3	-	-
(Han et al., 2007)	BJ, spring	162	9.1	6.0	3.3	-	-
(Han et al., 2007)	BJ, summer	79.6	28	19	9.5	-	-
(Han et al., 2007)	BJ, fall	107	12	11	6.2	-	-
(Han et al., 2007)	BJ, winter	198	15	8.5	6.5	-	-
(Wang et al., 2009d)	BJ, summer	~102	31	20	~20	2.6	-
(Wang et al., 2009d)	BJ, winter	~102	27	17	~12	2.5	-
(Sun et al., 2006)	BJ, winter, haze-fogs	220	9.7	6.3	4.5	0.9	0.1
(Sun et al., 2006)	BJ, winter, haze-fogs	37	4.6	2.5	3.8	4.1	0.6
(Wang et al., 2006c)	BJ, dust	409	3.8	1.2	0.99	1.7	0.35
(Wang et al., 2006c)	BJ, haze	179	22	14	10	1.0	0.34
(Wang et al., 2006c)	BJ, clear	107	10	8.6	4.7	2.8	0.52
(Yan et al., 2008)	NC, rural, summer, polluted	143	41	11	24	-	-

---

(Yan et al., 2008)	NC, rural, summer, clean	25	23	9.8	11	-	-
-----------------------	-----------------------------------	----	----	-----	----	---	---

---

Table 3b. Summary of PM<sub>2.5</sub> mass concentration and major ionic composition observed in Tongliao (TL), Urumuqi (UR), Xi'an (XN), and Shanghai (SH)

Sources	Description	PM <sub>2.5</sub> mass ( $\mu\text{g m}^{-3}$ )	SO <sub>4</sub> <sup>2-</sup> (%)	NO <sub>3</sub> <sup>-</sup> (%)	NH <sub>4</sub> <sup>+</sup> (%)	Ca <sup>2+</sup> (%)	Na <sup>2+</sup> (%)
(Shen et al., 2007)	TL, spring, dust	255	4.2	1.6	0.65	2.4	0.3
(Shen et al., 2007)	TL, spring, no-dust	104	4.9	1.4	0.82	2.0	0.8
(Shen et al., 2007)	TL, spring, pollution	118	15	6.7	4.4	1.8	1.0
(Li et al., 2008b)	UR annual	189	26	5.0	13	1.1	1.2
(Shen et al., 2009)	XN, haze	351	27	16	8.2	0.8	-
(Shen et al., 2009)	XN, dust	138	8.4	2.2	1.0	3.1	-
(Shen et al., 2009)	XN, normal	130	21	9.2	5.8	1.0	-
(Wang et al., 2006d)	SH, spring	135	8.6	6.7	3.0	1.1	0.4
(Wang et al., 2006d)	SH, summer	72	7.6	3.6	3.4	2.2	0.7
(Wang et al., 2006d)	SH, fall	96	9.0	3.8	3.7	0.8	0.4
(Wang et al., 2006d)	SH, winter	76	17	11	5.8	1.8	0.7
(Wang et al., 2006d)	SH, annual	95	11	6.6	4.0	1.3	0.6
(Fu et al., 2008)	SH, winter, normal	56	17	12	13	2.8	0.1
(Fu et al., 2008)	SH, winter, haze	311	25	17	11	0.8	0.6



Table 3c. Summary of PM<sub>2.5</sub> mass concentration and major ionic composition observed in Guangzhou, South China Sea (SC-Sea), and the four forests, i.e., Changbai Mountain Nature Reserve (CB), Dongping National Forest Park in Chongming Island (CM), Dinghu Mountain Nature Reserve (DH), and Jianfengling Nature Reserve in Hainan Island (HN).

Sources	Descript ion	PM <sub>2.5</sub> mass ( $\mu\text{g m}^{-3}$ )	SO <sub>4</sub> <sup>2-</sup> (%)	NO <sub>3</sub> <sup>-</sup> (%)	NH <sub>4</sub> <sup>+</sup> (%)	Ca <sup>2+</sup> (%)	Na <sup>2+</sup> (%)
(Lai et al., 2007)	GZ, summer	111	14	7.8	2.6	-	4.1
(Lai et al., 2007)	GZ, winter	82	21	5.0	2.4	-	4.5
(Hu et al., 2008)	GZ, fall	-	24	7.2	9.2	-	-
(Tan et al., 2009b)	GZ, winter, normal	95	8.7	4.9	3.6	2.5	0.87
(Tan et al., 2009b)	GZ, winter, haze	236	14	20	13	2.6	1.3
(Zhang et al., 2007b)	SC-Sea, winter	28	44	20	22	0.86	0.71
(Zhang et al., 2007b)	SC-Sea, spring	10	43	21	18	2.2	3.1
(Li et al., 2010b)	CB, summer	39	33	0.85	10	0.39	0.18
(Li et al., 2010b)	CM, summer	89	26	12	12	0.43	2.0
(Li et al., 2010b)	DH, summer	30	34	1.5	10	0.92	1.7
(Li et al., 2010b)	HN, winter	18	12	7.2	3.1	1.2	3.4

Table 4a. Summary of the classes of organic compounds ( $\text{ng m}^{-3}$ ) identified from PM<sub>2.5</sub> in Beijing (BJ) and from PM<sub>2.1</sub> in Baoji (urban), Mt. Tai (MT), Okinawa Island (OI) Guangzhou (GZ)

Sources	Description	n-Alkanes	PAHs	Fatty acids	Dicarboxylic acids	Hopanes	Total
(Huang et al., 2006)	BJ, spring	52	19	26	20	4	359
(Huang et al., 2006)	BJ, summer	39	9	370	27	2	452
(Huang et al., 2006)	BJ, autumn	183	65	483	42	9	792
(Huang et al., 2006)	BJ, winter	477	283	466	16	16	1283
(Huang et al., 2006)	BJ, annual	163	79	385	27	7	669
(He et al., 2006)	BJ, summer	51	16	314	52	5	502
(He et al., 2006)	BJ, autumn	333	119	512	58	14	1471
(He et al., 2006)	BJ, winter	375	259	363	27	14	1403
(Wang et al., 2009a)	Urban, spring	377	153	-	-	16	-
(Wang et al., 2009a)	Urban, winter	1461	500	-	-	57	-
(Wang et al., 2009a)	MT, summer	30	8	-	-	0.1	-

Table 4b. Summary of the classes of organic compounds ( $\text{ng m}^{-3}$ ) identified from  $\text{PM}_{2.5}$  in Changdao Island (CI)

Sources	Description	n-Alkanes	PAHs	Fatty acids	Dicarboxylic acids	Hopanes	n-Alkanols
(Wang et al., 2009a)	MT, winter	100	49	-	-	1	-
(Wang et al., 2009a)	OI, spring	5	1	-	-	-	-
(Feng et al., 2007)	CI, spring	90	29	172	-	2.2	28
(Feng et al., 2007)	CI, summer	26	7	102	-	2.4	23
(Feng et al., 2007)	CI, fall	55	21	131	-	2.1	20
(Feng et al., 2007)	CI, winter	214	123	291	-	4.6	29

# PROGRESSES IN THE ATMOSPHERIC ELECTRICITY RESEARCHES IN CHINA DURING 2006-2010

Xiushu Qie<sup>1</sup>, Yijun Zhang<sup>2</sup>, Qilin Zhang<sup>3</sup>, Baoyou Zhu<sup>4</sup>, Tie Yuan<sup>5</sup>, Tinglong Zhang<sup>6</sup>

1 Key Laboratory of Middle Atmosphere and Global Environment Observation (LAGEO), Institute of Atmospheric Physics, Chinese Academy of Sciences, Beijing 100029, China

2 Laboratory of Lightning Physics and Protection Engineering, Chinese Academy of Meteorological Sciences, Beijing 100081, China

3 College of Atmospheric Physics, Nanjing University of Information Technology, Nanjing 210044, China

4 School of Earth and Space Sciences, University of Science and Technology of China, Hefei 230026, China

5 College of Atmospheric Science, Lanzhou University, Gansu 730000, China

6 Laboratory for Climate Environment and Disasters of Western China, Cold and Arid Regions Environmental and Engineering Research Institute, Chinese Academy of Sciences, Lanzhou 730000, China

## ABSTRACT

Research progresses on atmospheric electricity in the last five years in China are briefly reviewed. This research area has been greatly expanded through artificially triggering lightning experiment and increased use of high time-spatial resolution detection and location techniques of lightning. The main results described in this review are summarized in the following five aspects, including processes and parameters inferred from artificially triggering lightning experiment, lightning physics and effects: observation and theoretical study, lightning activities associated with different thunderstorms, numerical simulation on thunderstorm electrification and lightning discharge, and response of lightning to the climate change.

## 1. Introduction

Atmospheric electricity is composed of a wide range of electric phenomena in the atmospheres including troposphere, stratosphere and even lower ionosphere. In recent years, atmospheric electricity has received more and more attention not only because of several new discovered phenomena, such as Sprites, Elves, Jets, and TGFs, but also because of its importance in research fields of severe convective storm, climate change, lightning forecasting and protection, and so on. Researches in atmospheric electricity in China mainly focus on lightning and thunderstorm electricity in recent years. In a paper from Qie et al. (2006), main progresses in atmospheric electricity during 1996-2004 were reviewed. The paper paid more attention to the researches on lightning discharges and electrical structure of thunderstorm. The knowledge on lightning and thunderstorm electricity has been

stimulated in the last five years because of new lighting detection technologies with high time-spatial resolution. In the present paper, research progresses in the lightning and thunderstorm electricity in China mainly from 2006 to 2010 will be reviewed.

## **2. Processes and parameters inferred from artificially triggering lightning**

Artificially triggering lightning experiments with rocket-trailing-wire technique were conducted separately in Binzhou, Shandong since 2005 (e.g. Qie et al., 2007a) and Conghua, Guangdong since 2006 (Li et al., 2010). A new-model rocket for artificial triggering lightning was developed and applied successfully into the experiment recently in China (Qie et al., 2010). The body of the rocket is made of composite material, and parachute is assembled inside the rocket. The new-developed rocket for triggering lightning provide a crucial tool not only for the study of lightning and its effects, but also for the data accumulation of lightning current waveforms which is essential to the lightning protection design. Two triggering techniques, classical triggering and altitude triggering, have been used during both experiments. Classical triggering technique involves launching a small rocket trailing a thin, grounded copper wire toward the charged cloud overhead. In altitude triggering technique, the rocket usually spools out 50-100 m of insulating nylon followed by several hundred meters of copper wire. The altitude triggering technique simulates natural lightning better than the classical one because of downward stepped leader and first return stroke can be triggered in altitude triggered lightning.

### **2.1 Discharge current and close electromagnetic field of triggered lightning**

The discharge current and close electromagnetic fields of lightning are two important parameters for both understanding of lightning physics and design of lightning protection. The current and corresponding close electromagnetic field were studied based on the data from the Shandong Artificially Triggering Lightning Experiment (SHATLE) which started from 2005 (Q. L. Zhang et al., 2006; 2007; Qie et al., 2007a; Y. Zhao et al., 2009). Figure 1 shows two of the triggered lightning pictures taken at two different distances during SHATLE 2005. According to Yang et al. (2010), the peak currents for 27 direct measured negative return strokes varied from 5.8 kA to 45.7 kA with a geometric mean (GM) of 14.1 kA. The GM of 10-90% risetime, 30-90% risetime and half-peak width in current waveforms were consistent with most of the results found in the literature. Based on the Diendorfer and Uman (DU) model, Q. Zhang (2009) calculated the return-stroke current waveforms and charge distribution along the lightning channel. The simulated current waveforms, being divided into breakdown and corona current components, are in agreement with the optical measurements when the two different discharge time constants are properly chosen.

Yang et al. (2008a) developed a magnetic field measuring system with two rectangular loops perpendicular to each other and detected the total horizontal magnetic field produced by lightning discharges. The magnetic fields at 60 m varied from 18  $\mu\text{T}$  to 148  $\mu\text{T}$  with a GM of 52  $\mu\text{T}$ . The peak value of the 10-90% risetime in magnetic field waveform was between 1 and 2  $\mu\text{s}$  with a minimum of 0.4  $\mu\text{s}$  and a maximum of 8.4  $\mu\text{s}$  (Yang et al., 2010). The vertical electric field changes of the leader/return stroke sequences of triggered lightning discharges at 60 m and 550 m

appear asymmetrical V-shaped (Qie et al. 2009a; Q. Zhang et al., 2008). The electric field changes of the dart leaders at 60 m and 550 m are 17.9 kV/m and 1.3 kV/m, respectively, yielding a horizontal distance dependence of  $d^{-1.18}$ .

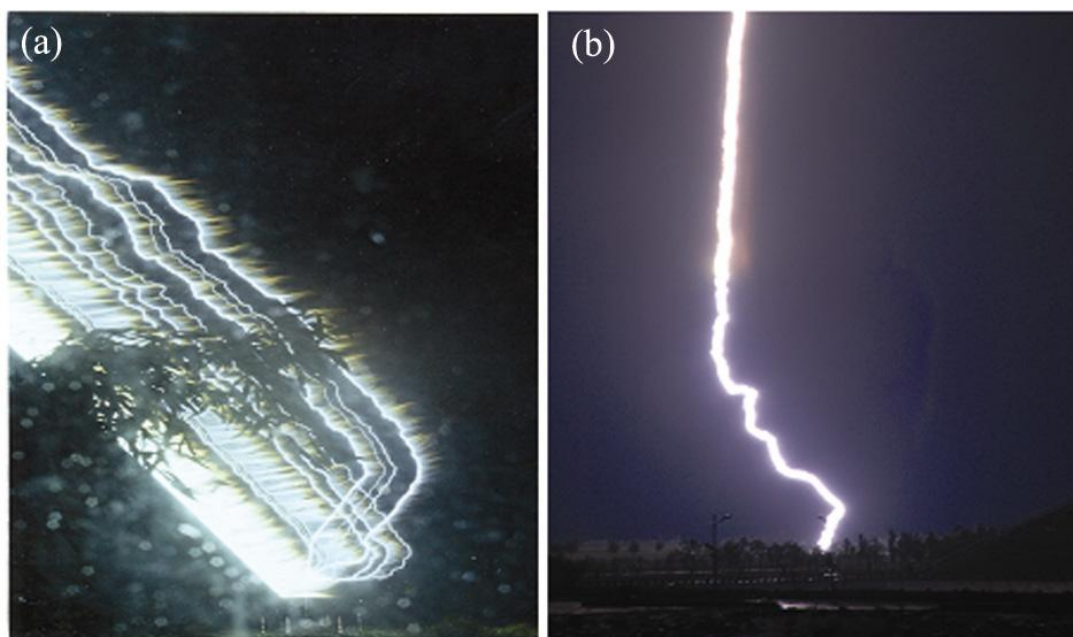


FIG. 1. Pictures of two triggered lightning flashes. (a) Flash 0503 taken at 60 m by using classical triggering technique. (b) Flash 0504 taken at 550 m by using altitude triggering technique. [Adapted from Qie et al. (2007a).]

## 2.2 Lightning processes and discharge channel features

Lu et al. (2009) found the 2-D propagation speed of the upward positive leader in its inception phase was about  $3.8\text{-}5.5 \times 10^4$  m/s. The stable downward negative leader propagated with a 2-D speed of about  $1.9 \times 10^5$  m/s, an average step length of about 3 m, and a stepping time interval varying from 6  $\mu\text{s}$  to 31  $\mu\text{s}$  with a mean value of 15  $\mu\text{s}$ . Yang et al. (2009) analyzed the initial discharge stages of two triggered flashes based on the synchronous data of the current and close electromagnetic field. C. Wang et al. (2010) found 7 large M components in a triggered lightning and the M-components have a GM duration of 2.2 ms and peak of 1.4 kA varied from 0.1 kA to 7.0 kA. The GM charge transferred by individual M event was 238 mC which range from 31 mC to 821 mC. Zheng et al. (2006) and J. Yang et al. (2006) calculated some parameters for artificially triggered lightning leader based on the slow electric field change data during SHATLE. The results indicated that the line density of charge along the leader channel was from  $49.3 \text{ mC m}^{-1}$  to  $130.0 \text{ mC m}^{-1}$ , the average dart leader speed was from  $0.23 \times 10^7 \text{ m s}^{-1}$  to  $1.48 \times 10^7 \text{ m s}^{-1}$ , the charge neutralized by subsequent return stroke was from 0.16 C to 1.21 C.

## 3. Lightning physics and effects: observation and theoretical study

In the last five years, field experiments of natural lightning aimed at the understanding on the lightning physics and effects have been conducted continuously, mainly using lightning location techniques and high speed video cameras. Incorporation with the theoretical study, some new phenomena has been revealed and explained.

### 3.1 Some new insights into the stepped leader and ground contacts

By using the high-speed video camera with a time resolution higher than 1000 frame per second (f/s) in correlation with broadband electric field change signatures, some new insights into the stepped leader in negative CG flashes have been documented (Qie and Kong 2007b; Lu et al. 2008a; b; Y. Zhang et al. 2009a; Kong et al., 2009). Qie and Kong (2007) and Kong et al. (2009) studied the progression features of the stepped leader with multiple grounded branches in detail. Figure 2 shows parts of the progression images of the branched downward stepped leaders which induced four return strokes in turn. The corresponding time differences between two adjacent peaks in the waveform of electric field change were about 4 ms, 9 ms, and 10 ms, respectively. The 1-D distances between two adjacent terminations from left to right, estimated from the images, were 184 m, 245 m, and 490 m, respectively. The average speed for the four branches was about  $1.1 \times 10^5 \text{ m s}^{-1}$ .

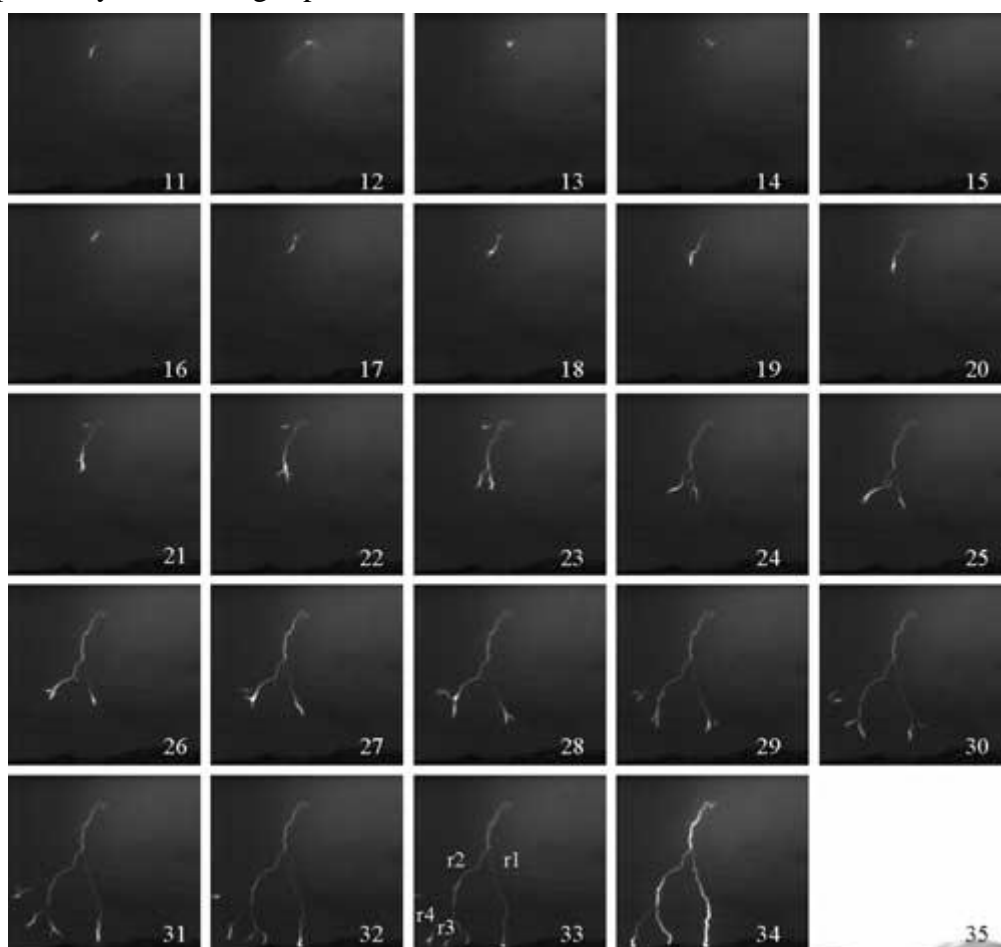


FIG. 2. Parts of the video frames from high-speed digital camera during the stepped leader progression from 11 ms to 35 ms with a time interval between two adjacent images of 1 ms. The corresponding time is shown in lower-right corner of the images. The return stroke occurred at 35 ms. [Adapted from Qie and Kong (2007).]

Lu et al. (2008a) analyzed the optical pulse characteristics of a downward stepped leader with six ungrounded branches, and found that the pulses originated from the

main channel and the branches were almost identical in terms of GM values of 10-90% rise time and half-peak width, which were around 0.4  $\mu\text{s}$  and 1.1  $\mu\text{s}$ , respectively. With the propagation of the leader toward the ground, the light intensity just prior to each pulse exhibited an apparent tendency of increase. From the statistic analysis on the waveform signatures of 59 lightning first return strokes, Kong et al. (2009) found that about 15.3% were characterized by two or more peaks separated in time by 4-486  $\mu\text{s}$ , which means one lightning could strike at more than one points, suggesting the necessary to reevaluate the present lightning density distribution, which assumes that one lightning strikes only one point. Lu et al. (2009b) performed a study of two associated upward lightning flashes that involved two adjoining tall grounded objects with a time difference of about 45.8 ms, and suggested that one upward lightning flash can trigger other upward lightning of opposite polarity from nearby tall grounded objects.

### 3.2 VHF radiation and 3-D mapping of lightning discharge channel

The lightning VHF radiation observations have been used to study the radiation characteristics from lightning discharges (Wang et al. 2007; Cao et al. 2008), narrow bipolar pulses (Zhu et al. 2007; G. Zhang et al. 2010; Zhu et al., 2010), and to track lightning discharge channel and infer the charge structure inside thunderstorm through the location techniques of VHF radiation pulses (G. Zhang et al. 2008; 2010; Qiu et al., 2009).

The 3-D images of the lightning progression were obtained successfully for the first time in China based on a 3-D Location System of Lightning VHF Radiation Pulses (LLR) (G. Zhang et al. 2010). Significant differences between the negative and positive CG flashes in terms of the initiation and propagation of the radiation sources were found. Figure 3 shows an example of 3-D channel evolution of a typical negative CG flash based on the LLR observation. The preliminary breakdown of negative CG flashes propagated at a speed of about  $5.2 \times 10^4 \text{ m s}^{-1}$ . The stepped leader of negative CG flashes was triggered by negative initial breakdown, and propagated downward at a speed of  $1.3 \times 10^5 \text{ m s}^{-1}$ . The locating results of lightning discharge channel are in good agreement with that depicted by lightning mapping array (LMA) (Y. Zhang et al., 2006a). G. Zhang et al. (2008) also developed a narrow band VHF interferometer and used into study on a -CG flash containing 19 strokes. They found that the preliminary breakdown events of the CG flash started from the negative charge region and exhibited a downward and then an upward propagation. The progression speed of initial stepped leaders was about  $10^5 \text{ m s}^{-1}$ , while that was about  $4.1 \times 10^6$  and  $6.0 \times 10^6 \text{ m s}^{-1}$  for dart leaders and dart-stepped leaders, respectively. The mean progression speed of M events was about  $7 \times 10^7 \text{ m s}^{-1}$ . A new type of lightning discharge, referred as narrow bipolar pulse (NBP) was also studied based on the LLR location images (G. Zhang et al. 2009). The NBP was originated at an altitude of about 10.5 km. As a distinct difference from normal IC flashes, their channels extended horizontally all around and produced a lot of radiation sources. The source power of the NBP could approach 16.7 kW, which is much greater than that of normal lightning discharges ranging from 100 mW to 500 W.

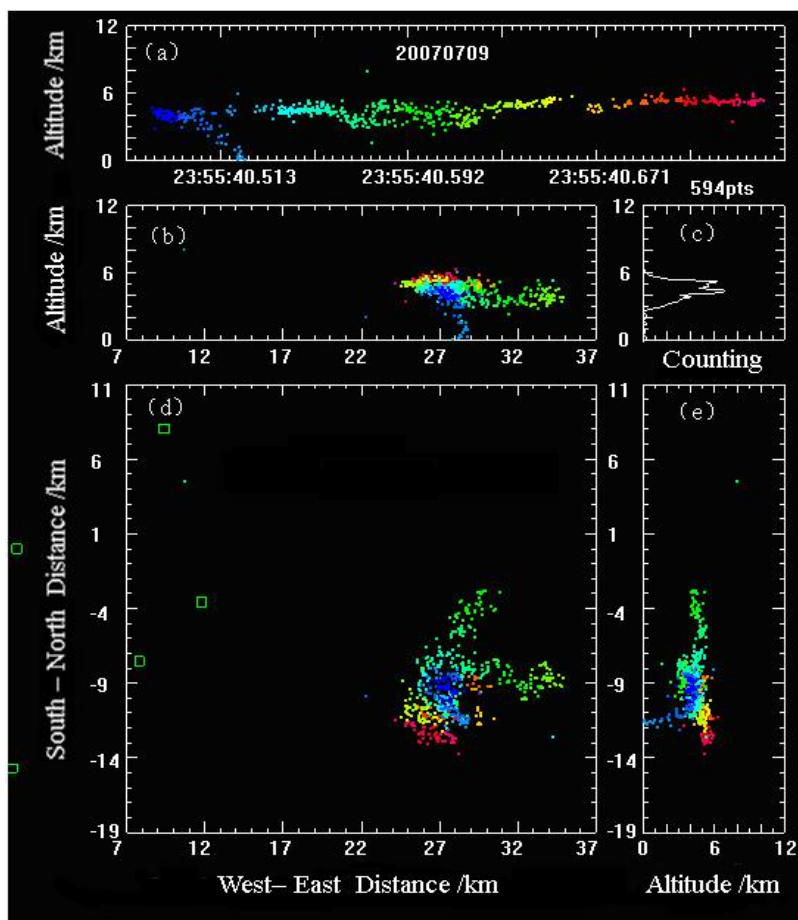


FIG. 3. 3-D channel evolution of typical negative CG flash based on the LLR observation. (a) The different panels show height-time evolution, (b) north-southward vertical projection, (c) height distribution of the number of radiation events, (d) plan view, and (e) east-westward vertical projection of lightning radiation sources. [Adapted from G. Zhang et al. (2009).]

### 3.3 Electromagnetic effects of return stroke and its non-linear fractal nature

Return stroke produces the most readily identifiable electromagnetic signature and the most serious lightning-induced damage. Yang et al. (2008) analyzed the characteristics of induced voltage in a horizontal conductor due to a nearby lightning discharge with 9 dart leader/return stroke sequences. The measured voltage induced by the return strokes varied from 4.6 kV to 18.6 kV. The simulated results showed that the induced voltage on both ends of the horizontal conductor would increase with increasing return stroke velocity and also with increasing height of the horizontal conductor.

Gou et al. (2007) suggested that lightning could be regarded as a large-scale cooperative phenomenon and it evolves in a self-similar cascaded way. Based on the electric field change waveforms recorded by the slow antenna system, Gou et al. (2006) found, using a technique of wavelet-based local effective Hölder exponent, that the Hölder exponents sharply decreased to its minimum with the occurrence of return stroke. The standard deviation of Hölder exponent reached its maximum just

before return stroke. Gou et al. (2009) also found that the fractal dimension of the electric field waveforms ranged from 1.2 to 1.5 with an average of 1.3. Zhao and Zhang (2009) found that the tortuosity of lightning channel should be taken into account in the calculation of lightning electromagnetic field when the tortuosity of the channel was considered. Gou et al. (2010) presents the analysis of fractal dynamics of lightning initiation process with a coherent approach, and find that there is an apparent long-range time correlated and nonlinear cascade behavior within the initiation breakdown process of the lightning. This result suggests that the initiation of lightning may be associated with progressively building up of correlated strong electrical field regions by self-similar scaling up (inverse cascading) of discharges across scales from small to large. The result may be promising toward our understanding of lightning initiation.

### **3.4 Spectra and electron density of lightning discharge channel**

The spectra of discharge channels are closely related to the plasma properties and the temperature of the channels (Yuan et al. 2006). More lines of OII with high excited energy were found in the spectra of IC lightning discharges in comparison with that of CG flashes (J. Wang et al. 2009). According to the relative intensities of spectra lines and transition parameters, the temperatures for individual lightning strokes and at different heights of the discharge channels were calculated by using multiple-line method by Ouyang et al. (2006). The result showed that the temperatures in return stroke channels varied from 29,000 K to 36,000 K. M. Zhang et al. (2007) calculated the electron density according to Ha line Stark broadening formula. It was found that the electron density varied from  $4.68$  to  $5.03 \times 10^{17} \text{ cm}^{-3}$ . Simultaneously, with Saha equation, the electron density was found to be from  $9.03$ - $17.5 \times 10^{17} \text{ cm}^{-3}$ . Generally, the more intense the lightning discharge, the higher the channel temperature, the higher the electron density and the relative concentration of highly ionized particles, but the lower the concentration of neutral atoms.

### **3.5 New observational evidences on positive CG lightning flashes**

Positive CG flashes are less understood than negative ones because of the lack of observation data. Kong et al. (2008) reported one positive CG flash with pronounced stepped leader. The 2-D propagation speed increased from  $0.1 \times 10^5 \text{ m s}^{-1}$  to  $3.8 \times 10^5 \text{ m s}^{-1}$  as the leader approached the ground. Using the data from LMA, J. Zhang et al. (2006b) found that a positive CG lightning could be divided into three stages. The first stage was the discharge process in cloud which lasted about 370 ms and propagated at a velocity of  $10^5 \text{ m s}^{-1}$ . During the stage after the return stroke of the positive CG lightning, the lightning channels propagated at a velocity of 2 times faster than that before the return stroke. This stage involved lots of positive fast impulses and corresponded to the continuing current process producing less and dispersed radiation points and more intensive radiation powers. During the final stage of the positive CG lightning, the lightning channels developed at a velocity equal to that before the return stroke and the radiation points appeared mainly at the end of channel. All of the radiation points of the positive CG lightning appeared in the positive charge region of cloud. Little or no radiation was detected during the positive leader just before the return stroke.

### 3.6 Lightning-induced red sprite above thunderstorms

Transient luminous events (TLEs), including sprites, elves, jets, halos and gigantic jets, are discharges that occur above the thunderstorms and last for a very short time. These short lived optical emissions in the mesosphere can be from the tops of the thunderclouds and reach up to the ionosphere, which provide direct evidence of coupling from the lower atmosphere to the upper atmosphere. The Chinese Sprites Observation Campaign (CSOC), aimed at understanding the characteristics of the sprites over mainland China and the relationships between sprites, lightning flashes and thunderstorms, has been conducted since the summer of 2007 (Yang et al. 2008c). Figure 4 shows some images of the recorded sprites. All of the observed sprites occurred in cluster, and their appearances were very different. The estimated bottom elevation of one columniform sprites was about  $47 \pm 12$  km and the top was  $86 \pm 15$  km. The vertical length of one carrot sprites was about 42 km, with the bottom at  $39 \pm 10$  km and the top at  $81 \pm 14$  km. The duration of the sprites varied from a minimum of 40 ms to a maximum of 160 ms with a mean value of 61 ms. All of the parental flashes that produced sprites were positive CG flashes which located in large stratiform precipitation regions with radar reflectivity between 20 dBZ and 40 dBZ. The time delay between parental +CG flashes and the associated sprites varied from 3.4 ms to 11.8 ms.

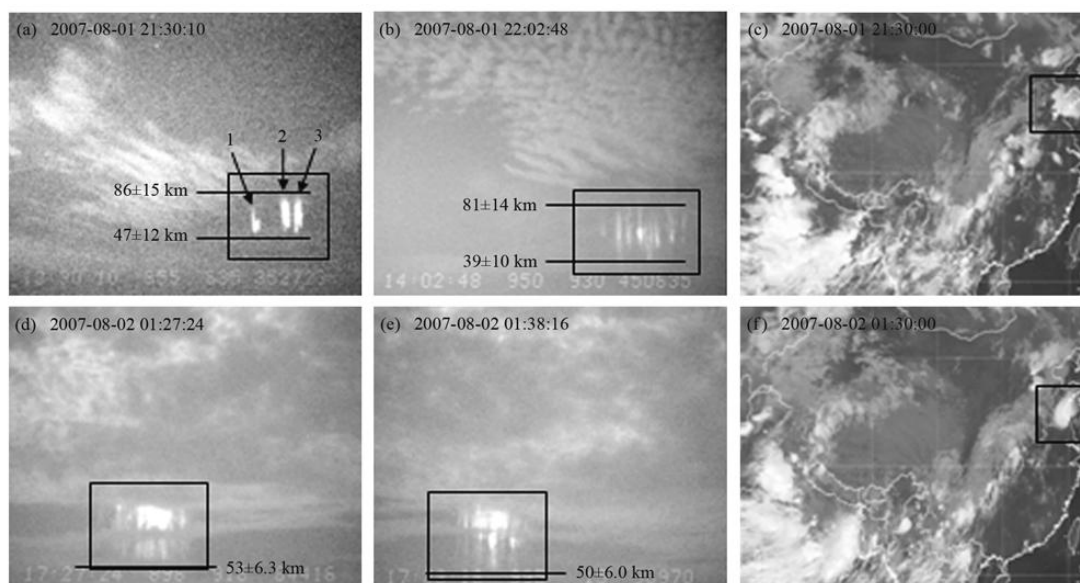


FIG. 4. Sprite images (a, b, d and e, squares mark the sprites). Satellite infrared weather maps of the sprites-producing thunderstorms, located southeast of the observation station, are shown in (c) and (f) (squares mark the thunderstorms). [Adapted from Yang et al. (2008c).]

### 4. Lightning activities associated with different thunderstorms

Lightning flash can be an indicator of vigorous convection, and the understanding of lightning activity in different thunderstorms is important in the severe convective research and forecasting. The lightning activity and its relationship with dynamic process and precipitation structure in different severe convective weather systems and

isolated thunderstorms in the Tibetan plateau have been studied in the last five years.

#### **4.1 Lightning characteristics in different severe thunderstorms**

The lightning characteristics in different thunderstorms such as hailstorms, mesoscale convective systems (MCSs), and squall lines have been studied. Significant differences of lightning characteristics have been found in severe storms related to different synoptic processes. The hailstorms usually presented dominant +CG flashes during the period of hail fall (Feng et al., 2006a; 2007; 2008; Liu et al., 2009). The +CG flashes took about more than 45% of total CG flashes in one Shandong hailstorm case (Feng et al., 2008), which was much higher than the climatic mean value (12.5%) in the region. The hail-falling was often reported in the region of dense +CG lightning. Sometimes hailstone appeared slightly at the right flank of the dense CG lightning region. The peak -CG flash rate usually occurred 0 to 20 minutes earlier than hailstone falling, but the peak +CG flash rate usually appeared at the time of or after the advent of hail fall. Based on the total lightning information from SAFIR3000 3-D lightning location system in Beijing, Zheng et al. (2009) found that the peak of the lightning frequency came about five minutes prior to the hail falling. Only 6.2% of the total lightning was CG lightning, among which 20% was positive.

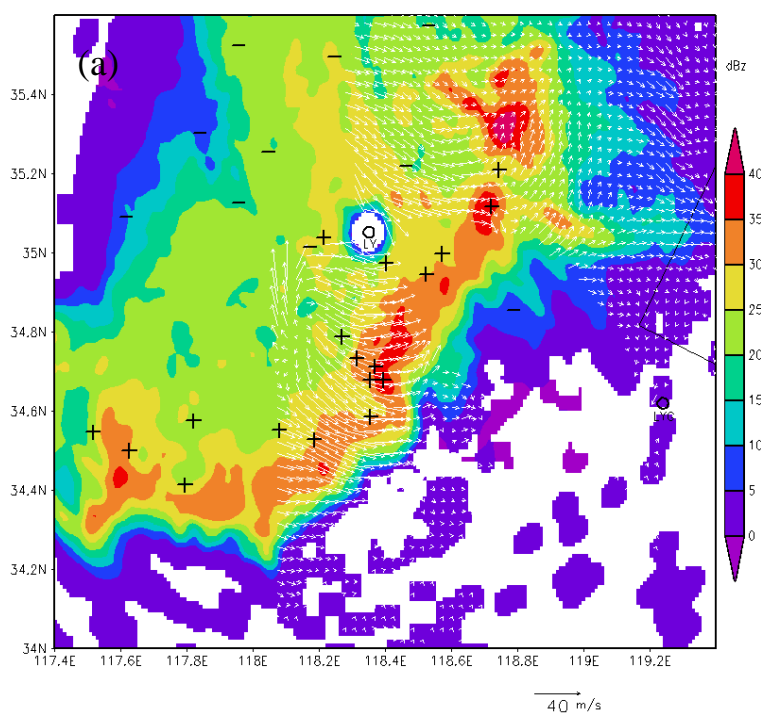
Feng et al. (2006b) and Liu et al. (2008) analyzed the evolution of CG flashes in typical mesoscale convective system (MCSs). They found that almost all the CG flashes were negative at the first developing stage. The CG flash rate was high (more than 10 flashes  $\text{min}^{-1}$ ) and -CG flash predominated during the mature stage of the storm. The CG flash rate declined rapidly with the increase of +CG lightning ratio at the dissipating stage. During the whole lifetime of MCS, most -CG flashes occurred in the strong convective echo regions with radar reflectivity stronger than 40 dBz, and its duration almost corresponds to the period of strong convection. Feng et al. (2009) studied a typical squall line system with damaging wind and hailstones causing great economic loss. It was shown that +CG flashes accounted for 54.7% of the total CG flashes. +CG flashes tended to occur on the right flank and negative ones on the left flank. Strong wind at the surface occurred in or near the regions with dense +CG flashes. Almost all +CG flashes occurred near the strong radar echo regions and in the front parts of the squall line. However, the -CG flashes almost exclusively occurred in the regions with weak and uniform radar echoes.

The electrical structure of the hailstorm was inverted in the stage of the hail falling, with the main negative charge region located around the  $-40^{\circ}\text{C}$  level and the main positive charge region around the  $-15^{\circ}\text{C}$  level (Zheng et al., 2009). In addition, a weak negative charge region existed below the positive charge region transitorily. After the hail falling, the electrical structure underwent fast and persistent adjustments and became a normal tripole. The charge structures in the convective region of supercell thunderstorms were inverted tripole (Y. Zhang et al., 2006c). The positive CG lightning discharges occurred in the main part of the thunderstorms and originated from the positive charge region located at the middle part of the thunderstorms, while the negative CG lightning discharges occurred in the anvil of the thunderstorm. There are three distinct flash activity regions in mature typhoons (Pan et al., 2009), a weak maximum in the eyewall regions (20-80 km from the center), a minimum between

80-200 km from the center, and a strong maximum in the outer rainbands (>200 km radius). The lightning in the outer rainbands was more than that in the inner rainbands, and less than 1% of flashes occurred within 100 km. Few lightning flashes occurred near the center after landfall. Each typhoon produced eyewall lightning outbreak during its intensification period and before the maximum intensity, indicating that lightning activity might be used as a proxy for typhoon intensity change.

#### 4.2 Relationship of lightning to precipitation and dynamical processes

Combing the ground-based Doppler radars and the cloud images from the Geostationary Meteorological Satellites (GMS), Liu et al. (2009) found that most flashes for the hailstorms occurred in the region with temperature lower than  $-40\text{ }^{\circ}\text{C}$ , while dense +CG flashes occurred in the region between  $-40\text{ }^{\circ}\text{C}$  and  $-50\text{ }^{\circ}\text{C}$ . -CG flashes occurred mostly in the relative weak radar echo region, and +CG flashes were distributed in the strong echo region especially with a large gradient of echo intensity. The comparison between the wind field retrieved from Doppler radar and the location of CG flashes indicated that the flashes were located in the convergent region at lower to middle levels. Feng et al. (2006b) found that the relationship between +CG and -CG flash number and cloud top brightness temperature in a MCS could be fitted preferably by 3 power polynomial. Feng et al. (2009) found that the dense +CG flashes usually corresponded to updraft regions of the squall line system, and did not occur in the core of the updraft, but just behind and close to the main updraft instead (refer to Figure 5). The rear in flow jet, between 3 and 6 km, played an important role in the formation of the bow echo and very strong wind at surface. Yuan and Qie (2010) found that most of lightning flashes occurred in the region of low brightness temperature for the squall line system, especially the region lower than 200 K, and a few flash could also be observed in the region of 240-260 K, which usually corresponded to the stratiform region of squall lines.



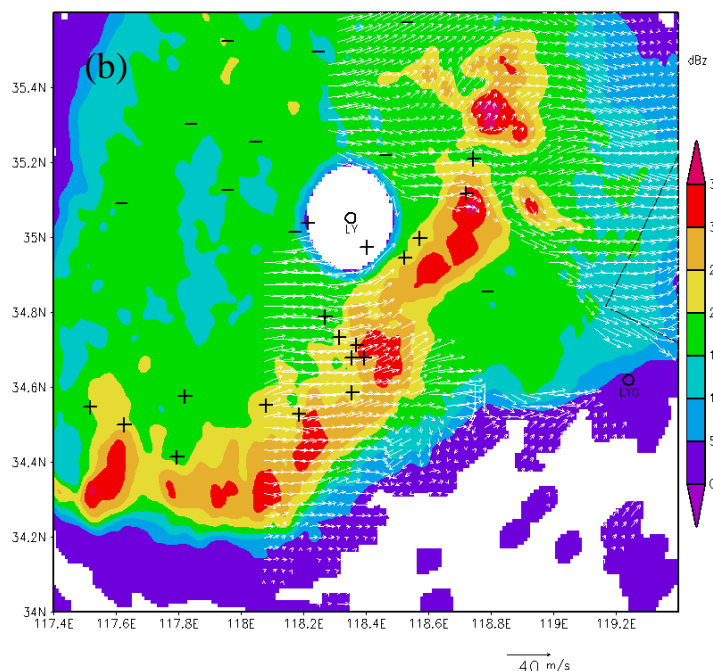


FIG. 5. Horizontal wind field retrieved and reflectivity at different levels. (a) at 3.0 km, and (b) at 6.0 km at 1021 UTC. '+', '-' standing for positive and negative CG flashes within 5 min centered around 1021 UTC. [Adapted from Feng et al. (2009).]

Based on the TRMM data, Feng et al. (2007) found that the probability of lightning occurrence was 20 times higher in convective region than in stratiform region. The convective rain contributed much more rainfall to the total than stratiform rain, and the convective rain took more than 85% of the total in two hailstorms. The linear relationship between flash rate and ice water content was obtained, and its correlation coefficient was about 0.69. The intensity of updrafts at 5 km MSL could be used as an indicator of lightning activities. Yuan and Qie (2010) found that convective rains only occupied half of area of stratiform rains, but the former contributed much more rainfall to the total than the latter. Most lightning flashes occurred near strong convective region, and a few flashes occurred in the stratiform region of the squall line. At 6 km MSL, most of lightning flashes occurred in the echo region between 35 and 50 dBZ, and fewer flashes in the echo region smaller than 30 dBZ. There was a strong relationship between flash rate and ice precipitation content at 7-11 km MSL at a convective cell scale. Yuan and Qie (2008) found that when maximum radar reflectivity at 7 km MSL reached 36 dBZ, the probability of lightning occurrence was 50% in the premonsoon season, and it increased to 38 dBZ in the monsoon season. The flash rate of precipitation systems could be expressed as functions of maximum storm top height, maximum snow depth and minimum polarization corrected temperatures (PCTs), respectively. Among those, the most stable one was the relationship between flash rate and maximum snow depth.

#### 4.3 Thunderstorm electricity in the Tibetan plateau and its surrounding areas

The thunderstorm electricity at four different plateau regions have been studied (e.g., Kong et al., 2006; Qie et al., 2009b; T. Zhang et al. 2009a; b; Cui et al., 2009), including Naqu located at the central Tibetan Plateau (31°29' N, 92°03' E, 4508

m MSL), Datong at Qinghai plateau (37°04' N, 101°35' E, 2560 m MSL), and Zhongchuan (36°36' N, 103°39' E, 1970 m MSL) and Pingliang (35°57' N, 106°69' E, 1630 m MSL) at Gansu Province in the Chinese loess plateau.

According to the polarity of surface electric (E) field, the thunderstorms in the four regions can be divided into two categories (Qie et al. 2009b). (1) Special-type: The surface E field underneath most of the thunderstorms has the same polarity as the clear sky, i.e., the surface E field is controlled by the positive charge inside thunderstorms (defined as negative). Qie et al. (2005a; b) suggested that this kind of thunderstorm was characterized by an unusual tripole charge structure with a larger-than-usual lower positive charge center (LPCC) existing at the base of thunderstorm, and nearly all the flashes were IC flashes which occur in the lower dipole. (2) Normal-type: The surface E field is positive when the thunderstorms are overhead, being consistent with the normal thunderstorm observed in the other prominent lower altitude regions during summer. This kind of thunderstorms also has a tripole charge structure, but the LPCC is weaker than the former.

The characteristics of the surface E field of thunderstorms in the four plateau regions are similar to each other, but the percentages of occurrence of the two types of thunderstorms are different. The percentage of special-type thunderstorms increases with altitude. The special-type thunderstorms took about 73%, 60%, 54% and 46% of the total in Nagqu, Datong, Zhongchuan and Pingliang region, respectively (Qie et al. 2009b). The Special-type thunderstorms in the Chinese inland plateau can be divided into three types (T. Zhang et al., 2009b): (1) IC-dominated type: no CG flashes occur; (2) -CG-dominated type: more than 50% CG flashes are negative; (3) +CG-dominated type: the dominated CG flashes are positive. There is a unique characteristic for the thunderstorms in the four plateau regions, which is that the flash rate is quite low comparing with other lower altitude regions (T. Zhang et al. 2009a; b). The mean flash rate was usually 1-3 flashes  $\text{min}^{-1}$  and the maximum flash rate was no more than 4-10 flashes  $\text{min}^{-1}$  in these regions. The thunderstorm is usually characterized by isolated cells, and the electrification is not strong. Furthermore, the 0°C layer is lower, which is favorable for the development of clouds, but the updraft is weak. Therefore, the electrification is weak and low flash rate is observed as a result.

#### **4.4 Charge structure inside the thunderstorm in the Tibetan plateau**

Using the data from the electric field changes from a seven-site network of slow antennas synchronized by Global Position System (GPS) with 1 $\mu$ s time resolution in Zhongchuan region, Cui et al. (2009) found that the both the upper dipole and lower dipole were the source of IC discharges. They analyzed 10 IC discharges and found the heights of IC discharge moments of lower five IC flashes were located between 3.3-5.6 km MSL and 6.8-7.7 km MSL for the upper five, respectively. Analyzing 16 negative CG flashes and two positive flashes in Datong region, T. L. Zhang et al. (2009a) found that negative charge region located at a range of 5.5-8.0 km MSL and two positive centers at heights of 8.0 km and 8.5 km MSL, respectively, and indicating that the charge structure of special-type storms could be represented basically by a tripole but with a larger-than-usual LPCC.

. The first electric field profile inside a special-type thunderstorm in Pingliang

region by using a balloon-borne electric field sounding system, based on the principle of point discharge, suggest that there were four charge regions with three layers inside the storm and one at the lower boundary of the storm (Z. Zhao et al., 2009). The LPCC region was between 4.5 to 5.3 km MSL (3 to  $-2^{\circ}\text{C}$ ). The main negative charge layer was between 5.4 to 6.6 km ( $-3$  to  $-10^{\circ}\text{C}$ ). The upper positive charge layer lied between 6.7 to 7.2 km ( $-11$  to  $-14^{\circ}\text{C}$ ), and the negative screening layer lied at the lower boundary. The observation results confirmed that the thunderstorms in the plateau regions have a tripole charge structure with a larger-than-usual LPCC.

The large LPCC may play an important role in the longer preliminary breakdown processes. D. Wang et al. (2009) found that the preliminary discharge of the thunderstorms in Zhongchuan region developed from the middle negative charge region to the LPCC based on the location of pulses from a seven-station network of fast antennas. Qie et al. (2005b) found that the weak LPCC is conducive to the occurrence of negative CG flash, while the larger LPCC is conducive to the polarity-inverted IC flashes or negative CG flashes with longer preliminary discharge.

A 3-D thunderstorm model coupled with dynamical and electrical processes was developed for studies on the spatial and temporal evolution of charge structure in the plateau regions (Guo et al. 2007a; b). It was found that the lower maximum disturbing central potential temperature, the reversal temperature and relative humidity in the middle layer were key parameters for the formation of the charge structure. The simulation results by using real sounding data indicated that both types of thunderstorms appeared to begin with the lower dipole of a normal tripole structure, rather than with the upper dipole followed by the development of a weaker lower positive charge region, and the convection was conducive to tripole charge structure in mature stage.

## **5. Numerical simulation on charge structure and lightning inside thunderstorm**

The numerical modeling is very useful in thunderstorm electrification and discharge processes, and is able to help discriminate the interactions between dynamic, microphysical processes and lightning discharges. On the basis of previous observations of the electric field and lightning features in thunderstorms, numerical simulation aimed at the understanding of the electrification and lightning discharge behaviors in thunderclouds have been conducted in China.

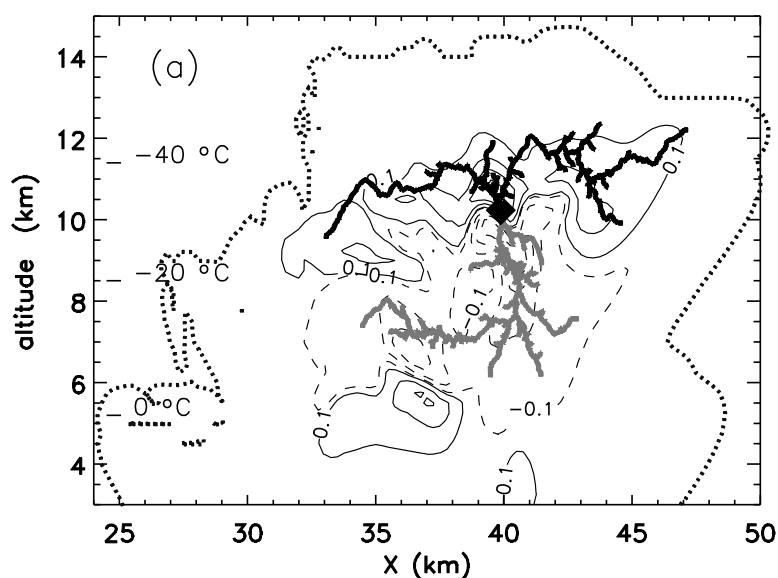
### **5.1 Simulation on charge structure inside the thunderstorm**

Guo et al. (2007a; b), used the 3-D thunderstorm model coupled with dynamical and electrical processes, found that inductive and non-inductive charging mechanism played a crucial role in the evolution of electrical structure within thunderstorms, and the electrical development depended highly on ice phase microphysical processes. The appearing time of maximal electric field was the same as that of maximal solid rainfall density and starting falling time of maximal ascending velocity, but later than maximal liquid rainfall density and maximal ascending velocity. Zhou et al. (2009a, 2009b) developed a 3-D numerical model simulating the electrification and discharge processes in a hail storm. The effects of the temperature and relative humidity profile on the charge structure in thundercloud were also analyzed by Zheng et al. (2007). In southern China, the value of convective available potential energy (CAPE) is large,

and the main positive and negative charge centers are raised to a high level, then dipole charge structure forms.

## 5.2 Simulation on lightning discharge channel

A 2-D fine-resolution (12.5 m) lightning model, including non-inductive and inductive charge separation mechanism and Stochastic lightning parameterization was proposed by Tan et al. (2006a; b; 2007). The hydrometeors considered in the cloud model included cloud droplet, rain, ice crystal, snow, graupel and hail. The bi-level branched channel structures, horizontal extension and maximum changes of vertical electric field simulated by the fine-resolution lightning model were in good agreement with previous observational results. Figure 6 shows a simulated IC flash and the corresponding charge distribution background with the tripole charge structure before the flash initiation. The bi-level branched channel structures, horizontal extension and maximum changes of vertical electric field simulated by the fine-resolution lightning model were in good agreement with previous observational results than those from a coarser model. Tao et al. (2009) added a CG lightning scheme in to the 2-D fine-resolution model, and produced the fine branched channel structure of CG lightning with different types of cloud charge distributions, such as dipole, tri-pole, bi-dipole and multi-layer charge structures. The subsequent neutralization of the residual charges in the channel volumes with surrounding dispersed cloud charges during the IC and CG lightning was also discussed by Tan et al. (2007) and Tao et al. (2009). It was found that some residual charges were deposited in the local volumes of cut-off and non-conducting leader channels after the lightning discharge terminated and these charges were gradually neutralized with surrounding dispersed cloud charges. This process should relate to the turbulence exchange, advection transport, and gravitational sedimentation and so on in thunderclouds.



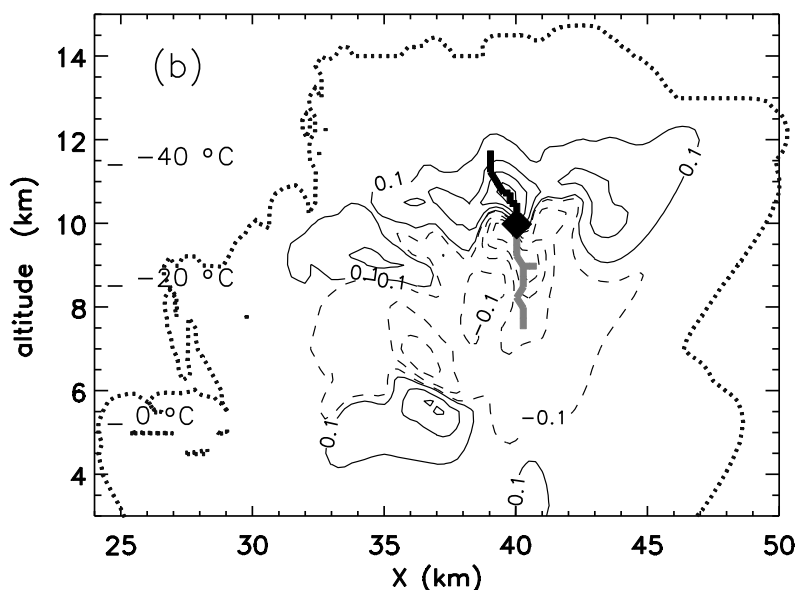


FIG. 6. A simulated IC flash with tripole charge structure at 2138 s, where black line is for negative leader, gray line for positive leader, black diamond for IC flash initiation, dotted for cloud confines, solid for positive charge, and dashed for negative charge with contour values starting at  $\pm 0.1 \text{ nC m}^{-3}$  with intervals of  $0.5 \text{ nC m}^{-3}$ . (a) For 12.5m resolution, and (b) for 250 m resolution. [Adapted from Tan et al. (2006a).]

### 5. Response of lightning to the climate change

The importance of lightning for climate studies is increasingly recognized with the increasing use of the satellite lightning observation and ground-based global lightning observation. Xiong et al. (2006) analyzed the responses of lightning activity to the surface relative humidity in global and regional scale using the LIS/OTD lightning data and NCEP metrological data from 1995 to 2002. It was found that the higher relative humidity resulted in more lightning activities at dry regions and less lightning activities at wet regions. The watershed of relative humidity for lightning production was about 72%-74%. Yuan and Qie (2008) investigated the lightning activity and precipitation characteristics before and after the onset of the South China Sea (SCS) summer monsoon using the TRMM satellite data from 1998 to 2005. The results showed that the lightning activity over the SCS began to enhance in April, peaked in May, and decreased after June. Compared to the premonsoon season, mean cell-level flash rate decreased 13% and mean flash optical radiance increased 15% during the monsoon season, respectively. The mean flash rate was higher during the premonsoon season. On the basis of the observations of PR and TMI, the vertical development of precipitation systems in the premonsoon season was stronger than that in the monsoon season, frequent lightning activity was observed as a result.

The relationships between lightning activities and a series of convective indices have been investigated, using 10-year LIS lightning data, over nine monsoon-prone areas in which high-impact weather (HIW) events were frequently observed (Dai et al. 2009). Correlation analysis for each study area showed that higher lightning flash rate and lightning probability were associated with more unstable air and smaller vertical

wind shear in a nearly saturated lower layer in most of the studied regions. But the correlation varied from region to region. The best correlation between lightning activities and convective indices was found in eastern and southern China, whereas the correlation was worst in some inland or basin topography regions in which topographic effects were more significant. Moreover, ambient moisture played a more important role in the convective development of thunderstorms in southern China than that in other regions.

### References:

- Cao, D. J., G. S. Zhang, T. Zhang, and Y. H. Wang, 2008: Analyses on VHF radiation of Cloud-to-Ground flashes in Pingliang loess plateau (in Chinese). *Plateau Meteor.*, **27(2)**, 365–372.
- Cui, H., X. Qie, Q. Zhang, T. Zhang, G. Zhang, and J. Yang, 2009: Intracloud discharge and the correlated basic charge structure of a thunderstorm in Zhongchuan, a Chinese Inland Plateau region. *Atmos. Res.*, **91(2-4)**, 425–429.
- Dai, J., Y. Wang, L. Chen, L. Tao, J. Gu, J. Wang, X. Xu, H. Lin, Y. Gu, 2009: A comparison of lightning activity and convective indices over some monsoon-prone areas of China. *Atmos. Res.*, **91(1-4)**, 438–452.
- Feng, G. L., X. S. Qie, T. Yuan, and Y. J. Zhou, 2006a: A case study of Cloud-to-Ground lightning activities in hailstorms under cold eddy synoptic situation. *Acta Meteor. Sin.*, **20(4)**, 489–499.
- Feng, G. L., X. S. Qie, and Y. J. Zhou, 2006b: A case study on characteristics of lightning activity in a mesoscale convective system (in Chinese). *Plateau Meteor.*, **25(2)**, 220–228.
- Feng, G. L., X. S. Qie, T. Yuan, and S. Z. Niu, 2007: Analysis on lightning activity and precipitation structure of hailstorms. *Sci. Chin. Ser. D-Earth Sci.*, **50 (4)**, 629–639.
- Feng, G. L., X. S. Qie, and S. J. Wu, 2008: Cloud-to-Ground lightning characteristics of hail clouds in Shandong province (in Chinese). *Chin. J. Atmos. Sci.*, **32(2)**, 289–299.
- Feng, G. L., X. S. Qie, J. Wang, and D. L. Gong, 2009: Lightning and doppler radar observations of a squall line system, *Atmos. Res.*, **91(2-4)**, 466–478.
- Gou, X. Q., Y. J. Zhang, X. S. Qie, W. S. Dong, 2006: Characterization of radiation field of return stroke of Cloud-to-ground lightning with local effective Hölder exponent (in Chinese). *Proc. CSEE*, **26(3)**, 75–78.
- Gou, X. Q., Y. J. Zhang, W. S. Dong, and X. S. Qie, 2007: Wavelet-based multifractal analysis of the radiation field of first return stroke in cloud-to-ground discharge (in Chinese). *Chinese J. Geophys.*, **50(1)**, 101–105.
- Gou, X. Q., M. L. Chen, Y. J. Zhang, W. S. Dong, and X. S. Qie, 2009: Wavelet multiresolution based multifractal analysis of electric fields by lightning return strokes, *Atmos. Res.*, **91**, 410–415.
- Guo, F. X., Y. J. Zhang, and M. H. Yan, 2007a: A numerical study of the charge structure in thunderstorm in Naqu area of the Qinghai-Xizang Plateau (in Chinese). *Chin. J. Atmos. Sci.*, **31(1)**, 28–36.

- Guo, F. X., Y. J. Zhang, M. H. Yan, and Y. Zhao, 2007b: Numerical study and observation of the relationship between surface electric field and precipitation in thunderstorm over Qinghai-Xizang plateau (in Chinese). *Plateau Meteor.*, **26(2)**, 257–263.
- Gou, X., M. Chen, Y. Du, and W. Dong, 2010: Fractal dynamics analysis of the VHF radiation pulses during initial breakdown process of lightning. *Geophys. Res. Lett.*, **37**, L11808, doi:10.1029/2010GL043178.
- Kong, X. Z., X. S. Qie, Y. Zhao, T. Zhang, G. S. Zhang, and W. S. Dong, 2006: An analysis of discharge processes of one cloud-to-ground lightning flash on the Qinghai-Xizang Plateau (in Chinese). *Chinese J. Geophys.*, **49(4)**, 993–1000.
- Kong, X. Z., X. S. Qie, and Y. Zhao, 2008: Characteristics of downward leader in a positive cloud-to-ground lightning flash observed by high-speed video camera and electric field changes. *Geophys. Res. Lett.*, **35**, L05816, doi:10.1029/2007GL032764.
- Kong, X. Z., X. S. Qie, Y. Zhao, and T. Zhang, 2009: Characteristics of negative lightning flashes presenting multiple-ground terminations on a millisecond-scale. *Atmos. Res.*, **91(1-4)**, 381–386.
- Li, J., W. T. Lu, Y. J. Zhang, W. S. Dong, D. Zheng, S. D. Chen, S. Qiu, T. Wang, H. Y. Liu, L.W. Chen, 2010: An altitude-triggered lightning with multiple branches and ground contacts. *J. Appl. Meteor. Sci.*, **21(1)**: 95-100,
- Liu, D. X., X. S. Qie, G. L. Feng, and S. J. Wu, 2008: Analyses on lightning temporal and spatial characteristics in the severe convective weather in north China (in Chinese). *Plateau Meteor.*, **27(2)**, 358–364.
- Liu, D. X., G. L. Feng, and S. J. Wu, 2009: Temporal and spatial characteristics of cloud-to-ground lightning of hailstorms over north China. *Atmos. Res.*, **91(2-4)**, 459–465.
- Lu, W., D. Wang, N. Takagi, V. Rakov, M. Uman, and M. Miki., 2008a: Characteristics of the optical pulses associated with a downward branched stepped leader. *J. Geophys. Res.*, **113**, D21206, doi:10.1029/2008JD010231.
- Lu, W. T., Y. J. Zhang, J. Li, D. Zheng, W. S. Dong, S. D. Chen, and F. Wang, 2008b: Optical observations on propagation characteristics of leaders in Cloud-to-Ground lightning flashes. *Acta Meteor. Sin.*, **22(1)**, 66–77.
- Lu, W. T., and Y. Zhang, X. Zhou, Q. Meng, D. Zheng, M. Ma, F. Wang, S. Chen, X. Qie, 2009a: Simultaneous optical and electrical observations on the initial processes of altitude-triggered negative lightning. *Atmos. Res.*, **9**, 353–359.
- Lu, W., D. Wang, Y. Zhang, and N. Takagi, 2009b: Two associated upward lightning flashes that produced opposite polarity electric field changes. *Geophys. Res. Lett.*, **36**, L05801, doi:10.1029/2008GL036598.
- Ouyang, Y. H., P. Yuan, X. S. Qie, H. B. Wang, X. D. Jia, and H. M. Zhang, 2006: Temperature study on lightning return stroke in the coastal area of Guangdong. *Spectrosc. Spectral. Anal.*, **26(11)**, 1988–1992.
- Pan L. X., X. S. Qie, D. X. Liu, D. F. Wang, and J. Yang, 2009: The lighting activities in super typhoons over the Northwest Pacific, *Sci. Chin. Ser. D-Earth Sci.*, **53(8)**, 1241-1248, doi: 10.1007/s11430-010-3034-z.

- Qie X., Y. Zhang and Q. Zhang, 2006: Characteristics of Lightning Discharges and Electric Structure of Thunderstorm. *Acta Meteor. Sin.*, **64(2)**, 244-257
- Qie, X., X. Kong, G. Zhang, T. Zhang, T. Yuan Y. Zhou, Y. Zhang, and H. Wang, 2005a: The possible charge structure of thunderstorm and lightning discharges in northeastern verge of Qinghai-Tibetan Plateau. *Atmos. Res.*, **76(1-4)**, 231-246.
- Qie, X. S., T. L. Zhang, C. P. Chen, G. S. Zhang, T. Zhang, and W. Z. Wei, 2005b: The lower positive charge center and its effect on lightning discharges on the Tibetan Plateau. *Geophys. Res. Lett.*, **32**, L05814, doi:10.1029/2004GL022162.
- Qie, X. S., Q. L. Zhang, and Y. J. Zhou, 2007a: Artificially triggered lightning and its characteristic discharge parameters in two severe thunderstorms. *Sci. Chin. Ser. D-Earth Sci.*, **50(8)**, 1241-1250.
- Qie, X. S., and X. Z. Kong, 2007b: Progression features of a stepped leader process with four grounded leader branches. *Geophys. Res. Lett.*, **34**, L06809, doi:10.1029/2006GL028771.
- Qie, X. S., and Coauthors, 2009a: Characteristics of artificially triggered lightning during Shandong artificial triggering lightning experiment (SHATLE). *Atmos. Res.*, **91(2-4)**, 310-315.
- Qie, X. S., T. L. Zhang, G. S. Zhang, and T. Zhang, 2009b: Electrical characteristics of thunderstorms in different plateau regions of China. *Atmos. Res.*, **91(2-4)**, 244-249.
- Qie, X. S., J. Yang, R. B. Jiang, J. F. Wang, D. X. Liu, C.X. Wang, Y.J. Xuan, 2010. A new-model rocket for artificially triggering lightning and its first triggering lightning experiment. *Chin. J. Atmos. Sci.*, (in Chinese), **34(5)**, 937-946.
- Qiu, S., B. H. Zhou, L. H. Shi, W. S. Dong, Y. J. Zhang, and T. C. Gao, 2009: An improved method for broadband interferometric lightning location using wavelet transforms. *J. Geophys. Res.*, **114**, D18211, doi:10.1029/2008JD011655.
- Tan, Y. B., S. C. Tao, and B. Y. Zhu, 2006a: Fine-resolution simulation of the channel structures and propagation features of intra-cloud lightning. *Geophys. Res. Lett.*, **33**, L09809. doi:10.1029/2005GL025523.
- Tan, Y. B., S. C. Tao, B. Y. Zhou, M. Ma, and W. T. Lu, 2006b: Numerical simulation of the bi-level and branched structure of intra-cloud lightning flashes. *Sci. Chin. Ser. D-Earth Sci.*, **49 (6)**, 661-672.
- Tan, Y. B., S. C. Tao, B. Y. Zhou, M. Ma, and W. T. Lu, 2007: A simulation of the effects of intra-cloud lightning discharges on the charges and electrostatic potential distributions in a thundercloud (in Chinese). *Chinese J. Geophys.*, **50 (4)**, 916-930.
- Tao, S. C., Y. B. Tan, B. Y. Zhu, M. Ma, and W. T. Lu, 2009: Fine-resolution simulation of cloud-to-ground lightning and thundercloud charge transfer, *Atmos. Res.*, **91**, 360-370.
- Wang C., X. Qie, J. Yang, R. Jiang, J. Wang, D. Liu, M. Yang, L. Pian, H. Yang, The Luminosity and Current Characteristics of M-component from Triggered-lightning in Shandong, *Proc. APEMC*, 2010, 1303-1306.
- Wang, D. F., X. S. Qie, T. Yuan, G. S. Zhang, T. Zhang, T. L. Zhang, and Q. L. Zhang, 2009: An analysis on the initial stage of intracloud lightning with the

- location technique of fast electric field change pulses (in Chinese). *Acta Meteor. Sin.*, **67(1)**, 165–174.
- Wang, J., P. Yuan, F. X. Guo, X. S. Qie, Y. H. Ouyang, and Y. J. Zhang, 2009: The spectra and temperature of cloud lightning discharge channel. *Sci. Chin. Ser. D-Earth Sci.*, **39(2)**, 229–234.
- Wang, Y. H., G. S. Zhang, T. Zhang, and D. J. Cao, 2007: Submicrosecond VHF radiation character on broadband wrap in lightning (in Chinese). *Proc. CSEE*, **27(9)**, 41–45.
- Xiong, Y. J., X. S. Qie, Y. J. Zhou, T. Yuan, and T. L. Zhang, 2006: Regional responses of lightning activities to relative humidity of the surface (in Chinese). *Chinese J. Geophys.*, 2006, **49(2)**, 367–374.
- Yang, J., X. S. Qie, Q. L. Zhang, X. Z. Kong, Y. Zhao, Y. J. Zhou, T. L. Zhang, G. L. Feng, Q. F. Xiao, 2006: Parameters of dart leader return stroke in artificially-triggered lightning (in Chinese). *Proc. CSEE*, **26(25)**, 125–129.
- Yang, J., X. S. Qie, G. S. Zhang, and H. B. Wang, 2008a: Magnetic field measuring system and current retrieval in artificially triggering lightning experiment. *Radio Sci.* **43**, RS2011. doi:10.1029/2007RS003753.
- Yang, J., X. S. Qie, J. G. Wang, Y. Zhao, Q. L. Zhang, T. Yuan, Y. J. Zhou, and G. L. Feng, 2008b: Observation of the lightning-induced voltage in the horizontal conductor and its simulation (in Chinese). *Acta Meteor. Sin.*, **57(3)**, 1968–1975.
- Yang, J., X. S. Qie, G. S. Zhang, Y. Zhao, and T. Zhang, 2008c: Red sprites over thunderstorms in the coast of Shandong province, China. *Chin. Sci. Bull.*, **53(7)**, 1079–1086.
- Yang, J., X. Qie, Q. Zhang, Y. Zhao, G. Feng, T. Zhang, and G. Zhang, 2009: Comparative analysis of the initial stage in two artificially-triggered lightning flashes, *Atmos. Res.*, **9**, 393–398.
- Yang, J., X. Qie, G. Zhang, Q. Zhang, G. Feng, Y. Zhao, and R. Jiang, 2010: Characteristics of channel base currents and close magnetic fields in triggered flashes in SHATLE. *J. Geophys. Res.*, doi:10.1029/2010JD014420, in press.
- Yuan, P., X. S. Qie, S. H. Lu, G. Y. Chen, and G. S. Zhang, 2006: The spectral properties of an intense lightning return stroke (in Chinese). *Spectrosc. Spectral Anal.*, **26(4)**, 733–737.
- Yuan, T., and X. S. Qie, 2008: Study on lightning activity and precipitation characteristics before and after the onset of the South China Sea summer monsoon. *J. Geophys Res.*, 13, D14101, doi:10.1029/2007JD009382.
- Yuan, T., and X. S. Qie, 2010: TRMM-based study on lightning activity and its relationship with precipitation structure of a squall line in south China (in Chinese). *Chin. J. Atmos. Sci.*, **34(1)**, 58-70
- Zhang, G. S., Y. X. Zhao, X. S. Qie, T. Zhang, Y. H. Wang, and C. P. Chen, 2008: Observation and study on the whole process of Cloud-to-Ground lightning using narrowband radio interferometer. *Sci. Chin. Ser. D-Earth Sci.*, **51(5)**, 694–708.
- Zhang, G. S., Y. H. Wang, X. S. Qie, T. Zhang, Y. X. Zhao, Y. J. Li, and D. J. Cao, 2010: Using lightning locating system based on Time-of-Arrival technique to study three-Dimensional lightning discharge processes. *Sci. Chin. Ser. D-Earth*

- Sci.*, 53(4): 591-602.
- Zhang, H. M., P. Yuan, S. H. Lu, and Y. H. Ouyang, 2007: Study on electron density of lightning return stroke (in Chinese). *Plateau Meteor.*, **26(2)**, 264–269.
- Zhang, Q. L., X. S. Qie, Y. J. Zhou, T. L. Zhang, X. Z. Kong, G. L. Feng, J. Yang, Y. Zhao, Y. J. Zhang, 2006: Electric field characteristics of leader and return in triggered lightning (in Chinese). *High Power Laser and Particle Beams*, **18(12)**, 2004–2010.
- Zhang, Q., X. S. Qie, X. Z. Kong, Y. J. Zhou, J. Yang, T. L. Zhang, G. L. Feng, and Q. F. Xiao, 2007: Comparative analysis on return stroke current of triggered and Natural Lightning Flashes. *Proc. CSEE*, 27(6), 67–71.
- Zhang, Q., X. Qie, Z. Wang, T. Zhang, and J. Yang, 2009: Simultaneous observation on electric field changes at 60 m and 550 m from altitude-triggered lightning flashes. *Radio Sci.*, 44, RS1011, doi:10.1029/2008RS003866.
- Zhang Q., X. Qie, Z. Wang, T. Zhang, Y. Zhao, J. Yang, and X. Kong, 2009: Characteristics and simulation of lightning current waveforms during one artificially triggered lightning. *Atmos. Res.*, **91(1-4)**, 387–392.
- Zhang, T. L., X. Qie, T. Yuan, G. Zhang, T. Zhang, and Y. Zhao, 2009a: Charge source of cloud-to-ground lightning and charge structure of a typical thunderstorm in the Chinese Inland Plateau, *Atmos. Res.*, **91(4)**, 475–480.
- Zhang, T. L., X. S. Qie, M. H. Yan, Y. Zhao, G. S. Zhang, T. Zhang, and Y. H. Wang, 2009b: A preliminary analysis for formation of electrical characteristics of thunderstorms in different altitude regions in Chinese inland plateau (in Chinese). *Plateau Meteor.*, **28(5)**, 1006-1017.
- Zhang, Y. J., Q. Meng, W. T. Lu, P. R. Krehbiel, X. S. Liu, and X. J. Zhou, 2006a: Charge structures and cloud-to-ground lightning discharges characteristics in two supercell thunderstorms, *Chin. Sci. Bull.*, **51(2)**, 198–212.
- Zhang, Y. J., Q. Meng, P. R. Krehbiel, X. S. Liu, M. H. Yan, and X. J. Zhou, 2006b: Spatiotemporal characteristics of positive cloud-to-ground lightning discharges and bidirectional leader of the lightning, *Sci. Chin. Ser. D-Earth Sci.*, **49**, 212–224.
- Zhang, Y. J., W. Lu, J. Li, W. Dong, D. Zheng, and S. Chen, 2009a: Luminosity characteristics of leaders in natural cloud-to-ground lightning flashes. *Atmos. Res.*, **91(2-4)**, 326–332.
- Zhang, Y., Q. Meng, W. Lu, M. Ma, D. Zheng, and P. R. Krehbiel, 2009b: Positive charge region in lower part of thunderstorm and preliminary breakdown process of negative cloud-to-ground lightning. *Acta Meteor. Sin.*, **23(1)**, 95–104.
- Zhao, Y., X. S. Qie, X. Z. Kong, G. S. Zhang, T. Zhang, J. Yang, G. L. Feng, Q. L. Zhang, D.F. Wang, 2009: Analysis on the parameters of the current waveforms of triggered lightning (in Chinese). *Acta Phys. Sin.*, **58(9)**, 6616–6625.
- Zhao, Z., and Q. Zhang, 2009: Influence of channel tortuosity on the lightning return stroke electromagnetic field in time domain. *Atmos. Res.*, **91(1-4)**, 404–409.
- Zhao, Z. K., and X. S. Qie, T. L. Zhang, T. Zhang, H. F. Zhang, Y. Wang, Y. She, B. L. Sun, and H. B. Wang, 2010: Electric field soundings and the charge structure within an isolated thunderstorm. *Chin. Sci. Bull.*, **55(9)**, 872-876, doi:

10.1007/s11434-009-0471-1.

- Zheng, D., Y. J. Zhang, W. T. Lu, Q. Meng, and X. S. Qie, 2006: Leader-return stroke model and calculation of artificial triggered lightning stroke's characteristics (in Chinese). *Proc. CSEE*, 26(23), 151–157.
- Zheng, D., Y. J. Zhang, M. Ma, Q. Meng, and W. T. Lu, 2007: Simulation study on the influence of atmospheric stratification on lightning activity. *Acta Meteor. Sin.*, **65(4)**, 622–632.
- Zheng, D., Y. J. Zhang, Q. Meng, W. T. Lu, and X. Y. Yi, 2009: Total lightning characteristics and electric structure evolution in a hailstorm. *Acta Meteor. Sin.*, **23(2)**, 233–249.
- Zhou, Z.M., and X. L. Guo, 2009a: 3D Modeling on relationships among intracloud lightning, updraft and liquid water content in a severe thunderstorm case (in Chinese). *Climatic Environ. Res.*, **14(1)**, 31–44.
- Zhou, Z. M., and X. L. Guo, 2009b: A three dimensional modeling study of multi-layer distribution and formation processes of electric charge in a severe thunderstorm (in Chinese). *Chin. J. Atmos. Sci.*, **33(3)**, 600–620.
- Zhu, B. Y., S.C. Tao, and Y. B. Tan, 2007: Initial observations of the lightning narrow bipolar pulses with very powerful VHF radiation (in Chinese). *Acta Meteor. Sin.*, **65(1)**, 124–130.
- Zhu, B., H. Zhou, M. Ma, F. Lv, and S. Tao, 2010: Estimation of channel characteristics of narrow bipolar events based on the transmission-line model. *J. Geophys. Res.*, 115, D19105, doi:10.1029/2009JD012021.



## PROGRESSES IN THE MIDDLE ATMOSPHERIC

### RESEARCHES IN CHINA DURING 2006-2010

Jianchun Bian<sup>1</sup>, Wen Chen<sup>2</sup>, Yuejuan Chen<sup>3</sup>, Yongyun Hu<sup>4</sup>, Chuanxi Liu<sup>1</sup>, Wenshou Tian<sup>5</sup>, and Jiyao Xu<sup>6</sup>

1 Key laboratory of Middle Atmosphere and Global Environment Observation, Institute of Atmospheric Physics, Chinese Academy of Sciences

2 Center for Monsoon System Research, Institute of Atmospheric Physics, Chinese Academy of Sciences

3 School of Earth and Space Sciences, University of Science and Technology of China

4 Dept. of Atmospheric and Oceanic Sciences, School of Physics, Peking University

5 College of Atmospheric Science, Lanzhou University

6 State Key Laboratory of Space Weather, Center for Space Science and Applied Research, Chinese Academy of Sciences

#### ABSTRACT

In China, researches in the middle atmosphere are relatively few, but some important progresses have been obtained during the last five years (2006-2010). In this national report, advances in the middle atmosphere are introduced from the following six aspects: middle atmospheric dynamics, stratosphere-troposphere exchange, stratosphere-troposphere coupling, chemistry-climate coupling, stratospheric satellite retrieval, and stratospheric processes over Tibetan Plateau.

**Keywords:** middle atmosphere, stratosphere-troposphere coupling, chemistry-climate coupling, Tibetan Plateau

#### 1. Introduction

In the research field of atmospheric sciences, the middle atmosphere receives relatively few focuses, except for ozone layer. In previous literatures, the middle atmosphere was almost thought to be controlled by upward propagation of wave activities generated in the troposphere and have little impact on the tropospheric weather and climate. However, recent studies suggest that anomalous signals in the stratosphere have hints in weather forecast, especially in winter (Baldwin & Thompson, 1998). Nowadays, more and more attention is paid to the middle atmosphere study.

In China, researches on the middle atmosphere during the last five years are mainly concerned about the middle atmospheric dynamics, stratosphere-troposphere exchange, stratosphere-troposphere coupling, chemistry-climate coupling, stratospheric satellite retrieval and stratospheric processes over Tibetan Plateau, which will be summarized in the following parts.

#### 2. Progress in Middle Atmospheric Dynamics

##### 2.1 Dynamical structures, tidal waves and planetary waves in mesopause region

Comparisons of monthly mean nighttime temperature profiles observed by the

sodium lidar at Colorado State University and TIMED/SABER overpasses are made by Xu et al. (2006). In the altitude range from 85 km to about 100 km, the two observations are in very good agreement. Though within each other's error bars, important differences occur below 85 km in the entire year and above 100 km in the summer season. Possible reasons for these difference are high photon noise below 85 km in lidar observations and less than accurate assumptions in the concentration of important chemical species like oxygen (and its quenching rate) in the SABER v1.06 retrieval above 100 km. However, the two techniques both show the two-level mesopause thermal structure, with the times of change from one level to the other in excellent agreement. Comparison indicates that the highlevel (winter) mesopause altitudes are also in excellent agreement between the two observations, though some difference (2–3 km) may exist in the low-level (summer) mesopause altitudes between ground-based and satellite-borne data. The comparison between the TIMED/SABER temperature observation with NRLMSISE-00 Empirical Atmospheric Model is also made (Xu et al., 2006).

TIMED/SABER temperature observations are used to study the global structure and variability of the mesopause altitude and temperature by Xu et al. (2007a). The results show that there are two distinctly different mesopause altitude levels: the higher level at 95–100 km and the lower level below 86 km. The mesopause of the middle- and high-latitude regions is at the lower altitude in the summer hemisphere for about 120 days around summer solstice and is at the higher altitude during other seasons. At the equator the mesopause is at the higher altitude for all seasons. In addition to the seasonal variation in middle and high latitudes, the mesopause altitude and temperature undergo modulation by diurnal and semidiurnal tides at all latitudes. The mesopause is about 1 km higher at most latitudes and 6–9 K warmer at middle to high latitudes around December solstice than it is around June solstice. These can also be interpreted as hemispheric asymmetry between mesopause altitude and temperature at solstice. Possible causes of the asymmetry as related to solar forcing and gravity wave forcing are discussed.

Xu et al. (2007b) presented a method of extracting zonal mean temperature and tides from TIMED satellite and discuss the features of the zonal mean temperature by using version 1.06 of the SABER temperature data. The global temperature structure is presented, and the mean variations at each latitude and altitude are decomposed into semiannual (SAO), annual (AO), and quasi-biennial (QBO) components. The results indicate that the SAO is strong in the tropical upper stratosphere, mesosphere, and lower thermosphere. The SAO phase is at the equinox at 85 km and at solstice at 75 km. The amplitude is large compared to the annual mean temperature structure, which leads to a mesospheric inversion layer (MIL) in the zonal mean temperature around the equator at equinox. The AO is most evident at middle latitudes and displays a clear hemispheric asymmetry at solstices. The QBO in temperature is strongest in the tropical lower stratosphere; its period there is 26.6 months. There are also weak QBO signals near the mesopause and throughout the middle atmosphere at midlatitudes. The analysis of longer-term variations of the zonal mean temperature, probably affected by the solar cycle but also containing any other trends, indicates that in most

regions, the zonal mean temperature decreases during the period of 5 years and is positively correlated with the solar radiation.

Some ground-based observations are used to study tidal waves and planetary waves. We use wind data observed by the Maui meteor radar (20.75 N, 156.43 W) to study the 8-h tide (Jiang et al., 2009). The results show that the 8-h tide is a regular and distinct feature over Maui. The meridional component of this wave is significantly larger than the zonal component. The meridional component exhibits a semiannual variation in amplitude, with peaks near the equinoxes, whereas the variation of the zonal component does not show this seasonal characteristic. Tidal waves of the low latitudes of China are analyzed by using the meteor radar at Fuke, China (19.5 N, 109.1 E) (Jiang, et al., 2010). The observed tides are compared with the linear tide model (Global Scale Wave Model, GSWM02), and the results show that Fuke diurnal tide agrees well with the model, but there are many differences between Fuke semidiurnal tide and the results from model.

The 6.5-day planetary waves over Wuhan (30.51N, 114.31E) were investigated on the basis of the meteor radar measurements within 78–98km height region during February 2002–December 2005 by Jiang et al. (2008a). The observations show that 6.5-day waves have a prominent seasonal variability and have larger amplitudes at equinoxes than at solstices. Intensive waves occur mostly between 84 and 98 km, and the zonal components of 6.5-day waves are a little larger than its meridional components on average. The main periods of 6.5-day waves are near 6–7 days in spring/winter season and 5–7 days (even extend to 8 days) in autumn months. However, these waves exhibit a downward progression when the amplitude is large. Robust wave events occur basically in eastward background winds. During the 4-year interval, the strongest waves were found in April–May of 2003 and 2004.

The planetary waves are analyzed by using six ground-based Radar observations (Jiang et al., 2008b). The strong mesospheric 6.5-day wave event occurred during April–May 2003 was studied detail. The analysis shows that the latitudinal structure of the mesospheric 6.5-day wave during April–May 2003 is basically in agreement with the theoretical Rossby mode  $(s, n) = (1, -2)$ . The main wave periods and the altitude distribution of large amplitude of this wave event varied with latitude. We also found the downward propagating wave phases, which indicates that the wave event originated in the lower atmosphere and propagated upward to the upper region.

The global structure and the seasonal variations of tidal waves were studied using satellite data in recent years. A new method of extracting zonal mean and tides from satellite observation was put forward. Seasonal variations of the migrating diurnal tide were extracted from Thermosphere, Ionosphere, Mesosphere, Energetics and Dynamics (TIMED) temperature data. And the diurnal tide in the equilibrium wind was also calculated (Xu et al., 2009a). The results show that there are strong quasi-biennial oscillation (QBO) signatures in the amplitude of the diurnal tidal temperature in the tropical region and in the wind near  $\pm 20^\circ$ . The magnitude of the QBO in the diurnal tidal amplitude reaches about 3 K in temperature and about 7 m/s (Northern Hemisphere) and 9 m/s (Southern Hemisphere) in meridional wind. Throughout the mesosphere, the amplitude of the diurnal tide reaches maximum

during March/April of years when the QBO in lower stratospheric wind is in the eastward phase. TIMED global temperature observed by SABER and the wind observed by TIDI are used to investigate the damping of the diurnal tide (Xu et al., 2009b). This damping is approximated by an equivalent Rayleigh friction (ERF). The results show that during some periods the ERF coefficient can be very large over narrow vertical regions of about 5 km. The magnitude and shape of the vertical profiles change with latitude and season. The peak in the vertical profile of ERF is larger and located at a higher altitude in summer than in winter and the ERF coefficients at  $40^\circ$  are stronger than at  $20^\circ$  in both hemispheres. The global distribution of atmospheric ozone observed by Aura/MLS is used to calculate the diurnal component in the ozone heating rate (Xu et al., 2010). The heating is decomposed into Hough modes and the annual (AO), semiannual (SAO), and quasi-biennial (QBO) periodicities of each Hough mode are presented. The results show that the majority of the O<sub>3</sub> heating goes into the symmetric (1,-2), (1,1) and (1,-4) modes. The largest propagating mode (1,1) and the largest trapped mode (1,-2) have obvious SAO signatures near 47 km, where the heating magnitude is largest. The strongest annual variation takes place in the (1,-1) mode near 45 km at the Dec/Jan solstice. A new parameterization of the diurnal component of the heating rate, which covers the vertical range from 10 km to 70 km, is developed based on the seasonal variations in each Hough mode.

The study on the interaction between gravity waves and tides was performed by using a compressible nonlinear two-dimensional gravity wave model (Liu et al., 2008). The numerical results show that tidal wind reduces the vertical wavelengths of the GWs when it is in the same direction as the wave propagation, and thus increases the perturbative shear and the likelihood of instability and wave breaking, especially for waves with shorter vertical wavelengths. Below the critical level, the breaking of GWs can increase the amplitude of diurnal tidal wind due to the momentum deposition. It is interesting that the gravity wave breaking not only accelerates the mean winds, but also increases the amplitudes of the diurnal tide at various altitudes.

Chen and Lu (2007) report in the article the seasonal variations of major atmospheric tides in the mesosphere and lower thermosphere region in the meridian at  $120^\circ\text{E}$ . One year long SABER/TIMED temperature measurements covering Nov. 2004 to Jan. 2006 were used to extract the tidal components with Fourier Least squares fit and FFT analysis, and to reconstruct the diurnal, semidiurnal and terdiurnal tides in the meridian. The migrating diurnal tides increase with altitude and attain maxima at 97 km height, then decrease sharply with altitude. The tides of other frequency increase with altitude and attain significant amplitude at 97 km height. Considering the behavior of vertical variation, the authors place their focus on introducing estimation results obtained at the 97 km altitude. For the tides of each frequency, the migrating and non-migrating components were examined separately to identify their respective contribution to the whole of the tides. The primary results showed that migrating component plays dominant role in charactering the general temporal and spatial distribution for both diurnal and semidiurnal tides. Regarding the diurnal tides, contribution of migrating component is the most dominant one during

spring equinox, which is characterized by the amplitude maxima at the equator and that at the tropics for both hemispheres. Moreover, the temporal variation of the diurnal tides at the tropical latitude in Northern hemisphere is consistent to the analysis result obtained by using meteor radar wind measurements taken in Wuhan (30°N, 114°E). Contributions of non-migrating tides are more significant in other seasons. During summer solstitial time in 2005, tidal modes (1, 0), (1, -3) and (1, -2) contribute together to form a diurnal tides active area from 20°N to 40°S with the maximal amplitude 20 K at the equator. Due to the domination of migrating component, semidiurnal tides occur at the tropical latitudes in both hemispheres. In northern hemisphere, the active tides area centers at autumn equinox with maximum 13 K. And in southern hemisphere, the active area centers at the time in between spring and summer equinox. The influences of non-migrating semidiurnal components are also clear during other seasons as several other centers with maximal amplitude are seen. Confined in the latitude range 40°S ~ 40°N, terdiurnal components exhibit much weaker activity with much smaller amplitudes than that of the diurnal and semidiurnal components. Current estimation results suggest that non-migrating terdiurnal components have amplitudes that are as large as and during most times larger than that of migrating component, and thus predominate the global distribution of terdiurnal tides in 2005.

## 2.2 Gravity waves in the middle atmosphere

Xu et al. (2006) study the evolution of the sodium layer in the presence of an overturning (or convectively unstable) gravity wave using model simulations and lidar observations. The simulations employ a time-dependent, nonlinear, photochemical dynamical 2-D model. The observations are a 9-day (210-hour) set of sodium density and temperature lidar measurements from Fort Collins, Colorado (41°N, 105°W). The evolution of large-scale (vertical wavelength of 30 km) and small-scale (vertical wavelength of 10 km) waves and the associated evolution of the sodium layer are simulated. The results show that the model and observations give similar behavior in the evolution of the sodium densities, mixing ratios, and potential temperature in response to large- and small-scale waves. The model and observations indicate that the sodium density perturbation has a more pronounced overturning behavior in the bottomside of the layer than the topside of the layer. The sodium density also has a more pronounced overturning behavior than the mixing ratio and potential temperature. The overturning signatures in the sodium density due to small-scale waves occur periodically at the wave period even before the wave itself becomes completely unstable. The study suggests that observations of single overturning events in sodium densities should be interpreted with caution and may not indicate complete overturning of a wave.

Based on the idea of MPI (Message Passing Interface) and the domain decomposition, two paralleled numerical models of the compressible nonlinear gravity wave propagation were developed, one is two-dimensional model (Liu, et al., 2009a), another is three-dimensional model (Liu, et al., 2009b). The Kelvin-Helmholtz (KH) billows which appear in the process of gravity wave (GW) propagation are simulated directly by using the compressible nonlinear

two-dimensional gravity wave model (Liu et al., 2009c). The braid structures and overturning of KH billows, caused by nonlinear interactions between GWs and mean flow, can be resolved precisely by the model. The simulated results support the findings in airglow studies that GWs propagating from below into the MLT region are important sources of KH billows. The onset of small scale waves and the wave energy transfer induce the shallower vertical wave number power spectral densities (PSD). Before the KH billows evolve, the mean wind is accelerated greatly by GWs. By contrast, as the KH billows evolve and mix with mean flow, the mean wind and its peak value decrease.

Some researches on the vertical wave number spectra of atmospheric fluctuations are made. The vertical wave number spectra of wind fluctuations using data with a height resolution of 25 m observed near the mesopause by 64 chaff rockets is studied by Wu and Xu (2006a). Direct measurement of Brunt-Vaisala frequency allows accurate calculations of spectral amplitude and local Richardson number. Individual vertical wave number spectra reveal considerable variability in both slope and amplitude, which is not consistent with the predictions of various saturation models. Mean vertical wave number spectra observed at different locations and seasons show great similarities. While the spectral amplitude predicted by the linear saturation model or saturated-cascade model is comparable to the spectral amplitude of the observed mean spectrum, those spectral amplitudes predicted by other saturation models are larger than the observed mean amplitude within a factor of 3. However, mean vertical wave number spectra observed at 69N exhibit significant seasonal variation with a shallower slope of  $-2.40$  and a larger spectral amplitude of  $2.6 \times 10^5$  ( $\text{m}^2/\text{s}^2$ )/(cyc/m) at  $m = 1/(4 \text{ km})$  in winter compared to that spectrum observed in summer. Very large mean wind shears, as high as  $42\text{--}77$  m/s/km, are observed to be present at several heights near the mesopause. Such strong mean shear profiles, together with the Brunt-Vaisala frequency squared  $N^2$  profiles, act collectively to produce dynamical instability regions of local Richardson number  $Ri$  smaller than 0.25. These regions are found to correlate well with the saturated gravity wave spectra. In contrast, the stable region of local Richardson number  $Ri$  larger than 0.4 observed at high latitude in winter is found to associate with an unsaturated gravity wave spectrum.

The temperature spectra from balloon soundings over Beijing are studied by Wu et al., (2006b). Vertical temperature profiles with a height resolution of 10m have been measured in the troposphere and lower stratosphere during March and April 2003 over the Beijing Meteorological Observatory. Vertical wave number spectra of six temperature profiles are presented. Results indicate that mean spectral slopes are about  $-1.9$  in the troposphere and  $-2.2$  in the lower stratosphere, which is believed to be the shallowest slopes ever measured by balloon borne radiosonde soundings. Mean spectral amplitudes at  $m=1/(100\text{m})$  are about 17 times larger in the troposphere and 4 times larger in the lower stratosphere than the predicted saturated spectral amplitudes. These results show that the observed temperature spectra do not obey current gravity wave saturation models, the “universal” atmospheric spectrum model, or the wind-shifting model, in both slope and amplitude.

The gravity wave effects are studied. For instance, we investigated the character of vertical wavenumber spectra of ozone fluctuations, to assess the possible roles of gravity wave field in ozone fluctuations, by using 12 ozone fluctuations obtained during June–August 2003 (Yuan, et al., 2009). Results indicate that mean spectral slopes in the wavenumber range from  $4.69 \times 10^{-4}$  to  $2.50 \times 10^{-3}$  cyc/m are about -2.91 in the troposphere and -2.87 in the lower stratosphere, which is close to the slope of -3 predicted by current gravity wave saturation models, which suggests that the observed ozone fluctuations are due primarily to atmospheric gravity waves. Mean vertical wavenumber spectra in area-preserving form reveal dominant vertical wavelengths of about 2.6 km in the troposphere and about 2.7 km in the lower stratosphere.

### 2.3 Airglow

The photochemical model for the OH Meinel bands nightglow emission is discussed by Gao et al. (2007). Both the expression for the number densities of OH ( $v \leq 9$ ) and the expression for the OH vibrational bands nightglow emission rates are derived from the photochemical model. The impact of chemical reaction,  $\text{HO}_2 + \text{O} \rightarrow \text{OH} (v \leq 6) + \text{O}_2$ , on the number densities of OH ( $v \leq 6$ ) and on the OH ( $v' - v''$ ) ( $v' \leq 6$ ) ( $v'$  represent the higher vibrational levels and  $v''$  represent the lower vibrational levels) vibrational bands emission are studied. The results indicate that the contribution of the reaction to the number densities increases with decreasing  $v$  and the contribution to the OH ( $v' - v''$ ) vibrational bands emission increases with decreasing  $v'$ . The calculations for vernal equinox, local midnight at (0°E, 45°N) show that the reaction makes the peak density for level  $v=1$  and the peak emission rate of the OH(1-0) vibrational band increase by about 33%, the peak density for level  $v=6$  and the peak emission rates of the OH(6- $v''$ ) vibrational bands increase by about 7%, the OH(1-0) band intensity increase by about 30%, and the OH(6- $v''$ ) bands intensities increase by about 11%. Furthermore, the reaction can make the widths of the altitude profiles for both the number densities and the vibrational bands emission rates increase, and the peak altitudes of these profiles lower by about 1km. The contribution of the reaction is sensitive to the atomic oxygen density and temperature. It increases with decreasing atomic oxygen density, and increases with increasing temperature almost linearly. And it is the strongest for summer solstice and the weakest for winter solstice.

The nocturnal variation and seasonal variation characteristics of OI5577 airglow intensity in 2000 and 2001 at 52°N are analyzed by Gao et al. (2006). By using the method of inverting atomic oxygen peak density from OI5577 intensity, the peak density of atomic oxygen is obtained. The nocturnal variation and seasonal variation characteristics of atomic oxygen peak density are discussed. The results show that the nocturnal variation characteristics of OI5577 airglow intensity change with seasons. In 2000, the peak intensity appears after 0000LT in spring, appears at 00:00LT in winter, and appears before 00:00LT in summer and autumn. In 2001, the peak

intensity appears before 00:00LT in spring and autumn, and appears at 0000LT in summer and winter. There are peaks of OI5577 airglow intensity in February, August and October in 2000. In 2001, there is a peak of OI5577 airglow intensity in September. As far as the main features are concerned, the nocturnal variation and seasonal variation characteristics of atomic oxygen peak density are consistent with those of OI5577 airglow intensity.

Gao et al. (2009a) develop a method for deriving the peak density of atomic oxygen in the MLT region from atomic oxygen [OI] 558 nm nightglow intensity. By using this method, the peak density of atomic oxygen is derived from the 558 nm airglow data observed at the ISTP SB RAS Geophysical observatory in 2000-2004. The results show that nocturnal variation of the 558 nm airglow intensity changes with season and have peaks in March, June and October, and larger values in the winter months. The nocturnal and the seasonal variations of the peak density of atomic oxygen are generally similar to those of 558 nm airglow intensity. Gao et al., (2009b) studied the method of retrieval of the oxygen density by using the OH airglow observation. The retrieval uncertainties of the oxygen density are analyzed.

#### *2.4 Influence of solar activity on the atmospheric circulation*

Based on reanalysis monthly data and sunspot cycle index, the influences of the 11-year sunspot cycle (SSC) in stratospheric and tropospheric circulation are investigated by using statistical analysis and dynamical diagnosis during northern winter (November to March). According to the east or west phase of stratospheric equatorial zonal wind quasi biennial oscillation (QBO), we've analyzed the solar effects in different situations. In east QBO phases, the solar effects focus on the equatorial upper stratosphere and south hemispheric stratosphere, where enhanced solar ultraviolet radiations heat up the stratospheric ozone layer, leading to the temperature increase apparently; the solar maxima events reinforce the south stratospheric Brewer-Dobson circulation, and result in the south polar areas warming; planetary wave plays a significant role in north high latitudes regions, hence the solar cycle signals could be nearly neglected. In west QBO phases, solar effects are more important in north hemisphere. In early winter, solar maxima effects are not only warming the equatorial stratospheric ozone, but also restraining the northern atmospheric B-D circulation, leading to the equatorial stratospheric temperature increase and zonal wind gradient change, hence the two waveguides of planetary wave are altered after those processes. In late winter, the polar waveguide of planetary wave is enhanced by solar effects and the B-D circulation is recovered gradually. After these procedures the temperature of northern polar stratosphere starts to increase conspicuously, accompanying by the decrease of equatorial zonal temperature.

#### *2.5 QBO*

The analyses also show that the seasonal variation, the quasi-biennial oscillation (QBO) signals and the long-term trends are clear for all the traces, and the trends of the traces gases in stratosphere are different. The variation trends of those trace gases in stratosphere were analyzed for various altitudes and latitudes (Chen et al. 2009a). The results show that the trends of the traces gases are different in various latitudes as well as in various levels of stratosphere. Comparing the trends of O<sub>3</sub> with the trends

of the other traces gases shows that the recovery of the ozone concentration after the mid-1990s is clear in the upper stratosphere, and the trend of O<sub>3</sub> from 1992 to 2005 is opposite to the trend of HCl, HF and water vapor. In the middle stratosphere, the variation of O<sub>3</sub> is complicated. Besides destroyed by the ozone-depleting substances, ozone concentration would be affected by the other factors. While the increase trends of ozone mixing ratio from 1997 to 2002 was opposite to the decrease trends of HCl, NO, NO<sub>2</sub> and water vapor. That means the benefits of Montreal Agreement, make the decrease of those traces, have won initial success for the recovery of the ozone concentration not only in upper stratosphere but also in middle stratosphere.

### 2.6 Stratospheric sudden warming (SSW)

The characteristics of the spatial and temporal distribution of the SSW were analyzed by using the daily averaged NCEP data from 1950 to 2003 (Deng and Chen 2006). The results show that: SSW in the Northern Hemisphere appeared so often that there were 69 SSW events during the 54 years and it occurred more than once a year on the average, even twice or thrice in some year; The location of the warming center of SSW in the Northern Hemisphere changed with height along clockwise direction, i.e. at lower level (near 16km), it mostly located in the northern tip of North America to the Arctic in the western hemisphere; at upper level (near 30km), it mostly located over the north of Eurasia to the Arctic; SSW in the North Hemisphere usually occurred firstly near 30 km over the north of Eurasia, and then extended and transported from upper levels to lower levels with the warming center shifted gradually to the north of North America in the western hemisphere; during SSW, the change of the temperature and the circulation in Stratosphere can affect the Troposphere, and lead to the change of the temperature and circulation in the Troposphere.

In order to investigate the characteristics of planetary wave activity during SSW, the abnormality of planetary wave of wave-number 1 and wave-number 2 in the mid-lower stratosphere in 18 major SSW events during 1979~2004 were analyzed (Deng et al. 2006) using the daily averaged NCEP data, and the distortion and the breakdown of polar vortex of the 18 major SSW events were also studied. Then the E-P flux and its divergence were calculated and analyzed to explain the activities of planetary wave and their relation with SSW. The results show that the planetary wave of wave-number 1 unusually grows in the pre-SSW period, and SSW takes place after the peak of the amplitude of wave 1, which agree with Labitzke's conclusions (1978,1981), however, the variations of the amplitude of planetary wave in various SSW events are much different, They show in the following three types: For type 1, the planetary wave of wave-number 2 in the pre-SSW period is very weak, it unusually grows too stronger in the mid-SSW period, while planetary wave of wave-number 1 becomes weak, which also accord with Labitzke's conclusions. In this type the polar vortex breaks down and splits into two cyclonic centers; For type 2, the planetary wave of wave-number 2 in the pre-SSW period is correspondingly stronger, nevertheless, in the mid-SSW period, both planetary wave of wave-number 1 and wave-number 2 are distinctly weak, at the same time, the polar vortex moves outside of the polar region, but does not breakdown; For type 3, planetary wave of

wave-number 2 in the pre-SSW period is not very strong, while it develops slightly in the mid-SSW period, however, it can not surpass planetary wave of wave-number 1 in any case, simultaneously, the polar vortex firstly moves out from the polar region and then asymmetric split in form occurs. Our results show that only the activities of planetary wave in type 1 SSW accord with Labitzke's conclusions. The activities of planetary wave in type 2 and type 3 SSW are much different from Labitzke's conclusions.

The calculated E-P flux and the E-P flux divergence show that the distribution of the E-P flux for the various type of SSW are much different, therefore the vertical transport of the planetary wave for various type of SSW are not the same. While in all events the E-P flux convergence for the wave-number 1 and wave-number 2 in the pre-SSW and mid-SSW appears in the stratosphere from middle and high latitude to the polar region, which causes zonal-mean western wind weakened, even become eastern wind. According to the theory of thermal wind, this means that temperature gradient from middle-high latitude to the pole reverse its direction, that is say the temperature suddenly turns high nearby the polar region.

The residual meridional circulation derived from the transformed Eulerian-mean thermodynamic equation and continuity equation can be separated into two parts: the slowly varying diabatic circulation and the transient circulation. Deng et al (2010) calculated and composite analyzed the transient and diabatic circulation for 14 stratospheric sudden warming (SSW) events from 1979 to 2002 by using the daily European Centre for Medium-Range Weather Forecasts (ECMWF) reanalysis data. Specially, the transient residual meridional circulation were calculated both with and without including the eddy heat transport term in the transformed Eulerian-mean thermodynamic equation to investigate the importance of the eddy heat transport term. The results show that the transient residual meridional circulation present rapid variations during SSWs, either with or without including the eddy heat transport term. In the mid-SSW periods, the transient residual meridional circulation showed two cells at high northern latitudes: an upper one, with upward motion at the pole and descending motion in mid-latitudes, and a lower one with circulation in the opposite sense. Totally different characteristics were observed in the pre-SSW and post-SSW periods.

The transient residual meridional circulation results with and without including the eddy heat transport term were carefully compared. Results indicated that although the patterns of transient residual meridional circulation with the eddy heat transport term were similar to that without the eddy heat transport term during SSW, the magnitudes in the upper stratosphere and high-latitude regions differed. Specifically, the transient residual meridional circulation with the eddy heat transport term was stronger than that without the eddy heat transport term, and its variations at SSW onset were more rapid. Therefore, the eddy heat transport term should be important in the upper stratosphere of the high-latitude regions. As for the diabatic circulation, its daily variations are small during SSW events, and its patterns are in agreement with its monthly average.

The variation of vertical distribution for ozone during stratospheric sudden

warming (SSW) was analyzed (Deng et al. 2009) by using ECMWF data. The results indicate that ozone mixing ratio increase during SSW and its maximum is mostly formed in the middle days of SSW. In the mean time, the high-value areas of ozone mixing ratio changes with height during SSW. So according to this, the variation of ozone mixing ratio with height during SSW can be divided into two kinds: 1) downward propagation: The high-value areas of ozone mixing ratio vertically propagate downward in the early days of SSW periods. In the course of the downward propagation of ozone mixing ratio, the maximum of ozone mixing ratio is formed in the middle days of SSW, and then move upward; 2) increasing thickness: The thickness of ozone high-value areas increases during SSW and ozone ratio also increase nearly, and the high-value areas of ozone mixing ratio dose not change with height in the early days of SSW, however, after SSW begins, the high-value areas of ozone mixing ratio move upward.

The two types of ozone variation with height during SSW are caused by the dynamics of the residual meridional circulation transport on ozone during SSW. Downward propagation of ozone is triggered by the transport effects of the residual meridional circulation in the early days of SSW. In that time, the strong northward motion of the residual meridional circulation from the mid-latitudes to the polar region synchronously occurs with the sharp downward motion in the polar region, which makes ozone transported from the mid-latitudes propagate downward. Consequently, downward propagation of ozone high-value areas occurs. Increasing thickness of ozone high-value areas is triggered by the transport effects of the residual meridional circulation in the middle days of SSW. In the middle days of SSW, the northward motion of the residual meridional circulation from the mid-latitudes to the polar region synchronously occurs with the upward and downward motions at 5 hPa. Therefore the upward flow causes the upward transportation of ozone from the mid-latitudes and the downward flow triggers the downward transportation of ozone, thus the thickness of ozone high-value areas increases during SSW. Ozone mixing ratio in the mid latitudes was also analyzed during SSW and the results indicates that ozone mixing ratio decrease in the mid latitudes during SSW.

In 2002, an unusual Antarctic stratospheric sudden warming occurred. In order to understand how the 2002 Antarctic SSW affect the distributions of the trace gases, Yi and Chen (2008) analyzed the distributions of the trace gases (O<sub>3</sub>, CH<sub>4</sub>, HCl, NO, NO<sub>2</sub> and H<sub>2</sub>O) in the stratosphere over Antarctica after the Antarctic SSW by using HALOE data. Results indicate that after the SSW over Antarctica, besides the ozone Hole weakened, large changes took place in the stratospheric trace gases. In 2002 the trace gases were mixed more evenly along latitude, the distribution of wave number 2 pattern was demonstrated obviously on the height-latitude section along 70°S, compared with the typical distribution of strong wave number 1 in 2003 and other normal years (without SSW). At the location of the south polar vortex for the normal year, the mixing ratios of O<sub>3</sub> and CH<sub>4</sub> increased, HCl and NO decreased, but NO<sub>2</sub> and H<sub>2</sub>O did not accorded with a given rules at all altitudes over Antarctic in 2002, which was related to the change of the vortex and the dynamical transportation after the SSW, and affected by the reduced polar stratospheric clouds and weakened

processes of heterogeneous chemistry.

### **3. Progress in Stratosphere-Troposphere Exchange**

#### *3.1 Finer structure in the tropopause layer*

High resolution radiosonde data from Beijing, China in 2002 are used to study the strong tropopause inversion layer (TIL) in the extratropical regions in eastern Asia (Bian and Chen, 2008). The analysis, based on the tropopause-based mean (TB-mean) method, shows that the TIL over Beijing has similar features as over other sites in the same latitude in Northern America. The reduced values of buoyancy frequency in 13-17 km altitude in winter-spring are attributed to the higher occurrence frequency of the secondary tropopause in this season. In the monthly mean temperature profile relative to the secondary tropopause, there also exists a TIL with somewhat enhanced static stability directly over the secondary sharp thermal tropopause, and a 4 km thickness layer with reduced values of buoyancy frequency just below the tropopause, which corresponds to the 13-17 km layer in the first TB-mean thermal profile. In the monthly mean temperature profile relative to the secondary tropopause, a TIL also exists but it is not as strong.

For individual cases, a modified definition of the TIL, focusing on the super stability and the small distance from the tropopause, is introduced. The analysis shows that the lower boundary of the newly defined TIL is about 0.42 km above the tropopause, and that it is higher in winter and lower in summer; the thickness of the TIL is larger in winter-spring.

#### *3.2 Stratosphere-troposphere exchange processes*

Ozone enhancement and loss were observed in the mid and upper troposphere over Lin'an, Kunming and Hongkong during March 27-29 2001 in the measurement of the electrical chemical cell (ECC) ozonesondes, and the upper tropospheric ozone enhances over Hongkong on March 29 1996 and over Lin'an on April 13, 2001. Basing on the NCEP/NCAR reanalysis data and GMS 5 water vapor imagery, Zheng et al (2008) analyzed the enhanced ozone source and the multi scale characteristics of ozone change in the mid and upper troposphere over South China. The results indicated that the intrusion of stratospheric air to the mid and upper troposphere occurred not only in the higher latitudes but also in the lower latitudes (over Kunming and Hongkong) over South China.

#### *3.3 Stratosphere-troposphere exchange climatology*

Zhan and Li (2008) investigated the Stratosphere-Troposphere Exchange (STE) of water vapor, emphasized its inter-decadal variations over Asia in boreal summer, and discussed the influences of atmospheric heat sources over the Tibetan Plateau and the tropical western North Pacific (WNP) on them by using the Wei method with reanalysis data from the European Centre for Medium-Range Weather Forecasts (ECMWF) for the years of 1958-2001. The climatology shows that the upward transport of water vapor across the tropopause in boreal summer is the most robust over the joining area of the South Asian Peninsula and Indian-Pacific Oceans (defined as AIPO). The upward transport over there can persistently convey the abundant water vapor into the stratosphere and then influence the distribution and variation of the stratospheric water vapor. The analysis shows that inter-decadal variations of the

water vapor exchange over the AIPO are significant, and its abrupt change occurred in the mid-1970s and the early 1990s. In these three periods, as important channels of the water vapor exchange, the effect of Bay of Bengal-East Asia as well as South China Sea was gradually weakening, while the role of the WNP becomes more and more important. Further studies show that atmospheric heat sources over the Tibetan Plateau and the WNP are two main factors in determining the inter-decadal variations of water vapor exchange. The thermal influences over the Tibetan Plateau and the WNP have been greatly adjusted over the past 44 years. Their synthesis influences the inter-decadal variations of the water vapor exchange by changing the Asian summer monsoon, but their roles vary with time and regions. Especially after 1992, the influence of heat source over the Tibetan Plateau remarkably weakens, while the heat source over the WNP dominates the across-tropopause water vapor exchange. Results have important implications for understanding the transport of other components in the atmosphere and estimating the impact of human activities (emission) on global climate.

Based on ECMWF data sets from 1958 to 2001, the cross-tropopause mass flux (CTF) over the Tibetan Plateau and its surrounding regions was calculated by Wei formula, and its spatial-temporal distribution and long-term trend was analyzed (Fan et al., 2008). Analysis results show that: (1) the CTF has a zonal distribution structure, and shows two distinct features on both sides of the subtropical jet. In the steep tropopause belt to the north of the jet, the CTF varies in a zonal wave-like pattern from TST (troposphere to stratosphere transport) to STT (stratosphere to troposphere transport) to TST, and so on, which is mainly caused by the horizontal CTF; and the CTF distribution on the south side is dominated by the vertical transport term. (2) In the longitude range (80E-105E), southern Tibetan Plateau and its southward regions are covered by TST, and the northern part by STT in winter-spring; however, the whole region from 20N to 40N is almost controlled by TST in summer-autumn. In all seasons, CTF is dominated by the vertical term to the south of the jet, and by the horizontal term in the steep tropopause belt, and by both terms to the further north. (3) The statistically regional averaged monthly CTF over the Tibetan Plateau and the Gulf of Bengal is controlled by TST in all seasons, with two maxima in February and July, which are caused by two different mechanisms, the vertical transport for while the horizontal term for February. (4) The regional mean annual CTF undergoes a transition from a decreasing trend before 1982 to a relatively stronger increasing trend afterwards.

Based on a Lagrangian dispersion model FLEXPART driven by the NCEP/NCAR global forecast system reanalysis data, Chen et al. (2010a) study the pathways and timescale of troposphere to stratosphere transport (TST) over the Asian monsoon regions during the summer of 2005 using the air parcels back trajectories, as well as the surface sources, defined in terms of the locations where each trajectory last left the atmospheric planetary boundary layer. The following conclusions are drawn in the paper: (1) The boundary layer sources are most located (approximately four fifths) vertically above two areas, one is the south of the Tibetan Plateau, the Indian Ocean, and the Bay of Bengal, and the other is the tropical western Pacific regions. These two

areas correspond to those regions previously identified as sources for active deep convection. Even though the two regions make the same contribution to transportation from the PBL to the base of tropopause layer (about 16 km), the transport from the tropopause layer to the stratosphere with a much smaller fraction (about 10%) arriving at the 20-22 km height is dominated by the former (approximately 75%). These analysis results emphasize the importance of Asian monsoon regions in the TST, with the Tibetan Plateau, the Indian Ocean, and the Bay of Bengal being the dominant source of the stratospheric “over-world air.” (2) The analysis of trajectories reveals that the air parcels arrive at and cross the tropopause mainly over the south of Tibetan Plateau and its adjacent areas (25°N-35°N, 90°E-110°E). These pathways represent a regional pattern and are largely co-controlled by the South Asia high circulation in the upper troposphere, the northern hemispheric subtropical jet and the equatorial easterly jet. Then about at 150 hPa, the most air parcels are transported westward, the rest entered the South Asian monsoon regions. (3) The results also reveal that there are two main processes in the TST. One is a fast transport process related to the convection uplift which can bring the boundary layer mass into the stratosphere in 1-2 days and make a contribution about 10%-30% of the overall mass transport. The other is a slow transport process relatively which may be related to the large-scale vertical transport due to atmospheric radiative heating in the upper troposphere. Overall, a part of transport from the boundary layer to the lower stratosphere is so rapid that this can represent an important route by which very short-lived substances, emitted at the surface, can influence the lower stratospheric ozone and other tracer budget.

A particle dispersion model combined with “domain filling” technique is applied to the analyzed data from Global Forecast System of National Centers for Environmental Prediction (NCEP/GFS) to study the troposphere-to-stratosphere mass transport (TST) and the stratosphere-to-troposphere mass transport (STT) over the Asian monsoon region for the period from June to August in 2005 (Chen et al. 2010b). A residence time criterion serves to distinguish between transient (reversible) exchange and irreversible exchange, and special emphasis is paid to the later mass exchange, which has great impact on the budget of chemical constituents in both the stratosphere and troposphere. The source and sink features in the irreversible exchange are also analyzed by trajectory-track method. The main conclusions can be summarized as follows: (1) The results show that the sensitivity of the Troposphere-Stratosphere mass Exchange (STE) distributions to the threshold residence time is pronounced at all latitudes. The major part of exchange air parcels return rapidly (within less than 1~2 days) to their “original sphere”. The quantitative STT and TST mass flux estimates are strongly dependent upon whether these transient events are considered or not. (2) In general, the overall analysis of STT, TST and net mass exchange reveals that upward and downward transport of mass at the middle and high latitude accompany with each other. The meridional distribution of the net flux reveals an upward branch in the subtropics, pronounced downward exchange in the mid-latitudes from 45°N to 55°N latitude and weak upward fluxes in high latitude region. Detailed geographical distributions show strong downward cross tropopause mass flux mainly in the north of Tibetan Plateau, which corresponds to the large scale

troughs in summer. The results also show that the whole Asian monsoon region is the region of upward cross tropopause mass flux. Tibetan Plateau and its adjoin regions are the main channels of the upward mass flux into the stratosphere, which makes a fraction contribution of 46%. (3) The four days source and sink characteristics of the irreversible mass exchange also reveal that the STT mainly come from the high latitude regions of west of 100°E and north of 50°N, and transport to the middle latitude areas, such as the northeast of China and north Korea. But the source and sink characteristics of TST reveal that the upward mass from the troposphere into the lowermost stratosphere can be transported to the high latitude and low latitude tropical regions respectively, which indicate that the TST of Asian monsoon have an enhanced potential for water vapor transportation into the stratosphere tropical pipe and play an important role in the global stratosphere water budget.

#### **4. Progress in Stratosphere-Troposphere Coupling**

##### *4.1 Stationary planetary wave activity and East Asian winter monsoon*

The variability of both the stationary planetary wave activity and the East Asian winter monsoon (EAWM) is strongly associated with the thermal contrast between oceans and land masses. Chen et al. (2008) explored the relationship between this wave activity and the EAWM on interannual timescale. It is found that, compared to the winters of low wave activity, the equatorward propagation of planetary waves in the middle and upper troposphere is stronger in the high wave activity winters. During these high activity winters, the weakening of the Siberian high and the Aleutian low decreases the northeasterly wind over East Asia, leading to a warming condition in the region especially in northeastern Asia. This relationship between the wave activity and the monsoon on interannual timescale is strongly modulated by the tropical quasi-biennial oscillation (QBO) of zonal winds in the stratosphere (Chen and Li, 2007). Only in the QBO easterly phase, the EAWM is closely related to the planetary wave activity with a significant warming/cooling in northeastern Asia. It is suggested that this modulation may arise from the indirect influence of the QBO induced polar and extra-tropical stratospheric circulation changes.

The mechanism for the relations of planetary wave activity to the EAWM may also well explain the weakening of EAWM around the late 1980s (Wang et al., 2009). The EAWM experienced a significant weakening around late 1980s. In the meantime, both the propagation and amplitude of quasi-stationary planetary waves have experienced obvious interdecadal variations, which are well related to those of the EAWM. Anomalous propagation of waves may weaken the East Asian jet stream. And reduced amplitude of waves may weaken both the Siberian high and the Aleutian low, which reduce the pressure gradient in between. Hence, the EAWM is weakened. Most recent work of Wang et al. (2010) also suggests that interdecadal variations of planetary wave propagation may account on the enhanced Ural blocking-East Asian winter climate relationship.

Further works of Chen and Kang (2006) interpreted the influence of Arctic Oscillation (AO) on the winter climate anomalies over East Asia with the anomalous planetary wave activity. They indicate that the AO firstly influences the strength of westerlies in the lower stratosphere over mid-high latitudes. Then the vertical

propagation of planetary wave is affected, which leads to anomalous propagation of planetary waves in the troposphere. In particular, the wavenumber-2 pattern of planetary waves, which contributes dominantly to the variability of the Siberian high and the Aleutian low, is significantly impacted. Hence, the induced surface southerly (northerly) anomalies cause a warming (cooling) in North China and Northeast China. Huang et al. (2007) choose recent two winters of 2005 and 2006 as the cases to analyze their relations to the stationary planetary wave activity. The EAWM is strong in 2005 with cold surface air-temperature in middle and high latitudes over the Eurasian continent. However, the winter of 2006 is warm with a weak EAWM. This difference has been shown to be closely associated with the AO. Their results confirm that the planetary wave activity plays a key role in the difference between these two winters.

#### *4.2 Downward influences on the EAWM from the stratosphere*

The interannual variations of the winter stratospheric polar vortex are investigated by Chen and Wei (2009a) through an EOF analysis. The leading mode (EOF1) reflects the intensity variation of the polar vortex and is characterized by a geopotential height seesaw between the polar region and the mid-latitudes. The second one (EOF2) exhibits variation in the zonal asymmetric part of the polar vortex, which mainly describes the stationary planetary wave activity. As the strongest interannual variation signal in the atmosphere, the QBO has been shown to influence mainly the strength of the polar vortex. On the other hand, the ENSO cycle, as the strongest interannual variation signal in the ocean, has been shown to be mainly associated with the variation of stationary planetary wave activity in the stratosphere. As both QBO and ENSO exert influence on the stratospheric polar vortex, Wei et al. (2007a) found that the QBO modulation on the polar vortex is significant only when the sea surface temperature (SST) anomaly is cold in the tropical eastern Pacific. The possible mechanism may be attributed to the interaction between the tropical eastern Pacific SST- and the QBO-associated planetary wave propagation.

Wei et al. (2007b) analyzed the effect of planetary wave activity on the stratospheric polar vortex breakup in boreal spring. The results indicate that the breakup time has large interannual variations with a long-term trend towards late. The breakup of the stratospheric polar vortex and the role of planetary waves are also investigated with focus on the differences between the southern and northern hemispheres (Wei et al., 2008). Strong activities of planetary waves are found before the breakup and the wave activities decline quickly afterwards. It is suggested that the upward planetary wave propagation determines the exact time of breaking. The long-term trend indicates that the breaking time of the stratospheric polar vortex has been postponed in both hemispheres, especially since the mid 1990s. With the reanalysis data of ERA40, Wang et al. (2007) investigated the climatology and annual cycle of zonally averaged meridional transport of westerly momentum by stationary waves in the northern hemisphere. The contribution from the planetary-scale and the synoptic-scale stationary waves is particularly analyzed in both the stratosphere and troposphere.

Possible influences of the stratospheric polar vortex on the tropospheric

circulation are also documented on both the interannual and intraseasonal timescales (Chen and Wei, 2009a; 2009b). On intraseasonal timescale, they found that the variability of planetary wave activity is closely associated with the low frequency variations of stratospheric polar vortex. The anomalous polar vortex in the stratosphere may have a downward influence on the short-term climate in the troposphere via the interaction with the planetary waves. In addition, this downward influence is particularly significant over East Asia.

#### *4.3 Ocean influences on polar vortex*

Using the polar vortex oscillation (PVO) index established in an isentropic potential vorticity coordinate and based on the NCEP/NCAR reanalysis data and the weekly NOAA-OISST-V2 SST data, the temporal and spatial connections of the stratospheric PVO to the ENSO tropical SST over monthly timescale are investigated (Ren and Xiang, 2010). It is found that the significant connections exist mainly at the inter-annual timescale of about 3-5 year, representing the relationships between the inter-annual PVO trend and the ENSO SST anomalies. Firstly, the temporal connections between the two phenomena are not contemporary as expected, but rather that the maximum negative correlation occurs when the ENSO tropical SST anomalies lead the PVO for 9-11 months. Warmer (colder) ENSO SST anomalies tend to be followed by a negative (positive) inter annual trend of PVO, or a weaker (stronger) polar vortex. The composite and statistical results further verify that there tend to be more and stronger negative PVO events followed in the case of a warmer ENSO SST event occurred in the previous period, and vice versa. The warmer ENSO SST may also favor a higher frequency of PVO events than colder SST regardless of positive or negative PVO events. Further, it is found that, following the significant responses in the tropical troposphere and stratosphere to the warmer ENSO SST, there exist a series of simultaneous poleward and downward propagations of temperature anomalies from the tropics to the polar region, which are coincidentally related with the PVO anomalies 9-11 months later. This linkage of the tropical SST to the extra tropical PVO trend implies basically new opportunities for the extended climate prediction.

As in the Northern Hemisphere, there exists a simultaneous poleward propagation of temperature anomalies in the stratosphere and equatorward propagation in the troposphere in the Southern Hemisphere's cold season (Ren & Cai, 2008). It takes about 110 days for anomalies of one polarity to propagate from the equator to the pole (or half the period of the complete cycle), nearly twice as long as in the Northern Hemisphere. The earlier poleward propagation of temperature anomalies in upper levels compared with those in lower levels results in an apparent downward propagation in the stratosphere. Accompanying the poleward- and downward-propagating warm (cold) anomalies is a successive leveling (steepening) of isentropic surfaces, reflecting a simultaneous reduction (strengthening) of the meridional temperature gradient and increase (decrease) of the vertical static stability. Following changes in the thermal fields are poleward- and downward- propagating zonal wind anomalies of the opposite sign.

The arrival of the poleward-propagating stratospheric thermal anomalies over the

polar region coincides with the beginning of the compensating equatorward advancement of tropospheric thermal anomalies of the opposite sign. The synchronized meridional propagation in the thermal fields results from the temporal variation between stronger and weaker meridional mass circulations, which is responsible for a meridional out-of-phase variability pattern in both the stratosphere and troposphere and a vertical out-of-phase pattern between stratospheric and tropospheric temperature anomalies at high latitudes. The vertical alignment of a warm high (cold low) anomaly in the stratosphere overlying a cold high (warm low) anomaly at the surface explains the apparent “equivalent barotropic” structure in the height anomalies.

Using the NCAR/NCEP reanalysis, Ren and Cai (2007) present evidence suggesting that the out-of-phase relationships of temperature anomalies both between the low and high latitudes and between the stratosphere and troposphere are intimately related to the meridional and downward propagation of anomalies of both signs. The temperature anomalies propagate poleward and downward above the tropopause and propagate equatorward below the tropopause. The characteristic time scale for anomalies of one polarity to propagate from the equator to the pole (or the half period of the complete cycle) is about 55 days. The relatively slow meridional propagation helps to explain the well-known seesaw oscillatory pattern between low and high latitudes found in monthly data. The equatorward propagation in the troposphere is synchronized with the poleward propagation of the stratospheric temperature anomalies of the opposite sign in both low and high latitudes, responsible for the out-of-phase relation between the stratospheric and tropospheric temperature anomalies in the polar region. Since it takes about 55 days for anomalies of one polarity to propagate from the tropics to the pole, such an intimate linkage between the anomalies in the deep tropics and high latitudes would imply a longer lead time for intra-seasonal climate prediction in the extratropics.

During recent decades, the tropical Indo-Pacific Ocean has become increasingly warmer. Meanwhile, both the northern and southern hemispheric polar vortices (NPV and SPV) have exhibited a deepening trend in boreal winter. Although previous studies have revealed that the tropical Indian Ocean warming (IOW) favors an intensifying NPV and a weakening SPV, how the tropical Pacific Ocean warming (POW) influences the NPV and SPV remains unclear. Li (2010) conducts a comparative analysis through ensemble atmospheric general circulation model (AGCM) experiments. The results show that, for the Northern Hemisphere, the two warmings exerted opposite impacts in boreal winter, in that the IOW intensified the NPV while the POW weakened the NPV. For the Southern Hemisphere, both the IOW and POW warmed the southern polar atmosphere and weakened the SPV. A diagnostic analysis based on the vorticity budget revealed that such an interhemispheric difference in influences from the IOW and POW in boreal winter was associated with different roles of transient eddy momentum flux convergence between the hemispheres. Furthermore, this difference may have been linked to different strengths of stationary wave activity between the hemispheres in boreal winter.

Although previous modeling studies reveal that radiative cooling effect of ozone

depletion plays a dominant role in causing the deepening of SPV, the simulated ozone-depletion-induced SPV deepening is stronger than the observed. This suggests that there must be other factors canceling a fraction of the influence of the ozone depletion. Whether the tropical Indian Ocean warming (IOW) is such a factor is unclear. This issue is addressed by conducting ensemble atmospheric general circulation model (AGCM) experiments (Li, 2009). And one idealized IOW with the amplitude as the observed is prescribed to force four AGCMs. The results show that the IOW tends to warm the southern polar stratosphere, and thus weakens SPV in austral spring to summer. Hence, it offsets a fraction of the effect of the ozone depletion. This implies that global warming will favor ozone recovery, since a warmer southern polar stratosphere is un-beneficial for the formation of polar stratospheric clouds (PSCs), which is a key factor to ozone depletion chemical reactions.

#### *4.4 AO impacts on eastern Asian weather/climate*

The possible influence of stratospheric sudden warming (SSW) on the weather/climate in China is investigated by Li et al. (2010) via the circulation property analysis of the SSW events from 1957 to 2002. The stratospheric circulation at higher latitude changes dramatically during SSW events. However, such change is not limited inside stratosphere. The resulted circulation anomalies can propagate downward and affect the weather and climate in troposphere. It is shown that, after strong SSW, the temperature and height anomalies on stratosphere can produce downward Arctic Oscillation (AO), which may result in the stronger Siberian-High, lower Aleutian-Low and deeper, westward East-Asian trough at 500 hPa. Then, East-Asian winter monsoon (EAWM) is enhanced which makes the temperature lower than normal in most parts of North China. Furthermore, the strong planetary wave before SSW can also lead to the enhancement of East-Asian trough, Siberian-High, Aleutian-Low, and the East-Asian winter monsoon thereby. El Nino can excite strong planetary wave propitious to the occurrence of strong SSW event, which may enhance the EAWM via the two processes mentioned above. The results in this paper may challenge the conclusion that El Nino event may weaken EAWM via troposphere process. Therefore, ENSO event may affect East-Asian winter monsoon and the weather/climate in China through the integration of more than one ways.

Based on the data analyses, Li et al. (2008) show that mei-yu precipitation may be influenced by the stratospheric atmosphere circulation anomaly through the Arctic Oscillation (AO) in the troposphere. The stratospheric atmosphere circulation in February is closely related to the AO in March. It may affect the AO through the downward propagating wave activity anomalies. The EOF1st and EOF3rd leading modes of 30hPa geopotential height in February are significantly associated with anomalous downward E-P flux in the subtropics and the polar region, respectively. The AO in March may in turn exert an influence on summertime circulation in East Asia, which is closely related to the summertime thermal condition of the tropospheric atmosphere over East Asia. The changes of thermal condition and the circulation over East Asia can then lead to anomalous convergence/divergence in Yangtze River Valley, and the anomaly of mei-yu precipitation.

The intraseasonal oscillation (ISO) is a fundamental phenomenon in the

atmosphere. It not only exists in the troposphere of the tropics, but also plays an important role in the atmospheric circulation of the stratosphere. Li et al. (2006) conducted a comparison between the characteristics of the ISO in the troposphere and stratosphere, and the result shows that there are significant similarities between the ISO over the high latitude areas in the troposphere and stratosphere. The Arctic Oscillation (AO) is the most significant low frequency mode of the Northern Hemisphere (NH) during the boreal winter both in the high/low level of the atmosphere. The feature of its spatial distribution is characterized as a “seesaw” pattern in atmospheric mass between the polar cap regions poleward of  $60^{\circ}$  N and the surrounding zonal rings centered near  $45^{\circ}$  N. The most significant variation happens in the polar cap. The positive phase of the ISO stands for the strengthening of the AO, while the negative phase of the ISO is for the weakening of the AO. The teleconnection patterns of the Northern Hemisphere (NH) during the boreal winter in 100 hPa and in 70 hPa (stratosphere) are also investigated. The teleconnection distribution shows there are negative correlation between the polar cap areas and the other areas. The AO dominates the intraseasonal (low frequency) climate variability in the stratosphere. It also can be seen from the teleconnection distribution that the main low frequency wave train is from the middle Euroasia land to the northwest Pacific, which consists of the zonal low frequency wave train (Euroasia land Siberia Pacific) and the meridional low frequency wave train (Euroasia Polar Pacific).

The relationship between the ISO in the stratosphere and troposphere is also studied in this paper. The pattern of the leading empirical orthogonal function (EOF) of the band filtered geopotential height in the stratosphere (30 hPa) and troposphere (500 hPa) are similar. There is also significant lag correlation between the principal component time series. It is shown in the analysis that the variability of the ISO in the stratosphere in the NH during the winter is ahead of the one in the troposphere, and the leading period is about 30 days. The SAMIL model is also used to do the numerical simulation. The result testifies that the low frequency disturbance in the stratosphere can excite the low frequency responses in the troposphere after 14 days, and the reaction would become the strongest after about 30 days. It makes clear that the anomalies in the stratosphere can pose an influence on the troposphere through the ISO activity.

By analyzing the distribution of the regression coefficient of the zonal wind at 200hPa and geopotential height at 500hPa on NAM indices, the linkage of NAM anomaly to the East Asian jet and the East Asian trough during SSW were studied, and the influence of SSW on East Asian was discussed (Deng et al. 2008). The results show that the NAM anomaly affects the lower troposphere with only strong SSW while it hardly affects the troposphere with weak SSW. There is new understanding that in the positive phase of NAM (with no SSW), the East Asian jet and the East Asian trough are weakened, while in the negative phase of NAM (with SSW), the East Asian jet and the East Asian trough are strengthened. In the meantime, the strengthened trend of the East Asian trough moves southward with the downward propagation of SSW and gradually influence the area of northeast China and north China. This implies that the winter monsoon tends to be stronger over East Asia

during SSW. According to this result, we consider that there is a certain influence of SSW on the winter weather over East Asia, thus SSW can be used as a factor to predict the winter monsoon over East Asia.

A serious snow storm and freeze calamity occurred in south part of China in Jan. 2008, which was seldom seen in the history with its extension, strength and long duration. In order to investigate the relationship between the anomaly of the stratospheric polar vortex and the serious snow storm and freeze calamity, the day by day variation of the stratospheric polar vortex from December 2007 to February 2008 has been analyzed using NCEP data (Chen et al. 2009b). The results show that before the occurrence of the snow storm and freeze calamity the stratospheric north polar vortex strengthen clearly with the NAM indices as large as +3.0 in the first ten days of January 2008; At the same time the polar vortex deformed and expanded to Asia and North America and the pressure went up over north Pacific and north Atlantic; The stratosphere over north part of Asia was dominated by a strong low center one month before the serious snow storm and freeze calamity. Moreover, the stratospheric circulation in middle-lower latitudes also changed significantly. These anomalies of the stratospheric circulation propagated downward and affected the troposphere. It is significant that as the stronger low trough extend downward, it moved to the east. Therefore the East Asian Trough in 500hPa was shift to the east of Siberia and the pressure in most part of Eurasia raised, and then a strong blocking high was developed in the region from Mediterranean Sea to the Ural Mountains since the middle of January, which moved slowly to the east and dominated Eurasia. The north-westerly flow in the front of the blocking high led the cold air from north area entered into China, which met the warm and wet air from Bay of Bengal and South China Sea in south part of China, and then caused the serious snow storm and freeze calamity. Our results show that this exceptionally serious snow storm and freeze calamity was connected not only with the changes of the tropospheric circulation, but also with the changes of the stratospheric circulation. Meaningfully, the changes of the stratospheric circulation were more than one month ahead of the snow storm and freeze calamity. Therefore it is helpful to improve the middle and long term weather forecast, especially for the serious meteorological calamity forecast, if we use the information of the stratospheric circulation to the weather prediction.

The anomalies of stratospheric polar vortex appear not only the changes of its strength, but also the changes of its location. So Yi (2009) divided the stratospheric polar vortex into three different patterns by using NCEP data. They are the weak polar vortex pattern (usually with SSW), the North American strong vortex pattern (the strong vortex center settles close to northern of North America) and Northeast Asian strong vortex pattern (the strong vortex center expands towards northeastern Asia). For the different polar vortex patterns, the 500hPa geopotential height, specially the East Asia trough and the North America trough, and the surface temperature were analyzed and discussed. The results show that both the changes of the strength and the location of the stratospheric polar vortex would lead to the lag response of geopotential height and surface temperature, but the effect of each pattern is different. During the weak polar vortex, the East Asia trough strengthen in the early stage, then weakened

gradually, while the North America trough weakened in the beginning, and then strengthen clearly. At the same time, the surface temperature in the north part of Eurasia drop down, while in most part of China, specially in south part of China, it is warmer. When the stratosphere is dominated by the strong polar vortex, their effects on North America are also different from East Asia. During the period of the strong polar vortex, the North America trough strengthen and East Asia trough weaken. Particularly, when the strong vortex center expands to North America, the North America trough strengthened more rapidly and East Asia trough weakened more clearly. In the case of strong polar vortex, the significant cool down occurs in the large area of East Asia, and the cold center moved towards the south and brought about more influence in the south region in the pattern of Northeast Asian stronger vortex. When the center of stratospheric polar vortex close to North America, the drop in temperature in the northeast of North America is larger, in wider area, keep longer and recovered more slowly. Usually the anomalies of the stratospheric polar vortex precede the changes of the North America trough and East Asia trough and the surface temperature, so it is useful for the weather and climate prediction.

The dry adiabatic air should move along isentropic surface and in the same time its potential vorticity would be conservated, this principle was used to explore the downward progress and mechanism of stratospheric polar vortex anomalies (Yi et al., 2009; Yi, 2009). The vertical structure of potential temperature and potential vorticity are obvious different between strong and weak vortex. During strong polar vortex, the isentropic surfaces in stratosphere are higher in north polar regions and descend towards middle latitudes, therefore when polar vortex extended towards the south, the cold air with high potential vorticity would move along declining isentropic surfaces and bring the cold air from higher polar regions to lower middle latitudes in troposphere to form a sunken high potential vorticity center. While during weak polar vortex, the isentropic surfaces in stratosphere are lower in north polar region and ascend towards middle latitudes, cold air with high potential vorticity is located near the mid-high latitudes in stratosphere, the descending cold air would bring high potential vorticity to higher latitudes and polar region, so that it is difficult to form and keep high potential vorticity center in low or mid latitudes in troposphere. The north polar vortex in January, 2008 was northeast Asian strong vortex pattern, the meridional extension of high potential vorticity air from polar regions reached to low latitudes in troposphere over South China, high potential vorticity center formed and developed, obviously related to the widen snow calamity at the same time in South China. The strong polar vortex in January, 2009 had some influence on the cold weather in North China, but the vortex split and became very weak soon after, stratospheric high potential vorticity air extended poleward, cold air was limited to arctic and surrounding regions and could not expand towards the south, so that it is warm in South part of China.

## **5. Progress in Chemistry-Climate Coupling**

### *5.1 Chemistry-Climate Interaction*

Tian et al. (2010) developed a new, computationally efficient coupled stratosphere-troposphere chemistry-climate model. This newly developed CCM has

been evaluated with various observations and it shows good performance in simulating important chemical species and their interdependence in both the troposphere and stratosphere. The modeled total column ozone is in good agreement with MIPAS satellite ozone profiles and TOMS total column ozone observations. The observed CO tape recorder is also successfully captured by the new CCM and ozone-CO correlations are in accordance with ACE observations. Additionally, the simulated stratosphere-to-troposphere ozone flux, which controls upper tropospheric OH and O<sub>3</sub> concentrations, is found to be more realistic in the new coupled model compared to the STOCHEM model

Using a detailed, fully coupled chemistry-climate model, Tian et al. (2009, AAS) investigated the effect of increasing stratospheric water vapor on ozone depletion and temperature change. They found that increasing stratospheric water tends to accelerate the recovery in the northern high latitudes and delay it in the southern high latitudes. The modeled ozone recovery is more significant between 2000–2050 than between 2050–2100, driven mainly by the larger relative change in chlorine in the earlier period.

Xie et al (2008) studied the radiative effect of ozone and GHG changes on the stratosphere and troposphere exchange (STE) and found that increasing ozone is likely to warm the tropopause and cause more tropospheric water vapor entering into the stratosphere. Their results also show that sea surface temperature (SST) changes associated with increasing atmospheric greenhouse gases (GHG) have a profound impact on the STE. Without corresponding SST changes, the radiative effects of the CO<sub>2</sub> doubling on the STE is less significant than a global 15% O<sub>3</sub> increase.

The HALOE trace gases data from 1992 to 2005 show that NO<sub>x</sub> and ClO<sub>x</sub> play different roles in the ozone photochemical destruction in the stratosphere (Shi et al., 2010). The simulations with SOCRATES3 model indicate that: (1) The ozone depletions of polar areas in summer are mainly attributed to the chemical process of NO<sub>x</sub>; (2) the ozone variations in the Northern sub-polar areas in spring and in the Southern sub-polar areas in winter are mostly contributed by the dynamical transportation. This study also shows that the photochemical mechanisms of ozone loss in the Antarctic and Arctic stratosphere in spring are different. Heterogeneous reactions of polar ClO<sub>x</sub> and homogeneous reactions of sub-polar NO<sub>x</sub> regulate the ozone loss in the Antarctic areas in spring. However, homogeneous reactions of ClO<sub>x</sub> and NO<sub>x</sub> dominate the ozone loss in the Arctic areas in spring. The analyses of the contributions of the dynamical transportation and the photochemical process to the ozone show that 45% of the variation in the entire lower and middle stratosphere and the tropical upper stratosphere is attributed to the dynamical transportation, and 65% of the variation in the upper stratosphere at high latitudes is attributed to the photochemical process.

A coupled chemical/dynamical model (SOCOL-Solar Climate Ozone Links) is applied to study the impacts of future enhanced CO and NO<sub>x</sub> emissions over eastern China on regional chemistry and climate (Wang et al., 2010). The result shows that the increase of CO and NO<sub>x</sub> emissions has significant effects on regional chemistry, including NO<sub>x</sub>, CO, O<sub>3</sub>, and OH concentrations. During winter, the CO concentration

is uniformly increased in the northern hemisphere by about 10 ppbv. During summer, the increase of CO has a regional distribution. The change in O<sub>3</sub> concentrations near eastern China has both strong seasonal and spatial variations. During winter, the surface O<sub>3</sub> concentrations decrease by about 2 ppbv, while during summer they increase by about 2 ppbv in eastern China. The changes of CO, NO<sub>x</sub>, and O<sub>3</sub> induce important impacts on OH concentrations. The changes in chemistry, especially O<sub>3</sub>, induce important effects on regional climate. The analysis suggests that during winter, the surface temperature decreases and air pressure increases in central-eastern China. The changes of temperature and pressure produce decreases in vertical velocity. We should mention that the model resolution is coarse, and the calculated concentrations are generally underestimated when they are compared to measured results. However, because this model is a coupled dynamical/chemical model, it can provide some useful insights regarding the climate impacts due to changes in air pollutant emissions.

The impact of sulfate aerosol, ClO<sub>x</sub> and NO<sub>x</sub> perturbations for two different magnitudes of CH<sub>4</sub> sources on lower stratospheric ozone is studied by using a heterogeneous chemical system that consists of 19 species belonging to 5 chemical families (oxygen, hydrogen, nitrogen, chlorine and carbon) (Wang & Yang, 2006). The present modeled photochemical system can present several different solutions, for instance, periodic states and multi-equilibrium states appearing in turn under certain parameter domains, through chlorine chemistry and nitrogen chemistry together with sulfate aerosol as well as the increasing magnitude of CH<sub>4</sub> sources. The existence of catastrophic transitions could produce a dramatic reduction in the ozone concentration with the increase of external sources. Just in terms of aerosol, it is not an important factor to decide the nonlinear behaviors of the heterogeneous system under the current conditions (Wang & Yang, 2007). However, if the heterogeneous system is controlled jointly by aerosol and a source of reactive chlorine (ClO<sub>x</sub>) or a source of reactive nitrogen (NO<sub>x</sub>), the heterogeneous chemistry may produce significant influence on nonlinear behaviors of the system through chlorine chemistry and nitrogen chemistry. And in some parameters range, it can be presented as the existence of multi-equilibrium solutions which could produce a folding transition.

### *5.2 Stratospheric polar warming: observations and simulations*

Climate changes in stratospheric polar regions play important roles in global climate change. It does not only affect stratospheric polar ozone, especially the Antarctic ozone hole, but also have influences on the troposphere and surface. In the last quarter of the 20th century, one of the most dramatic changes in stratospheric polar region is severe ozone depletion. Associated with severe ozone depletion, the polar stratosphere has displayed strong cooling trends. It was generally thought that the strong cooling in the Antarctic stratosphere is mainly due to the radiative effect of severe ozone depletion and partly due to increasing greenhouse gases that has radiatively cooling effect on the stratosphere.

In contrast to the greatly emphasized Antarctic stratospheric cooling in austral spring and summer and its possible influences on tropospheric climate, Hu and Fu (2009) reported stratospheric warming over a large portion of the Southern

Hemisphere (SH) high latitudes in austral winter and spring. The 28-year lower stratospheric temperature trends for SH high latitudes in austral winter and spring months, derived from microwave sounding unit channel-4 data (MSU-T<sub>4</sub>) show that warming trends occur in all these months. In June, July, and August, the warming trends are weak and statistically not significant. In September and October, the warming trends are strong and statistically significant, with maximum warming of 7–8 °C over the 28 years. In November, cooling trends are dominant, while warming trends are relatively weak and not significant. The warming trends are not right over the polar cap, but centered at about 65°S. The temperature trends show a wavenumber-1 like spatial pattern (a secondary wavenumber-2 pattern can also be identified in September), with eastward shifting in these months. The warming area in September matches the climatological location of high temperatures in the SH stratosphere in austral winter and spring. The spatial pattern in October resembles minor sudden warmings in the Arctic stratosphere, suggesting a tendency of the polar vortex shifting off the polar cap. The cooling trends, especially those in October and November, are due to Antarctic ozone depletion. It is noticed that the stratospheric sudden warming in 2002 has an important contribution to the warming trends in September and October. However, the maximum warming trends are still up to 5 – 6 °C even if the 2002 warming is excluded, and the spatial trend pattern remains the same.

Warming trends are dominant over SH high latitudes, and that the magnitudes of warming trends are much larger than that of cooling trends. However, zonal average would largely reduce the warming magnitude in September. For October, warming trends take nearly half of the SH high-latitude area and have almost equal magnitudes to that of cooling trends (the maximum warming is slightly weaker than the maximum cooling). Zonal average would lead to weak cooling trends in this month. Due to the strong cooling in November and mismatch of locations of warming trends in September and October, conventional seasonal average over the three months yields a maximum warming of about 2.5 °C over the 28 years.

Warming trends in the stratospheric Antarctic are also found in NCEP/NCAR reanalysis, and they match satellite-inferred MSU-T<sub>4</sub> trends exceptionally well in both spatial patterns and magnitudes in all winter and spring months. For both September and October, warming trends are found at all stratospheric layers in the reanalysis data. The spatial patterns of warming trends are similar at these levels. Warming magnitudes increase with altitudes and reach the maximum value of about 11 °C at 30 hPa. At 70 hPa, the maximum warming for both months is greater than 7 °C. One can find that the spatial patterns of warming trends tilt toward the pole with increasing altitudes. In particular, more than half of the polar region is dominated by warming trends in October. Hu et al. (2007) found similar warming trends using different reanalysis data, such as reanalyses from NCEP/Department of Energy and European Center for Medium-Range Weather Forecasts.

The stratospheric warming shown above cannot be explained by radiative effects of increasing greenhouse gases and ozone depletion. It is because increasing greenhouse gases in the atmosphere leads to surface and tropospheric warming but

stratospheric cooling. Ozone depletion during the past few decades has also contributed to stratospheric cooling, especially in the Antarctic lower stratosphere in spring and summer. Therefore, the observed stratospheric warming is likely caused by increased wave activity from the troposphere into the stratosphere because polar stratospheric temperature is also determined by planetary-scale waves. Over 1979-2006, the trends in EP flux vectors and EP flux divergence averaged over August-September-October (ASO), using NCEP/NCAR reanalysis show enhanced wave fluxes from the troposphere into the stratosphere between 50 °S and 90 °S and enhanced equatorward wave propagation between 30 °S-50 °S. EP flux divergence show negative trends in the stratosphere and upper troposphere between about 45 °S and 70 °S. The negative trends indicate enhanced EP flux convergence in these regions. The significant enhancement of EP flux convergence in the stratosphere suggests an intensified Brewer-Dobson circulation and thus enhanced dynamical heating in the polar stratosphere. On the other hand, EP flux divergence shows strong positive trends in the middle troposphere between about 30 °S and 70 °S. The positive trends are indicative of increased wave activity generation.

To examine whether the high-latitude stratospheric warming is a response to SST warming, Hu and Fu (2009) carried out GCM simulations with prescribed SST and sea ice. Five ensemble members of simulations were performed over 1950-2002, forced with observed monthly time-varying SST. Ozone, well-mixed greenhouse gas concentrations, and all other atmospheric compositions are fixed at the 1950 level to isolate the impact of time-varying SST. Trends in ensemble-mean monthly temperatures from GCM simulations at 70 hPa for 1979-2002 show that there exist warming trends over the Antarctic in all winter and spring months, with strong warming in ASO. The lack of stratospheric cooling in GCM simulations (as compared with observations) is because ozone depletion and increasing greenhouse gases are not included in the simulations. The spatial distribution of simulated temperature trends show a wavenumber-1 pattern, with eastward shifting. The locations of simulated maximum warming trends in August and September match observations very well, while that in October does not due to the lack of eastward shifting. The ensemble-mean maximum warming trend occurs in September and October, which is about 3.5 °C over 1979-2002. In June, July, and November, the warming trends are relatively weak, about 1.0 °C for the 24 years. It appears that the seasonality of the simulated warming trends is consistent with observations. Compared with MSU T<sub>4</sub> trends (about 0.29 °C per decade), the simulated warming trends are weaker (about 0.15 °C per decade), which is about half in magnitudes. However, individual simulations show more realistic warming trends. For example, the maximum warming can be as large as about 6 °C over the 24 years in individual simulations. It is found that the reduction of the warming in ensemble mean is largely because of the location mismatch of maximum warming trends between individual simulations.

To verify whether the simulated stratospheric warming in SH high latitudes is related to increasing wave fluxes, we show the trends in simulated EP flux vectors and EP flux divergence. Similar to that in Figure 3, the arrows are generally upward at high latitudes in both the troposphere and the stratosphere, and the stratosphere and

mesosphere all show enhanced convergence of EP fluxes (i.e., negative trends in EP flux divergence). These suggest that the simulated stratospheric warming is indeed related to increasing wave fluxes due to SST forcing.

Temperature trends derived from MSU-T4 also show warming in the stratospheric Arctic in winter (figures not shown). Maximum warming is up to 11 °C over 1979-2006. Hu and Jiang (2009) have carried out GCM simulations forced by observed time varying SST. It is found that SST forcing can reproduce the observed Arctic warming, but with weaker warming magnitudes of about 4~5 °C over the same period. Using AMIP (atmospheric model intercomparison project) simulations results, Hu and Pan (2009) have done multi-model ensemble analysis. They found most AMIP models can reproduce stratospheric Arctic warming. The largest warming trend is about 6 °C over 1979-1999.

The observed strong stratospheric warming may have important implications for ozone-hole recovery. It is well understood that extremely low temperatures in Antarctic winter and spring are one of the critical conditions for severe ozone depletion and the formation of the Antarctic ozone hole. Low polar temperatures lead to the formation of polar stratospheric clouds (PSC), on which heterogeneous chemical reactions involving man-made chlorine take place and result in rapid ozone depletion. The cold conditions also cause the strong Antarctic vortex that provides an isolated environment for polar ozone depletion. According to the simulation results, as SST warming continues as a consequence of increasing greenhouse gases, stratospheric warming in SH high latitudes will also continue. The warming may reduce PSC formation in part of the Antarctic polar region, which slows down heterogeneous chemical reaction rates. Consequently, the warming would cause reduction of the severity and duration of the Antarctic ozone hole. Moreover, the associated increasing wave activity in the SH stratosphere would also cause the Antarctic polar vortex weakened and more ozone transported into the polar region from low latitudes. These will all benefit the recovery of the Antarctic ozone hole, in addition to the decline of ozone depleting substances.

## **6. Progress in Satellite Measurement and Validation**

### *6.1 China satellite to monitor middle atmosphere*

In May 2008, an FY-3 Satellite was launched by National Satellite Meteorological Center of China Meteorological Administration, which is a Chinese second-generation polar orbit meteorological satellite. Onboard this satellite, two main payloads, Ultraviolet Total Ozone Unit (TOU) and Solar Backscatter Ultraviolet Sounder (SBUS), are used to monitor the atmospheric species in the middle atmosphere. These two instruments provide the ozone monitoring globally for the first time for Chinese Satellite.

The main purpose of TOU is to measure the Earth backscatter ultraviolet radiation for retrieving daily global map of atmospheric ozone (Wang et al, 2010a). TOU scans through the sub-satellite point in a direction perpendicular to the orbital plane. The instrument's IFOV is 3.6°×3.6°, and the spatial resolution is about 50 km×50 km at nadir. A mirror scanned perpendicular to the orbital plane in 3.6° step from 54° on the right side of satellite nadir to 54° on the left (relative to direction of

flight), for a total of 31 samples, the swath width is 2908 km. TOU has three operation modes: (1) normal scan mode to measure backscattered solar radiance; (2) wavelength calibration mode to monitoring the wavelength drift; and (3) radiometric calibration mode to measure the solar irradiance through three diffuser plates.

Retrieval of global total column ozone for the first year measurements was validated by comparison with AURA/OMI, Meteop/GOME-2 global ozone products and ground-based ozone measurement data (Wang et al., 2010b). Results show that TOU has a consistent spatial and temporal distribution with OMI and GOME-2. TOU total ozone retrieval has a 3% rms relative error compared with AURA/OMI ozone product and 4.2% rms relative error with ground-based measurements. The maximum difference between satellite retrieval and ground-based measurements was found in the Antarctica ozone hole.

As part of the in-orbit validation of FY-3, a retrieval trial was carried out for the SBUS measurements during 17-30 July, 2008 (Huang et al., 2010). The retrieved ozone profiles were compared with those from the National Oceanic and Atmospheric Administration (NOAA) satellite SBUV/2. The results show that the precision of the measurements and retrieved profiles are quite good. The averaged relative difference percentages of the ozone profiles retrieved from SBUS and those from SBUV/2 are within +/- 7%.

#### *6.2 Cloud effect on the retrieval of total ozone from satellite observation*

Currently, in the TOMS ozone retrieval algorithms, cloud is treated as an opaque Lambertian reflector and the effective reflectivity of the cloud top height is considered to be independent of wavelength. Simulation calculation of atmospheric radiative transfer shows that the reflectivity of cloud top height is dependent on the wavelength because of the integrated effect of cloud scattering, Rayleigh scattering and ozone absorption (Jiang et al., 2007). In addition, cloud is not opaque and radiation can penetrate into the cloud even though the optical thick cloud. Simulating calculations using the V7 algorithm show the multiple scattering below the cloud top height, especially in the cloud can enhance the ozone absorption path length. The effect can make the retrieval value of total ozone amount larger than the actual one, and this phenomena is called "cloud absorption effect". A new inversion algorithm is developed to reduce the error caused by "cloud absorption effect".

The cloud effect on retrieval precision of total ozone from satellite measurements is analyzed with the reference of ground-based total ozone observations (Zheng, 2008). Retrieval errors of satellite total ozone (Total Ozone Mapping Spectrometer, TOMS; Global Ozone Monitoring Experiment, GOME) exhibit obvious increasement with growth of ground-scene cloud fractions at all the ground stations (Waliguan, Xianghe, Longfengshan, and Kunming) in China. Based on the information of cloud fraction and cloud top height from FRESCO (Fast Retrieval Scheme for Clouds from the Oxygen A-band), it's found that retrieval errors of GOME increase only when the FRESCO cloud fraction is above 50%. With the growth of FRESCO cloud top height, the relative errors of GOME total ozone exhibit an obvious increasement at Xianghe and Waliguan with a maximum error of 3%. With the growth of TOMS effective reflectivity, the relative errors of TOMS total ozone increase with the maximum above

2%. It is speculated that there is a high possibility that the contribution of ozone within or below the cloud to the satellite total ozone has been over-estimated in the retrieval algorithms of satellite total ozone.

### 6.3 Validation of ozone retrievals from satellite observation

Ozonesondes launched from Beijing, China, over a 3 year time period are used to evaluate the performance of ozone profile retrievals in the upper troposphere and lower stratosphere (UTLS) from two new spaceborne instruments, the Atmospheric Infrared Sounder (AIRS, version 4 retrieval) on the NASA Aqua satellite and the Microwave Limb Sounder (MLS, version 1.5 retrieval) on the NASA Aura satellite (Bian et al., 2007). Qualitatively, both satellite data sets can reproduce the gradients and variability of ozone in the UTLS region. Quantitatively, the agreement between the AIRS and ozonesonde ozone profiles is largely within 10% in the UTLS region (from 400 to 70 hPa). The statistical difference between the retrieval and ozonesonde data is minimum in the vicinity of the tropopause. The MLS ozone profiles also show good quality in the UTLS region with the best performance between 147 and 46 hPa.

Global Ozone Monitoring Experiment (GOME) with the second Earth Remote Sensing (ERS-2) on board launched in 1995. To evaluate the performance of GOME over China, ozonesonde observations at three stations, Lhasa (1998-1999), Xining (1996), and Beijing (2002-2003) are used to validate ozone profiles from GOME (Cai et al., 2009). Statistical bias determination and precision validation show that in the lower and middle troposphere, the mean biases are significant within 5% at Lhasa and Xining and within 10% at Beijing. In the upper troposphere and lower stratosphere, the mean biases are within 10% at Lhasa and Xining and within 20% at Beijing. In the middle and upper stratosphere, the mean biases are within 5% at all three locations. The GOME monthly mean ozone concentration at 0—2.5 km correlates well with surface ozone measurements, basically capturing the temporal variations of surface ozone at Lhasa, Waliguan, and Linan. In conclusion, from lower troposphere to upper stratosphere, GOME data used here has strong ability to reflect ozone distribution and dynamic changes in China.

## 7. Progress in stratospheric processes over Tibetan Plateau

### 7.1 Wintertime ozone mini-hole process over Tibetan Plateau

For the first time, the “ozone minihole” (OMH) phenomenon is discovered over the Tibetan Plateau region in December 2003 using both satellite and ground-based measurements (Bian et al., 2006). Systematic studies are devoted to both the tropospheric and stratospheric dynamics responsible for the formation of 14 extreme OMH events (two standard deviations below the climatological mean) between 1979 and 2003 (Bian, 2009). The results show that all persistent events (lasting for at least 2 days) are associated with dynamics in both the upper troposphere and lower stratosphere region (below 25 km) and middle stratosphere (25–40 km) (Liu et al., 2010). Ozone reduction below 25 km is generally caused by the uplift of local tropopause and northward transport of tropical ozone-poor air associated with an anomalous anticyclone in the upper troposphere (Bian et al., 2006; Bian, 2009; Liu et al., 2010). These anticyclonic anomalies are closely related to anomalous tropical deep convective heating (Liu et al., 2009, 2010). Especially, in December 2003 event,

the anomalous anticyclone is phase-locked with the tropical Madden-Julian Oscillation. Meanwhile, another 15–46% reduction of Tibetan total column ozone is contributed by the transport of ozone-poor vortex air and/or the displacement of the “low-ozone pocket” inside the full-grown Aleutian High. The latter stratospheric process can be regarded as a unique formation mechanism of OMH events in East Asia, though it only happened twice in the 14 events.

### *7.2 Summertime Stratospheric Processes over Tibetan Plateau*

Tian et al. (2008) examined the effect of the Tibetan Plateau (TP) on the total column ozone (TCO) distribution using a chemistry climate model combined with various observations. They reported that the low TCO over the TP is closely related to large-scale uplift and descent of isentropic surfaces implied by seasonal and longitudinal variations in the tropopause height. They also pointed out that the TCO low over the TP is mainly due to transport processes rather than chemistry.

Zhang et al. (2010) found that the TP has a significant effect on tropopause fold events which are thought to contribute a large part to the STE over the TP. The propagation of the tropopause fold can be affected by the underlying terrain height, but the terrain height has no significant effect on the morphology of folds. The troposphere to stratosphere transport is found to be persistent and almost stationary over the windward slope of the TP during the evolution of folds.

### *7.3 Stratospheric Chemical Species Trend over Tibetan Plateau*

It is found from the analysis of SAGE II dataset that there was a decreasing trend of stratospheric ozone over the Tibetan Plateau (TP) in 1985-2004 (Liu, et al., 2007). The changes in total column ozone mainly resulted from the ozone from 15 km to 50 km, wherein the role of the ozone from 25 km to 50 km was almost equal to that from 15 km to 25 km. From comparing the ozone changes between the TP and east part of China (ECHN), it can be clearly seen that the differences between the two areas was mostly ascribed to the difference of ozone changes from 15 km to 25 km. The trend for May to July was similar to that for yearly average, and the difference of trends between the two areas also mainly occurred in the low stratosphere from 15 km to 25 km. Time serials of aerosol area density over the TP show that big volcanic eruptions significantly affected the stratospheric aerosols over the TP, and the influences continuously lasted for about 6 years. Since 1997 the aerosol area density has increased between 18 km and 25 km over the TP, with a maximum growth of about 4% to 5% per year at 23 km, but decreased between 16 km and 17 km. Meanwhile, the temperature below 37 km has decreased over the TP, and it decreased faster over the TP than over the ECHN. From 37 km to 50 km, the temperature has increased, and it increased faster over the TP than over the ECHN. Both the aerosol increase and temperature decrease in the low stratosphere over the TP would all enhance the role of heterogeneous reactions.

The vertical distribution of the trace gases (NO, NO<sub>2</sub>, HCl, HF, CH<sub>4</sub>, H<sub>2</sub>O and O<sub>3</sub>) over Qinghai-Xizang Plateau were studied (Chen et al. 2006a, 2006b, Bi et al. 2008). And the distributions and variations of aerosol concentration, volume density, surface area density over the Qinghai-Xizang Plateau were also analyzed (Zhou et al. 2008). The significant difference between the mixing ratio of various trace gases over

Qinghai-Xizang plateau and those over the same latitudes (outside of the Plateau, similarly hereinafter) appears also in the region from upper troposphere and lower stratosphere, except NO. In summer, O<sub>3</sub> and HCl mixing ratios in upper troposphere and lower stratosphere over Qinghai-Xizang Plateau are less comparing with those averaged in the same latitudes, while H<sub>2</sub>O, CH<sub>4</sub> and NO<sub>2</sub> mixing ratio over Qinghai-Xizang Plateau are higher in that layer. The situations in winter are just contrary. The difference between NO mixing ratio over Qinghai-Xizang Plateau and that averaged in the same latitudes appears mainly in the middle and upper stratosphere. However, the differences for H<sub>2</sub>O, CH<sub>4</sub> and NO<sub>2</sub> in middle and upper stratosphere are not as significant as those near the tropopause. The differences for O<sub>3</sub> and HCl in middle stratosphere are clear, especially for HCl in summer and both O<sub>3</sub> and HCl in winter. As to the aerosol concentration, there is a higher value of aerosol concentration over the Plateau near the tropopause, which locates beneath the tropopause (~120 hPa) in summer and above the tropopause (~100 hPa) in winter. The main differences in aerosol densities among Qinghai-Xizang Plateau, the eastern part of China and North Pacific occur below 60hPa. In summer the differences are the most notable: aerosol concentration at 120hPa over the Plateau is 1.8 times as large as that over the Plain, and 5.5 times as large as that over the Ocean.

Using radiosonde data and satellite observations, Zhang and Zhou (2008) investigated the air temperature change over the Tibetan Plateau in the period of 1979-2002. It is shown that the air temperature in the lower stratosphere and upper troposphere was out of phase with that in the middle and lower troposphere. The temperature decreased and a decreasing trend appeared in the lower stratosphere and upper troposphere. The amplitude of the temperature decrease in both the annual and the seasonal mean over the Tibetan Plateau was larger than that of the global atmosphere. In the middle and lower troposphere over the Tibetan Plateau, the temperature increased and the increasing trend was stronger than that over the regions in the same latitudes in eastern China. Meanwhile, an analysis of the satellite observed ozone data in the same period of 1979-2002 shows that over the Tibetan Plateau, the total ozone amount declined in each season, and the ozone depleted the most compared to other regions in the same latitudes. Thus, the ultraviolet radiation absorbed in the lower stratosphere and upper troposphere over the Tibetan Plateau becomes less than that over other regions in the same latitudes, and more ultraviolet radiation could enter into the troposphere. This may result in a strong cooling in the lower stratosphere and upper troposphere and an intense warming in the middle and lower troposphere over the Tibetan Plateau. Therefore, the more serious depletion of the ozone over the Tibetan Plateau possibly explains why the air temperature change over the Tibetan Plateau differs from that over other regions in the same latitudes.

#### References:

1. Bi, Y., Y. Chen, R. Zhou, et al., 2008: Study on H<sub>2</sub>O and CH<sub>4</sub> distribution features and seasonal variations over Qinghai-Xizang Plateau using HALOE data. Plateau Meteorology (in Chinese), 27 (2), 249-258.
2. Bian, J., 2009: Features of ozone mini-hole events over the Tibetan Plateau, Adv.

- Atmos. Sci., 26 (2), 305–311.
3. Bian, J., A. Gettelman, H. Chen, and L. L. Pan, 2007: Validation of satellite ozone profile retrievals using Beijing ozonesonde data, *J. Geophys. Res.*, 112, D06305, doi:10.1029/2006JD007502.
  4. Bian, J., G. Wang, H. Chen, et al., 2006: Ozone mini-hole occurring over the Tibetan Plateau in December 2003. *Chin. Sci. Bull.*, 51 (7), 885–888.
  5. Bian, J., and H. Chen, 2008: Statistics of tropopause inversion layer over Beijing. *Adv. Atmos. Sci.*, 25(3), 381-386.
  6. Cai, Z., Y. Wang, X. Liu, et al, 2009: Validation of GOME ozone profiles and tropospheric column ozone with ozone sonde over China. *Journal of Applied Meteorological Science*, 20 (3), 337~345.
  7. Chen, B., X. D. Xu, J. C. Bian, et al., 2010a: Sources, pathways and timescales for the troposphere to stratosphere transport over Asian monsoon regions in boreal Summer. *Chinese Journal of Atmospheric Sciences (in Chinese)*, 34(3), 495-505.
  8. Chen, B., X. D. Xu, J. C. Bian, et al., 2010b: Irreversible stratosphere-troposphere mass exchange characteristics over the Asian summer monsoon region. *Chinese Journal Geophysics*, 53 (5), 1050-1059.
  9. Chen, W., L. Gu, K. Wei, et al., 2008: Studies of the dynamical processes of East Asian monsoon system and the quasi-stationary planetary wave activities. *Chinese J. Atmos. Sci. (in Chinese)*, 32, 950-966.
  10. Chen, W., and L. Kang, 2006: Linkage between the Arctic Oscillation and winter climate over East Asia on the interannual timescale: Roles of quasi-stationary planetary waves. *Chinese J. Atmos. Sci. (in Chinese)*, 30, 863-870.
  11. Chen, W, and T. Li, 2007: Modulation of northern hemisphere wintertime stationary planetary wave activity: East Asian climate relationships by the Quasi-Biennial Oscillation. *J. Geophys. Res.*, 112, D20120, doi:10.1029/2007JD008611
  12. Chen, W., and K. Wei, 2009a: Interannual variability of the winter stratospheric polar vortex in the Northern Hemisphere and their relations to QBO and ENSO. *Adv. Atmos. Sci.*, 26 (5), 855-863, doi:10.1007/s00376-009-8168-6.
  13. Chen, W., and K. Wei, 2009b: Anomalous propagation of the quasi-stationary planetary waves in the atmosphere and its roles in the impact of the stratosphere on the East Asian winter climate. *Adv. Earth Sci. (in Chinese)*, 24, 272-285.
  14. Chen, Y., C. Shi, R. Zhou, et al., 2006a: The vertical distribution and trends of the trace gases in stratosphere over China. *Chinese Journal of Geophysics*, 49 (5), 1165-1174
  15. Chen, Y., R. Zhou, C. Shi, et al., 2006b: Study on the trace species in the stratosphere and their impact on climate. *Advance in Atmospheric Sciences*, 23 (6), 1020-1039.
  16. Chen, Y., M. Yi, Y. Bi, et al., 2009a: A study of the trends of the trace Gases in Stratosphere. *Advances in Earth Science (in Chinese)*, 24 (3), 308-319.
  17. Chen, Y., R. Zhou, S. Deng, 2009b: The relationship between the stratospheric circulation anomalies and the exceptionally serious snow storm and freeze

- calamity. *Journal of University of Science and Technology of China* (in Chinese), 39 (1), 15-22.
18. Chen, Z. Y., and D. R. Lu, 2007: Seasonal variations of the MLT tides in 120° E meridian. *Chinese J. Geophys.* (in Chinese) , 50 (3), 691-700.
  19. Deng, S., and Y. Chen, 2006: The spatial and temporal distribution of the stratospheric sudden warming. *Journal of University of Science and Technology of China* (in Chinese), 36 (4), 445-452.
  20. Deng, S., Y. Chen, Q. Chen, et al., 2006: Planetary wave activity during stratospheric sudden warming. *Chinese Journal of Atmospheric Sciences* (in Chinese), 30 (6), 1236-1248.
  21. Deng, S., Y. Chen Yuejuan, T. Luo, et al., 2008: The possible influence of Stratospheric sudden warming on East Asian weather. *Advance in Atmospheric Sciences*, 25 (5), 841-846.
  22. Deng, S., Y. Chen, T. Luo, et al., 2009: The vertical distribution characteristics of ozone during stratospheric sudden warming (in Chinese). *Chinese Journal of Atmospheric Sciences*, 33 (3), 459-467.
  23. Deng, S., Y. Chen, T. Luo, et al., 2010: Transient characteristics of residual meridional circulation during stratospheric sudden warming. *Advance in Atmospheric Sciences* (to be published).
  24. Fan, W., W. Wang, J. Bian, et al., 2008: The distribution of cross-tropopause mass flux over the Tibetan Plateau and its surrounding regions. *Chinese Journal of Atmospheric Sciences* (in Chinese), 2008, 32 (6), 1309-1318.
  25. Gao, H., J. Xu, W. Yuan, et al., 2006: The temporal variation characteristics of OI5577 airglow intensity and peak density of atomic oxygen in 2000 and 2001 at 52°N. *Chin. J. Space Sci.* (in Chinese), 26 (4), 250-256.
  26. Gao, H., J. Xu, W. Yuan, et al., 2007: The contribution of reaction  $\text{HO}_2 + \text{O} \rightarrow \text{OH} + \text{O}_2$  to OH nightglow. *Chinese Journal of Geophysics*, 50 (4), 884-890.
  27. Gao, H., J. Xu, A. V. Mikhalev, et al., 2009a: The estimate of the peak density of atomic oxygen between 2000 and 2004 at 52N // - *Proc. SPIE*, 7296, 72960M; doi:10.1117/12.823817.
  28. Gao, H., J. Xu, G. Chen et al., 2009b: Impact of the uncertainties of input parameters on the atomic oxygen density derived from OH nightglow. *Chin. J. Space Sci.* (in Chinese), 29 (3), 304-310.
  29. Hu, Y, J. Zhu, and J. Liu, 2007: Antarctic stratospheric winter warming since 1979. *ACTA Meteorologica SINICA*, 65, 773-783.
  30. Hu, Y., and Q. Fu, 2009: Stratospheric warming in Southern-Hemisphere high latitudes. *Atmos. Chemis. & Phys.*, 9, 4329-4340.
  31. Hu, Y., and L. Pan, 2009: Arctic stratospheric winter warming forced by SST increases. *Geophys. Res. Lett.*, 36, L11707, doi:10.1029/2009GL037832.
  32. Hu, Y., and T. Jiang, 2009: GCM simulations on stratospheric Arctic warming in early winter. *Chinese J. Atmos. Sci.* (in Chinese), 33, 1058-1070.
  33. Huang, F. X., N. Q. Liu, M. X. Zhao, et al., 2010: Vertical ozone profiles deduced from measurements of SBUS on FY-3 satellite. *Chinese Sci Bull*, 55, 943-948, doi: 10.1007/s11434-009-0281-5

34. Huang, R., K. Wei, J. Chen, et al., 2007: The East Asian winter monsoon anomalies in the winters of 2005 and 2006 and their relations to the quasi-stationary planetary wave activity in the northern hemisphere. *Chin. J. Atmos. Sci.* (in Chinese), 31, 1033-1048.
35. Jiang G, J. Xiong, W. Wan, et al., 2008a: Observation of 6.5-day waves in the MLT region over Wuhan. *Journal of Atmospheric and Solar-Terrestrial Physics*, 70, 41-48.
36. Jiang, G., J. Xu, J. Xiong, et al., 2008b: A case study of the mesospheric 6.5-day wave observed by radar systems. *J. Geophys. Res.*, 113, D16111, doi:10.1029/2008JD009907.
37. Jiang, G., Xu J., and S. J. Franke, 2009: The 8-h tide in the mesosphere and lower thermosphere over Maui (20.75 N, 156.43 W). *Ann. Geophys.*, 27, 1989-1999.
38. Jiang, G., J. Xu, J. Shi, et al., 2010: The first observation of the atmospheric tides in the mesosphere and lower thermosphere over Hainan, China. *Chinese Sci Bull* (in Chinese), 55 (1), 1-8.
39. Jiang, F., Y. J. Wang, Z. X. Liu, et al., 2007: A theoretical study on the effect of ozone below cloud on total ozone retrieved by TOMS and a new inversion algorithm. *Chinese J. Geophys.* (in Chinese) , 50 (2), 364-369.
40. Li, C., S. Cheng, and J. Pan, 2006: The relationship between the intraseasonal oscillations in the Northern Hemisphere during the boreal winter in the stratosphere and troposphere. *Chinese Journal of Atmospheric Sciences* (in Chinese), 30 (5), 744-752.
41. Li, C., W. Gu, J. Pan, 2008: Meiyu, Arctic Oscillation and stratospheric circulation anomalies. *Chinese J. Geophys.* (In Chinese), 51 (6), 1632-1641.
42. Li, L., C. Y. Li, Y. K. Tan, et al., 2010: Stratospheric sudden warming impacts on the weather/climate in China and its role in the influences of ENSO. *Chinese J. Geophys.*, 53 (7), 1529-1542.
43. Li, S. L., 2009: The influence of tropical Indian Ocean warming on the Southern Hemispheric stratospheric polar vortex. *Sci China Ser D-Earth Sci*, 52(3), 323-332, doi: 10.1007/s11430-009-0029-8
44. Li, S. L., 2010: A comparison of polar vortex response to Pacific and Indian Ocean warming. *Adv. Atmos. Sci.*, 27 (3), 469-482, doi: 10.1007/s00376-009-9116-1.
45. Liu, C., Y. Liu, Z. Cai, et al., 2009: A Madden-Julian Oscillation- triggered record ozone minimum over the Tibetan Plateau in December 2003 and its association with stratospheric "low-ozone pockets", *Geophys. Res. Lett.*, 36, L15830, doi:10.1029/2009GL039025.
46. Liu, C., Y. Liu, Z. Cai, et al, 2010: Dynamic formation of extreme ozone minimum events over the Tibetan Plateau during northern winters 1987–2001, *J. Geophys. Res.*, 115, XXXXXX, doi:10.1029/2009JD013130.
47. Liu, X., J. Xu, W. Li, et al., 2009a: Parallel numerical model for the simulation of gravity wave's nonlinear propagation. *Chin. J. Space Sci.* (in Chinese), 29 (3), 296-303.
48. Liu, X., J. Xu, W. Li, et al., 2009b: Parallel numerical model for the simulation of

- three dimensional gravity wave's propagation. *Chin. J. Space Sci.* (in Chinese), 29 (6), 563-572.
49. Liu, X., J. Xu, H. Gao, et al., 2009c: Kelvin-Helmholtz billows and their effects on mean state during gravity wave propagation. *Ann. Geophys.*, 27, 2789–2798.
  50. Liu, X. J. Xu, H. Liu, et al., 2008: Nonlinear interactions between gravity waves with different wavelengths and diurnal tide. *J. Geophys. Res.*, 113, D08112, doi:10.1029/2007JD009136, 2008.
  51. Liu, Y., C. Guo, W. Li, et al., 2007: Trends of stratospheric ozone and aerosols over Tibetan Plateau. *Acta Meteor Sinica*, 65 (6), 938-945.
  52. Liu, Y., and C. Lu, 2010: The influence of the 11-year sunspot cycle on the atmospheric circulation during winter. *Chinese Journal Geophysics*, 53 (6), 1269-1277.
  53. Ren, R., and C. Xiang, 2010: Temporal and spatial connections of the stratospheric polar vortex oscillation to the ENSO tropical SST anomalies (in Chinese). *Acta Meteorologica Sinica*, 68 (3), 285-295.
  54. Ren, R. C., and Ming Cai, 2008: Meridional and downward propagation of atmospheric circulation anomalies. Part II: southern hemisphere cold season variability. *J. Atmos. Sci.*, 65, 2343-2359, doi: 10.1175/2007JAS2594.1
  55. Ren, R.-C., and M. Cai, 2007: Meridional and vertical out-of-phase relationships of temperature anomalies associated with the Northern Annular Mode variability, *Geophys. Res. Lett.*, 34, L07704, doi:10.1029/2006GL028729.
  56. Shi, C., Y. Chen, B. Zheng, et al., 2010: A Comparison of the Contributions of Dynamical Transportation and Photochemical Process to Ozone's Seasonal Variation in the Stratosphere. *Chinese Journal of Atmospheric Sciences* (in Chinese), 34 (2), 399-406.
  57. Tian, W. S, M. P. Chipperfield, and Q. Huang, 2008: Effects of the Tibetan Plateau on total column ozone distribution. *Tellus*, 60B, 4, 622-635, doi: 10.1111/j.16000889.2008.00338.x.
  58. Tian W., M. P. Chipperfield, D. Lu, 2009: Impact of increasing stratospheric water vapor on ozone depletion and temperature change. *Adv. Atmos. Sci.*, 26 (3), 373-380, doi: 10.1007/s00376-009-0373-9.
  59. Tian, W. M. Chipperfield, D. Stevenson, et al., 2010: The effects of stratosphere-troposphere chemistry coupling on tropospheric ozone. *J. Geophys. Res.* (In press)
  60. Wang, G. L., and P. C. Yang, 2006: On the Nonlinear Response of Lower Stratospheric Ozone to NO<sub>x</sub> and ClO<sub>x</sub> Perturbations for Different CH<sub>4</sub> Sources. *Adv. Atmos. Sci.*, 23 (5), 750-757, doi:10.1007/s00376-006-0750-6.
  61. Wang, G. L., and P. C. Yang, 2007: On the nonlinear response of lower stratospheric ozone to NO<sub>x</sub> and ClO<sub>x</sub> perturbations. *Chinese J. Geophys.* (in Chinese), 50 (1): 51-57.
  62. Wang, G. L., P. C. Yang, C. X. Liu, et al., 2010: Impacts of future NO<sub>x</sub> and CO emissions on regional chemistry and climate over eastern China. *Adv. Atmos. Sci.*, 27(4), 750-760, doi:10.1007/s00376-009-9101-8.
  63. Wang, L., W. Chen, R. Huang, et al., 2007: The climatology and annual cycle of

- meridional transport of westerly momentum by stationary waves in the northern hemisphere. *Chin. J. Atmos. Sci.* (in Chinese), 31, 377-388.
64. Wang, L., W. Chen, W. Zhou, et al., 2010: Effect of the climate shift around mid 1970s on the relationship between wintertime Ural blocking circulation and East Asian climate. *International Journal of Climatology*, 30, 153-158.
  65. Wang, L., R. Huang, L. Gu, et al., 2009: Interdecadal variations of the East Asian winter monsoon and their association with quasi-stationary planetary wave activity. *Journal of Climate*, 22, 4860-4872.
  66. Wang, W. H., X. Y. Zhang, X. Q. An, et al., 2010b: Analysis for retrieval and validation results of FY-3 Total Ozone Unit (TOU). *Chinese Sci Bull*, 55, 3037-3043, doi: 10.1007/s11434-010-3240-2
  67. Wang, Y. M., Y. J. Wang, W. H. Wang, et al., 2010a: FY-3 satellite ultraviolet total ozone unit. *Chinese Sci Bull*, 55, 84-89, doi: 10.1007/s11434-009-0335-8
  68. Wei, K., W. Chen, R. Huang, 2007a: Association of tropical Pacific sea surface temperatures with the stratospheric Holton-Tan Oscillation in the Northern Hemisphere winter. *Geophys. Res. Lett.*, 34:L16814, doi:10.1029/2007GL030478
  69. Wei, K., W. Chen, R. Huang, 2007b: Dynamical diagnosis of the breakup of the stratospheric polar vortex in the Northern Hemisphere. *Science in China Series D: Earth Sciences*, 50 (9), 1369-1379.
  70. Wei, K., W. Chen, R. Huang, 2008: Comparison of the roles of wave activities in the breakup of the stratospheric polar vortex between the Southern and Northern Hemispheres. *Chin. J. Atmos. Sci.* (in Chinese), 32, 206-219
  71. Wu, Y. F., and J. Xu, 2006a: Comparison of horizontal velocity spectra derived from chaff rockets with saturation models. *J. Geophys. Res.*, 111, D13109, doi:10.1029/2005JD006065.
  72. Wu, Y. F., J. Xu, W. Yuan, et al., 2006b: Spectral analysis of 10-m resolution temperature profiles from balloon soundings over Beijing, *Ann. Geophys.*, 24, 1-8.
  73. Xie, F., W. Tian, and M. P. Chipperfield, 2008: Radiative effect of ozone change on stratosphere-troposphere exchange, *J. Geophys. Res.*, 113, D00B09, doi:10.1029/2008JD009829.
  74. Xu, J., C.-Y. She, W. Yuan, et al., 2006: Comparison between the temperature measurements by TIMED/SABER and lidar in the midlatitude. *J. Geophys. Res.*, 111, A10S09, doi:10.1029/2005JA011439.
  75. Xu, J., Q. Ji, W. Yuan, et al., 2006: Comparison between the TIMED observed global temperature distribution and the NRLMSISE-00 empirical atmospheric model. *Chin. J. Space Sci.* (in Chinese), 26 (3), 177-182.
  76. Xu, J., H.-L. Liu, W. Yuan, et al., 2007a: Mesopause structure from thermosphere, ionosphere, mesosphere, energetics, and dynamics (TIMED)/sounding of the atmosphere using broadband emission radiometry (SABER) observations, *J. Geophys. Res.*, 112, D09102, doi:10.1029/2006JD007711.
  77. Xu, J., A. K. Smith, W. Yuan, et al., 2007b: Global structure and long-term variations of zonal mean temperature observed by TIMED/SABER. *J. Geophys. Res.*, 112, D24106, doi:10.1029/2007JD008546.

78. Xu, J., A. K. Smith, H.-L. Liu, et al., 2009a: Seasonal and quasi-biennial variations in the migrating diurnal tide observed by Thermosphere, Ionosphere, Mesosphere, Energetics and Dynamics (TIMED). *J. Geophys. Res.*, 114, D13107, doi:10.1029/2008JD011298.
79. Xu, J., A. K. Smith, H.-L. Liu, et al., 2009b: Estimation of the equivalent Rayleigh friction in MLT region from the migrating diurnal tides observed by TIMED, *J. Geophys. Res.*, doi:10.1029/2009JD012209.
80. Xu, J., A. K. Smith, G. Jiang, et al., 2010: The seasonal variation of the Hough modes of the diurnal component of ozone heating evaluated from Aura/MLS observations, *J. Geophys. Res.*, doi:10.1029/2009JD013179.
81. Xu, J., A. K. Smith, R. L. Collins, et al., 2006: Signature of an overturning gravity wave in the mesospheric sodium layer: Comparison of a nonlinear photochemical-dynamical model and lidar observations, *J. Geophys. Res.*, 111, D17301, doi:10.1029/2005JD006749.
82. Yi, M., and Y. Chen, 2008: Distribution of stratospheric trace gases after the Antarctic sudden warming. *Journal of University of Science and Technology of China (in Chinese)*, 38(1), 41-49.
83. Yi, M., 2009: Study of the anomaly of stratospheric polar Vortex and its impact on the troposphere. PhD dissertation (in Chinese), University of Science and Technology of China.
84. Yi, M., Y. Chen, R. Zhou, et al., 2009: Analysis on isentropic potential vorticity for the snow calamity in South China and the stratospheric polar vortex in 2008. *Plateau Meteorology (in Chinese)*, 28 (4), 880-888.
85. Yuan, W., J. Xu, Y. Wu, et al., 2009: Vertical wavenumber spectra of atmospheric ozone measured from ozonesonde observations. *Advances in Space Research*, 43, 1364-1371.
86. Zhan, R., and J. Li, 2008: Influence of atmospheric heat sources over the Tibetan Plateau and the tropical western North Pacific on the inter-decadal variations of the stratosphere-troposphere exchange of water vapor. *Science in China (D)*, 51 (8), 1179-1193.
87. Zhang, M., W. Tian, L. Chen, et al., 2010: Cross tropopause mass exchange associated with a tropopause fold event over the North-eastern Tibetan Plateau. *Advance in Atmospheric Sciences*, 26, do:10.1007/s00376-010-9129-9.
88. Zhang, R., and S. Zhou, 2008. The air temperature change over the Tibetan Plateau during 1979-2002 and its possible linkage with ozone depletion. *Acta Meteorologica Sinica*, 66 (6), 916-925.
89. Zheng, X., 2008: Investigating on effect of cloud on the precision of total ozone from satellite measurements over China regions. *Chinese Journal of Atmospheric Sciences (in Chinese)*, 32 (6), 1431-1444.
90. Zheng, Y. G., J. Chen, C. Y. Chan, et al., 2008: Identifying method of ozone enhancement and multi-scale characteristics of ozone change in the mid-upper troposphere over South China. *Chinese J. Geophys. (in Chinese)*, 51 (3), 668-681.
91. Zhou, R., Y. Chen, Y. Bi, et al., 2008: Aerosol distribution over the Qinghai-Xizang Plateau and its relationship with O<sub>3</sub>. *Plateau Meteorology (in*

Chinese), 27(3), 500-507.